Gravitational-wave data analysis for standard and non-standard sources of compact binary coalescences in the third LIGO-Virgo observing run

Elisa Nitoglia

▶ **To cite this version:**

Elisa Nitoglia. Gravitational-wave data analysis for standard and non-standard sources of compact binary coalescences in the third LIGO-Virgo observing run. Astrophysics [astro-ph]. Université Claude Bernard - Lyon I, 2023. English. NNT : 2023LYO10143 . tel-04577839

HAL Id: tel-04577839
https://theses.hal.science/tel-04577839

Submitted on 16 May 2024

HAL is a multi-disciplinary open access archive for the deposit and dissemination of scientific research documents, whether they are published or not. The documents may come from teaching and research institutions in France or abroad, or from public or private research centers.

L'archive ouverte pluridisciplinaire **HAL**, est destinée au dépôt et à la diffusion de documents scientifiques de niveau recherche, publiés ou non, émanant des établissements d'enseignement et de recherche français ou étrangers, des laboratoires publics ou privés.

THESE de DOCTORAT DE
L'UNIVERSITE CLAUDE BERNARD LYON 1

Ecole Doctorale N° 52
Physique et Astrophysique

Discipline : Astrophysique

Soutenue publiquement le 20/09/2023, par :
Elisa Nitoglia

Gravitational-Wave Data Analysis for Standard and Non-Standard Sources of Compact Binary Coalescences in the Third LIGO-Virgo Observing Run

---

Devant le jury composé de :

Pannarale, Francesco	Professeur Associé, Université de Rome La Sapienza (Italie)	Rapporteur
Christensen, Nelson	Directeur de Recherche, CNRS Nice	Rapporteur
Augier, Corinne	Professeure des Universités, Université Lyon 1	Présidente
Marion, Frédérique	Directrice de Recherche, CNRS Annecy	Examinatrice
Sordini, Viola	Chargée de Recherche-HDR, CNRS Lyon	Directrice de thèse
Chierici, Roberto	Directeur de Recherche, CNRS Lyon	Co-directeur de thèse

UNIVERSITÉ CLAUDE BERNARD LYON 1

Abstract

Ecole Doctorale de Physique et Astrophysique (ED N° 52)
Department de Physique

Doctor of Philosophy

Gravitational-Wave Data Analysis for Standard and Non-Standard Sources of Compact Binary Coalescences in the Third LIGO-Virgo Observing Run

by Elisa NITOGLIA

This PhD thesis presents a comprehensive investigation into the detection of gravitational wave signals from compact binary mergers, with a specific focus on the analysis of data from the third observing run of the LIGO-Virgo Collaboration.

The manuscript begins by providing an introduction to the fundamental principles of the theory of General Relativity, including the prediction of the existence of gravitational-waves and an overview of the astrophysical sources that generate these waves. It also provides a detailed description of interferometers, the instruments used in gravitational-wave observatories, and their basic functioning.

Subsequently, the manuscript focuses on advanced data analysis techniques developed to extract gravitational-wave signals from the detector noise. Special attention is given to the Multi-Band Template Analysis (MBTA) pipeline, which the author actively contributes to as part of the MBTA team. The functioning and methodology of the MBTA pipeline are described in detail, highlighting its role in the detection and analysis of gravitational-wave signals.

The manuscript then proceeds to present the results obtained from the standard analysis conducted to search for signals originating from the coalescence of binary black holes, binary neutron stars, and black hole-neutron star binaries in the data collected during the third observing run. The analysis includes a comprehensive examination of the observed signals, their properties, and the astrophysical implications of the detected mergers.

Additionally, the manuscript explores the latest advancements in the search for gravitational waves emitted by sub-solar mass binaries, which involve binary systems comprising at least one object with a mass below the mass of the Sun, providing an in-depth investigation into the methodology and results of the sub-solar mass search during the third observing run.

Through this comprehensive investigation, the manuscript aims at contributing to the advancement of gravitational-wave astronomy, offering a comprehensive exploration of gravitational-wave research, encompassing the main achievements of the third observing run in both standard and sub-solar mass searches.

Contents

List of Abbreviations

ASD	**A**mplitude **S**pectral **D**ensity
BBH	**B**inary **B**lack **H**ole
BH	**B**lack **H**ole
BNS	**B**inary **N**eutron **S**tar
CBC	**C**ompact **B**inary **C**oalescence
CMB	**C**osmic **M**icrowave **B**ackground
CRS	**C**ombined **R**anking **S**tatistic
DBH	**D**ark **B**lack **H**ole
DM	**D**ark **M**atter
EB	**E**arly PBH **B**inary
EOS	**E**quation **O**f **S**tate
EMRI	**E**xtreme **M**ass **R**atio **I**nspirals
ER	**E**xcess **R**ate
FAR	**F**alse **A**larm **R**ate
FF	**F**itting **F**actor
FFT	**F**ast **F**ourier **T**ransform
GR	**G**eneral **R**elativity
GW	**G**ravitational **W**ave
GWTC	**G**ravitational **W**ave **T**ransient **C**atalog
IFAR	**I**nverse **F**alse **A**larm **R**ate
ISCO	**I**nnermost **S**table **C**ircular **O**rbit
LB	**L**ate PBH **B**inary
ΛCDM	**Λ** **C**old **D**ark **M**atter
LIF	**L**ocal **I**nertial **F**rame
LVK	**L**IGO **V**irgo **K**AGRA
MBTA	**M**ulti **B**and **T**emplate **A**nalysis
MDC	**M**ock **D**ata **C**hallenge
NR	**N**umerical **R**elativity
NS	**N**eutron **S**tar
NSBH	**N**eutron **S**tar **B**lack **H**ole
PBH	**P**rimordial **B**lack **H**ole
PI	**P**air **I**nstability
PN	**P**ost **N**ewtonian
PSD	**P**ower **S**pectral **D**ensity
PTA	**P**ulsar **T**iming **A**rray
RT (bank)	**R**eal **T**emplate (bank)
SMBHB	**S**uper **M**assive **B**lack **H**ole **B**inary
SSM	**S**ub **S**olar **M**ass
SNR	**S**ignal to **N**oise **R**atio

TT	**T**ransverse **Traceless** gauge
VT (bank)	**V**irtual **T**emplate (bank)
WD	**W**hite **D**warf
WDM	**W**arm **D**ark **M**atter

Physical Constants

Boltzmann Constant	$k_B = 1.380\,649 \times 10^{-16}\,\mathrm{g\,cm^2\,s^{-2}\,K^{-1}}$
Parsec	$1pc = 3.09 \times 10^{18}\,\mathrm{cm}$
Proton Mass	$m_p = 1.6726 \times 10^{-24}\,\mathrm{g}$
Reduced Planck Constant	$\hbar = 1.0546 \times 10^{-27}\,\mathrm{g\,cm^2\,s^{-1}}$
Solar Mass	$M_\odot = 1.989 \times 10^{33}\,\mathrm{g}$
Speed of Light	$c = 2.9979 \times 10^{10}\,\mathrm{cm\,s^{-1}}$
Universal Constant of Gravitation	$G = 6.6720 \times 10^{-8}\,\mathrm{cm^3\,g^{-1}\,s^{-2}}$

Introduction

The study of gravitational waves has undergone a remarkable journey, spanning over a century of scientific exploration and culminating in the groundbreaking detection of confirmation of their existence. This journey began with the visionary work of Albert Einstein and the development of the theory of General Relativity, presented in 1915, which constitutes a profound understanding of gravity described as the curvature of spacetime caused by massive objects. One of the key predictions of this theory was the existence of gravitational waves: ripples in the fabric of spacetime itself emitted by accelerating massive objects. For several decades, the concept of gravitational waves remained purely theoretical, awaiting the technological advancements necessary for their direct detection. Scientists recognised the potential significance of these elusive waves, as they offered a new window into the Universe and the potential to unveil phenomena otherwise invisible to traditional astronomy.

The quest to detect gravitational waves began in earnest in the 1960s, with pioneering efforts led by scientists such as Joseph Weber, who developed the first resonant mass detectors. These early experiments aimed to directly detect the faint signals of gravitational waves, but their results were met with skepticism and controversy. However, the field took a monumental leap forward in the early 1990s with the proposal and subsequent development of the Laser Interferometer Gravitational-Wave Observatory (LIGO) by physicists Rainer Weiss, Kip Thorne, and Ronald Drever, and the Virgo interferometer. LIGO and Virgo consist of kilometer-scale interferometers that use laser beams to measure infinitesimal changes in the distances between mirrors caused by passing gravitational waves.

After decades of meticulous engineering and technological advancements, the LIGO detectors became sensitive enough to detect the minuscule distortions induced by gravitational waves. On September 14, 2015, the historic moment arrived: an unmistakable gravitational-wave signal was detected. This signal, named *GW*150914, originated from the merger of two black holes located over a billion light-years away. The detection of this event marked the first direct observation of gravitational waves and confirmed Einstein's century-old prediction. It was a monumental achievement that ushered in a new era of gravitational-wave astronomy. Since this groundbreaking detection, the gravitational-wave research has experienced a rapid expansion. Advanced LIGO and other international collaborations, such as Advanced Virgo, have continued to observe numerous gravitational-wave events, including mergers of binary black holes, binary neutron stars, and even black hole-neutron star systems.

Simultaneously, while the standard gravitational-wave searches focus on high-mass objects, there is an emerging interest in exploring the gravitational-wave signatures

from sub-solar mass systems. By studying the as-yet-undetected gravitational waves emitted by these objects, it is possible to gain valuable insights into their formation mechanisms, evolution, and the underlying physical processes governing their behaviour. The sub-solar mass research has been performed since the Initial LIGO, experiencing remarkable progress, driven by the quest to uncover the mysteries surrounding objects with masses below the solar threshold. Through a multi-faceted approach encompassing data analysis techniques, this thesis delves into the exploration of the results of the latest third observing run of the LIGO-Virgo-KAGRA collaboration. This manuscript is structured as follows:

Chapter I serves as a comprehensive review of the fundamental principles of the gravitational wave generation. It starts by exploring the theory of General Relativity, providing the theoretical foundation for understanding gravitational waves. Moreover, it examines the various potential sources of gravitational waves, shedding light on the astrophysical phenomena that can generate these elusive signals.

In Chapter II, the focus shifts towards the practical implementation of gravitational wave detection. The chapter provides an explanation of the basic functioning of interferometers, the key instruments used in gravitational wave observatories. It also introduces the current network of detectors, highlighting the milestones achieved during the initial observing runs.

Chapter III is dedicated to the Multi Band Template Analysis (MBTA) search pipeline for compact binary coalescences. It presents a thorough description of the MBTA methodology, which plays a crucial role in identifying and characterising gravitational wave signals from binary systems since the very first observing run.

In Chapter IV, the focus zooms in on the LIGO-Virgo third observing run. This chapter provides a comprehensive summary of this observing period, with a particular emphasis on the standard search for signals originating from binary black holes, binary neutron stars, and black hole-neutron star binaries in which the candidate actively participated and contributed. Notable detections and significant findings from the third observing run are highlighted, offering a glimpse into the exciting discoveries made during this period.

Finally, Chapter V reports a detailed description of the sub-solar mass search conducted during the third observing run. This chapter holds special importance, as the candidate played a key role as the main analyst for the MBTA search pipeline. Furthermore, the active involvement in the paper writing team of the LIGO-Virgo-KAGRA paper further underscores the candidate's contribution.

Through the organisation of these five chapters, this manuscript offers a comprehensive exploration of gravitational wave research. It encompasses theoretical foundations, experimental apparatuses, data analysis techniques, and significant observational findings. By presenting this comprehensive overview, the manuscript aims to contribute to the broader understanding of gravitational-wave science and its implications for astrophysics and cosmology.

CHAPTER1

The Fascinating World of Gravitational Waves

Newton's laws of motion and his universal law of gravitation provide a good description of many phenomena in the Solar System on a macroscopic scale. They accurately predict the motion of celestial bodies, have been confirmed by several observations, and continue to be widely used in many areas of astrophysics. However, they are not accurate when applied to strong gravitational fields, such as the ones produced by compact objects, or when considering high speeds, such as those near to the speed of light. Einstein's theory of General Relativity (GR), which was published in 1915 [182], provides a more accurate description of gravity by treating it as a manifestation of the curvature of spacetime caused by the presence of matter and energy. This theory has been extensively tested and is one of the pillars of modern physics. In the following chapter the basic concepts of GR will be exposed, as well as one of its main predictions: the existence of gravitational waves.

1.1 The Theory of General Relativity

This section explains how the theory of GR predicts the existence of gravitational waves (GWs). Starting from Einstein's equations, some assumptions will be made which will allow us to derive the wave equation, and its characteristics.

1.1.1 Einstein Equations

In the theory of GR, space and time are treated as a single entity known as spacetime. This four-dimensional manifold is mathematically represented by the metric tensor $g_{\mu\nu}$, which encodes information about the distances and angles between points, called events and labeled by four coordinates $x^\mu = (x^0, x^i)$ describing the coordinate time (x^0) and the position (x^i). The metric tensor is crucial in the theory of GR because it defines the spacetime structure and is determined by the distribution of matter and energy in the Universe. The line element ds^2, which is proportional to $g_{\mu\nu}$, can be used to describe the spacetime distance between two points with coordinates x^μ and $x^\mu + dx^\mu$

$$ds^2 = g_{\mu\nu} dx^\mu dx^\nu \ . \tag{1.1}$$

Equation (1.1) clearly shows how a change in the line element reflects a change in the geometry of spacetime, which curvature is mathematically described by the Riemann tensor

$$R_{\kappa\lambda\mu\nu} = g_{\kappa\alpha} R^\alpha_{\lambda\mu\nu} = g_{\kappa\alpha}(\Gamma^\alpha_{\lambda\nu,\mu} - \Gamma^\alpha_{\lambda\mu,\nu} - \Gamma^\alpha_{\sigma\nu}\Gamma^\sigma_{\lambda\mu} + \Gamma^\alpha_{\sigma\mu}\Gamma^\sigma_{\lambda\nu}) \ , \tag{1.2}$$

where the notation $\Gamma^{\alpha}_{\lambda\nu,\mu}$ indicates the partial derivative of $\Gamma^{\alpha}_{\lambda\nu}$ with respect to x^{μ}, and $\Gamma^{\alpha}_{\lambda\nu}$ are the Christoffel's symbols, which can be expressed as a linear combination of the first derivatives of the metric tensor as

$$\Gamma^{\alpha}_{\lambda\nu} = \frac{1}{2} g^{\alpha\gamma} \left(g_{\gamma\lambda,\nu} + g_{\gamma\nu,\lambda} - g_{\lambda\nu,\gamma} \right) . \tag{1.3}$$

Therefore, the Riemann tensor is derived from $g_{\mu\nu}$ and it is a measure of the deviation of the spacetime from being flat, or Minkowskian, for which $R_{\kappa\lambda\mu\nu} = 0$. Other relevant quantities that describe the curvature of the spacetime can be derived from the Riemann tensor: the Ricci tensor $R_{\mu\nu} = g^{\alpha\beta} R_{\alpha\mu\beta\nu}$ and the scalar curvature $R = g^{\mu\nu} R_{\mu\nu}$ that describe the local and overall curvature respectively. While all these previous quantities describe the curvature of the spacetime, hence the gravitational field, they do not provide any information about its source, which instead is described by the stress-energy tensor $T^{\mu\nu}$. The stress-energy tensor is defined at each point in spacetime and its components determine how much energy and momentum are present in that region of spacetime, therefore it describes the distribution of matter and energy in the Universe. The Einstein field equations (1.4) connect the curvature of spacetime, as represented by the Ricci tensor and the scalar curvature, with the distribution of matter and energy, as represented by the stress-energy tensor

$$R_{\mu\nu} - \frac{1}{2} g_{\mu\nu} R = \frac{8\pi G}{c^4} T_{\mu\nu} , \tag{1.4}$$

where the left-hand term is called Einstein tensor. From Eq. (1.4), it is possible to argue that the gravitational field is connected to the geometry of the spacetime and related to the distribution of matter and energy in it. In vacuum, where there is no matter or energy present, $T_{\mu\nu} = 0$, implying that the Ricci tensor and the scalar curvature also vanish. However, the Riemann tensor does not necessarily vanish in vacuum unless the gravitational field vanishes or is uniform and constant. This means that the spacetime may still be curved as in the case of black holes (BHs), for example. A BH is defined as an object with such strong gravity that not even light can escape its grasp. This is due to the matter and energy that falls into it and gets compressed to an extremely small size and infinite density, resulting in a point-like singularity where the standard laws of physics break down. According to the theory of GR, anything that crosses the event horizon, defined as the region surrounding a massive object where the escape velocity exceeds the speed of light, becomes irretrievable. Despite the absence of matter inside a BH as found in ordinary objects, its strong gravitational field is still present. This is a unique feature of GR: gravity is not a force between masses, but rather it is the curvature of spacetime caused by the presence of matter and energy.

1.1.2 Linearised Einstein Field Equations

The linearised theory of gravity, also known as the weak field approximation, is a simplification of the full theory of GR that is used to describe the behaviour of particles moving in a weak and stationary gravitational field. In this approximation, the metric tensor is assumed to be the sum of the flat Minkowskian spacetime metric tensor $\eta_{\mu\nu} = diag(-1, 1, 1, 1)$ and a small perturbation $h_{\mu\nu}$, which represents the weak gravitational field, as

$$g_{\mu\nu} = \eta_{\mu\nu} + h_{\mu\nu} \qquad \left| h_{\mu\nu} \right| \ll 1 , \tag{1.5}$$

in other words, we are examining a field that is so weak that the metric is nearly flat. The assumption that the perturbation is small, allows us to keep only terms linear in $h_{\mu\nu}$ in the expansion of Einstein equations and discard higher order terms. By defining the trace-reversed perturbation $\bar{h}_{\mu\nu} = h_{\mu\nu} - \frac{1}{2}\eta_{\mu\nu}h$ and imposing the harmonic gauge conditions $\partial_\nu \bar{h}^{\mu\nu} = 0$, the Einstein field equations can be simplified to the form

$$\Box \bar{h}_{\mu\nu} = -\frac{16\pi G}{c^4} T_{\mu\nu} \,, \tag{1.6}$$

where $\Box = \eta_{\mu\nu}\partial_\mu\partial_\nu$ is the d'Alambertian. Eq. (1.6) is the wave equation with a source term, which in vacuum reduces to

$$\Box \bar{h}_{\mu\nu} = 0 \,. \tag{1.7}$$

The choice of the harmonic gauge condition makes the equations of propagation of GWs take a form similar to that of Maxwell's equations in the Lorenz gauge. The simplest solution to the wave equation (1.7) is a plane wave solution of the form

$$\bar{h}_{\mu\nu} = A_{\mu\nu} e^{ik_\alpha x^\alpha} \,, \tag{1.8}$$

where $A_{\mu\nu}$ is the polarisation tensor, containing information about amplitude and polarisation of the propagating wave, while k_α is the wave vector. Eq. (1.8) describes a wave that is uniform in all directions and propagates in a specific direction with a specific frequency and amplitude.

1.1.3 Transverse-Traceless Gauge

The transverse-traceless gauge, or TT gauge, is a specific choice of coordinates that can be used to reduce the number of independent components of the perturbation $h_{\mu\nu}$ from ten to only two, and to easily identify the physical properties of the waves. In this gauge, the time components of the perturbation are set to zero ($\bar{h}_{\mu 0} = 0$), which means that the wave is transverse to its direction of propagation, and the sum of the diagonal components of the perturbation is null ($\bar{h}^\mu_\mu = 0$), therefore the matrix is traceless and $h_{\mu\nu}$ and $\bar{h}_{\mu\nu}$ coincide. When combined with three additional conditions given by the symmetry of $h_{\mu\nu}$, there are a total of eight conditions that the perturbation must satisfy. This leaves only two independent components, corresponding to the two degrees of freedom of the wave. When applied to a plane wave propagating along the z-axis, the TT gauge allows to identify the two functions that represent the possible polarisation states of the wave

$$h^{TT}_{\mu\nu} = \begin{bmatrix} 0 & 0 & 0 & 0 \\ 0 & h_+ & h_\times & 0 \\ 0 & h_\times & -h_+ & 0 \\ 0 & 0 & 0 & 0 \end{bmatrix} \,, \tag{1.9}$$

where h_+ and $h_\times$ are the plus and cross polarisations. The polarisation matrix is fully described by two real numbers h_+ and $h_\times$, that can be measured by analysing the strain of a GW on a detector, as we will see in the following chapter. It is relevant to note that the polarisation of a GW is not a fixed property of the wave and can change as the wave propagates through a medium.

1.2 Gravitational Waves Meet Matter

So far it has been demonstrated how the Einstein's theory predicts the existence of GWs. In this section the effect induced by a GW on a free-falling particle will be analysed.

1.2.1 Geodesic Deviation

The effects of a weak gravitational field on matter can be computed by using the linearised metric and the appropriate equations of motion, such as the geodesic equation

$$\frac{d^2x^\alpha}{d\tau^2} + \Gamma^\alpha_{\mu\nu}\left[\frac{dx^\mu}{d\tau}\frac{dx^\nu}{d\tau}\right] = 0\,, \tag{1.10}$$

where τ is the particle's proper time. The first term represents the motion of a free particle and the second term represents the effect of gravity on the particle's motion. In a locally inertial frame (LIF), the spacetime is flat and the second term of the geodesic equation vanishes, reducing the equations of motion to only the first term. This is known as the principle of equivalence, which states that the effects of gravity are indistinguishable from those of acceleration in a LIF. In the weak-field limit, since the deviation of the particle's motion from a straight line is small, the equation of geodesic reduces to the Newton's law of gravitation.

Equation (1.10) describes the path of a test particle moving in a curved spacetime without affecting the spacetime itself. However, to infer information about the curvature it is necessary to compare the motion of two test particles, separated by the vector δx^α, and the followed geodesics, observing any deviation from the path of a particle in a flat spacetime. This deviation is called geodesic deviation and it is proportional to the Riemann tensor, which represents the tidal force experienced by the particle, which therefore encodes the spacetime's curvature

$$\frac{d^2\delta x^\alpha}{d\tau^2} = R^\alpha_{\beta\mu\nu}\frac{dx^\beta}{d\tau}\frac{dx^\mu}{d\tau}\delta x^\nu\,. \tag{1.11}$$

In a flat spacetime, all geodesics appear as straight lines and all the components of the Riemann tensor are zero. From Eq. (1.11), this implies that the relative acceleration of the particles is null, thus the particles remain at rest. On the other hand, the passage of a GW affects the system, inducing a relative motion, and changing the proper distance between particles. Let's consider then two free-falling particles with coordinates x^μ_A and x^μ_B initially at rest on the y-axis, with constant coordinate separation

$$\delta x^\mu = x^\mu_B - x^\mu_A\,, \tag{1.12}$$

and a GW propagating on the z-axis in the TT-gauge. The metric is

$$ds^2 = g_{\mu\nu}dx^\mu dx^\nu = (\eta_{\mu\nu} + h^{TT}_{\mu\nu})dx^\mu dx^\nu\,. \tag{1.13}$$

When the wave reaches the particles, their proper distance

$$\Delta l = \int ds = \int_{y_A}^{y_B} |g_{yy}|^{\frac{1}{2}} dy = \int_{y_A}^{y_B} |1 + h^{TT}_{yy}(t-z)|^{\frac{1}{2}} dy \tag{1.14}$$

varies. This conclusion may seems in contradiction with the fact that the coordinate separation in Eq. (1.12) remains constant. The key point is that in GR non-tensorial

quantities are not appropriate to describe physical processes, due the fact that they are not covariant under coordinate transformations. In other words, they are not suited to discriminate between real physics effects, and artefacts induced by the coordinate frame choice.

1.2.2 Ring of Test Masses

It is possible to analyse the effect induced by the passage of a GW on a ring of free-falling particles that is placed perpendicular to the direction of propagation of the wave. Following Eq. (1.9), a wave that propagates along the z-axis has components

$$h^{TT}_{xx} = -h^{TT}_{yy} = h_+, \qquad h^{TT}_{xy} = h^{TT}_{yx} = h_\times \,, \tag{1.15}$$

which are independent and can be considered separately. Therefore, looking at the effects produced only by the plus polarisation h_+, the polarisation matrix becomes

$$h_+ = A_+ \cos(\omega(t-z)) \qquad h_\times = 0 \,. \tag{1.16}$$

Similarly, when $h_+ = 0$ and $h_\times \neq 0$ the polarisation matrix is

$$h_\times = A_\times \cos(\omega(t-z)) \qquad h_+ = 0 \,. \tag{1.17}$$

The ring, initially in equilibrium, stretches and shrinks periodically when the GW passes through it. This effect, visually shown in Fig. 1.1, is caused by the fact that the GW induces a periodic change in the distance between the particles in the ring. For GW signals generated from the coalescence of two compact objects (see Sec. 1.3.2.3), this effect is known as the "chirping" effect, as the wave causes the ring to oscillate at a frequency and amplitude that increase as the wave passes through the ring, and it is used to detect GWs.

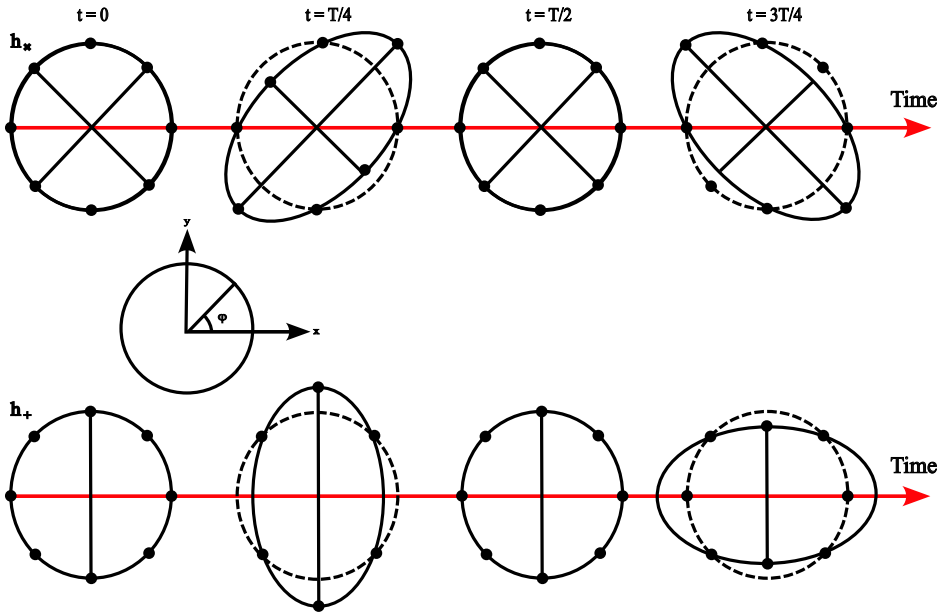

FIGURE 1.1: Deformation of a ring of particles due to the passage of a $\times$ polarised GW (top) and a $+$ polarised wave (bottom) while the dashed circles indicate the test particles position in the absence of GW signal [259]. Each step in the graph corresponds to a quarter of period.

1.3 Gravitational-Wave Signals

Any form of mass and energy is a potential source of GWs, as long as the second time derivative of the quadrupole moment is non-zero. This statement can be derived with the quadrupole formalism, as shown in the following section, where the possible GW sources detectable with ground-based detectors will also be listed, with particular emphasis on sub-solar mass binaries, as it is one of the main focus of this manuscript.

1.3.1 The Quadrupole Formalism

The quadrupole formalism is a mathematical approach used to describe GWs emitted by systems that are evolving in time under the strong assumptions of weak gravitational field (see Eq. (1.5)) and slow motion, which means that the typical velocities of the system are much smaller than the speed of light $v_{typical} \ll c$. With these approximations, it is possible to develop the solutions of Eq. (1.6) in the form of retarded potentials [196],

$$\bar{h}_{\mu\nu}(t,r) = \frac{4G}{rc^4}\int_{source} T_{\mu\nu}\left(t-\frac{r}{c},x'\right)d^3x' \,, \tag{1.18}$$

with $\mu,\nu = 0,1,2,3$. Eq. (1.18) is the GW signal emitted by a source, at leading order, that can be rewritten as [196]

$$\bar{h}^{ik}(t,r) = \frac{2G}{c^4}\frac{1}{r}\frac{d^2}{dt^2}q^{ik}\left(t-\frac{r}{c}\right) \,, \tag{1.19}$$

where $i,k = 1,2,3$ and q^{ik} is the quadrupole moment tensor, defined as [196]

$$q^{ik}(t) = \frac{1}{c^2}\int_V T^{00}(t,x^n)x^i x^k d^3x. \tag{1.20}$$

Equation (1.19) is the quadrupole formula and describes the GW emitted by a gravitating system evolving in time. The factor $\frac{2G}{c^4}$ only affects the intensity of the source, and is of order $10^{-50}s^2g^{-1}cm^{-1}$, that explains the typical weakness of GWs. Therefore, any form of energy or mass can be a source of GWs, as long as the second time derivative of the quadrupole moment of the system is non-zero. However, in order to have detectable signals, the sources need to be massive and compact and the acceleration violent enough to induce a strong gravitational field. Consequently, these sources must originate from astrophysical phenomena. It is possible to demonstrate that the energy radiated in GWs by an evolving binary system per unit time is [196]

$$\frac{dE_{GW}}{dt} = \frac{32}{5}\frac{G^4}{c^5}\frac{\mu^2M^3}{l_0^5} \,, \tag{1.21}$$

where M is the total mass of the binary system, $\mu = \frac{m_1m_2}{M}$ the reduced mass, and l_0 the orbital separation. The expression in Eq. (1.21) can be considered as an average over several periods, in a regime where the orbital parameters do not change significantly over the time interval taken to perform the average. This is called adiabatic regime and, by balancing the energy lost in GWs with the change in the orbital energy, it is possible to compute several quantities such as the time of the coalescence, as well as the evolution of the orbital separation, angular velocity and orbital period.

1.3.2 Categorisation of Gravitational Wave Signals

Based on their characteristics, we can classify GW signals searched for with terrestrial interferometers in three broad categories: continuous signals, stochastic signals and transient signals. All these categories will be developed below, with a focus on transient signals generated by coalescing compact binaries, which are the sources that are of most interest in this thesis.

1.3.2.1 Continuous Gravitational Waves

Continuous waves [52, 53, 87, 253, 331, 338, 342] are a class of GW signals characterised by a roughly constant frequency and amplitude during the observing period, as shown in Fig. 1.2. These signals can originate from various astrophysical sources such as pulsars or, more in general, rotating asymmetric NSs. This is because, although intense gravitational forces tend to make NSs nearly spherical by flattening any irregularity with their own gravity, spinning NSs can be asymmetrically deformed, due to bulges or uneven mass distributions, that enable them to emit GWs. Deformed NSs can also be the result of the action of their strong magnetic field, that can induce small ellipticities. Independently of what causes the deformations, it is known that rotating NSs emit GWs at twice their rotation frequency. Notably, approximately one-fifth of the observed NSs have spin frequencies surpassing 5 Hz and, in certain cases, even reaching 700 Hz. Therefore, the GWs generated by these rapidly rotating NSs are expected to lie within the frequency sensitivity range of current GW detectors, even though with a fainter intensity compared to other sources of GWs, given that the energy emitted by these sources is generally lower.

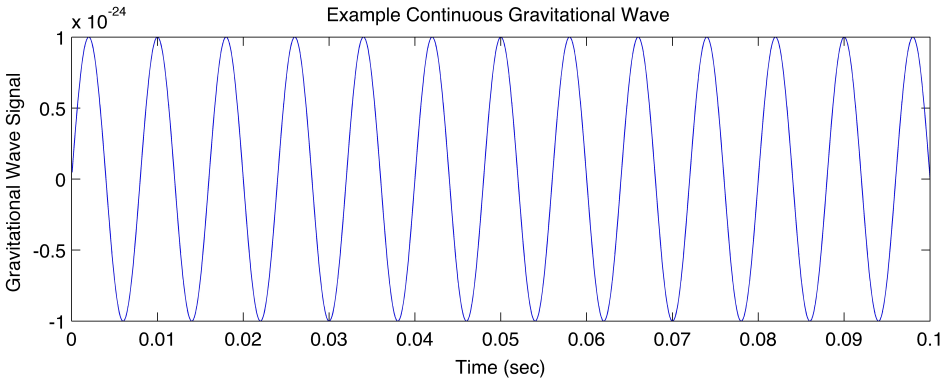

FIGURE 1.2: An example signal from a continuous wave source [2].

1.3.2.2 Stochastic Gravitational Wave Background

Stochastic GWs [68, 143, 312] are a type of signals that arise from the random superposition of a large number of individual, unresolved GW sources distributed across the Universe. They can have various origins, including primordial processes in the early Universe, such as cosmic inflation or phase transitions, as well as astrophysical phenomena like the cumulative effect generated by transient and continuous signals. GWs of this kind are generated with a broad range of frequencies, spanning from very low frequencies (nHz) to higher frequencies (kHz), and due to their random nature, they are typically observed as a background noise-like signal, as shown in Fig. 1.3, that permeates the entire frequency band of GW detectors. Detecting a stochastic GW is more challenging compared to other sources and it can only be

inferred by combining the output of multiple detectors with a wide geographic distribution, and calculating their cross-correlation looking for a common signal.

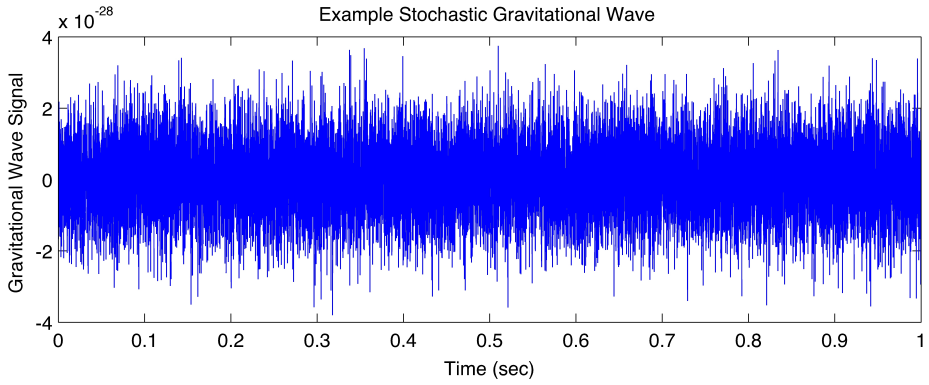

FIGURE 1.3: An example signal from a stochastic GW source [4].

1.3.2.3 Transient Gravitational Waves

The main characteristic of transient GW signals are their unpredictability and their finite duration. They can be categorised into two main types based on the predictability of their shape: burst events, unmodelled, and Compact Binary Coalescences (CBC), with a known shape. Burst GWs come from astronomical transient phenomena during which an abrupt variation of energy induces the emission of GWs such as supernova explosions, rapid variations in the rotation of pulsars or other violent cosmic events. It is hard to predict the possible shape of these signals (see Fig. 1.4) since the expected frequencies, amplitudes and durations depend on the nature of the source other than the considered models [17, 47, 54]. On the other

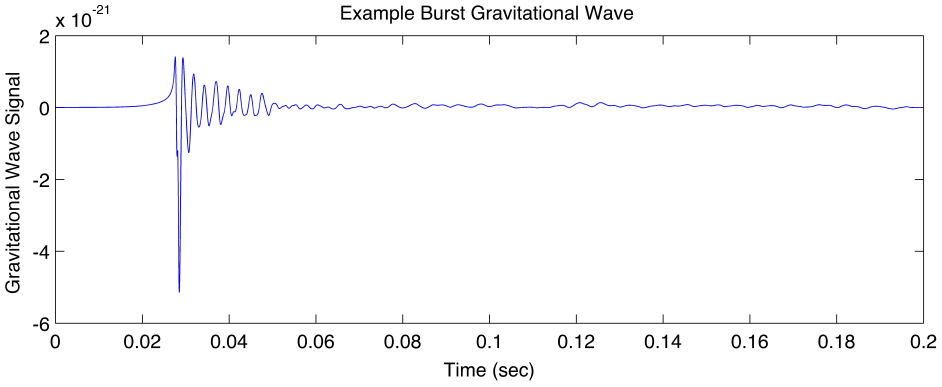

FIGURE 1.4: An example signal from a burst source [1].

hand, CBCs signals are originated from the end-of-life coalescence of binary systems composed by two compact objects such as NSs or BHs like Binary Black Holes (BBHs), Binary Neutron Stars (BNSs), and Neutron Star Black Hole binaries (NSBHs). These objects are "compact" in the sense that they have strong gravitational fields, while the term "coalescence" refers to the process by which these objects gradually spiral closer together due to the emission of GWs until they eventually merge into a single object. The emitted GWs, shown in Fig. 1.5, have well-defined time evolution, as will be explained in more details in the following Sec. 1.3.3.

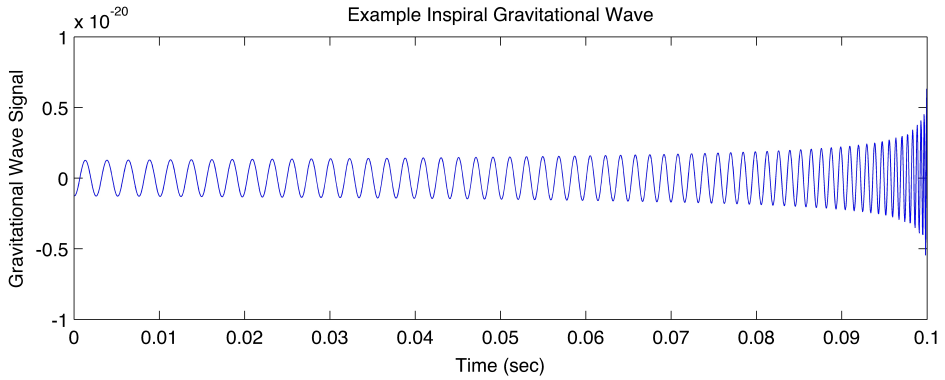

FIGURE 1.5: An example signal from a CBC GW source [3].

1.3.3 Compact Binary Coalescences Emitted Signal

Starting from Eq. (1.19) it is possible to predict the characteristics of the emitted GWs. A binary system with total mass $M = m_1 + m_2$, and reduced mass $\mu = \frac{m_1 m_2}{M}$ on the $x - y$ plane orbits with Keplerian frequency

$$\omega_K = \sqrt{\frac{GM}{l_0^3}}\,, \tag{1.22}$$

with l_0 being the distance between the two objects m_1 and m_2. The components of the quadrupole moment become

$$q_{ij} = \frac{\mu}{2} l_0^2 A_{ij} + const\,, \tag{1.23}$$

so that Eq. (1.19) in the TT-gauge, becomes

$$h_{ij}^{TT} = -\frac{2G}{c^4 r}\frac{\mu}{2} l_0^2 (2\omega_K)^2 A_{ij}^{TT}\left(t - \frac{r}{c}\right) = -h_0 A_{ij}^{TT}\left(t - \frac{r}{c}\right)\,. \tag{1.24}$$

where h_0 is the amplitude of the emitted wave, while A_{ij}^{TT} depends on the orientation of the line of sight with respect to the orbital plane, and determines the polarisation of the wave. For instance, a GW emitted in the direction orthogonal to the orbital plane has the polarisation matrix A_{ij} defined as

$$A_{ij}(t) = \begin{bmatrix} \cos 2\omega_K t & \sin 2\omega_K t & 0 \\ \sin 2\omega_K t & -\cos 2\omega_K t & 0 \\ 0 & 0 & 0 \end{bmatrix}\,. \tag{1.25}$$

In this case the wave has both polarisations and, since h_{xx}^{TT} and h_{xy}^{TT} are cosine and sine of the same phase and amplitude, the wave is circularly polarised. In the case of a wave emitted along the x-axis, and similarly for a wave emitted on the y-axis, the polarisation matrix becomes

$$A_{ij}(t) = \begin{bmatrix} 0 & 0 & 0 \\ 0 & -\frac{1}{2}\cos 2\omega_K t & 0 \\ 0 & 0 & \frac{1}{2}\cos 2\omega_K t \end{bmatrix}\,, \tag{1.26}$$

so that the emitted wave is linearly polarised. These equations show that the frequency of the emitted GW is at first order twice the orbital frequency, with an amplitude directly proportional to the masses of the compact objects and inversely proportional to their orbital separation, and inversely proportional to the distance of the system from the observer. During the evolution of the coalescence the orbital separation l_0 decreases, the orbital frequency w_K increases and the amplitude of the GW increases, so as its frequency. Equations (1.22) and (1.24) seem to suggest that, as $l_0 \to 0$, the GW amplitude and the frequency diverge. This comes from the approximations assumed at the beginning, that are not accurate in describing the dynamic of the system, and therefore are no longer valid, as the binary shrinks and approaches the merger phase. Indeed, the late inspiral and the following stages, which occur in a strong gravity regime, can only be described using numerical relativity.

1.3.3.1 Emitted Signal

As the two compact objects orbit, they emit GWs, carrying away energy and angular momentum from the system, and therefore causing them to spiral towards each other down to the merger. The emitted signal is divided into three phases (Fig. 1.6): the inspiral, during which the gravitational fields and velocities are still relatively weak, the merger, which occurs when the two objects are close enough that they start to fuse, and finally the ring down or post-merger phase, when the newly formed object settle down to a stable state.

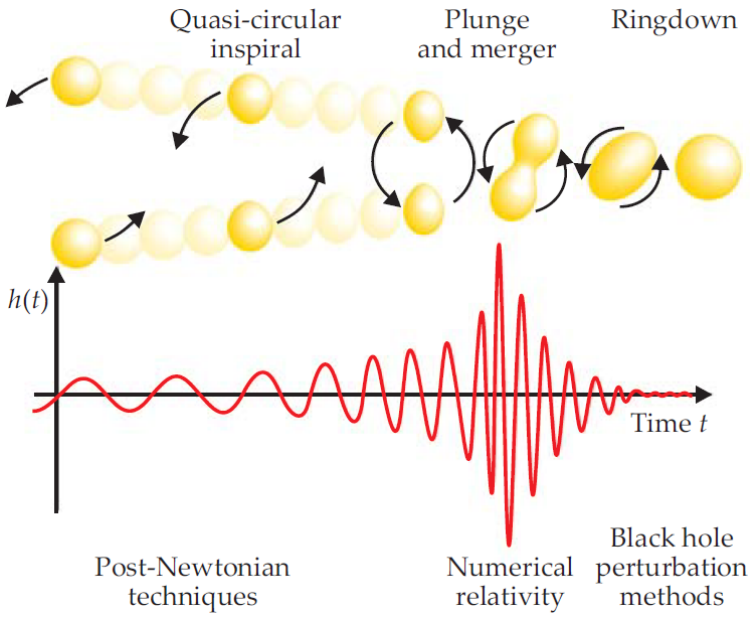

FIGURE 1.6: An example signal from an inspiral GW source [106].

1.3.3.2 Waveform Models

The importance of modelling GW waveforms from compact binaries lies in the fact that these waveforms are used in template-based GW data analyses, aiming to detect the signals and measure the properties of the sources. As there is no analytical solution to the two-body problem in GR, due to the highly non-linear nature of Einstein's equations, it is crucial to have approximate solutions, for comparison with data in order to detect a signal and perform unbiased statistical inferences, whose goal is to

draw objective conclusions regarding the properties of the source, such as masses and spins, without introducing assumptions. To obtain a complete waveform, it is necessary to combine different approaches for the description of the different phases of the binary's evolution. The inspiral phase, up to the innermost stable circular orbit (ISCO) located at

$$r_{ISCO} = \frac{6GM}{c^2} \tag{1.27}$$

for a binary system with total mass M, can be modelled with the so called post-newtonian (PN) theory [359], originally developed by Einstein himself to find solutions to the field equations. It consists in expanding solutions as a series of approximations in powers of v/c. As the two objects approach each other, the higher PN orders become more and more important. The late inspiral and the merger, which occur in the strong gravity regime, can only be modelled using numerical relativity (NR) [113] which seeks to directly integrate the Einstein's equations. Finally, the post-merger phase, or ring down, is described by using perturbation theory [305]. It is often useful to combine PN expansions of the inspiral phase with NR simulations of the late inspiral and merger to form the so called hybrid waveforms. This approach uses the strengths of both methods, since the PN approach becomes less accurate as the binary shrinks and the NR approach becomes more computationally intensive as the number of simulated cycles increases. Two of the major challenges in building complete waveforms models come from the description of tidal effects in NSs, requiring extra modelling for the description of matter contained within them, and the computational cost needed by NR to perform simulations with several orbital cycles before the merger. For instance, more cycles are needed in the spinning case and for unequal-mass binaries [215], and the process becomes more complicated if precession, induced by gravitational interaction with nearby massive objects, is also considered [321].

1.4 CBC Sources of Gravitational Waves

CBC GWs originate from the inspiral and merger of compact objects. In addition to BBHs, NSBHs, and BNSs, which are the most extensively studied and well-known CBC sources, other exotic CBC systems may emit detectable GW signals. The upcoming section provides a concise overview of the primary CBC sources along with alternative sources, offering a glimpse into the diverse range of CBC phenomena.

1.4.1 Stellar Sources of Gravitational Waves

According to the standard theory of stellar evolution [319, 328], compact objects form at the end point of the evolution of sufficiently massive main-sequence stars. When the hydrogen burning in the core is exhausted, the stars exit the so-called "main sequence" and their fate after gravitational collapse depend on its mass. If the mass is smaller than approximately 0.5 $M_\odot$ [319], it forms directly a White Dwarf (WD) [136, 323]. If the star has a larger mass at the end-point of its main sequence, it contracts and heats up, reaching core temperatures that activate new nuclear reactions which halt temporarily the collapse. Once again exhausted the nuclear fuel, if the mass of the progenitor star is in the range $(0.5, 8.0 - 10.0)\ M_\odot$ [319], the hot core collapses until a WD is formed. Composed mainly of carbon, oxygen and helium, WDs have masses comparable to that of the Sun, up to the Chandrasekhar limit of 1.4 $M_\odot$ [136], but are much more compact, and are supported against gravitational collapse by electron degeneracy pressure. If the mass of the progenitor star is in the

range $(8.0, 20.0 - 30.0)\ M_\odot$ [319], nuclear processes are able to burn elements heavier than carbon and oxygen, and exothermic reactions may proceed up to ^{56}Fe, which is the most stable element in nature and no heavier element could be produced with exothermic fusion reactions. The star at this point has a layered structure with the heavier element in the core, and progressively lighter elements in the surrounding layers. As the core density increases, nuclei heavier than ^{56}Fe are formed through endothermic reactions which subtract energy to the star up to the point where the core mass becomes larger than the critical mass (around $1.26 - 1.37\ M_\odot$ depending on the composition of the star), and the gravitational attraction prevails leading to the collapse of the star. At this stage the core, composed mainly of neutrons due to electron capture induced by extreme pressure and temperature, is so rigid that the infalling matter bounces back producing a violent shock wave that ejects most of the material external to the core in the outer space in a supernova explosion. The remnant of this explosion is a nebula and a central NS [254, 293], whose critical mass is in the range $2.0 - 3.0\ M_\odot$ [105], depending on its equation of state. NSs are supported against further collapse by neutron degeneracy pressure, and exhibit unique properties due to their composition and high gravitational fields, such as strong magnetic field or high spins. The lower limit for a stable NS is generally expected to lie in the range of approximately $1.1 - 1.2\ M_\odot$ [340]. This range closely aligns with the previously measured minimum mass of NSs until a recent evaluation of the central NS mass within the supernova remnant HESS J1731-347 [177], which yielded an estimate of about $0.77^{+0.20}_{-0.17}\ M\odot$. Finally, if the mass of the progenitor is greater than $20.0 - 30.0\ M_\odot$ [319], at the end of its thermonuclear evolution it collapses to form a BH [221, 291]. Once formed, these objects continue to interact with their surroundings, in some cases forming binary systems through dynamical interactions and gravitational captures.

1.4.2 Beyond the Standard Theory of Stellar Evolution

In addition to the most common CBC sources (BBH, BHNSs and BNSs) there are: Super Massive Black Hole Binaries (SMBHB), composed of BHs with masses of order $10^6 - 10^{10} M_\odot$, Extreme Mass Ratio Inspirals (EMRI), in which the components of the binary are a super massive BH and a stellar mass compact object, and Sub-Solar Mass (SSM) binaries, composed of at least one compact object with a mass under $1 M_\odot$. Among all these additional sources, SSM binaries and the associated search are of particular interest for this thesis, as the author was directly involved in it during the LIGO-Virgo third observing run. There are no widely accepted astrophysical formation channels that predict the existence of SSM objects more compact than white dwarfs, nevertheless several alternative theories link the existence of those objects to: the gravitational collapse of overdensities in the early Universe that could form Primordial Black Holes (PBHs) [132, 223], or the cooling with subsequent collapse of Dark Matter (DM) halos [90, 140, 165, 326]. DM is a form of matter that does not emit, absorb, or interact with electromagnetic radiation and whose nature is still unknown, making it one of the modern unsolved mysteries in cosmology and particle physics. Specifically, the observations of the large motions of galaxies in clusters [364], the motions of stars and gas in galaxies [181, 313, 317, 318], the large-scale structure in the Universe [102, 103, 295, 296, 347], gravitational lensing [329], and the CMB observations [80, 110] reveal that DM possesses considerable mass, remains stable over billions of years, primarily interacts via gravity, is distinct from baryonic matter, and is mainly concentrated in large halos of galaxies

and in clusters of galaxies [101, 102]. DM is divided into a "hot" and a "cold" components, pertaining to the characteristic and velocities at which the DM particles move in the Universe, respectively relativistic and non-relativistic. Beside baryons, the only electromagnetically neutral, stable and massive particles that exist in the Standard Model are the neutrinos, which are so light that they have relativistic speeds and constitute a good example of hot DM. On the other hand, cold DM particles move at non-relativistic speeds, and are considered to make up the largest part of DM in the Universe as they allow to form clumps and structures more efficiently, which matches observations of the large-scale structure of the Universe. Globally, it is estimated that approximately 27% of the entire mass-energy content of the Universe is attributed to DM, while the rest consists of approximately 68% of dark energy and approximately 5% of ordinary matter [80]. In the standard Λ Cold Dark Matter (ΛCDM) cosmological model [80], which states that the Universe is isotropic and homogeneous on a large scale and which includes a cosmological constant Λ in the Einstein field equations to account for the observed accelerated expansion of the Universe, it is assumed that the whole DM is cold, providing an explanation for the dynamics of galaxies and galaxy clusters which exhibit more gravitational attraction than their electromagnetic radiation can explain. However, it is important to emphasise that alternative DM models exist. These include Warm Dark Matter (WDM) [243, 351], possessing properties between those of hot and cold DM, fuzzy dark matter [210, 211, 229, 230, 235, 263, 339], which proposes DM as an ultra-light scalar field condensing into a galaxy-sized Bose-Einstein condensate, the dark fluid hypothesis [91, 112, 118, 209] suggesting that DM and dark energy are a single entity, and self-interacting DM [128, 336]. Another interesting idea is the hypothesis that PBHs constitute a significant part, if not all, of the DM [79, 131, 137, 145, 275, 353] content of the Universe. With such model, there is no need to introduce a new particle and the only assumption is that some over-densities in the early Universe collapsed into BHs [362]. DM composed of PBHs presents several observable signatures which can constrain its parameter space, as will be detailed in the following. Such effects allow placing upper limits on the abundance of PBHs, generally indicated as the fraction of DM in PBHs f_{PBH}.

1.4.2.1 Primordial Black Holes

The hypothesis of the formation of BHs in the early Universe was first suggested by Zel'dovich and Novikov in 1967 [362], and independently by Hawking in 1971 [223]. Shortly after, the idea was advanced that PBHs could contribute to forming a portion of the Universe's DM content [137], and that their presence could have effects on the formation and evolution of galaxies [268]. From the standard theory of stellar evolution we know that when a star exhausts its nuclear fuel, it will undergo gravitational collapse if its mass is greater than 1.4 $M_\odot$, forming either a NS or a BH with a radius given by the Schwarzschild radius $\frac{2GM}{c^2}$. For BHs formed in the early Universe, and in particular during the radiation era which goes from 10^{-6} s to 10^4 s after the Big Bang, their mass depends on their formation time [223, 362]. In order to have PBH formation at a time t, densities of the order of the cosmological density are necessary. Thus, the mass of the resulting PBHs should be of the order of the mass within a region of the size of the Hubble horizon, defined as [129, 133]

$$M_H \approx \frac{c^3 t}{G} \approx 10^{15}\, g\left(\frac{t}{10^{-23}\, s}\right), \tag{1.28}$$

from which it is possible to state that PBHs could span an enormous mass range: those formed at the Planck time (10^{-43} s) would have the Planck mass (10^{-5} g), whereas those formed 1.0 s after the Big Bang would have masses of $10^5\ M_\odot$. Therefore, PBHs could be produced with any mass, in contrast to what happen for stellar BHs which, according to the Tolman-Oppeheimer-Volkoff limit [292, 346], can have masses only above $\sim 3\ M_\odot$. Additionally, BHs may radiate thermally [220] with a temperature

$$T = \frac{\hbar c^4}{8\pi G M k_B} \approx 10^{-7}\left(\frac{M}{M_\odot}\right)^{-1} K\,, \tag{1.29}$$

where $\hbar$ is the reduced Planck constant and k_B is the Boltzmann constant. The emission of the Hawking radiation causes them to slowly lose mass until they eventually completely evaporate on a timescale of

$$\tau(M) \approx \frac{\hbar c^4}{G^2 M^3} \approx 10^{64}\left(\frac{M}{M_\odot}\right)^3 yr\,. \tag{1.30}$$

Hence, only BHs smaller than 10^{15} g would have evaporated by the present epoch (10^{10} yrs), which correspond to those formed at times earlier than 10^{-23} s. The process of evaporation may produce detectable effects that can be probed in a variety of experiments to estimate the abundance of PBHs across different mass ranges. This is illustrated in Figure 1.7, where is shown the energy fraction of DM in PBHs (f_{PBH}), which represents the ratio of the energy density of PBHs (Ω_{PBH}) to the energy density of DM (Ω_{DM}), as function of the PBH's mass. The process of PBH evaporation is expected to emit a significant background of γ rays [130] and cosmic rays [234], and its non-detection puts constrains in the mass range $M_{PBH} < 10^{10}$ g via the INTEGRAL and COMPTEL observations [152, 169, 250, 251], other than data on the diffuse supernova neutrino background at Super-Kamiokande [166]. In particular, the maximum fraction allowed is $f_{PBH} \leq 2 \cdot 10^{-8}(M_{PBH}/(4 \cdot 10^{-4}))^{3+\epsilon}$, with $\epsilon \sim 0.1 - 0.4$ [131]. Moreover, the radiation emitted by accretion can shift the peak of CMB anisotropy spectrum, establishing limits on f_{PBH} for masses $\geq 10.0\ M_\odot$ [304, 325]. The non-observation of microlensing effects, generated when a compact object passes in front of a star along the line of sight, and characterised by a temporary increase in the star's brightness, can constrain the fraction of PBH with masses ranging in $5 \cdot 10^{-10} - 10^3\ M_\odot$ [207, 299], and is currently about $f_{PBH} \leq 0.01 - 0.1$ by the MACHO [86] and EROS surveys [345], the Subaru Hyper Suprime Cam (HSC) in Andromeda [280] and the Optical Gravitational Lensing Experiment (OGLE) in the Galactic bulge [281]. However, the presence of 6 microlensing events in the OGLE data [273] shows agreement with the possibility of PBHs of mass $M \sim 10^{-5}\ M_\odot$, with a fraction of $f_{PBH} \sim 0.03$. Nevertheless, caution is required in interpreting this as definitive evidence for PBH existence, as these events could also be attributed to free-floating planets. The lack of detection of PBH mergers by the LIGO-Virgo-KAGRA collaboration offers an alternative way for constraining their abundance by demanding that the predicted merger rates of PBH binaries do not exceed those measured through GWs [41, 42, 65, 66], and by using the non-observation of a stochastic GW background of mergers expected from a population of PBHs [139], establishing upper limits for PBH masses ranging in $1.0 - 300.0\ M_\odot$. Moreover, it is possible to identify the presence of PBH in clusters as this would lead to an increase of the velocity dispersions of the stars and cause the cluster to expand over time. Such dynamical constraints are obtained with observations of populations with high mass to luminosity ratios, as those are more sensitive to this effect, obtaining upper bounds in the range $10.0 - 10^4\ M_\odot$ [121]. The analysis of spectral lines, such as in the Lyman-α

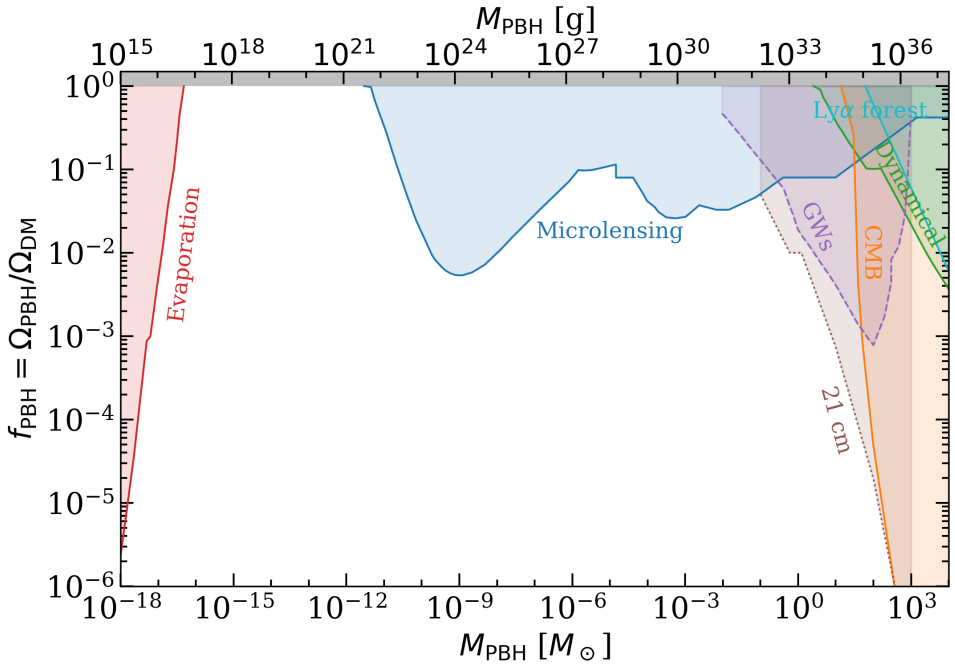

FIGURE 1.7: Collection of constraints on the fraction of PBHs with respect to DM as function of the PBH mass from [353]. Impact of PBHs evaporation on the γ-ray background [130] and on the Cosmic Microwave Background (CMB) spectrum [234] (solid red); non-observation of micro-lensing events from the MACHO [86], EROS [345], Kepler [208], Icarus [290], OGLE [281] and Subaru-HSC [161] collaborations (solid blue); PBH accretion signatures on the CMB [325] (solid orange); dynamical constraints as disruption of stellar systems by the presence of PBHs on wide binaries [271] and ultra-faint dwarf galaxies [121] (solid green); power spectrum from the Lyα forest [275] (solid cyan); merger rates from GWs from individual mergers [240] or from searches of stochastic gravitational wave background [41] (dashed purple); forecasts from the 21 cm power spectrum with SKA sensitivities [266] and from 21 cm forest prospects [352] (dotted brown).

forest [79], or the 21 cm line signal from the hyperfine structure of the hydrogen [117, 119, 224, 266, 332, 352] has also been employed to establish constraints on the upper limit of the permissible fraction of PBHs. The mechanisms for the formation of PBH binaries are categorised based on the cosmological era in which they originate. The first mechanism involves the formation of PBH pairs during the radiation epoch [84, 233, 276, 303, 309, 310, 350], when the gravitational force acting between the components overcomes the cosmic expansion, and the pairs decouple from the Hubble flow. The merger rate of such Early PBHs Binaries (EB) with the approximations provided in [233], and validated with numerical N-body simulations in [310], reads [144, 206, 233, 245, 310]

$$\frac{dR_{EB}}{d\ln m_1 d\ln m_2} = \frac{1.6\cdot 10^6}{Gpc^3 yr} f_{sup} f_{PBH}^{53/37} f(m_1) f(m_2) \left(\frac{M}{M_\odot}\right)^{-32/37} \eta^{-34/37}, \tag{1.31}$$

where m_1 and m_2 are the two binary component masses, M is the total mass of the system, $\eta = (m_1 m_2)/M^2$ the symmetric mass ratio, f_{sup} a suppression factor that accounts for PBH early binary disruption due to matter inhomogeneities and interactions with nearby PBHs, and $f(m_i)$ the PBH mass function. The second binary formation mechanism occurs at later times, during the matter era [233, 310], when PBHs may form bound states by tidal captures. The merger rate for these Late PBHs

Binaries (LB) is [144, 145, 303]

$$\frac{dR_{LB}}{d\ln m_1 d\ln m_2} = R_{clust}\cdot f_{PBH} f(m1) f(m2) \frac{(m_1+m_2)^{10/7}}{(m_1 m_2)^{5/7}}\,, \tag{1.32}$$

where R_{clust} is a scaling factor that incorporates the PBH clustering properties, and it is set to $\sim 420 yr^{-1} Gpc^{-3}$. Close encounters are relatively rare events, so the clustering mechanism of PBHs formed during the radiation-dominated era is more efficient in producing binaries, resulting in a higher merger rate, which makes them more interesting targets for GW detection.

1.4.2.2 Cooling of Dark Matter Halos

It is widely acknowledged that the majority of the matter in the Universe is in the form of dark matter, which particle nature is still unknown. The atomic dark matter model [74, 193–195, 238, 239] proposes the introduction of a new type of particles that interact with each other through the analogous of the electromagnetic force, mediated by a massless dark photon. In this model, DM is composed of a light fermion of mass m_c, and a heavy fermion of mass m_X. Those particles can combine to form hydrogen-like atoms, called "dark atoms", that cluster forming halos of DM gas, which undergo cooling and collapse through mechanisms similar to those that occur in gravitationally bound clouds of hydrogen. In the absence of dark nuclear physics that could counterbalance the gravitational pressure with fusion-induced radiation, the only possible final state of the gravitational collapse of DM is a Dark-sector Black Hole (DBH), whose minimum mass M_{min}^{DBH} is set by the Chandrasekhar limit at [326]

$$M_{min}^{DBH} = 1.457\left(\frac{m_p}{m_X}\right)^2 M_\odot, \tag{1.33}$$

where m_p is the proton mass and m_X the mass of the heavy fermion. If dark matter has dissipative properties, only a portion of the gas can cool down, and even then, only a fraction f of that gas would eventually form into compact objects. Using Population III-star formation studies [123], it is possible to use an initial mass function $P(m) \propto m^{-b}$ ranging from M_{min} to $M_{max} = rM_{min}$, where r ranges in $[2, 1000]$ log-uniformly and b ranges in $[-1, 2]$ uniformly. The faction f of DM ending in DBHs can thus be derived from their merger rates, modelled as a function of the chirp mass m_{chirp}, the merger time t_m and the set of parameters $\theta = \{M_{min}, r, b\}$, as [327, 333]

$$R_i(m_{chirp}|t_m,\theta) = P_i(m_{chirp}|t_m,\theta)\left[\frac{dP_i(t_m = 10Gyr,\theta)}{dt}\right]\frac{\rho_{DM}\cdot f\cdot f_{binary}}{\langle M\rangle}\,, \tag{1.34}$$

where $\rho_{DM} = 3.3\cdot 10^{19} M_\odot Gpc^{-3}$ is the fraction of DM that can cool in the Universe, $f_{binary} = 0.26$ [122] is the fraction of binary systems compared to total DBHs, $\langle M\rangle$ is the mean component mass of DBH in binaries for the considered prior distribution, $P_i(m_{chirp}|t_m,\theta)$ is the chirp mass distribution of binary systems merging at t_m for some θ, and $P_i(t_m = 10Gyr,\theta)$ the probability that the merger time for the binaries equals 10 Gyr (roughly the age of the Universe) for some θ.

CHAPTER2

Gravitational Wave Detection Principles

The first attempts to directly detect GWs were made by Joseph Weber in the 1960's. His experimental apparatus was a cylindrical bar of aluminium, equipped with piezoelectric crystals designed to measure the expansion and contraction of the bar, producing an electric signal. In 1969 he made his first [356] of many announcements, according to which he had evidence for the discovery of GW radiation. Unfortunately, all the attempts made by other groups to replicate the results failed to see signals like the ones observed by Weber. Further analyses, performed during the years, highlighted numerous technical mechanisms that could have contributed to Weber's false coincidences. Nevertheless, his work laid the foundation for future GW detection efforts. In 1974, Russell A. Hulse and Joseph H. Taylor discovered the first indirect evidence of emission of GWs through their groundbreaking detection of the first binary pulsar [231]. Their findings showed a measure of the orbital period decay of the pulsar, which precisely describes the angular momentum and energy loss due to gravitational radiation emission predicted by general relativity. This indirect detection motivated further searches, pursued with laser interferometers, suggested for the first time by Gertsenshtein and Pustovoid in 1962 [203], whose first prototypes were build starting from 1971 by Robert L. Forward and colleagues at Hughes Research Laboratories [199, 272], in 1972 by Rainer Weiss and others at the Massachusetts Institute of Technology (MIT) [322], and later by Heinz Billing and colleagues in Germany [330], and by Ronald Drever, James Hough and colleagues in Scotland [344]. The first generation of large-scale GW detectors, known as Initial LIGO, became operational in the early 2000s. These interferometers, located in Hanford (Washington), and Livingston (Louisiana), used powerful lasers and extremely sensitive mirrors to measure the stretching and squeezing of spacetime caused by the passage of GWs. Despite their sensitivity, they remained incapable of directly detecting actual GW signals. A significant upgrade to the LIGO detectors, known as Advanced LIGO [5, 26, 50], was completed in 2015. This upgrade improved the sensitivity of the interferometers, increasing their potential of detecting GWs. Later in the same year, Advanced LIGO made history by detecting the first confirmed GW signal - a merger involving two BHs [18, 20–22, 25, 26, 32, 34–36, 44, 45, 48, 51, 70, 78]. The Virgo detector [71] (Italy) is another GW interferometer which joined forces with Advanced LIGO to enable more accurate localisation of GW sources and improve overall detection capabilities. Japan's KAGRA detector [94, 192], based on a cryogenic technology, is also working towards GW detection. There are also plans for future generations of detectors, such as Cosmic Explorer [46, 135, 154, 179, 184, 311], the LISA detector [252], and the Einstein Telescope [183], which aim to push the sensitivity even further. The following chapter will discuss the detectors currently used in the identification of GWs, and the milestones achieved during the first two observing runs.

2.1 Laser Interferometers

The detectors that are currently operational are Michelson interferometers, which exploit the phenomena of interference between coherent light beams, generated by variations in the proper separation between mirrors, that change the light travel time along the arms, resulting from the passage of GWs.

2.1.1 Optical Scheme

The basic optical scheme of the current ground-based GW detectors is a Michelson interferometer, with two identical arms that are perpendicular to each other and enlightened by a 1 064 nm laser beam. Future detectors, like the Einstein telescope [183] low-frequency interferometer, could be using a 2 nm laser light. The mirrors are suspended and isolated from the ground to prevent external disturbances and to allow them to behave as free-falling test masses. The advanced suspension system is composed by multi-stage superattenuators, that reduce the ground movements by a factor 10^{2N}, with N being the number of pendulum stages. The current Virgo detector have 6 stages of pendulums, as shown in Figure 2.1, thus the attenuation of ground movements is of order 10^{12}.

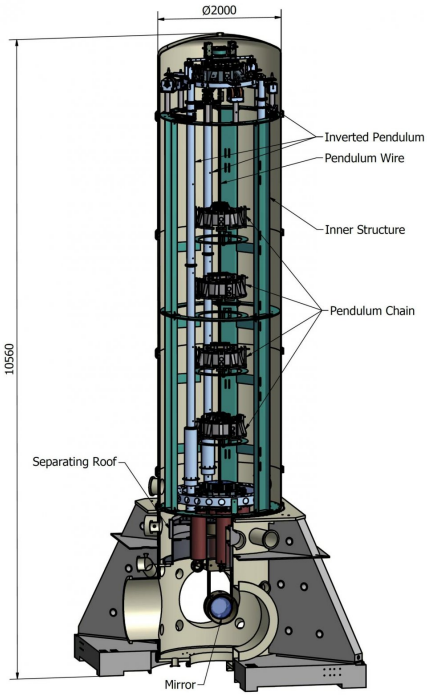

FIGURE 2.1: Side view of the VIRGO superattenuator, composed of a series of pendulum that reduce the horizontal seismic vibrations that reach the mirrors. Horizontal vibration dampers are also visible. The last suspended element is a mirror payload. Image from [150].

After being sent on a suspended Beam Splitter (BS), the laser beam is separated in two components, each carrying 50% of the intensity, that travel along the arms and, after being reflected by the suspended mirrors at the end of each arm, are recombined at the BS and part of the resulting beam goes to a photo-detector at the output port as shown in Figure 2.2.

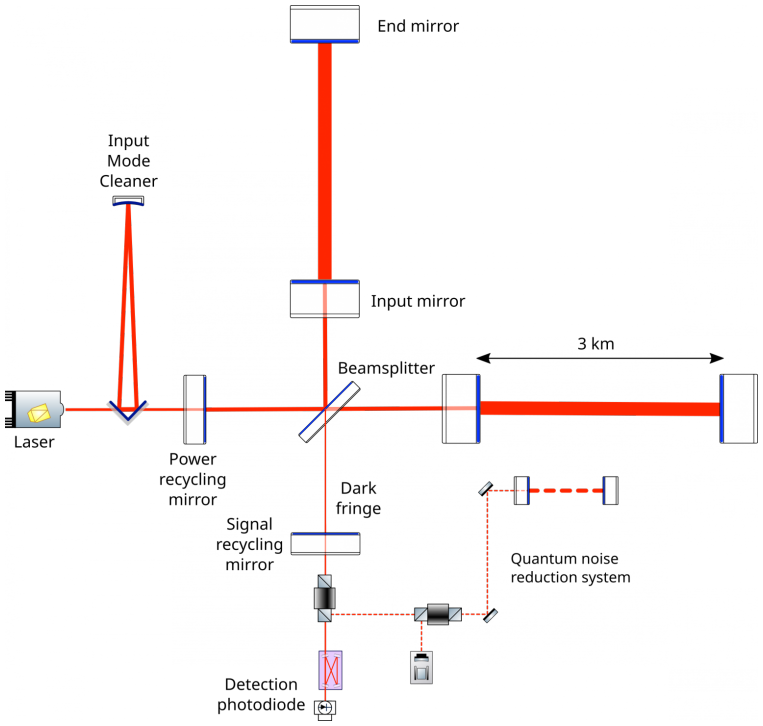

FIGURE 2.2: Optical layout of the Advanced VIRGO detector [149].

The passage of a GW through the interferometer causes a variation in the light travel time between the mirrors, resulting in a change in the arm length $\Delta L = \frac{h(t)L}{2}$. This leads to a phase shift in the recombined beams, causing a change of the intensity of the light at the photo-detector.

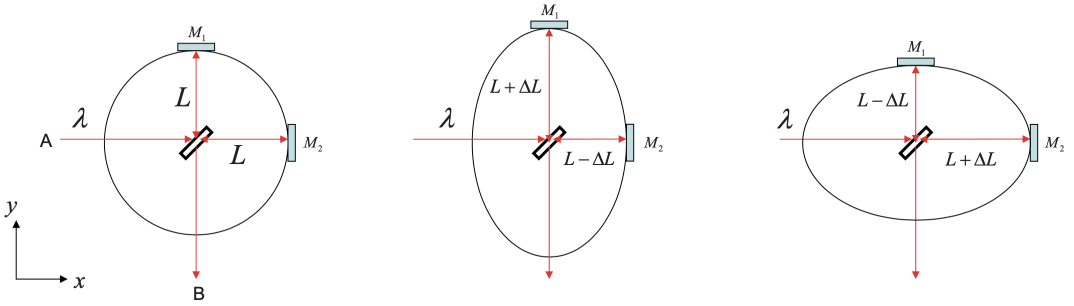

FIGURE 2.3: Simplified schematic Michelson interferometer acting as a GW detector and the effect of plus polarised wave passing perpendicularly through the plane of the interferometer.

To detect the extremely faint spacetime perturbation produced by a GW on the detector arms, equivalent to a differential strain of $10^{-22} - 10^{-21}$ for sources at few tens of Mpc, interferometers need to be very large. A solution adopted in ground-based interferometric GW detectors to increase the effective arm length, hence the strain effect on their arms, as well as the intensity of the measured dephasing of the recombined light beams, is the implementation of Fabry-Pérot cavities, realised by placing two highly reflective mirrors at the beginning of each arm. The photons entering the cavity are reflected back and forth, producing a build up of the power stored in the cavity, allowing for the amplification of even the slightest phase shifts ϕ_{cav}. The increment on the dephasing is $\delta\phi_{cav} = \frac{4\pi}{\lambda} \cdot \frac{2\mathcal{F}}{\pi} \cdot \delta L$, where λ is the

wavelength of the laser, $\mathcal{F}$ the finesse of the cavity, and δL the difference in the arms length. Additionally, the current interferometers are equipped with power and signal recycling cavities. Power recycling cavities focus on increasing the overall laser power circulating within the interferometer arms, and it involves the use of a partially reflecting mirror placed before the BS in the interferometer. The enhanced power circulating in the interferometer improves the detector's sensitivity to GWs by increasing the amplitude of the interferometric signal. The signal recycling cavities, on the other hand, involve the introduction of an additional mirror into the interferometer's arms, which redirects a portion of the output signal back into the interferometer itself. This technique is primarily used to tailor the interferometer's frequency response to match the expected frequency range of GW signals. By adjusting the properties of the signal recycling mirror, such as its reflectivity, it's possible to enhance the interferometer's sensitivity to specific frequency bands. Signal recycling helps improve the signal-to-noise ratio (SNR) of the detector for targeted frequency ranges, making it more effective at detecting GW signals within those bands. Moreover, an innovative quantum technique called squeezing is used to mitigate the effects of quantum noise that can limit the sensitivity particularly in the high-frequency region. By using specialised optical devices called squeezers, GW detectors can manipulate the uncertainty principle, redistributing quantum fluctuations between position and momentum measurements. This allows for a temporary reduction in quantum noise in one parameter at the expense of an increase in the other, effectively narrowing the noise in the parameter most crucial for the measurement. As an example, for design sensitivity in the Advanced LIGO detectors, assuming a 125 W of laser input power, the resulting power circulating in the arms would be 750 W [126].

2.1.2 Detector Response

The sensitivity of these extremely precise instruments is not isotropic. Their response depends on the direction of the GW propagation with respect to the detector's plane. In other words the detector's sensitivity is highest when the GW propagates normally to detector's plane, and null when the GW is propagating parallel to it with an angle of 45° with the x and y arms. Denoting the position of the source in the sky and the polarisation angle, that indicates the angle between the vertical of the detector and the projection of the $\times$ polarisation on the detector's plane, respectively with the angles (θ, ϕ) and ψ as in Figure 2.4, the explicit form of the beam pattern functions that gives the response of the detector is

$$\begin{aligned} F_+(\theta,\phi,\psi) &= \frac{1}{2}\left(1+\cos^2\theta\right)\cos(2\phi)\cos(2\psi) - \cos\theta\sin(2\phi)\sin(2\psi)\,, \\ F_\times(\theta,\phi,\psi) &= \frac{1}{2}\left(1+\cos^2\theta\right)\cos(2\phi)\sin(2\psi) + \cos\theta\sin(2\phi)\cos(2\psi)\,. \end{aligned} \tag{2.1}$$

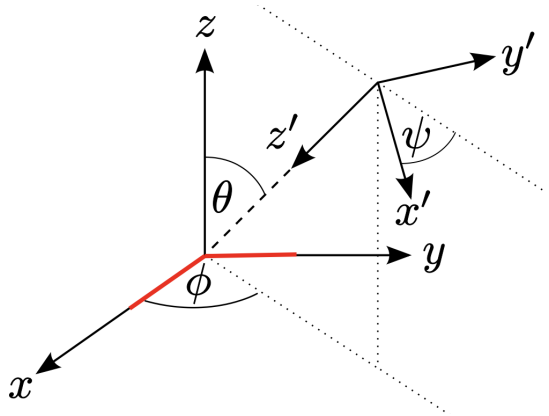

FIGURE 2.4: The sky angles (θ, ϕ, ψ) between the detector (red lines), placed in the reference system (x, y, z), and the incoming GW, produced by the source located in the reference system (x', y', z'), and propagating along the z'-axis [265].

The antenna response patterns for the plus and cross polarisations are shown in Figure 2.5 where a polarisation angle of $\psi = 0$ is assumed. The GW strain $h(t)$ induced on the detector depends on its antenna response to the two polarisations of the GW, and can therefore be written as a linear combination of each polarisation multiplied by the antenna response functions in Eq. (2.1)

$$h(t) = F_+(\theta, \phi, \psi)h_+(t) + F_\times(\theta, \phi, \psi)h_\times(t)\,, \tag{2.2}$$

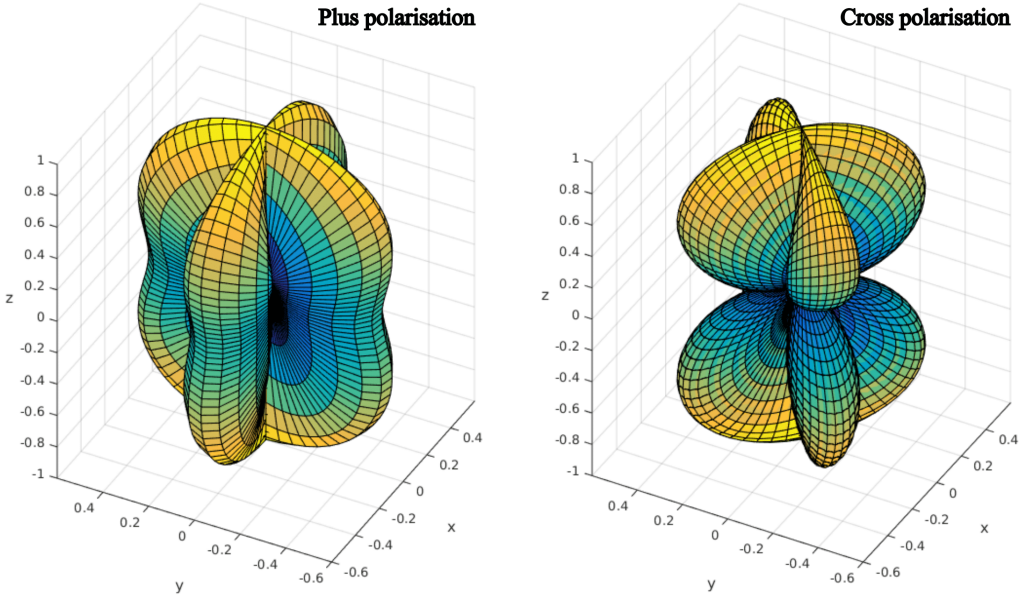

FIGURE 2.5: Plus and cross antenna response pattern for a Michelson interferometer placed at the center. The shape and the colours represent the magnitude of $F_{+/\times}$, ranging from a null value (blu) up to the maximum (yellow). Image from [97].

2.1.3 Sensitivity and Noise Sources

The GW strain in Eq. (2.2), or the output of the GW detector, is a time-series $s(t)$ which describes the oscillation states of the test masses, and it is a combination of

the GW signal $h(t)$, if present, and noise $n(t)$

$$s(t) = h(t) + n(t) \,. \tag{2.3}$$

The challenge in detecting GWs is to separate $n(t)$ from $h(t)$ and reduce the noise so that the GW signal can be clearly distinguished. The power spectral density (PSD) $S_n(f)$, expressed in Hz^{-1}, represents the distribution of the power of the noise across different frequencies. It gives information about which frequency components of the noise are contributing more power and which are contributing less, identifying the minimum value of the GW signal that can be detectable. The PSD is defined, for infinite observing time, by taking the Fourier transform of the time-domain noise signal and squaring the magnitude of the resulting frequency-domain signal as [260]

$$\langle \tilde{n}^*(f)\tilde{n}(f')\rangle = \frac{1}{2}\delta(f-f')S_n(f) \,, \tag{2.4}$$

where $\langle\cdot\rangle$ refers to the average over time, $\tilde{n}$ denotes the Fourier transform and the $\tilde{n}^*$ its complex conjugate. By assuming $\langle n(t)\rangle = 0$, it is possible to obtain $\langle n^2(t)\rangle$ as the integral of $S_n(f)$ [260]

$$\langle n^2(t)\rangle = \int_{-\infty}^{\infty} df \int_{-\infty}^{\infty} df' \langle n^*(f)n(f')\rangle = \frac{1}{2}\int_{-\infty}^{\infty} S_n(f)df = \int_0^{\infty} S_n(f)df \,, \tag{2.5}$$

where $S_n(f)$ is also called single-sided spectral noise, emphasising the fact that the integral extends only over physical frequencies ($f > 0$). Eq. (2.5) indicates that the noise of a detector can be characterised by $\sqrt{S_n(f)} = A_n(f)$, which is also called amplitude spectral density (ASD). The sensitivity of current ground-based interferometers describes the amplitude of the GW signals that they are capable of detecting, as well as the frequency range over which they are most sensitive. The sensitivity is represented with the dashed line in Figure 2.6, between $\sim$ 20Hz and $\sim$ 4000Hz, and it is limited by various noise sources that can be classified as either displacement noise, which affects the motion of the suspended mirrors causing a differential change in the arm cavity lengths; or sensing noise, which appears in the readout signal but is not caused by a physical movement of the mirrors. The main sources of noise that limit the sensitivity of interferometers are: seismic noise [188], which is present at lower frequencies and to which earthquakes, weather conditions, and human activity contribute; thermal noise [81, 171, 217, 358], which is caused by the thermal energy of the instrument's components and is divided in coating thermal noise [217], that arises from the thermal fluctuations within the thin coatings applied to the mirrors, and Brownian motion, which arises from the random motion of particles in a material due to their thermal energy; quantum noise [153, 300, 358], which arises from the quantum nature of light and the uncertainty principle, and is generated by random fluctuations in the number of photons in the laser light used in the interferometer, leading to shot noise [279] and radiation pressure noise [159]; and lastly, Newtonian noise [108], which refers to noise caused by local variations in the gravitational field due to the motion of matter near the detector. In addition to selecting an optimal location for the detector, advanced suspension systems [95] are used to minimise any potential movements of the optical elements, while squeezed light states [300], optical filters [176], and advanced coatings [185] for the optics are employed to diminish the impact of other sources of noise. Moreover, the presence of residual gas [261] in the beam tubes would worsen the performance of the laser; for this reason the vacuum system is maintained at a pressure below 10^{-12} Bar and

the noise curve of the interferometer includes only the most dominant residual gas component, hydrogen.

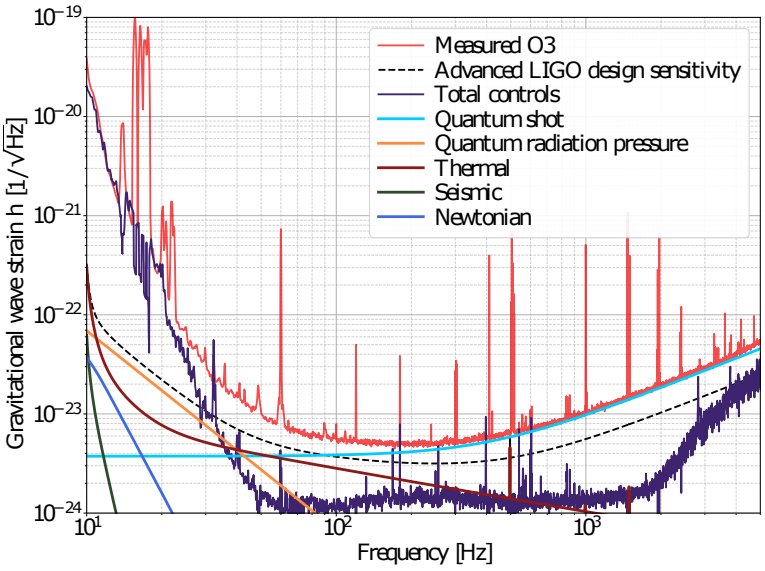

FIGURE 2.6: Simplified O3 LIGO Hanford noise budget [126]. The noise curve represents the Fourier-transform of the time series of the detector output in order to show the frequency content of the noise as an amplitude spectral density.

In addition to known noise sources, there are also transient noise events known as glitches [163, 204, 274, 306]. These events are characterised by their loudness, short duration (ranging from a fraction of second to several seconds), and high SNR. Glitches can originate from a variety of sources, including environmental perturbations, detector malfunctions, technical issues, and control systems. In order to understand these events, thousands of auxiliary sensors are placed to closely monitor the detector and its environment. In Figure 2.7 are presented six identified families of glitches, for five of which a signal in one of the auxiliary channel allowed to identify the source. The so-called "noise hunting" [92, 168, 264] process aims to identify glitches and to correlate them with unusual detector behaviours or environmental disturbances. Glitches are typically filtered from the data using a combination of techniques, which may include pass-band filtering, used to extract the frequency components of interest in the data, which correspond to the expected frequency range of GW signals, data quality vetoes, that consist in removing periods of poor data quality due to known environmental or instrumental factors that affects the detector's sensitivity and that are identified by auxiliary channels, and gating, which consists in setting to zero the data around an identified glitch [186]. Data quality vetoes and gating serve similar purposes of identifying and mitigating the impact of noise on the data. However, the former are used to indicate when the data are known to have excess noise, and the exception to this process is gating, which is applied independently of the vetoes, and it is internal to the data analysis stream pipelines. These techniques remove the known glitches and the loud ones, but not all of them. Those who survive are removed in subsequent steps of the data analysis with matched filtering and signal consistency checks, which will be discussed in Chap. 3.

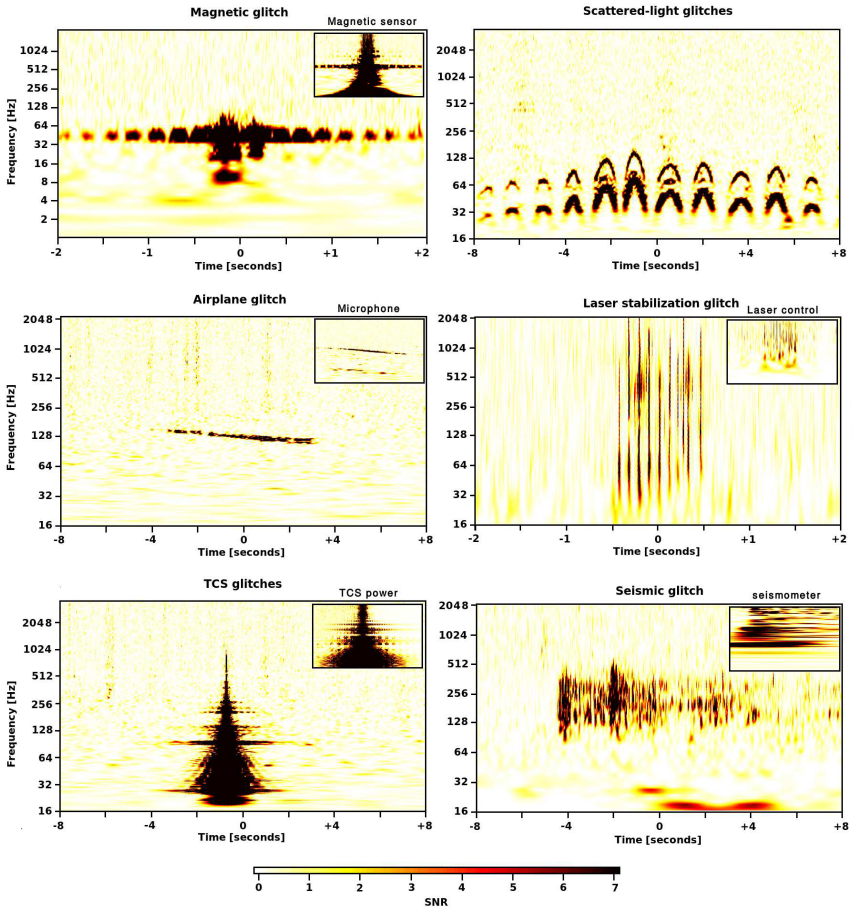

FIGURE 2.7: Time-frequency visualisations of some examples of noise transient observed in the Virgo detector [189], the colour scale indicates the SNR. The glitches are caused by various factors, in order: power-line disturbances, scattered light from seismic activity, instabilities in the thermal compensation system, passing airplanes, laser stabilisation issues, and seismic events.

In addition to the sensitivity curve, the binary neutron star (BNS) range [85] (in Figure 2.8) is another quantity used to evaluate the performances of a detector and compare it to the other detectors. It represents the distance (in Mpc) at which a BNS merger, consisting of two 1.4 $M_\odot$ neutron stars, would generate a signal-to-noise ratio (SNR) of 8.0, averaged over all possible sky positions and polarisations.

2.2 Current Detector Network

The development of ground-based interferometric detectors dates back to the 1980s [344], and since then, their technology has been continuously improved and refined. The first pioneering apparatuses were Initial LIGO, consisting of two identical 4-km long interferometers in Livingston (US), and Hanford (US), and Initial Virgo, located in Pisa (IT). Scientific operations of the LIGO detectors began in 2002 [344], and in 2007 the Virgo detector joined [151]. The LIGO-Virgo Collaboration carried out a sequence of GW searches. The earlier runs were primarily used for commissioning, testing, and calibration of the detectors, while the fifth science run (S5) [15, 37–39, 43, 202, 354] and the sixth science run (S6) [6–9, 12, 13, 142, 156, 314] were fully operational science data collection phases, during which no confirmed detections of GWs were reported. The two Advanced LIGO [5, 26, 50] detectors began scientific

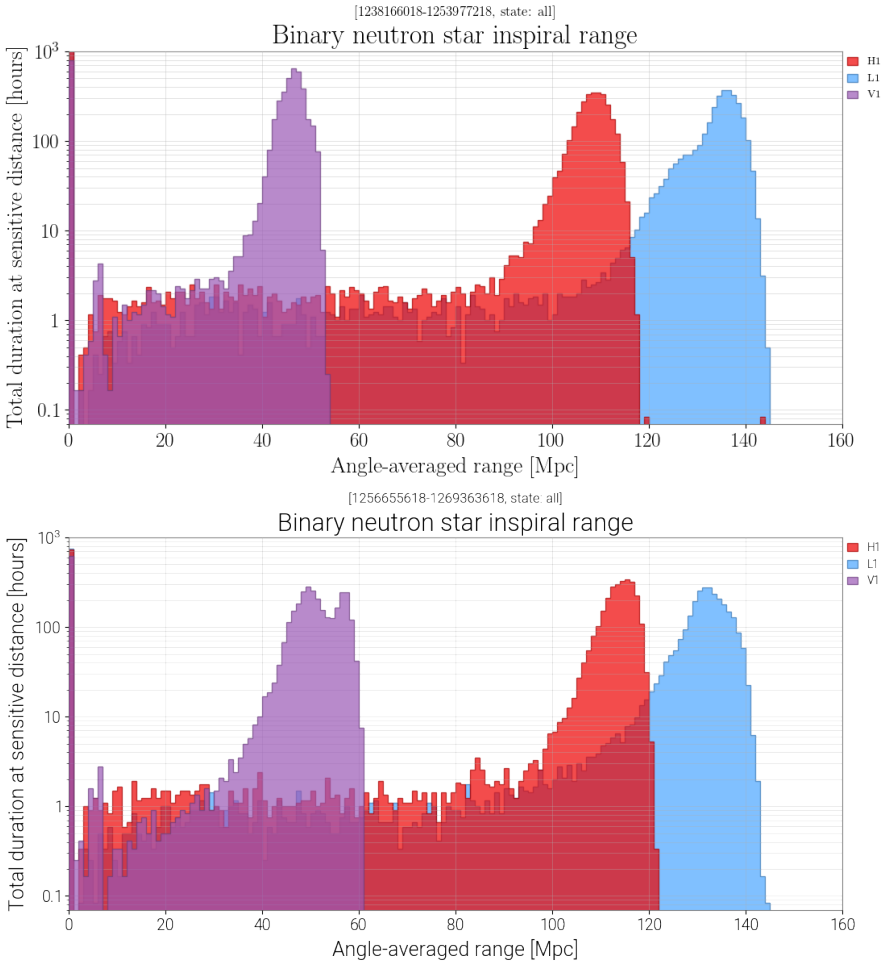

FIGURE 2.8: Total time of operation at a given sensitivity averaged over all sky positions and source orientations during the first half of the third observing period [212] (O3a, upper plot) and during the second half of the third observing run [213] (O3b, bottom plot) for the LIGO Livingston (L1, blue), LIGO Hanford (H1, red) and Virgo (V1, violet) detectors as function of the average sensitivity measured in Mpc. The reported values in this plots are computed by comparing the noise curves with a predicted GW signal that could arise from the merger of a BNS.

operations in September 2015, starting the search for GW signals with the first observing run (O1). Between the first and the second observing run (O2), started on November 2016, several upgrades were implemented in both LIGO detectors to improve their sensitivity from a BNS range of approximately 60 Mpc to approximately 80 Mpc [31]. Before the end of the run the works on the Advanced Virgo [71] site were completed and the detector joined the data taking on August 2017, with a BNS inspiral range of approximately 25 Mpc [31]. The third observing run (O3) started on April 2019 with an enhanced sensitivity and robustness of three detectors [72, 73, 167]. During the first (second) half of it, the BNS median inspiral range for the three detectors were: 108 Mpc (115 Mpc) for LIGO Hanford, 135 Mpc (133 Mpc) for LIGO Livingston and 45 Mpc (51 Mpc) for Virgo [58–60]. The current network of GW detectors (showed in Figure 2.9) includes also the GEO600 (DE) facility, mainly used for testing and development of new technologies, and the KAGRA detector [94] in the Kamioka mine (JP), that has joined the fourth data taking period (O4), started on May 2023, with a BNS range of 1.5 Mpc [361]. In the future, KAGRA is expected to

improve its sensitivity, in particular below 100 Hz, thanks to the underground site and cryogenic mirrors [192].

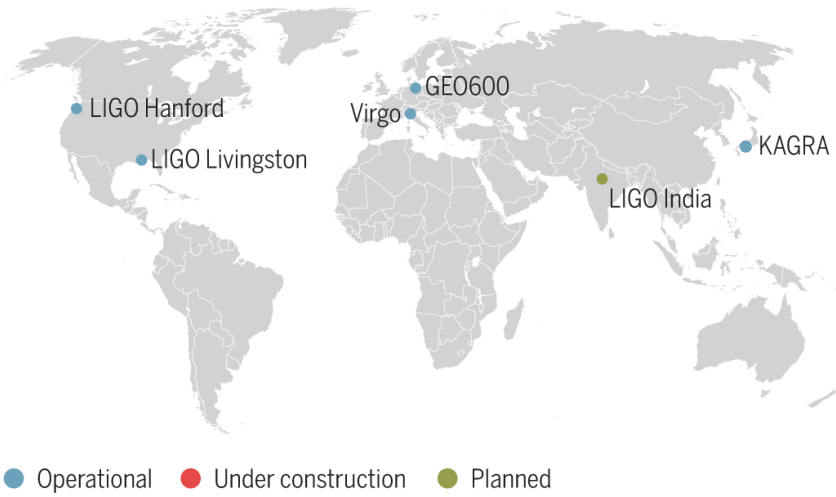

FIGURE 2.9: Map of the actual network of interferometers used in the search and development for GWs.

In the coming years, more detectors will join the search for GWs, such as LIGO-India [256] (IND), which is planned to start taking data in 2027, and with which the sky coverage of the network will be greatly enhanced. Additionally, several next-generation ground-based observatory (Einstein Telescope [183] and Cosmic Explorer [46, 135, 154, 179, 184, 311]) and a space-based interferometer (LISA [252]) are being designed. The Einstein Telescope [120] will achieve an improved sensitivity by increasing the size of the interferometer's arms up to 10 kms, and by implementing a series of new technologies including a cryogenic system to cool some of the main optics, new quantum technologies to reduce the fluctuations of the light, and a set of infrastructural and active noise-mitigation measures to reduce environmental disturbances. In its design concept [191], Cosmic Explorer will be even bigger, featuring two facilities each housing a single interferometer, one with arms measuring 40 km in length, while the other with arms measuring 20 km in length. The LISA interferometer, with its space-based configuration [197], will be an extremely large equilateral triangle detector, with arms that will extend about 2.5 million kilometers, that will allow the scientific community to study regions of the GW spectrum that are inaccessible from Earth. Its sensitivity will be focused in the low frequency band, between 0.1 Hz and 1 Hz, targeting sources including ultra-compact binaries in our Galaxy, supermassive BH mergers and extreme mass ratio inspirals, as well as other possible exotic, unknown sources. Moreover, the Pulsar Timing Array (PTA) [93] group aims to observe the timing variations of a network of millisecond pulsars caused by the passage of low-frequency GWs [170, 237, 258], which are difficult to detect using ground-based interferometers, by combining data from multiple radio telescopes around the world.

2.3 Milestones from the First and Second Observing Runs

So far three observing runs (O1, O2 and O3) have been completed by the LIGO-Virgo Collaboration with advanced detector configuration. In this section the main achievements of O1 and O2 are reviewed, while the following chapters (Chap. 4 and Chap. 5) are dedicated to O3, which represents the focus of this thesis.

2.3.1 O1

The first observing run of Advanced LIGO [31], namely O1, started on 2015 September 12th 00:00:00 UTC and ended on 2016 January 19th 16:00:00 UTC, collecting 49 days of simultaneous observation time in two detectors: LIGO Hanford and LIGO Livingston. During this period, the synchronous detection of a transient GW signal occurred on 2015 Sept 14th, becoming the first direct detection of GWs and the first observation of a BBH merger [34]. In addition to it, two other BBH transient GW signals were detected [19, 27], listed in Table 2.1.

2.3.1.1 GW150914: The Very First Detection

On September 14, 2015 at 09:50:45 UTC, the Hanford and Livingston detectors observed a coincident signal: the first GW event ever witnessed [18, 20–22, 25, 26, 32, 34–36, 44, 45, 48, 51, 70, 78]. It was generated by the coalescence of two BHs with individual masses of $35.6^{+4.7}_{-3.1}\ M_\odot$ and $30.6^{+3.0}_{-4.4}\ M_\odot$ (see Table 2.1), producing at the output of the detectors the signal showed in Figure 2.10, and that formed a final BH with mass of $63.1^{+3.4}_{-3.0}\ M_\odot$, radiating away $3.1^{+0.4}_{-0.4}\ M_\odot c^2$ of energy in GWs. GW150914 was a breakthrough event in the field of astronomy and physics as it provided direct evidence for the existence of GWs, validating the theory of General Relativity and the possibility of having BH mergers occurring within the Hubble time. Additionally, before its detection, there was limited observational evidence of BHs with masses above $25M_\odot$. Indeed, most of the know BHs at that time were found through X-ray binaries, which tend to have BHs with masses around 10.0 $M_\odot$ or less, leading to the speculation that BHs with larger masses were rare or nonexistent. The detection of GW150914, however, showed that BHs with larger masses do exist, challenging our previous understanding. This historic event, which led to the awarding of the 2017 physics Nobel Prize [286] and the CNRS gold medal [146], opened the era of gravitational-wave astronomy, enabling scientists to study the Universe in a completely new way, and providing valuable insights into the properties of BHs and other extreme objects.

2.3.2 O2

The second observing run, O2 [31], started on 2016 November 30th 16:00:00 UTC and ended on 2017 August 25th 22:00:00 UTC, with 117 days of simultaneous LIGO-detector observing time. The inclusion of the Virgo detector in the search for GWs on August 1st 2017 marked the start of the three-detector observations of GWs and greatly enhanced the sky localization capabilities of the detected events. The second observing run marks another great achievement: the first detection of a merging BNS system [29], in addition to other seven BBH events, listed in Table 2.1.

2.3.2.1 GW170817: The First GW signal with Electromagnetic Counterpart

GW170817 [29], the first signal of a BNS coalescence, originated from the merger of two NSs with masses $1.46^{+0.12}_{-0.10}\ M_\odot$ and $1.27^{+0.09}_{-0.09}\ M_\odot$ (see Table 2.1), was the most remarkable detection during the second observing run. Detected by LIGO Hanford and LIGO Livingston (see Figure 2.11a), it was followed 1.7 s after the coalescence by a short-duration gamma-ray burst, GRB 170817A [23, 24, 82, 198], detected by Fermi-GBM [205] and INTEGRAL SPI-ACS [324]. The signal was not visible in Virgo data, due to its lower BNS horizon and orientation of the source with respect to the detector [29]. The combination of information from all three interferometers allowed

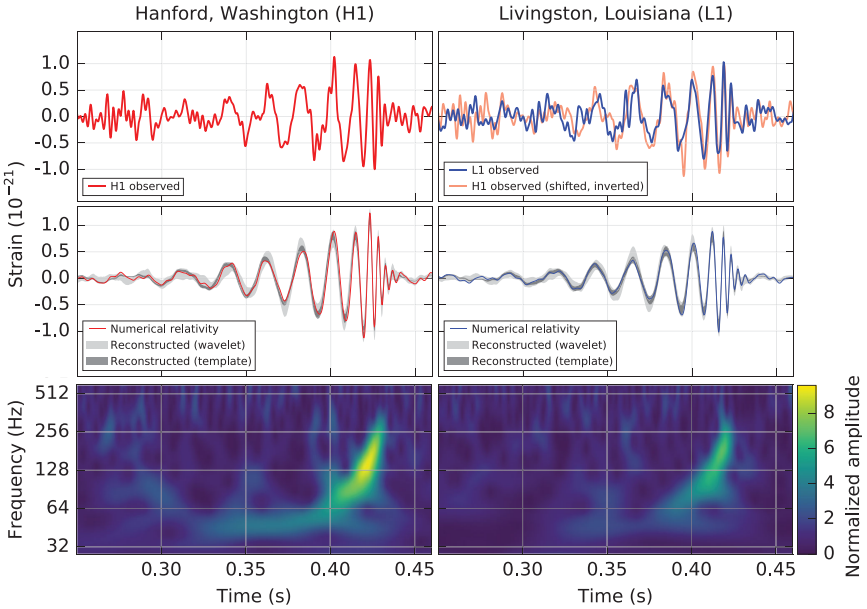

FIGURE 2.10: The GW event GW150914 observed by LIGO Hanford (H1, left panels), and LIGO Livingston (L1, right panels). The top panels show the detected strains, the middle panels show the the GW strain projected onto each detector in the $35 - 350$ Hz frequency band, while the bottom panels are a time-frequency representation of the strain data evolution [34].

to restrict the sky localization of the source to an area of 28 deg^2, as shown in Figure 2.11b, and the identification of the host galaxy: NGC 4993 [115]. This allowed for an extended electromagnetic follow-up campaign [33] during which were observed the optical counterpart [157, 278, 335, 349], the near-infrared [141], radio [83] and ray [262] emissions. This coincidence detection represents the first electromagnetic signature physically associated with a GW source and marks the dawn of multi-messenger astrophysics with GWs. The initial proposals of mass ejection mechanisms linked to BHNS and BNS mergers were suggested in [255] and [180, 341] respectively. Later numerical simulations have shown that in the final orbits leading to the merger, the NSs may undergo tidal disruption and emit tails of decompressed NS material. This was observed in several studies, such as [107, 228, 288, 307, 308, 315]. Moreover, when the two NSs collide, further dynamic ejection of matter occurs at their interface [355]. The occurrence of the GW signal and the subsequent electromagnetic counterpart in a rare observational simultaneity prompted the unification of various research areas including astrophysics, general relativity, and nuclear physics.

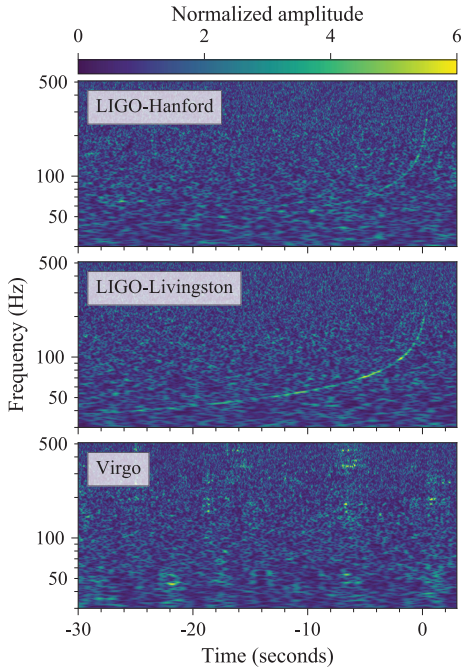

(A) Time-frequency representations of the GW event GW170817 observed by LIGO Hanford (top panel), and LIGO Livingston (middle panel) and Virgo (bottom panel).

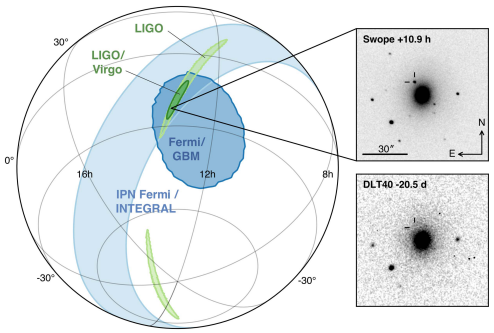

(B) Sky location for GW170817 from Hanford-Livingston (light green contours) and Hanford-Livingston-Virgo (dark green contours), with triangulation from the time delay between Fermi and INTEGRAL (light blue), and Fermi-GBM (dark blue).

FIGURE 2.11: GW170817 in time-frequency representation in (A) and it's hosting galaxy NGC4993 in (B), 20.5 days before the merger (bottom panel) and 10.9 hours before it (top panel), highlighting the presence of a new object [33].

TABLE 2.1: Parameters of all the confident detections of GW events made during O1 and O2 [134].

GW events in O1 and O2								
GW event and time (UTC)	Luminosity Distance (Mpc)	Mass 1 ($M_\odot$)	Mass 2 ($M_\odot$)	Effective Spin	$\mathcal{M}$	Remnant Mass ($M_\odot$)	Remnant Spin	Radiated Energy ($M_\odot c^2$)
GW150914 09:50:00	440^{+150}_{-170}	$35.6^{+4.7}_{-3.1}$	$30.6^{+3.0}_{-4.4}$	$-0.01^{+0.12}_{-0.13}$	$28.6^{+1.7}_{-1.5}$	$63.1^{+3.4}_{-3.0}$	$0.69^{+0.05}_{-0.04}$	$3.1^{+0.4}_{-0.4}$
GW151012 09:54:00	1080^{+550}_{-490}	$23.2^{+14.9}_{-5.5}$	$13.6^{+4.1}_{-4.8}$	$0.05^{+0.31}_{-0.20}$	$15.2^{+2.1}_{-1.2}$	$35.6^{+10.8}_{-3.8}$	$0.67^{+0.13}_{-0.11}$	$1.6^{+0.6}_{-0.5}$
GW151226 09:54:00	450^{+180}_{-190}	$13.7^{+8.8}_{-3.2}$	$7.7^{+2.2}_{-2.5}$	$0.18^{+0.20}_{-0.12}$	$8.9^{+0.3}_{-0.3}$	$20.5^{+6.4}_{-1.5}$	$0.74^{+0.07}_{-0.05}$	$1.0^{+0.1}_{-0.2}$
GW170114 10:11:00	990^{+440}_{-430}	$30.8^{+7.3}_{-5.6}$	$20.0^{+4.9}_{-4.6}$	$-0.04^{+0.17}_{-0.21}$	$21.4^{+2.2}_{-1.8}$	$48.9^{+5.1}_{-4.0}$	$0.66^{+0.08}_{-0.11}$	$2.2^{+0.5}_{0.5}$
GW170608 02:01:00	320^{+120}_{-110}	$11.0^{+5.5}_{-1.7}$	$7.6^{+1.4}_{-2.2}$	$0.03^{+0.19}_{-0.07}$	$7.9^{+0.2}_{-0.2}$	$17.8^{+3.4}_{-0.7}$	$0.69^{+0.04}_{-0.04}$	$0.9^{+0.0}_{-0.1}$
GW170729 18:56:00	2840^{+1400}_{-1360}	$50.2^{+16.2}_{-10.2}$	$34.0^{+9.1}_{-10.1}$	$0.37^{+0.21}_{-0.25}$	$35.4^{+6.5}_{-4.8}$	$79.5^{+14.7}_{-10.2}$	$0.81^{+0.07}_{-0.13}$	$4.8^{+1.7}_{-1.7}$
GW170809 08:28:00	1030^{+320}_{-390}	$35.0^{+8.3}_{-5.9}$	$23.8^{+5.1}_{-5.2}$	$0.08^{+0.17}_{-0.17}$	$24.9^{+2.1}_{-1.7}$	$56.3^{+5.2}_{-3.8}$	$0.70^{+0.08}_{-0.09}$	$2.7^{+0.6}_{-0.6}$
GW170814 10:30:00	600^{+150}_{-220}	$30.6^{+5.6}_{-3.0}$	$25.2^{+2.8}_{-4.0}$	$0.07^{+0.12}_{-0.12}$	$24.1^{+1.4}_{-1.1}$	$53.2^{+3.2}_{-2.4}$	$0.72^{+0.07}_{-0.05}$	$2.7^{+0.4}_{-0.3}$
GW170817 12:41:00	$40.0^{+17.0}_{-15.0}$	$1.46^{+0.12}_{-0.10}$	$1.27^{+0.09}_{-0.09}$	$0.00^{+0.02}_{-0.01}$	$1.186^{+1.000e-0.3}_{-1.000e-0.3}$	≤ 2.8	≤ 0.89	≥ 0.04
GW170818 02:25:00	1060^{+420}_{-380}	$35.4^{+7.5}_{-4.7}$	$26.7^{+4.3}_{-5.2}$	$-0.09^{+0.18}_{-0,21}$	$26.5^{+2.1}_{-1.7}$	$59.4^{+4.9}_{-3.8}$	$0.67^{+0.07}_{-0.08}$	$2.7^{+0.5}_{-0.5}$
GW170823 13:13:00	1940^{+970}_{-900}	$39.5^{+11.2}_{-6.7}$	$29.0^{+6.7}_{-7.8}$	$0.09^{+0.22}_{-0.26}$	$29.2^{+4.6}_{-3.6}$	$65.4^{+10.1}_{-7.4}$	$0.72^{+0.09}_{-0.12}$	$3.3^{+1.0}_{-0.9}$

CHAPTER3

MBTA Analysis Framework

The search for GWs is a complex and challenging task that requires sophisticated techniques capable of analysing data and identifying these elusive signals [158, 236, 260]. Data analysis plays a crucial role in the process of extracting the foreground GW candidates from data collected by ground-based interferometers, as it involves spotting weak signals buried in the background noisy data and determining their properties [186], such as their source location, the components masses, and their spins. In the following chapters the terms "background" and "foreground" are used to distinguish between different sources of signals present in the data. The background refers to the collection of signals that includes instrumental noise, environmental disturbances, and other types of non-astrophysical signals. On the other hand, the foreground refers to the astrophysical signals or events that are the primary focus of the analysis. In this chapter, the fundamentals of the CBC search pipelines are outlined, with a detailed discussion of the unique features and characteristics of the Multi-Band Template Analysis (MBTA) pipeline [10, 75, 76, 96], which is used throughout this thesis work.

3.1 Analysis Stream

The analysis stream, also known as pipeline, of GW data analysis refers to a series of steps that are undertaken in order to extract and analyse GW signals from data. In the search for GW candidates, multiple, independently designed and implemented search pipelines are employed for the detection of CBC mergers across the entire sky: GstLAL [214, 267, 320], MBTA [10, 75, 76, 96], PyCBC [285, 348], SPIIR [226] and cWB [244]. These pipelines are able to work in two different approaches: online and offline. Online searches analyse data from multiple detectors in near real-time as it is being collected in order to identify and alert astronomers of potential GW signals with a typical latency of seconds, and enable rapid followups by telescopes to search for electromagnetic emissions from the same astrophysical source. Offline searches, on the other hand, involve analysing data after the end of the observing run. This approach allows for more sophisticated analysis techniques to be applied, as the entire data set can be processed at once with more computational resources available and a better estimation of the background noise. The goal of the detection techniques is to identify potential instances of GW signals within the data. Following detection, the next step involves parameter estimation [31, 58–60, 62, 63, 164], which aims to estimate the specific parameters associated with the sources responsible for generating the detected GW signals.

3.2 Data Segments

The data collected by each detector is a time series $s(t)$, divided into time intervals called "science segments", that correspond to continuous periods during which the interferometer is operating in a nominal state, resulting in stable and reliable data, suitable for analysis (as shown in Fig. 3.1). Each stretch of data is further divided into

FIGURE 3.1: Plots of the time periods when the LIGO Livingston (L1), LIGO Hanford (H1) and Virgo (V1) detectors were operating in coincidence during the first half (top panel) and the second half (bottom panel) of the third observing run. Tall blocks indicate times of observing mode, while narrow blocks indicate periods when the interferometers were in operational state, but not in observing mode [212, 213].

smaller data segments, corresponding to at least the length of the longest template in the template bank (see Section 3.5), that are Fast Fourier Transformed (FFT) in the frequency domain. The FFT algorithm is efficient in rapidly computing the discrete Fourier transform of a sequence of N equally spaced data points, optimised to have a complexity of $\mathcal{O}(\frac{N}{\log N})$. In order to extract a GW signal from noisy data, the detector strain is first pre-processed by bandpass filtering, done by multiplying its Fourier transform by a window function that selects the frequencies at which the detector

sensitivity is adequate, and then computing the inverse Fourier transform to obtain the filtered signal in the time domain.

3.3 Detector Characterisation and Data Quality

The following step in the analysis stream is to remove any unwanted noise source, such as instrumental artefacts or environmental disturbances. This is done by using gating (introduced in Section 2.1.3), veto flags and signal processing techniques, which aim to reduce the rate of false positives and to improve the probability of detection of a real GW signal [14, 167]. Data quality veto flags identify periods when data may be contaminated by noise or other issues that could mimic or mask a real GW signal. Different factors, such as seismic activity, magnetic interference, or instrumental glitches can lead to such corruption. They are broadly classified into two veto flags categories [60, 186, 187]: CAT1 veto flags denote periods when a crucial component of the detector is not operating as intended, while CAT2 veto flags mark times when there is a known physical coupling to the GW channel, as for example times of high seismic activity. These flags are usually set by automated algorithms that scan the data for anomalies, identifying bad data quality periods, and excluding them from further analysis. As mentioned earlier, in addition to the veto flags, the data analysis stream pipelines incorporate a gating process. In the MBTA pipeline, the gating procedure is triggered whenever the BNS range value falls below a threshold of 60% of the median range observed over the past 10 seconds [96]. Fig. 3.2 shows an example of data quality evaluation in a sample week during the third observing run.

3.4 Matched Filtering

The presence of modelled CBC signals in the pre-processed data is then established via a matched-filtering technique, which correlates the detector data with a template waveform that represents the expected GW signal from a particular astrophysical source (see Section 1.3.3.2). Since this method relies on comparing the detector data with a pre-determined waveform template, it is only suitable for modelled searches where the expected signal is reasonably well understood. By regarding the strain measured $s(t)$ at the detector's output port as a superposition of the GW signal $h(t)$ and noise $n(t)$, as in Eq.(2.3), the matched filtering selects a filter $h_{template}(t)$ that best matches the GW signal of interest in order to detect it. The output of this matched filtering process is quantified by the SNR ρ, which serves as a measure of how effectively the signal stands out from the background noise, and is computed as [260]

$$\rho = \frac{\langle s|h_{template}\rangle}{\sqrt{\langle h_{template}|h_{template}\rangle}}\,, \tag{3.1}$$

where $\langle s|h\rangle$ denotes the inner product between the template and data, with the inverse PSD of the detector (introduced in Section 2.1.3) as the weighting factor

$$\langle s|h_{template}\rangle(t) = 4\Re\int_{f_{low}}^{f_{high}} \frac{\tilde{s}(f)\tilde{h}^{*}_{template}(f)}{S_n(f)} e^{i2\pi ft} df\,, \tag{3.2}$$

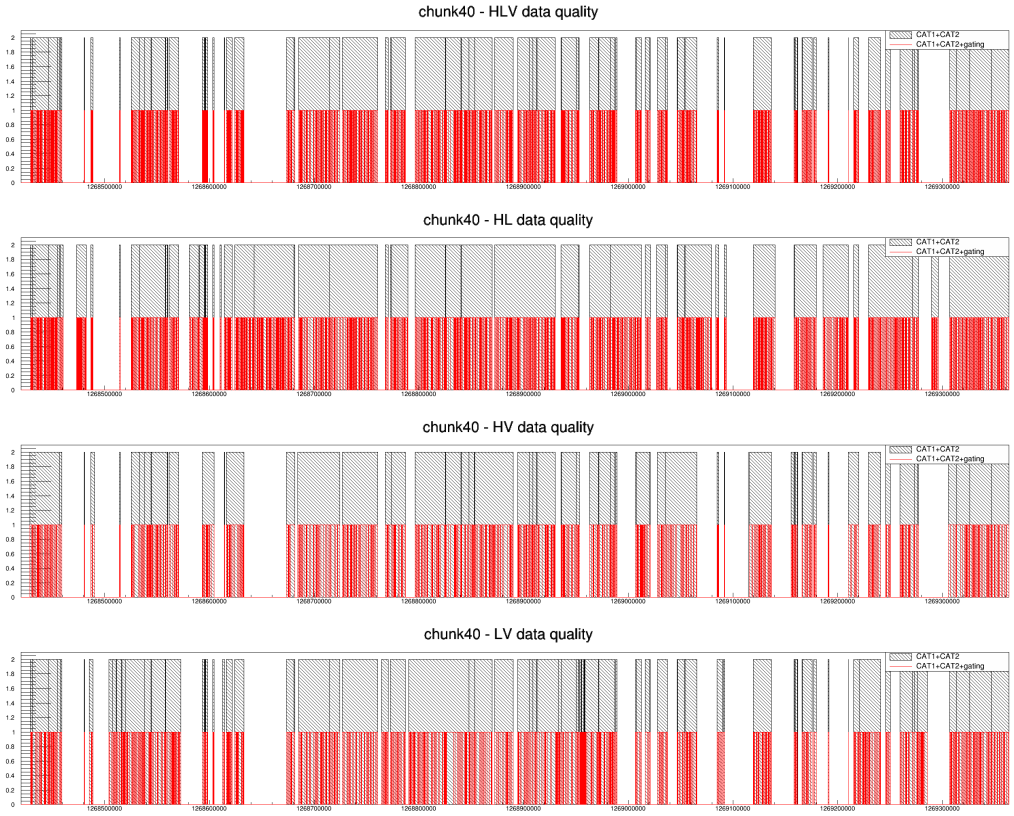

FIGURE 3.2: Evaluation of the data quality from data in between GPS times 1268420276 and 1269561620 of the third observing run, showing good data segments (filled histograms), CAT1+CAT2 vetoes (black), and CAT1+CAT2+gating vetoes (red) for different types of coincidences. In this specific case, of 13.2 days, a total of 9.42 days had at least two detectors with a good data quality.

in which f_{low} and f_{high} are the frequency limits determined by the bandwidth of the data, the tildes denote the Fourier transform and the asterisk the complex conjugate. This technique naturally returns a measure of the SNR and can be proven to be optimal in recovering a known signal. In cases where the noise is stationary and Gaussian, meaning that its statistical properties remain constant over time, the SNR alone would provide a reliable measure of the performance of the filter used to extract GW signals. In such cases, the SNR would accurately reflect the strength and significance of the GW signal relative to the background noise. However, as the detector data typically contains non-Gaussian and non-stationary noise transients, as reported in Section 2.1.3, further measures are required to assign a meaningful statistical significance to candidate signals, as will be discussed in Section 3.6. Moreover, due to the multiple possible combinations in the wide range of masses and spins that lead to a broad phenomenology of waveforms, a template bank (introduced in Section 3.5) is used to filter the data, covering the target parameter space of interest. Each waveform within the bank is used to filter the detector data, ensuring that any signal falling within the specified mass and spin ranges matches at least one of the templates within a certain margin of error. This maximum allowable error is determined when designing the template bank and influences the number of templates needed, as a smaller margin of error necessitates a greater number of templates to ensure adequate coverage. The innovative characteristic of MBTA is that it splits the

matched filtering into two (or more) frequency bands, which are processed independently and then recombined to form a unified waveform. By employing this strategy, MBTA is able to capture and analyse different frequency components of the signal in a more effective way. The logic behind this approach is that the high-frequency band in MBTA uses smaller windows in the FFT since it contains a smaller portion of the signal compared to the low-frequency band. This technique offers two immediate advantages: it reduces the number of cycles over which the signal is tracked, resulting in sparser template banks in each frequency band; and second, it lowers the computational costs associated with the FFT used in the filtering process. The complete bandwidth SNR is then determined by combining the matched filter outputs from the two frequency bands as

$$\rho_{full} = 4\Re\left[\int_{f_{low}}^{f_c} \frac{\tilde{s}(f)\tilde{h}^*_{template}(f)}{S_n(f)} e^{i2\pi ft} df + \int_{f_c}^{f_{high}} \frac{\tilde{s}(f)\tilde{h}^*_{template}(f)}{S_n(f)} e^{i2\pi ft} df\right], \quad (3.3)$$

where the value of the frequency boundary f_c separating the low and high frequency bands is selected to ensure that the SNR is evenly distributed between the two bands. Its specific value depends on the characteristics of the waveform source. In practice, determining the optimal value for f_c involves studying the properties of the waveform, such as its frequency content, duration, and amplitude. The aim is to find a value for f_c that provides a balanced distribution of SNR, optimising the detection performance in both frequency bands. This approach involves applying matched filtering independently to the data from each detector in the network using the same template bank. Once the SNRs are computed for each detector, the next step is to generate triggers, which are points in the detector strain time series where the SNR exceeds a chosen threshold. This is done by dividing the time series into separate windows and identifying the maximum SNR within each window. Triggers that occur close in time (usually within 20 ms of any trigger in the cluster) are grouped by a clustering algorithm, as they are likely to originate from the same event, and then the local maximum is selected. The triggers are then down-selected by applying the criterion of coincidence across the detector network. To qualify as a candidate event, the MBTA pipeline conducts a coincident test on triggers from different detectors. This test necessitates that any trigger observed in any detector within the network exhibits consistent arrival time and template parameters. In other words, it must correspond to the same template across all detectors and have a time delay within the expected gravitational wave travel time between the interferometers, as will be described in Section 3.6. In case multiple detectors catch the same GW signal, the corresponding combined SNR ρ_{comb} is computed as the square root of the quadrature sum of the individual SNRs

$$\rho_{comb} = \sqrt{\sum_{i=1}^{N} \rho_i^2}, \quad (3.4)$$

where N indicates the number of detectors involved in the coincidence. In practice, the SNRs ρ_i in Eq. (3.4) do not directly correspond to the output of the matched filtering. Instead, they are re-weighted SNRs that take into account periods of noise. The details of this re-weighting process are explained in Section 3.6.

3.5 Template Banks

A template bank is a set of waveforms generated based on a given model and target volume of the parameter space [269, 270]. These waveforms serve as a reference against which the detector data is compared in the matched filtering process in order to identify GW signals. Waveforms for binary system mergers are characterised by a set of 15 parameters classified between intrinsic parameters, such as masses and spins of the components, and extrinsic parameters such as inclination, polarisation, sky position of the source, arrival time and phase of the GW. If one of the compact objects in the binary system is a NS, its properties, specifically the Equation of State (EOS), need to be taken into account. The EOS describes the relationship between the pressure, density, and other physical properties inside the NS and is encoded in the so called tidal deformability, which quantifies the response of a NS to the tidal forces exerted by a companion object in a binary system [109, 111, 227, 246–248]. Incorporating the tidal deformability into the analysis increases the complexity of the parameter space, which becomes larger. Performing the matched filtering at every point of this potentially huge space would be computationally prohibitive, thus the size of the template bank must be limited by marginalising over some of the parameters, resulting in a reduced loss of SNR, and slightly decreasing the detection efficiency of the template bank. Typically, the parameters over which the bank is created are the component masses $m_{1,2}$ and the dimensionless aligned spins $\chi_{1,2} = \mathbf{S}_{1,2}/m_{1,2}$, and its generation involves a trade-off between computational costs and accuracy [98, 147, 301]. It is noteworthy to remember that employing a template bank constructed with a restricted set of parameters is not a concern because the primary objective of the detection process is to detect the presence of GW signals rather than precisely determine the source parameters. The subsequent step of parameter estimation [31, 58–60, 62, 63, 164] can be carried out on the identified candidates to obtain more accurate information about the source parameters. Thus, the limited parameter space covered by the template banks adequately serves the initial detection phase. A larger number of templates can improve the accuracy of the matched filtering, and so the accuracy of the search, but at the cost of increasing the computational resources needed. Conversely, a smaller number of templates can reduce the computational costs, but may result in missed signals. Since the parameters of the source are not known a priori, the templates in the bank are placed in such a way that any signal matches one of them with a certain margin of error [297], identified as the distance between neighbouring templates, or match $\mathcal{M}$, defined as the maximum overlap $\mathcal{O}(h_1, h_2)$ between two nearest templates $h_1(f; \lambda_{intr})$ and $h_2(f; \lambda_{intr} + \Delta\lambda_{intr})$ where λ_{int} is the set of intrinsic parameters over which the template is built [297]

$$\mathcal{M}(h_1, h_2) = \max \left[\mathcal{O}(h_1, h_2) \right] , \tag{3.5}$$

with [297]

$$\mathcal{O}(h_1, h_2) = \frac{\langle h_1 | h_2 \rangle}{\sqrt{\langle h_1 | h_1 \rangle \langle h_2 | h_2 \rangle}} \in [0, 1] , \tag{3.6}$$

and $\langle h_1 | h_2 \rangle$ the noise-weighted inner product as defined in Eq. (3.2). The overlap in Eq. (3.6) represents the fraction of signal power that would be detected when searching for a signal h_1 using a template waveform h_2. The creation of a template bank consists in generating templates distributed throughout the space by varying the values of the parameters within specified ranges [348]. The resulting placement of templates is non-uniform to ensure an optimal coverage, indeed more templates

are required to search for mergers with low mass components than for those with high mass components, as the mismatch $(1-\mathcal{M})$ between waveforms changes more rapidly at low masses than at high masses. This means that small variations in the masses of light binary systems have a larger impact on the mismatch with respect to massive systems, whose waveform mismatch is less affected by the same mass variation. An efficient template bank should strike a balance between adequately covering the parameter space and avoiding unnecessary over-coverage [348]. This optimisation is crucial for the matched filtering process, which is computationally demanding and constitutes a significant portion of the analysis. By carefully designing the template bank to provide sufficient coverage without excessive redundancy, computational resources can be used more efficiently, reducing the computational cost without invalidating the overall efficiency of the analysis. Therefore, it is crucial to optimise the placement and minimise the number of templates needed while maintaining a high detection efficiency, ensuring that all possible GW signals are covered while avoiding redundancy, thus reducing the computational costs of the search. There are two main classes of template-placement algorithms that have been developed and presented in the literature [298]: the stochastic [99] and the geometric placement [316]. In the stochastic placement algorithm, waveforms are randomly generated in the parameter space, and only newly generated waveforms that have an overlap smaller than the pre-set minimal match (typically 0.97) with at least one existing waveform in the template bank are added to the bank. All other waveforms are rejected. The idea is to continuously generate new templates until the desired detection efficiency is achieved. Although this algorithm provides a robust method to generate an efficient template bank that optimally covers the parameter space, it can be computationally expensive as it requires creating a large number of trial waveforms, many more than the actual number of templates required in the bank. In the geometric placement algorithm, a metric in the parameter space is defined and used to create a regular lattice on which waveforms are placed. The distance between neighbouring points in the metric corresponds to a fixed minimal match [297]. This can be seen by Taylor-expanding Eq. (3.5) about $\Delta\lambda_{intr} = 0$, at which there is the maximum unit value of the match, to obtain [297, 348]

$$\mathcal{M}(\lambda_{intr}, \Delta\lambda_{intr}) \approx 1 + \frac{1}{2}\left(\frac{\partial^2 \mathcal{M}}{\partial\Delta\lambda^i \partial\Delta\lambda^j}\right)_{\Delta\lambda^k=0} \Delta\lambda^i \Delta\lambda^j \,, \tag{3.7}$$

which suggests the definition of a metric

$$g_{ij}(\lambda) = -\frac{1}{2}\left(\frac{\partial^2 \mathcal{M}}{\partial\Delta\lambda^i \partial\Delta\lambda^j}\right)_{\Delta\lambda^k=0} , \tag{3.8}$$

so that the mismatch between nearby templates is the square root of the proper distance between them [297, 348]

$$1 - \mathcal{M} = g_{ij}\Delta\lambda^i \Delta\lambda^j = ds^2 \,. \tag{3.9}$$

Therefore, the minimal match, chosen based on the desired balance between detection efficiency and computational costs, determines the spacing among templates in the metric, and so the total number of templates in the bank. In practice, a metric is usually developed for inspiral-only TaylorF2 [241, 242] waveforms, as it has analytic derivatives and exhibits a globally flat metric, other than being computationally efficient because based on a post-Newtonian expansion that provides a reasonably accurate description of the inspiral phase of CBC signals. The TaylorF2 metric is

applicable mainly to low-mass binary systems, where the inspiral phase dominates the signal, as for more massive systems the merger and ring down phases become significant. For searches that require a wider parameter space, a combined hybrid approach is often used to create the template bank. This involves starting with a geometric placement algorithm at low masses, and then filling in the remaining parameter space using the stochastic placement algorithm. The geometric approach avoids the computational costs of randomly generating and checking waveforms, but it may lead to an inefficient coverage if the metric does not reflect the true distribution of signals in that parameter space. Nevertheless, it is widely used due to its simplicity and computational efficiency. In practice, however, templates waveforms differ somewhat from the signals. True GW signals from spiralling binaries are exact solutions to the Einstein equations for two bodies of non-negligible mass, while the templates used in the search for these signals are, at best, finite-order approximations of the exact solutions (see Section 1.3.3.2). Moreover, true signals are characterised by several parameters, part of which are neglected in the construction of the search templates. Thus, true signals lie outside the submanifold formed by the search templates in the full manifold of all possible detector outputs. The standard measure used to assess the efficiency of a bank in recovering GW signals is the Fitting Factor (FF) [89], defined as the maximum match of an injected signal s_{inj}, which assumes a waveform model, over all the templates in the bank

$$FF = \max_{\lambda} \left[\mathcal{M}\left(s_{inj}, h_{template}(\lambda) \right) \right] \in [0,1] \, . \tag{3.10}$$

To evaluate the performance of a template bank in terms of SNR recovery, figures of merit such as signal recovery fraction and effective fitting factor [124, 219] are used. Assuming a perfect template bank where all fitting factors are unity, the total number of sources N_{opt} expected to be detected above a given SNR threshold ρ_0 is proportional to

$$N_{opt} \propto \int \sigma^3(\nu') p(\nu') d\nu' \, , \tag{3.11}$$

where $p(\nu')$ is the model used for the distribution of the parameters of interest ν' excluding the distance, and $\sigma(\nu')$ is the distance at which the expected SNR for a signal with parameters ν' is equal to the specified threshold ρ_0. In practice, the template bank may not have a $FF = 1$ in the entire parameter space. As a result, the number of detected signals N_{obs} above a certain SNR threshold are reduced compared to the ideal case mentioned earlier, which can be expressed as

$$N_{obs} \propto \int FF^3(\nu') \sigma^3(\nu') p(\nu') d\nu' \, , \tag{3.12}$$

where $FF(\nu')$ is the fitting factor between the GW signal with parameters ν' and the template bank. The signal recovery fraction α is defined as the ratio of observed to optimal number of signals

$$\alpha \equiv \frac{N_{obs}}{N_{opt}} = \frac{\int FF^3(\nu') \sigma^3(\nu') p(\nu') d\nu'}{\int \sigma^3(\nu') p(\nu') d\nu'} \in [0,1] \, , \tag{3.13}$$

and is used to express the bank performance in terms of effective fitting factor FF_{eff}, which represents the average SNR recovered for the observed population of sources,

mathematically expressed as [218]

$$FF_{eff} \equiv \alpha^{1/3} \,. \tag{3.14}$$

As introduced in Section 3.4, the MBTA pipeline is designed to perform matched filtering in two (or more) frequency bands [96]. Therefore, it requires multiple sets of template banks: a Virtual Template bank (VT) covering the full frequency range, and two (or more) Real Template banks (RT) for the low and high frequency bands separately. Each virtual template is associated to a low-frequency and a high-frequency real template, identifying the combinations that best match the virtual template. The matched filtering is performed with RT banks in the two frequency bands individually, then the triggered templates are recombined at the boundary frequency f_c and associated with the "closest" virtual template.

3.6 Signal Consistency Checks

Triggers generated by the matched filtering correspond to instances of high SNR in the SNR time series and can be caused by either noise transients or true astrophysical GW signals. This is because the matched filter can also produce high values of SNR when a template in the bank matches well with an instrumental noise artefact. To select triggers likely to come from real GW signals, a coincidence requirement is imposed, which involves requiring triggers to be observed in multiple detectors within a time window that accounts for the expected arrival time delay of the GW signal: ± 15 ms for the time of flight of HL coincidences, and ± 35 ms for HV and LV coincidences. Furthermore, triggers that come from the same astrophysical source are expected to exhibit correlation not only in time but also in the phase and amplitude of the signal, hence a consistency requisite is imposed for which it is required that the same trigger activates the same template in data from all the detectors. Only triggers that pass these tests are considered as candidate GW astrophysical events. This correlation information and the individual ranking statistic (SNR) values are then used when building the Combined Ranking Statistics (CRS) of double coincidences by adding to the quadratic sum of the individual ranking statistics, which is a term quantifying how probable the measured parameters are for a population of sources [96, 97, 285], as

$$CRS^2_{ij} = \rho^2_{rw,ER,i} + \rho^2_{rw,ER,j} + 2\ln(P_{\Delta t_{ij}} P_{\Delta\Phi_{ij}} P_{\Delta d_{eff,ij}}) \,, \tag{3.15}$$

where $P_{\Delta t_{ij}}$, $P_{\Delta\Phi_{ij}}$ and $P_{\Delta d_{eff,ij}}$ are the probabilities on the time difference, phase difference and effective distance ratio of the same source seen in two detectors i and j. These probability distributions are built by using a population of simulated signals uniformly distributed in volume, neglecting any correlation between these parameters, for which the expected SNR in each detector is estimated as

$$SNR \propto \frac{range}{d_{eff}} \times \left(\frac{M_{chirp}}{1.2}\right)^{5/6} \,, \tag{3.16}$$

where $range$ is the BNS range of the considered detector and d_{eff} is the effective distance of the simulated signal measured in this detector, which depends on the detector antenna pattern, the polarisation of the wave, the luminosity distance, the position in the sky and the inclination of the binary. In order to avoid biasing the

search based on assumptions about astrophysical populations, no intrinsic parameters such as masses or spins are considered. Instead, parameters depending on the position and orientation of the source with respect to the observer, and on the sensitivities and antenna patterns of the detectors are considered. By construction, the greater the detection statistic value, the more likely the event is to be an astrophysical signal. For triple coincidences the combined ranking statistic is computed as

$$CRS^2_{ijk} = CRS^2_{ij} + CRS^2_{ik} - \rho^2_{rw,ER,i} \,. \tag{3.17}$$

The $\rho_{rw,ER,i}$ in Eq. (3.15) and Eq. (3.17) are re-weighted SNRs that reduce the impact of low-quality triggers occurring during periods of high noise activity, and are defined as [96]

$$\rho_{rw,ER} = \begin{cases} \rho_{rw} & \text{if } ER \leq 0.3 \\ \rho_{rw}[1 - (ER - 0.3)^2] & \text{if } ER > 0.3 \end{cases} , \tag{3.18}$$

where ER is the Excess in the Rate of triggers $R_{(\rho \geq \rho_{min})}$ during poor data quality periods. This excess is quantified in Hertz and is measured as the median, evaluated on a short period around the trigger, of the rate of triggers above a ρ threshold divided by the rate of triggers once the χ^2 cut is applied and the re-weighted SNR is considered. Mathematically, it reads [96]

$$ER(t_0) = \text{median}_{[t_0+t_{offset}-10\text{s},t_0+t_{offset}]} \left[\frac{R_{(\rho \geq \rho_{min})}(t) - R_{(\rho_{rw} \geq \rho_{min})}(t)}{R_{(\rho \geq \rho_{min})}(t)} \right] , \tag{3.19}$$

where $t_{offset} = 0$ s for the online search to reduce the latency, and $t_{offset} = 7$ s for the offline analysis. The ρ_{rw} in Eq. (3.18) is the reweighted SNR, used to discriminate the good events from the background, and it is defined as [96]

$$\rho_{rw} = \begin{cases} \rho & \text{if } \chi^2_{auto} \leq 1 \\ \rho \left(\frac{10+\chi^{10}_{auto}}{11} \right)^{-1/8} & \text{if } \chi^2_{auto} > 1 \end{cases} , \tag{3.20}$$

in which χ_{auto} is the auto-chisquare, a consistency test value used to estimate the goodness of fit between the observed data and the template waveform. The parametrisation and numerical values used in Eq. (3.20) have been determined empirically based on data analysis and injection runs. This approach ensures that the selected parameters align with the actual characteristics observed in the data. Furthermore, triggers are assigned a statistical significance, which is determined by the rate at which detector noise produces events with an SNR as high as the given trigger. As the detector noise is unpredictable, the distribution of this statistic is unknown. Therefore, it is necessary to estimate the significance of an event by calculating the False Alarm Rate (FAR), as discussed in the next section.

3.7 False Alarm Rate

The False Alarm Rate (FAR) is a pipeline-specific quantity and is a measure of the rate at which noise or other non-astrophysical sources in the detector produce triggers with a combined ranking statistic as large as the one associated to a given trigger. In other words, it quantifies the likelihood that an event with a given SNR is due to random noise fluctuations rather than a real astrophysical signal. The FAR

is measured in Hz and, when associated to an event, it represents the rate at which similar events, arising from random noise fluctuations, would be observed: a higher value of the FAR indicates a larger probability that the event under consideration is a false alarm rather than a genuine astrophysical signal. Due to the unpredictable and non-stationary nature of detector noise, as well as the inability to isolate the detector from the background, the FAR cannot be determined analytically. Therefore, it is necessary to estimate it empirically by making fake coincidences from single-detector triggers, excluding all the triggers that are known to be part of loud coincidences, as those are likely to be produced by real astrophysical events. The FAR computation is based on the assumption of noise from different detector being uncorrelated, and it is done by counting the number of triggers N_i with a CRS exceeding a certain threshold in the data collected during a given range of time T_i, to obtain the trigger rate above threshold $R_i = N_i/T_i$. Then, this value is combined with the probability of a time coincidence with a trigger in a second detector j, given by the product of the time window allowed for the coincidence dt_{ij} and the trigger rate of the second detector R_j. Moreover, to ensure consistency between templates activated in the matched filtering, the algorithm counts the number of pairs of triggers M_{ij} with independent arrival time and consistent templates, which have a CRS_{ij} above threshold, to estimate their probability. This count is obtained by considering all possible combinations of triggers with CRS_{ij} above threshold, taken from the set N_i of triggers from the first detector and the set N_j of triggers from the second detector, so that the associated probability is $M_{ij}(\mathrm{CRS}_{ij})/(N_iN_j)$. Therefore, for double coincidences, the FAR is computed as

$$\mathrm{FAR}_{ij}(\mathrm{CRS}_{ij}) = R_i \cdot dt_{ij} R_j \cdot \frac{M_{ij}(\mathrm{CRS}_{ij})}{N_i N_j} = \frac{M_{ij}(\mathrm{CRS}_{ij}) dt_{ij}}{T_i T_j} \,. \tag{3.21}$$

Triple coincidences are built as pairs of double coincidences sharing the same trigger in one detector (typically Hanford). Therefore, their FAR is derived from the one of double coincidences, avoiding to count twice the triggers in the shared detector. The FAR of a triple is computed as the integral, over all the combinations that pass the CRS cut, of the product of the FARs of the doubles, re-normalised by the time interval T_{ijk} during which the three detectors have contributed to the triggers accumulation, and by the number of triggers in the shared detector as

$$\mathrm{FAR}_{ijk}(\mathrm{CRS}_{ijk}) = \iint FAR_{ij} FAR_{ik} \frac{T_{ijk}}{N_i} dCRS_{ij} dCRS_{ik} \,. \tag{3.22}$$

In practice, due to the computational expense associated with evaluating the FAR, the estimation of the CRS for the background is not performed for every single trigger. Instead, it is calculated periodically at specific time intervals. The computation based on Eq. (3.22) returns a relation between CRS and FAR, depending on the coincidence type and parameter space region, that can be used to associate a FAR to a coincidence starting from its CRS. An example of FAR vs CRS for coincidences is shown in Fig. 3.3. To account for the different ability to capture astrophysical signals of the various coincidence types, a trial factor is applied to the FAR values assigned to the different coincidences. These trial factors $k_{coinc} \leq 1$, are estimated with Monte Carlo studies. On top of the detector combination, an additional $k_{region} = 1/3$ trial factor is applied to account for the parallel searches running on the three regions (BNS, BBH and BHNS). Thus, the MBTA pipeline initially assigns a FAR to events separately for each coincidence type and parameter space region, and then modify it taking into account the appropriate trials factors. Overall, the Inverse False Alarm

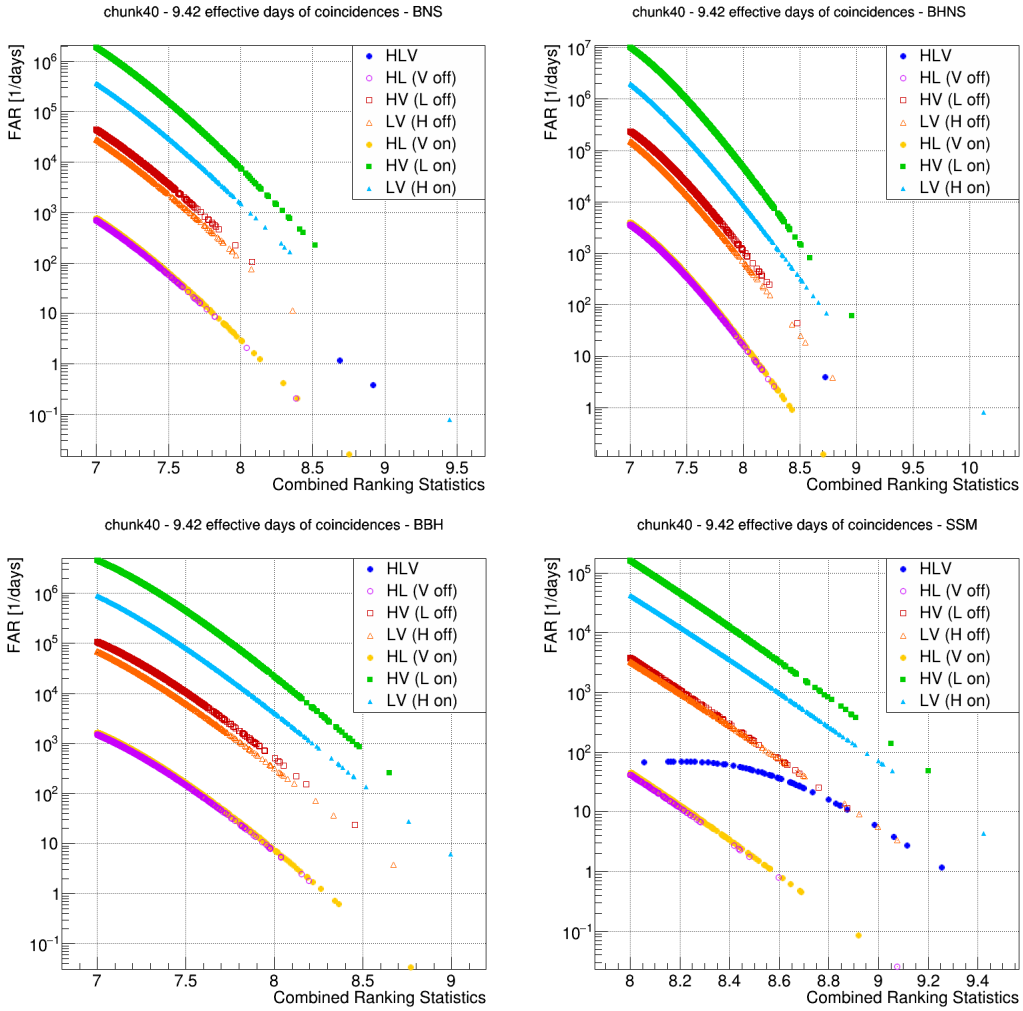

FIGURE 3.3: Distributions of the FAR as function of the CRS for all the coincidences in data between GPS times 1268420276 and 1269561620 displayed for the four types of sources searched for during the third observing run: BNS (top left), BHNS (top right), BBH (bottom left), and SSM (bottom right). Different markers identify different types of coincidences: HL, HV, LV for double coincidences during double detector time, HL-Von, HV-Lon, LV-Hon for double coincidences in triple-detector time and HLV for triple coincidences.

Rate $IFAR = FAR^{-1}$ of a cluster of triggers is computed from the FAR for that particular type of coincidence in that particular region as

$$IFAR = \frac{k_{region} k_{coinc}}{FAR} . \tag{3.23}$$

In case of an event, several templates can be triggered. All templates within a given time window are clustered in one trigger, carrying the parameters of the template returning the highest SNR. As the clustering procedure is applied on coincidences, and not on the single-detector triggers used to build the background model, an additional $k_{cluster}$ trial factor has to be taken into account, so that

$$IFAR = \frac{k_{region} k_{coinc}}{k_{cluster} FAR} . \tag{3.24}$$

This latter trial factor is computed as the inverse over the number of triggers in a cluster.

The FAR calculation is a very delicate step for search pipelines, as it directly affects the significance associated to possible detections. It is important to make sure that the noise model, built in the case of MBTA from all the combinations of the single detector triggers, is well representative of the actual background. In this context, one potential source of bias arises from the selection of a significance threshold to define a trigger. Another factor that can introduce bias are variations in the noise properties and the presence of non-Gaussian features, such as instrumental artefacts or environmental disturbances. If such features are present in the data used for FAR evaluation, but not in the analysed data, or vice versa, the significance of triggers can be over or underestimated. During the O3 offline analysis, the FAR was evaluated over the whole chunk of data. To monitor the time dependence and fluctuations, the same calculation was also performed in periods of 6 hours, as shown in Fig. 3.3. The distributions show how the value of FAR associated to two different CRS thresholds vary over time, where the visible fluctuations are a combination of FAR evolution and statistical effects from the limited samples of single-detector triggers available over 6 hours (depending on the detectors duty cycles). These variations lead to fluctuations in the FAR time evolution during the specific chunk in analysis, as shown in Fig. 3.4 where is displayed the FAR evolution at different time-slices in a sample chunk. Finally, a delicate aspect of the FAR evaluation is that the pipeline can be lead to associate a FAR to a coincidence event observed with a CRS beyond the CRS range covered by all the combinations of the single detector triggers. In this case, MBTA makes the conservative choice of using the lowest FAR evaluated on the whole chunk. Other pipelines in the LVK follow more aggressive procedures, which involve extrapolation to low FAR values. It can thus happen that the FAR associated to very loud events can differ significantly from one pipeline to another. Typically, the FAR association is monitored on data, by means of IFAR cumulative plots. If the FAR determination is healthy, the number of triggers with a given FAR must be well represented by their FAR times the effective observing time.

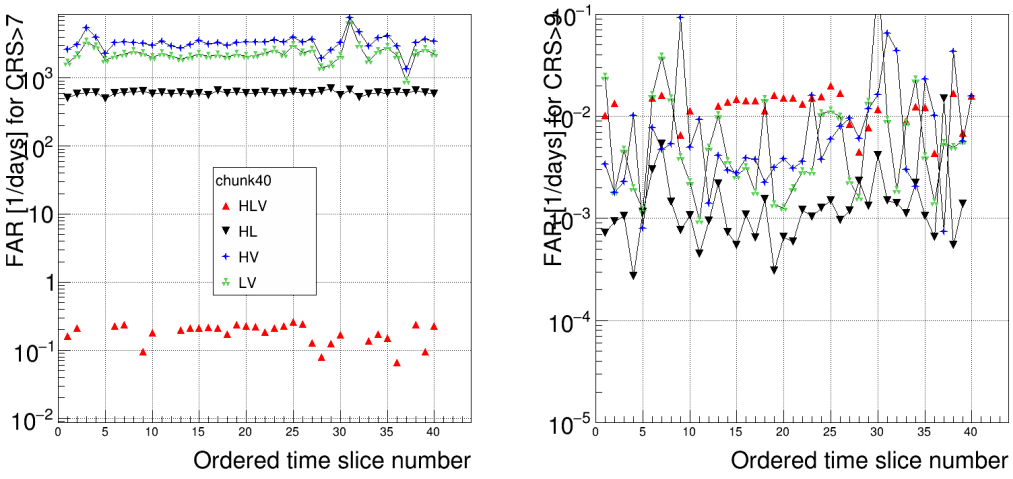

(A) Evolution of the FAR for BNS coincidences for CRS > 7 (left plot) and CRS > 9 (right plot).

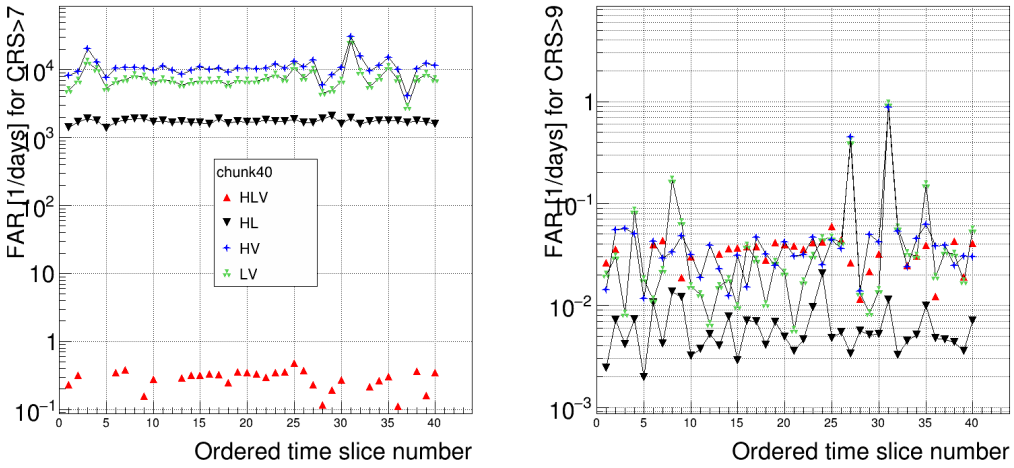

(B) Evolution of the FAR for BBH coincidences for CRS $>$ 7 (left plot) and CRS $>$ 9 (right plot)

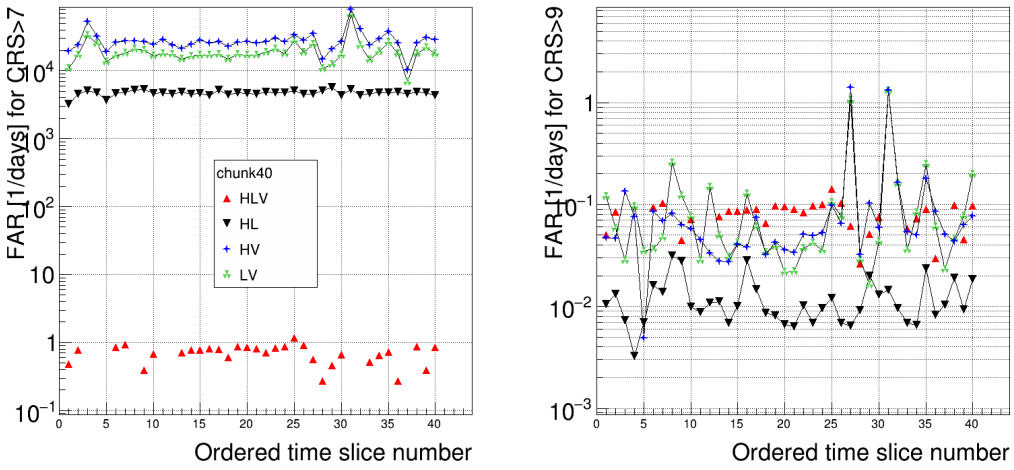

(C) Evolution of the FAR for BHNS coincidences for CRS $>$ 7 (left plot) and CRS $>$ 9 (right plot)

FIGURE 3.4: Time evolution of the FAR in a sample chunk between GPS times 1268420276 and 1269561620 built before clustering and before trial factors, for HLV (red), HL (black), HV (blue) and LV (green) for BNS (top panel), BBH (middle panel) and BHNS (bottom panel) coincidences. Each point corresponds to a subchunk of 50 000 seconds.

3.8 Software Injections

To evaluate the sensitivity of the search pipeline, simulated gravitational waveforms are injected into the data as software injections, and then re-extracted using matched filtering on the streaming time series [11, 12, 127]. Generating a set of injections requires creating simulated signals from a synthetic population of a particular type of source, covering the explored parameter space as shown in Fig. 3.5. The injection set is then analysed to estimate the search sensitivity to the specific source, at a particular significance level, typically expressed in terms of the IFAR. When a signal is observed in the data, the knowledge of the pipeline efficiency allows to constrain rates of sources and their population in the parameter space. If a search does not report any detections, the estimated sensitivity can be used to establish upper limits on the coalescence rate R of the desired source [11, 12, 40, 49, 69, 127]. Suppose a set

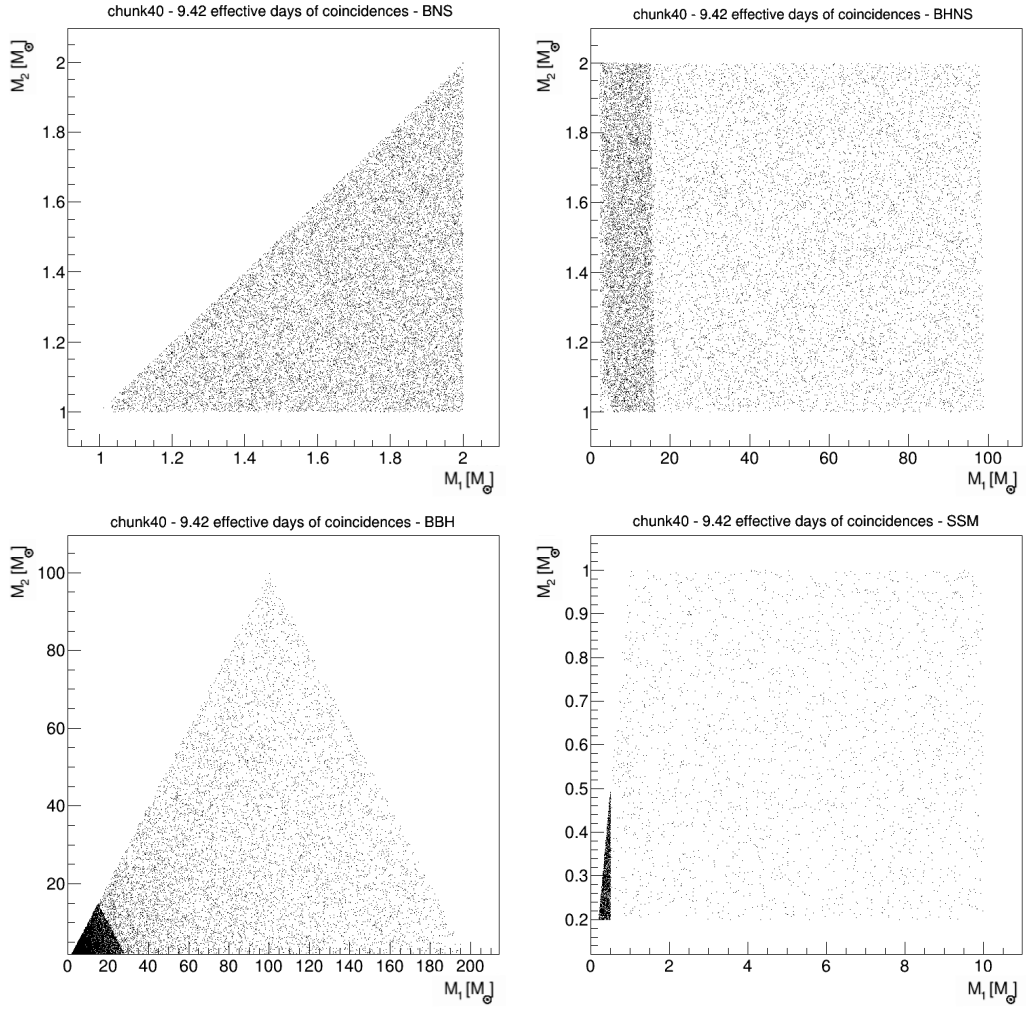

FIGURE 3.5: Distributions of injections in the (m_1, m_2) plane in data between GPS times 1268420276 and 1269561620 displayed for the four types of sources searched for during the third observing run: BNS (top left), BHNS (top right), BBH (bottom left), and SSM (bottom right).

of N_{tot} injections uniformly distributed in a comoving volume V, defined as

$$V = \frac{4}{3}\pi d_c^3 \left(\frac{m_{chirp}}{k}\right)^{15/6} (1+z)^{-1/2} , \tag{3.25}$$

over a duration T_{tot} in the data, where k is a constant equal to $2.8 \cdot (0.25)^{0.6}$. The search averaged spacetime sensitive volume $\langle VT \rangle$ at a given reference IFAR is computed as

$$\langle VT \rangle = \frac{N_{rec}}{N_{tot}} \langle VT_{tot} \rangle , \tag{3.26}$$

where N_{rec} is the number of recovered injections with an IFAR greater than the chosen threshold. The merger rate at a specified confidence level γ can be computed using the loudest event statistic method, as described in [114], as

$$\mathrm{R}_\gamma = \frac{-\ln(1-\gamma)}{\langle VT \rangle} . \tag{3.27}$$

3.9 Probability of Astrophysical Origin

The expectation of the noise in different regions of the parameter space varies, as the same level of noise is not expected across all parameters values. The increasing number of GW detections, and therefore the enhanced understanding of GW source population, has enabled the computation of the probability of candidate events being of astrophysical origin, denoted as p_{astro}. The MBTA pipeline computes p_{astro} by dividing the parameter space into separate bins, and by taking into account $N_{coinc} = 7$ coincidence types (HL, HV, LV, HL-Von, HV-Lon, LV-Hon, HLV) [88]. This segmentation is driven by the presence of distinct types of sources that can be detected in different regions. By dividing the parameter space, it is possible to analyse and track the distributions of foreground sources more effectively. The parameter space is segmented in 45 bins in chirp mass m_{chirp}, and 4 bins in mass ratio $q = m_1/m_2$ (with $m_1 \geq m_2$) for a total of $N_{bins} = 165$ bins in the $m_{chirp} - q$ parameter space, as shown in Fig. 3.6. The motivation behind the fine segmentation in the dimension of the de-

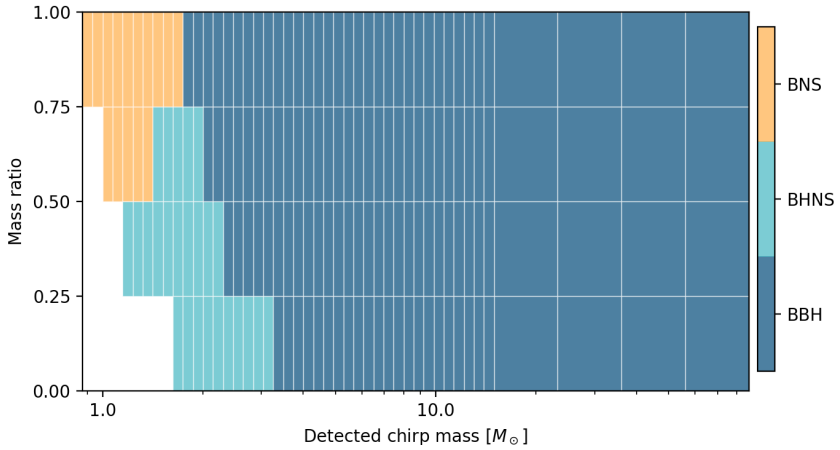

FIGURE 3.6: Segmentation of the $m_{chirp} - q$ parameter space used by MBTA to compute p_{astro}. Each segment is assigned a distinct color, representing one of the three CBC source categories that are associated with that particular bin.

tected m_{chirp} is due to the fact that it is a well-measured parameter in GW signals. In contrast, a coarse division of the parameter space is used for the mass ratio, which is poorly measured. The probability of astrophysical origin is then computed as the sum over the three categories of sources $\alpha \in \{\text{BNS, NSBH, BBH}\}$ of the probability $p_\alpha(x^2)$ for a trigger with combined ranking statistic x (defined in Eq. (3.15)) to belong to a specific source category

$$p_{astro}(x^2) = \sum_\alpha p_\alpha(x^2) \,, \tag{3.28}$$

where

$$p_\alpha(x^2) = \int_0^\infty p(\Lambda_0, \vec{\Lambda_1}|\vec{x^2}) \frac{\Lambda_\alpha f_\alpha(x^2)}{\Lambda_0 b(x^2) + \vec{\Lambda_1} \cdot \vec{f}(x^2)} d\Lambda_0 d\vec{\Lambda_1} \,. \tag{3.29}$$

In Eq. (3.29), $\vec{x^2}$ denotes the list of x^2 values of the N_{trig} triggers with x greater or equal to a certain threshold x_{th}. The term $p(\Lambda_0, \vec{\Lambda_1}|\vec{x^2})$ represents the posterior distribution of counts, which is proportional to the product of the prior distribution $\pi(\Lambda_0, \vec{\Lambda_1})$ on background counts Λ_0 and astrophysical counts $\vec{\Lambda_1} = \{\Lambda_\alpha\}$, and the

likelihood $p(\vec{x^2}|\Lambda_0, \vec{\Lambda_1})$ of the data given the expected astrophysical and background counts

$$p(\Lambda_0, \vec{\Lambda_1}|\vec{x^2}) \propto \pi(\Lambda_0, \vec{\Lambda_1}) p(\vec{x^2}|\Lambda_0, \vec{\Lambda_1}) \,. \tag{3.30}$$

Eq. (3.29) depends on the type of coincidence and on its corresponding bin in the $m_{chirp} - q$ parameter space through the background b and foreground f density distributions. The computation of the background density distribution $b_{i,j}$ is performed for each coincidence type j and each bin i, by analysing months of data collected when at least the Hanford and Livingston detectors are in observing mode, using a process similar to the one used in the FAR computation. On the other hand, the foreground is estimated using the injection sets in Table 3.1, by assuming that the number of sources detected above a SNR threshold is proportional to the detection volume, assumed to be constant over the observing period [88]. This method is well suited for offline analysis, but its computational cost poses challenges for its implementation in low-latency (online) searches. For this reason, a parametrisation of the p_{astro} as function of the combined ranking statistic x is used to fit the data and speed the estimation of p_{astro}

$$p_{astro,i,j}(x^2) = \left[1 + exp\Big(- a_{i,j} \cdot (x^2 - x^2_{50\%,i,j})\Big)\right]^{-1} , \tag{3.31}$$

where $x^2_{50\%,i,j}$ is the combined ranking statistics at $p_{astro,i,j} = 0.5$, and $a_{i,j}$ the slope of the parametrised curve at $x^2_{50\%,i,j}$. In Fig. 3.7 is shown the consistency between the fit of the parametrised p_{astro} and the observed data computed with the full computation. Using a parametrised approach has several advantages: it enables the

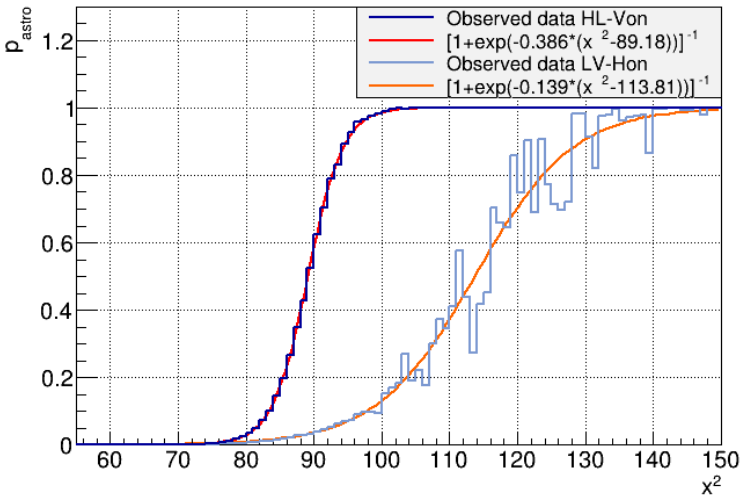

FIGURE 3.7: p_{astro} as function of the squared combined ranking statistics x^2. The dark (light) blue histogram are the observed data for the HL-Von (LV-Hon) coincidences with parameters in $1.15M_\odot \leq m_{chirp} < 1.23M_\odot$ and $0.5 \leq q < 0.75$ ($12.13M_\odot \leq m_{chirp} < 13.0M_\odot$ and $0.0 \leq q < 0.25$), while the red (orange) curves is the fit with parametrisation in Eq. (3.31) [88].

extraction of more precise values for p_{astro} in regions where it exhibits rapid variation with x^2; it allows for extrapolation of the trend of p_{astro} to higher combined ranking statistics that may not be formally computed; and it helps to smooth out statistical fluctuations that may arise in sparsely populated bins. To further prove the robustness of the parametrised approach, it is possible to compare the p_{astro}

values obtained with Eq. (3.31) with those produced by the full computation for the GW candidates reported by MBTA in the first half of the third observing run (O3a) in [59], as shown in Fig. 3.8. The minor observed discrepancies can be attributed to various factors, among which: the goodness of the fit used to estimate the parametrised p_{astro}, the use of the mean value of the posterior distributions of astrophysical counts in the parametrisation, and the interpolation of the p_{astro} values, particularly useful in cases when there are rapid variations in its value as function of x^2. The accuracy of this source classification has been further evaluated by analysing

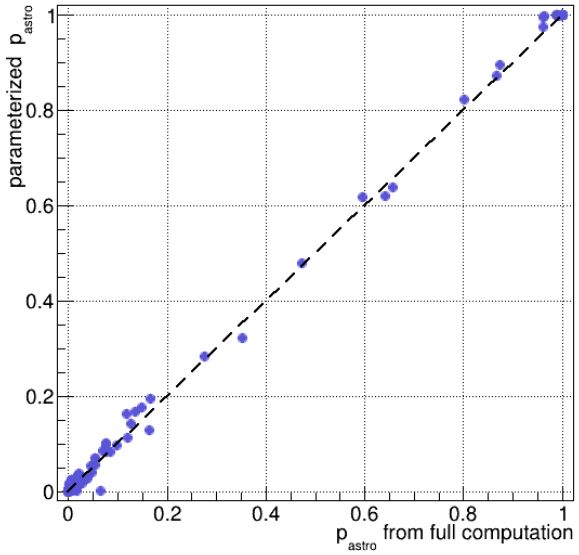

FIGURE 3.8: Comparison between p_{astro} values computed by using the parametrisation and values computed by using the posterior distribution for the O3a MBTA candidate events [88].

a set of injections in O3a data, whose parameters are reported in Table 3.1, and by determining, for each of them, the source class α with the highest p_α. The confusion

Injections parameters					
	Mass distribution	Mass range ($M_\odot$)	Spin range	Spin orientations	Maximum redshift
BBH (inj)	$p(m_1) \propto m_1^{-2.35}$ $p(m_1\|m_2) \propto m_2$	$2.0 < m_1 < 100.0$ $2.0 < m_2 < 100.0$	$\|\chi_{1,2}\| < 0.998$	isotropic	1.9
BBH (pop)	power law + peak [63]	$5.0 < m_1 < 80.0$ $5.0 < m_2 < 80.0$	$\|\chi_{1,2}\| < 0.998$	isotropic	1.9
NSBH	$p(m_1) \propto m_1^{-2.35}$ uniform	$2.5 < m_1 < 60.0$ $1.0 < m_2 < 2.5$	$\|\chi_1\| < 0.998$ $\|\chi_1\| < 0.4$	isotropic	0.25
BNS	uniform	$1.0 < m_1 < 2.5$ $1.0 < m_2 < 2.5$	$\|\chi_{1,2}\| < 0.4$	isotropic	0.15

TABLE 3.1: Parameters distributions used to generate injections of GW signals to define the p_{astro} performances [88].

matrix in Fig. 3.9 shows how the source classification is performing correctly for BNS and BBH sources, while a non-negligible fraction of NSBH injections are classified

either as BNS or BBH. This is due to the degeneracy of the m_{chirp} value, which, although well measured, can still result in misclassification when combined with the poorly measured mass ratio. A careful reader may have noticed that among the CBC

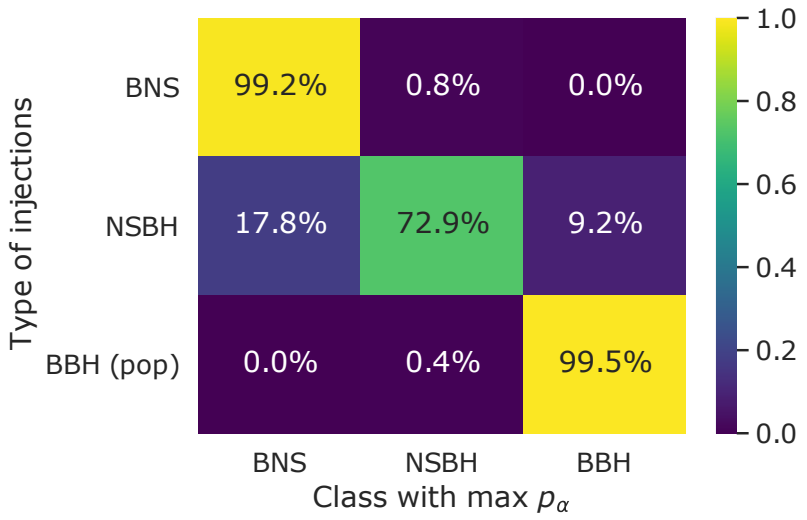

FIGURE 3.9: Confusion matrix of simulated GW signals in O3a data [88]. The colorbar represents the percentage of recovered injections associated to a specific source.

sources taken into account in the computation of p_{astro} there are not SSM sources, as so little is known about their nature and astrophysical population distribution. In GW analysis, the p_{astro} value plays an important role in the interpretation of GW detections as it contributes for a better differentiation between genuine astrophysical events and noise, as well as helping to characterise the sources responsible for generating the detected GW signal, improving the readiness for possible electromagnetic followups. In practice, a p_{astro} threshold of 0.5 was set for the selection of candidate events in the Gravitational Wave Transient Catalog (GWTC) of second half of the third observing run (O3b) [60]. This threshold value is particularly advantageous because it strikes a balance between capturing significant astrophysical events and maintaining a manageable number of candidates.

CHAPTER4

O3 Standard Search

The third observing run (O3) of the LIGO-Virgo Collaboration started on 2019 April 1th 15:00:00 UTC and ended on 2020 March 27th 17:00:00 UTC, resulting in a total of 82 significant CBC detections [58–60] in data collected from three detectors: LIGO Hanford, LIGO Livingston and Virgo. Given the long duration of the run, it was split into two segments: the initial 6 months, known as O3a, and the subsequent 5 months, referred to as O3b. The following chapter focuses on the offline search conducted on O3 data to detect mergers of BBH, BHNS, and BNS systems across the entire sky. The data collected during the run is divided into segments called "chunks," which typically span a duration of approximately 7 days. Each chunk is analysed independently, taking into consideration the varying coincidence times during which multiple detectors are actively acquiring data simultaneously. During O3, a total of 40 chunks were generated from the data, distributed between the first (22 chunks) and second (18 chunks) half of the run. Throughout the standard search of the third observing run, author of this manuscript played an active role in the MBTA team by contributing to the analysis of specific data segments.

4.1 Search Summary

The O3 duty cycles, which refer to the fraction of the total duration of the run in which the instruments were actively observing, were: approximately 74% (246 days) for LIGO Hanford, 76% (254 days) for LIGO Livingston, and 76% (250.8 days) for Virgo. In total, the three-interferometer network was in observing mode for approximately 47% (156.4 days) of the time, while at least two detectors were observing for 83% (275.4 days) of the time, and for 96.7% (319.3 days) of the time at least one interferometer was observing. For comparison, during the second observing run (O2), the duty cycles were approximately 62% for LIGO Hanford and 61% for LIGO Livingston; both detectors were in observing mode for approximately 46.4% of the time, and at least one detector was in observing mode during approximately 75.6% of the time. During the transition from the first to the second half of the third observing run, various upgrades were implemented [58, 60], designed to tackle noise couplings that impact the BNS detection range (see Section 2.1.3), and mitigate light scattering that can degrade data quality, improving detectors resilience against environmental conditions. Overall, these enhancements improved the median BNS inspiral range increasing it from 45 Mpc during O3a to 51 Mpc in O3b for Virgo, from 108 Mpc in O3a to 115 Mpc in O3b LIGO Hanford. However, there was a slight decrease in sensitivity for LIGO Livingston, with the median BNS inspiral range decreasing from 135 Mpc in O3a to 133 Mpc in O3b. Fig. 4.1 shows the evolution of the detector's sensitivity, as quantified by the BNS inspiral range, throughout the

three observing runs. Figure 4.2 shows a comparison of the sensitivities of the de-

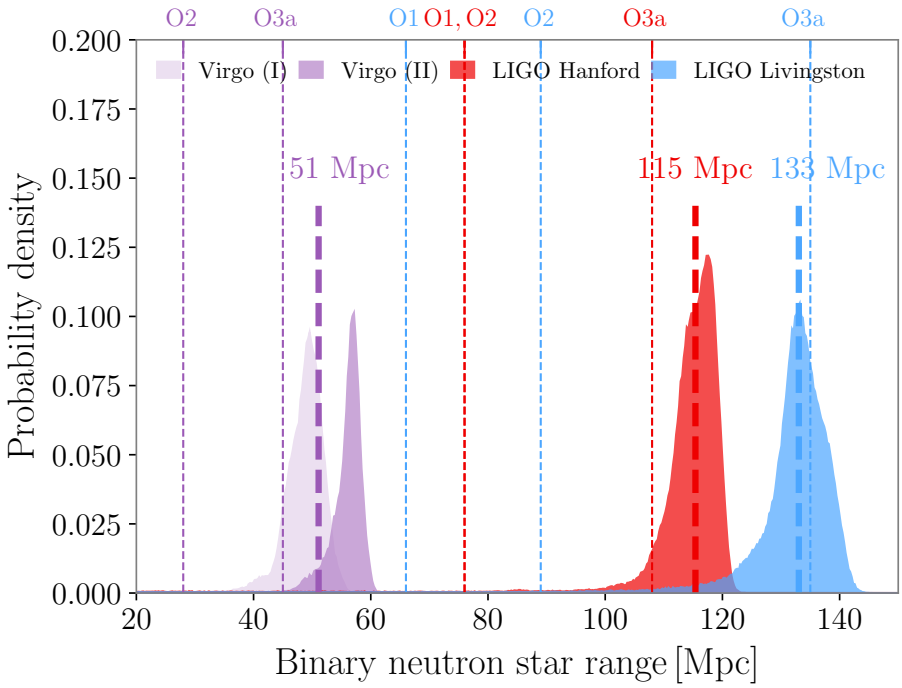

FIGURE 4.1: Distribution of the BNS inspiral ranges and their median values in the second half of the third observing run for LIGO Livingson (blue), LIGO Hanford (red) and Virgo (violet). The data for Virgo is reported for two intervals: before (I) and after (II) 2020 January 28 to highlight the impact of detector upgrades implemented during O3b on the range (for reference appendix B.2 of [60]). For comparison, the BNS inspiral range medians are also shown across the previous runs.

tectors during O3a and O3b, as characterised by the ASD of the strain output. At the end of the run, the coherent WaveBurst (cWB) unmodelled pipeline [244] and three matched-filtering pipelines, namely GstLAL [214, 267, 320], PyCBC [285, 348], and for the first time the MBTA offline search pipeline [10, 75, 76, 96], participated to the archival offline analysis. After discussing the specific features of MBTA incorporated into the template bank, as well as the monitoring and identification of candidate events, the following sections present an overview of the results obtained from the offline analysis performed by all the pipelines [58–60].

4.2 Template Bank

The template bank used by MBTA during O3 to search for BNS, NSBH and BBH signals spans the parameter space reported in Table 4.1. It was created by using the `lalapps_cbc_sbank` [257] aligned-spin bank generator that uses a stochastic algorithm placement, introduced in Section 3.5. The virtual template bank consists of a comprehensive collection of 727 992 templates, and is shown in Fig. 4.3. To ensure that it adequately covers the desired region in parameter space, satisfying the minimum match tolerance of 0.97, the effectiveness of the bank is assessed by computing the effective fitting factor, introduced in Eq. (3.14), for several GW simulated signals drawn within the target parameter space. The choice of waveform used in the matched filtering depends on the binary masses. Specifically, the SpinTaylorT4 [124, 125] waveform model is used when both binary masses are lighter

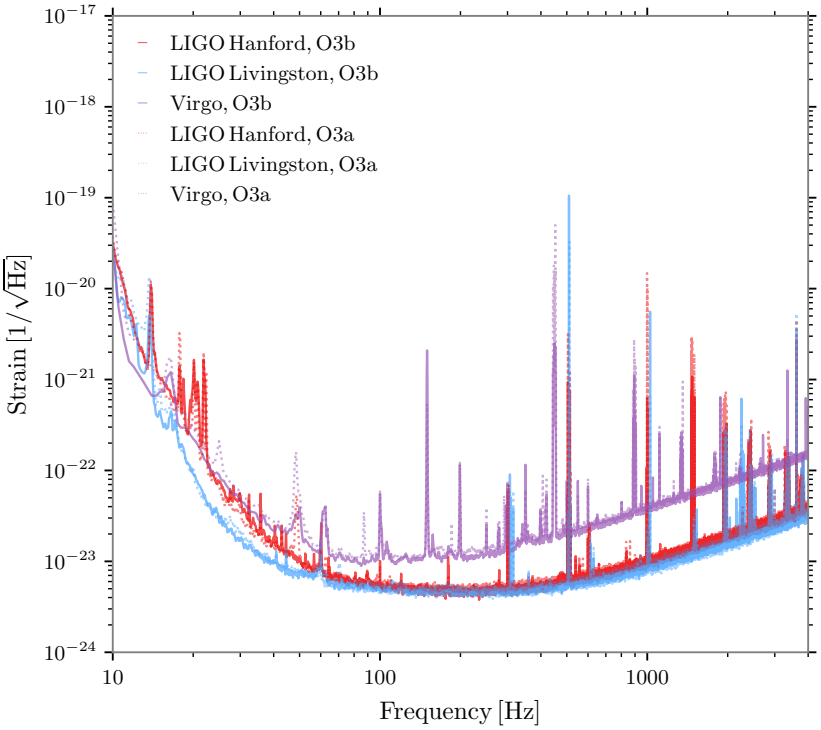

FIGURE 4.2: Amplitude spectral density of the LIGO Livingston (blue), LIGO Hanford (red) and Virgo (violet) interferometers during O3a (dotted lines) and O3b (solid lines).

Templates Bank Parameters			
	BNS	NSBH	BBH
Heaviest mass (m_1) $[M_\odot]$	$[1.0, 2.0]$	$[2.0, 99.0]$	$[2.0, 195.0]$
Lightest mass (m_2) $[M_\odot]$	$[1.0, 2.0]$	$[1.0, 2.0]$	$[2.0, 195.0]$
Total mass $(m_1 + m_2)$ $[M_\odot]$	$[2.0, 4.0]$	$[2.0, 100.0]$	$[4.0, 200.0]$
Mass ratio $(m_1/m_2 \geq 1)$	–	$[1.0, 97.989]$	–
Individual aligned spins $\chi^z_{1,2}$	$[-0.05, 0.05]$ if $m_{1,2} \leq 2.0$ $M_\odot$ $[-0.997, 0.997]$ else		
Minimal match	0.97		
Waveform approximant	TaylorF2	SEOBNRv4_ROM	
Virtual templates low frequency cutoff (f_0) [Hz]	25.0	23.0	
Virtual templates high frequency cutoff (f_{max}) [Hz]	2048.0		
LF and HF bands separation frequency	80.0	85.0	85.0
Total number of virtual templates	27441	524016	176535
Total number of real HF templates	7806	133659	50429
Total number of real LF templates	1901	12200	6206

TABLE 4.1: MBTA O3 template bank parameter space for the standard search.

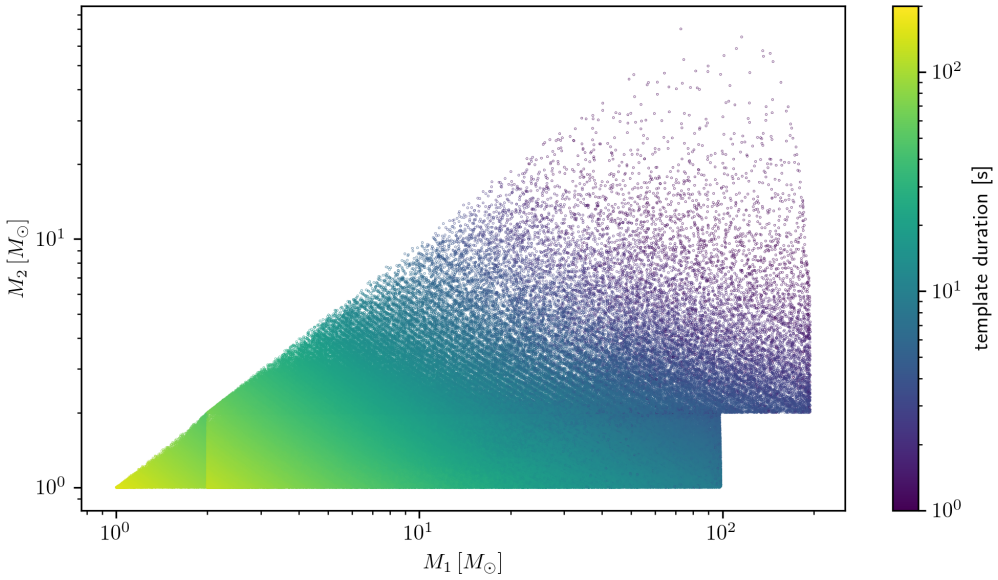

FIGURE 4.3: The O3 template bank used by MBTA in the search for BNS, NSBH and BBH signals. Each dot corresponds to a different template in the bank while the colorbar represents the template duration.

than 2.0 $M_\odot$, while the SEOBNRv4 [116] waveform model is employed if the mass of at least one of the components exceeds 2.0 $M_\odot$. These models are chosen based on their suitability for specific mass regimes in order to accurately describe the GW signals generated by the binary systems under consideration. Specifically, the SpinTaylorT4 model, which is a PN expansion, is suitable for lighter binary masses, as these signals in the detectors are dominated by the inspiral phase. On the other hand, the SEOBNRv4 model is better suited for systems with heavier component masses, as it describes the waveform up to the ring down phase, which becomes relevant as the mass of the system increases and enters the frequency sensitivity range of the detectors.

4.3 Monitoring

The offline MBTA analysis flow follows two steps referred to as the "closed box" and "open box" analyses, which serve as metaphors for the blind analysis technique employed. During the "closed box" phase, the data are analysed with superimposed simulated CBC signals, while the subsequent "open box" phase involves the analysis of "unblinded" data looking for potential GW signals. The primary purpose of this analysis technique is to minimise biases and ensure the validity of the results. The purpose of the closed box analysis is to evaluate the search performance by overlaying simulated signals onto the data and assessing the pipeline sensitivity and efficiency in detecting different types of GW sources (see Section 3.8). The injections sets, whose parameters are listed in Table 4.2, are generated with the `lalapps_inspinj` [257] algorithm separately for BBH, NSBH and BNS signals. Injections are then inserted into the data stream with a time spacing of 12 seconds, and subsequently the matched filtering is performed on this new stream. The pipeline's ability to detect and accurately characterise each type of signal is determined based on the efficiency in recovering injections and on the level of agreement between the recovered parameters and their injected values. An injection may fail to be detected

Injections Campaign Parameters			
	BNS	NSBH	BBH
Heaviest mass (m_1) $[M_\odot]$	$[1.0, 2.0]$	$[2.0, 100.0]$ $[2.0, 99.0]$	$[2.0, 100.0]$ $[2.0, 195.0]$
Lightest mass (m_2) $[M_\odot]$	$[1.0, 2.0]$	$[1.0, 2.0]$	$[2.0, 100.0]$ $[12.0, 195.0]$
Total mass $[M_\odot]$	$[2.0, 4.0]$	$[3.0, 17.0]$ $[17.0, 100.0]$	$[4.0, 30.0]$ $[30.0, 200.0]$
Individual aligned spins $\chi^z_{1,2}$	$[-0.05, 0.05]$	$[-0.05, 0.05]$ for m_2 $[-0.997, 0.997]$ for m_1	$[-0.997, 0.997]$
Distance [Mpc]	$[20.0, 400.0]$	$[70.0, 500.0]$ $[70.0, 1000.0]$	$[150.0, 2000.0]$ $[150.0, 6000.0]$
Waveform approximant	SpinTaylorT4_3.5PN	SEOBNRv4pseudo4PN	

TABLE 4.2: parameter space of the injection campaign performed in O3 data. One set of BNS injections was generated for the analysis, while for BBH and BHNS two sets of injections were produced.

due to several reasons, including: insufficient SNR, if the amplitude of the injected signal is too weak to exceed the detection threshold of the search algorithm, or if the injection falls in a blind spot of the detectors sensitivity, as the detectors may have reduced sensitivity in certain areas of the sky or frequency range; parameters mismatch between injection and search template bank, when the parameters of the injected signal are not covered by the search template bank; noise presence, in which case the injected signal may be hidden by noise even if it matches a search template. The majority of missed injections are characterised by low SNR values, as shown in Fig. 4.4 as a function of the decisive distance, which is defined as the second smallest effective distance, which in turn is the physical distance of the binary when it is seen face-on and located directly above or below the detector [222], and it is computed as a combination of the actual distance of the source d and the geometry of the detection as [158, 260]

$$d_{eff} = \frac{d}{\sqrt{F_+^2 \frac{(1+\cos i)^2}{4} + F_\times^2 \cos^2 i}}, \tag{4.1}$$

where the angle i represents the inclination of the source with respect to the detector. When the binary system is seen face-on $|\cos i| = 1$, the denominator reduces to $F_+^2 + F_\times^2 \leq 1$, so that $d_{eff} \geq d$. If an injection coincides with a glitch present in the background, it can be affected by the gating process and consequently missed. Fig. 4.4 displays scatter plots where the light blue and dark blue dots represent the injections that were successfully detected by the search algorithm. On the other hand, the black circles represent the missed injections, and the red stars indicate the gated ones. These plots clearly show that the gating process tends to have a greater impact on high-SNR BBH injections compared to BNS ones. This is because BBH systems produce short signals, which can resemble loud glitches or noise patterns in the data. As a result, during the gating process, BBH injections may be mistakenly

identified as noise and subsequently removed from further analysis. Missed injections with high SNR values undergo individual follow-up analysis to investigate the reasons behind the failure to detect these signals.

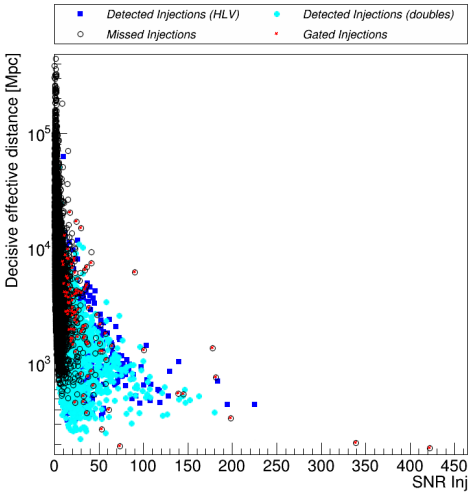

(A) BBH: scatterplot of effective distance as function of injected SNR.

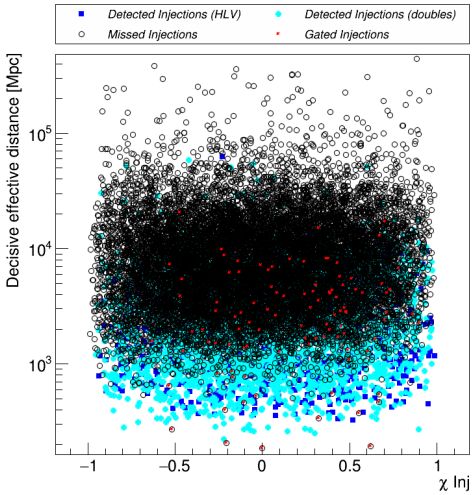

(B) BBH: scatterplot of effective distance as function of effective spin.

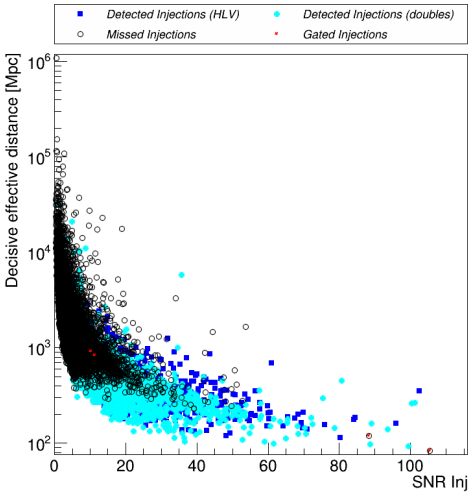

(C) BHNS: scatterplot of effective distance as function of injected SNR.

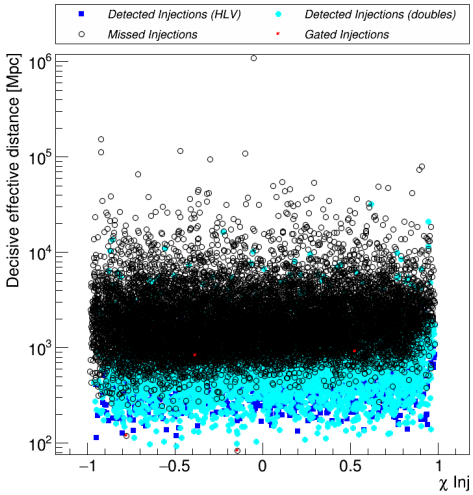

(D) BHNS: scatterplot of effective distance as function of effective spin.

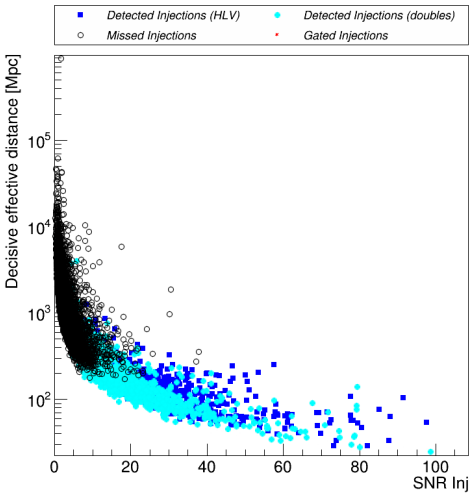

(E) BNS: scatterplot of effective distance as function of injected SNR.

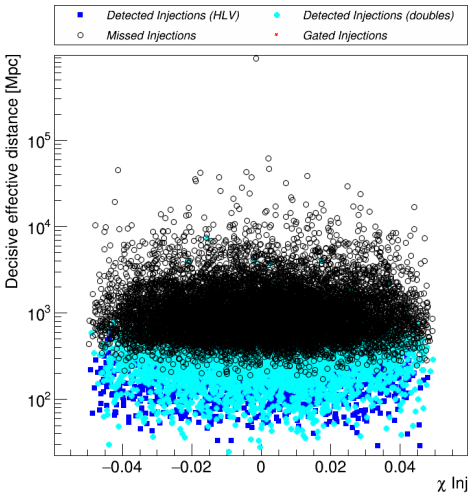

(F) BNS: scatterplot of effective distance as function of effective spin.

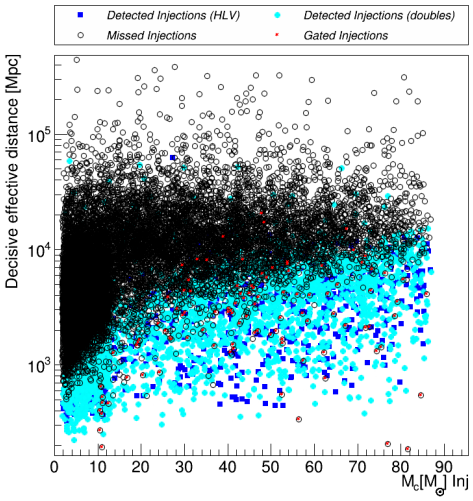

(G) BBH: scatterplot of effective distance as function of injected chirp mass.

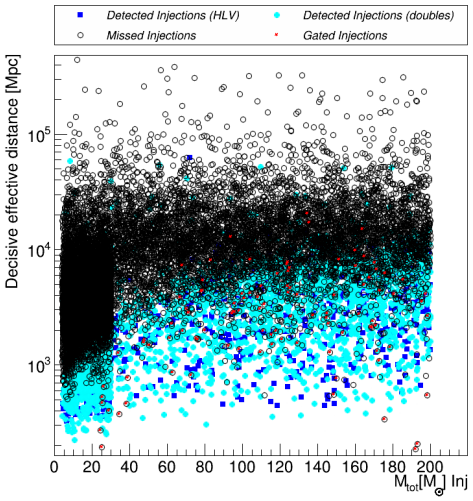

(H) BBH: scatterplot of effective distance as function of injected total mass.

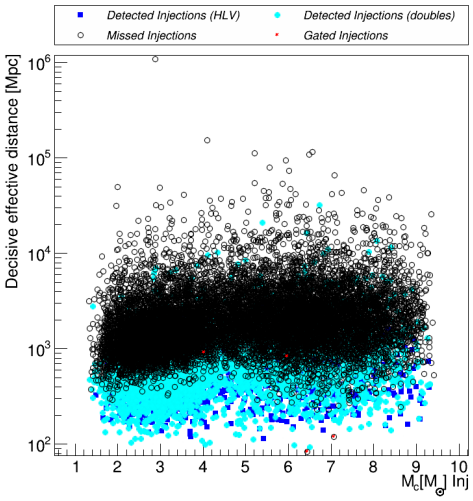

(I) BHNS: scatterplot of effective distance as function of injected chirp mass.

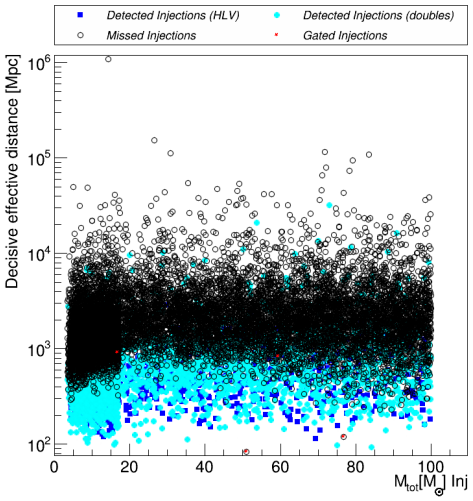

(J) BHNS: scatterplot of effective distance as function of injected total mass.

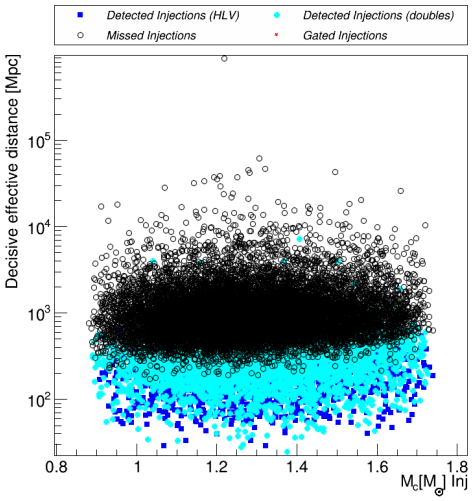

(K) BNS: scatterplot of effective distance as function of injected chirp mass.

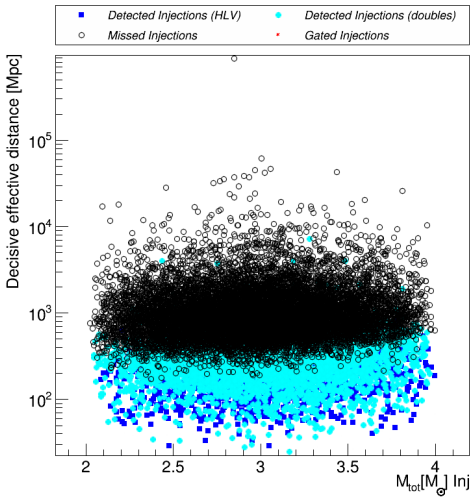

(L) BNS: scatterplot of effective distance as function of injected total mass.

FIGURE 4.4: Found and missed injections in a sample chunk between GPS times 1268420276 and 1269561620 for BBH (top row), BHNS (middle row) and BNS (bottom row) for doubles (light blue) and triples (dark blue) detected injections, considered as such if they have an $SNR \geq 7$. The open dots show missed injections, and the red stars show missed injections that have activated the gating.

This detailed examination aims to identify the specific factors or issues that contributed to the missed detection, allowing for a deeper understanding of the limitations and potential improvements of the analysis pipeline. One of the potential causes for a missed injection that should not be overlooked is the limitation of the template bank used in the analysis, which is specifically designed for aligned spin configurations and has a discrete and limited parameter space. Consequently, this can result in a loss of detection volume, leading to some signals not being captured by the templates and hence remaining undetected. Furthermore, based on the analysis of Fig. 4.4, a clear trend emerges where the likelihood of missed injections increases for more distant sources, as the SNR scales inversely with the distance. However, no distinct trend is observed as function of the effective spin, chirp mass or total mass of the system. The quality of the recovered parameters is assessed by comparing them with the injected values. The chirp mass of the binary systems is the parameter that can be most accurately constrained in the analysis, as shown in Fig. 4.5 for BNS, BBH and BHNS injections, due to the fact that it is well encoded in the frequency evolution of the binary [34] through the following equation

$$m_{chirp} = \frac{(m_1 m_2)^{3/5}}{(m_1 + m_2)^{1/5}} = \frac{c^3}{G}\left[\frac{5}{96}\pi^{-8/3} f^{-11/3}\dot{f}\right]^{3/5}, \tag{4.2}$$

where m_1 and m_2 are the masses of the components of the binary system, while f and $\dot{f}$ are the observed frequency and its time derivative.

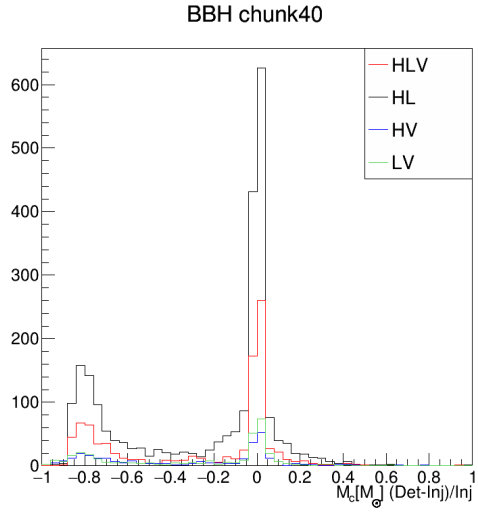

(A) Recovery accuracy of chirp mass for BBH injections.

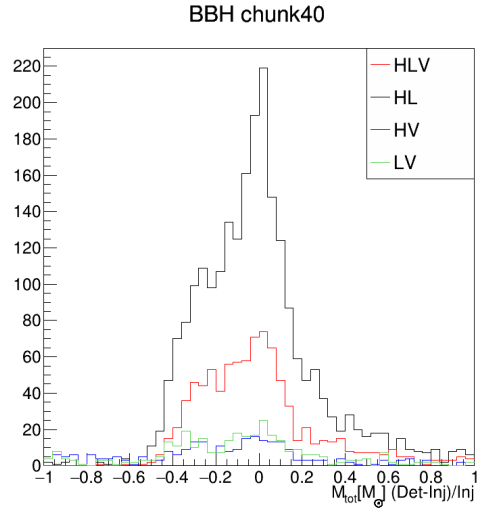

(B) Recovery accuracy of total mass for BBH injections.

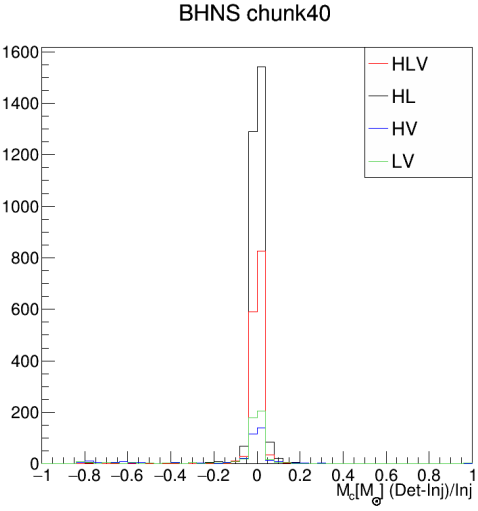

(C) Recovery accuracy of chirp mass for BHNS injections.

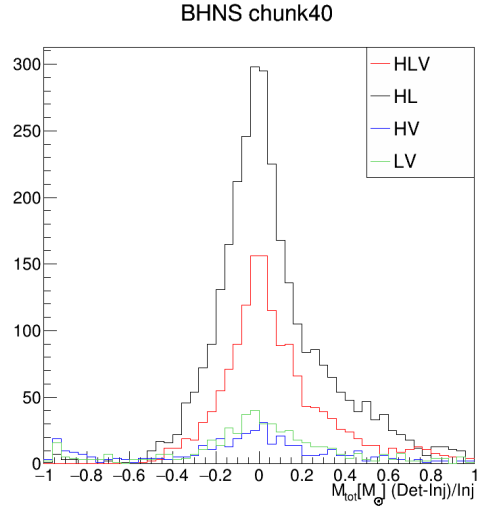

(D) Recovery accuracy of total mass for BHNS injections.

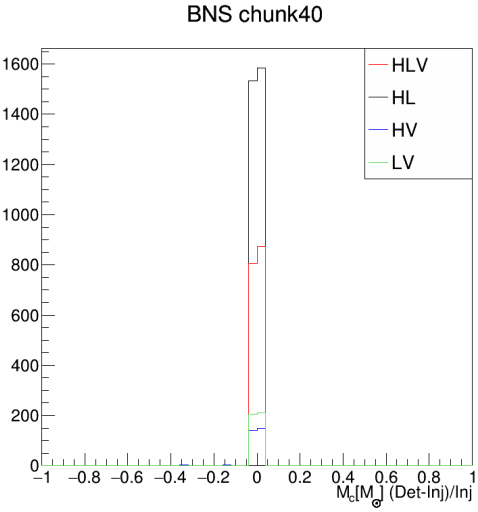

(E) Recovery accuracy of chirp mass for BNS injections.

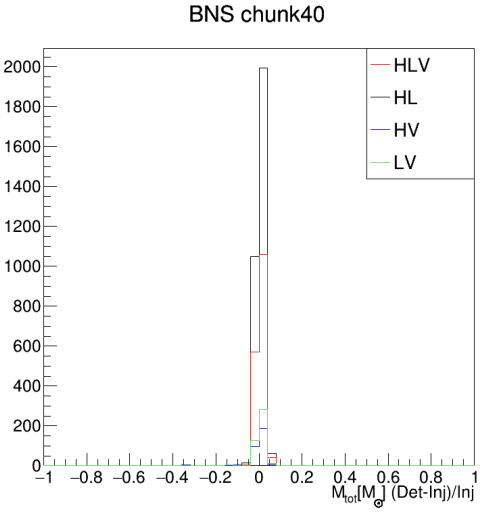

(F) Recovery accuracy of total mass for BNS injections.

FIGURE 4.5: Recovery accuracy of chirp mass for HLV (red), HL (black), HV (blue) and LV (green) for BBH (top plots), BHNS (middle plots) and BNS (bottom plots) coincidences in a sample chunk between GPS times 1268420276 and 1269561620 plotted as relative difference of chirp mass (total mass) as function of the injected chirp mass (total mass).

The histograms in Fig. 4.5 show that for both high-mass signals and low-mass signals the parameter that exhibits the most precise measurement is the chirp mass. The variations in the pipeline's ability to accurately recover the correct mass for BBH, BHNS and BNS systems can be attributed, in part, to the distinct densities of template placement in the template bank (see Fig. 4.3). The template bank contains a greater number of templates at lower masses, enabling a wider selection of templates that closely match the data. Conversely, at higher masses, the availability of templates is comparatively lower. This disparity in template density can contribute to the differences observed in the pipeline performance in recovering the chirp mass and total mass values across different types of binary systems. However, it is important to emphasise that the primary focus of the detection pipelines is to identify the presence of the signals rather than precisely estimating their parameters, which is a step performed at a later stage. The injections campaign provides valuable insights regarding the detection efficiency of the search pipeline, as demonstrated in Fig. 4.6a with respect to the decisive distance, and in Fig. 4.6b with respect to the injected chirp mass of the simulated BNS signals, while in Fig. 4.7 and Fig. 4.8 the same plots are shown for BBH and BHNS signals respectively. These figures reveal an anticipated trend, wherein the pipeline exhibits a higher efficiency in detecting signals that are closer or that are emitted by massive sources, as these tend to produce higher SNR values. As a consequence, there is an increased probability of these signals being detected as triple coincidences. The second most probable type of detections consists of HL coincidences, primarily attributed to the higher sensitivity of the LIGO detectors and their relative proximity which implies comparable sensitivities across the same regions of the sky. When looking at differential efficiencies, it is important to take into account the relative population of injections (shown in the insets of the plots) in the same variable, in order to estimate the total efficiency. Moreover, when presenting the results in various bins, interpreting the values can be challenging as they are integrated over additional variables that are not explicitly displayed.

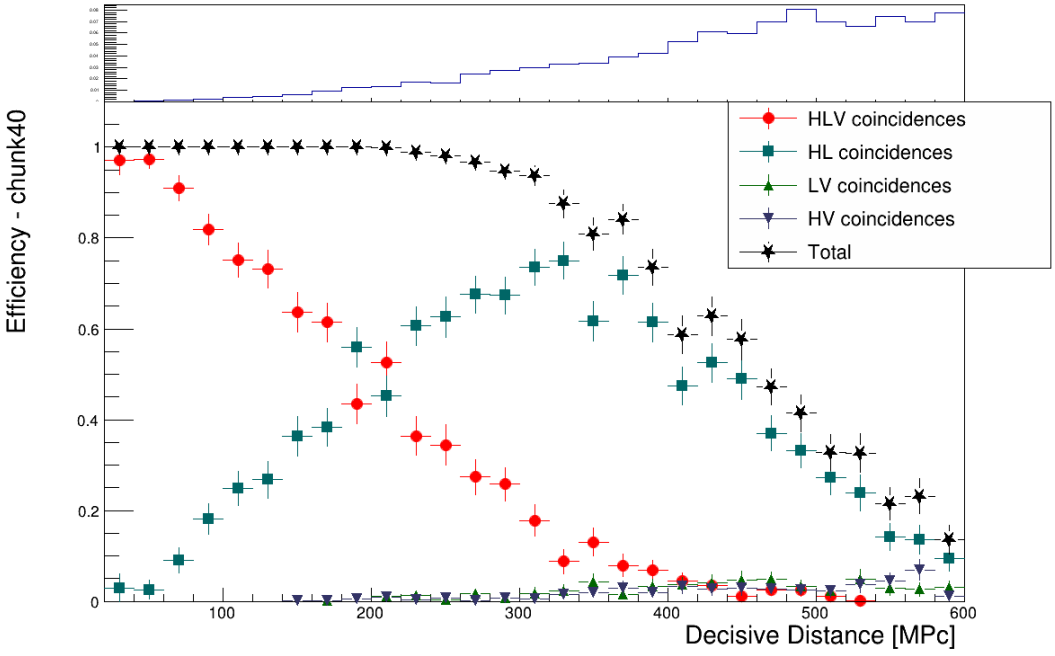

(A) Efficiency of detection as function of the decisive distance for BNS injections.

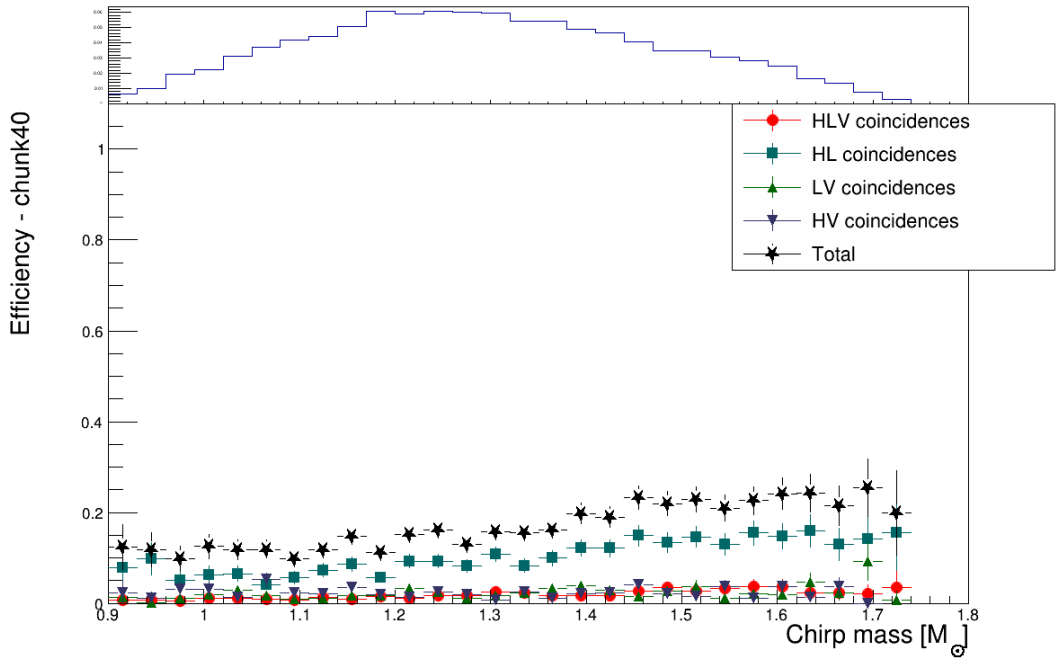

(B) Efficiency of detection as function of the chirp mass for BNS injections.

FIGURE 4.6: Efficiency of detection for BNS injections in a sample chunk between GPS times 1268420276 and 1269561620 for HLV (red circles), HL (dark green squares), HV (blue reversed triangles) and LV (light green triangles) for BNS coincidences. In this plot the 4 categories of coincidences are mutually exclusive, so that the efficiencies can be summed over, resulting in the total efficiency (black stars). The insets above the plots display the distribution of injections.

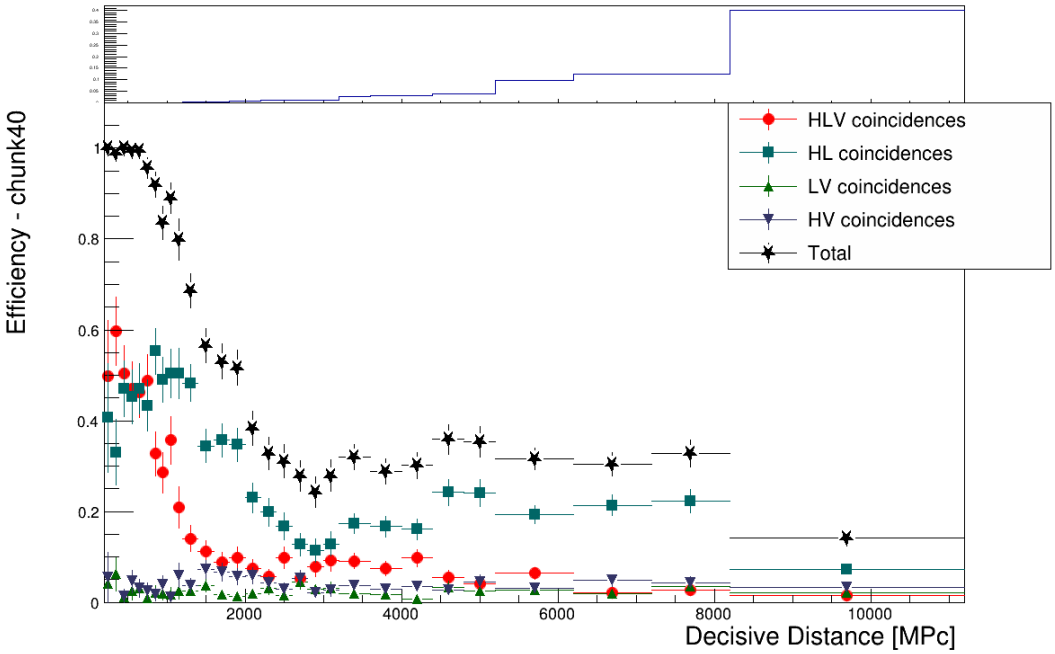

(A) Efficiency of detection as function of the decisive distance for BBH injections.

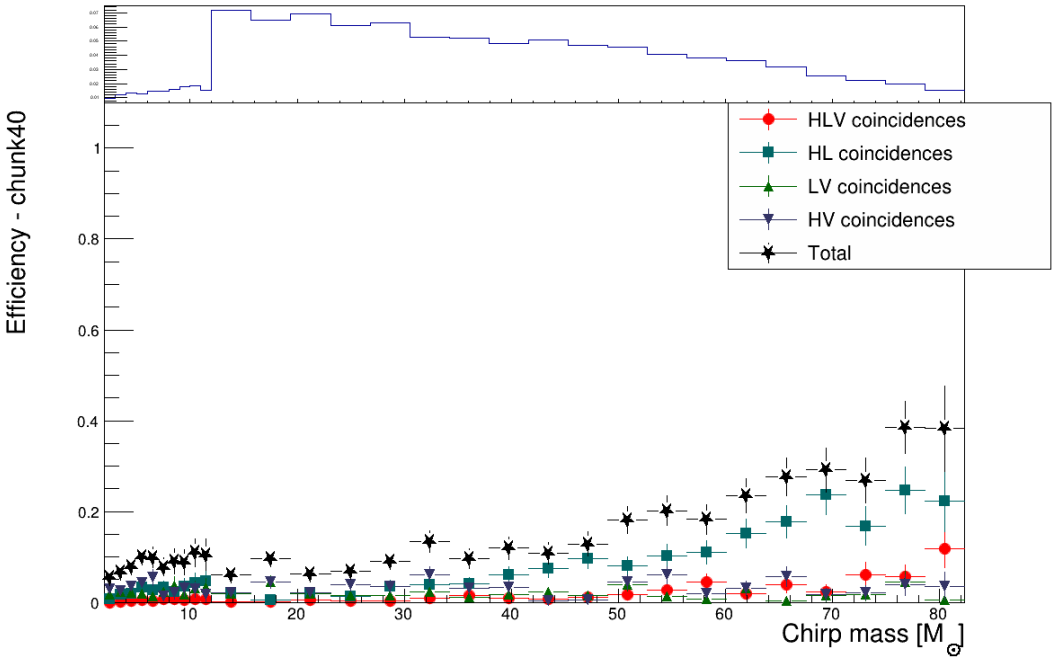

(B) Efficiency of detection as function of the chirp mass for BBH injections.

FIGURE 4.7: Efficiency of detection for BBH injections in a sample chunk between GPS times 1268420276 and 1269561620 for HLV (red circles), HL (dark green squares), HV (blue reversed triangles) and LV (light green triangles) for BBH coincidences. In this plot the 4 categories of coincidences are mutually exclusive, so that the efficiencies can be summed over, resulting in the total efficiency (black stars). The insets above the plots display the distribution of injections.

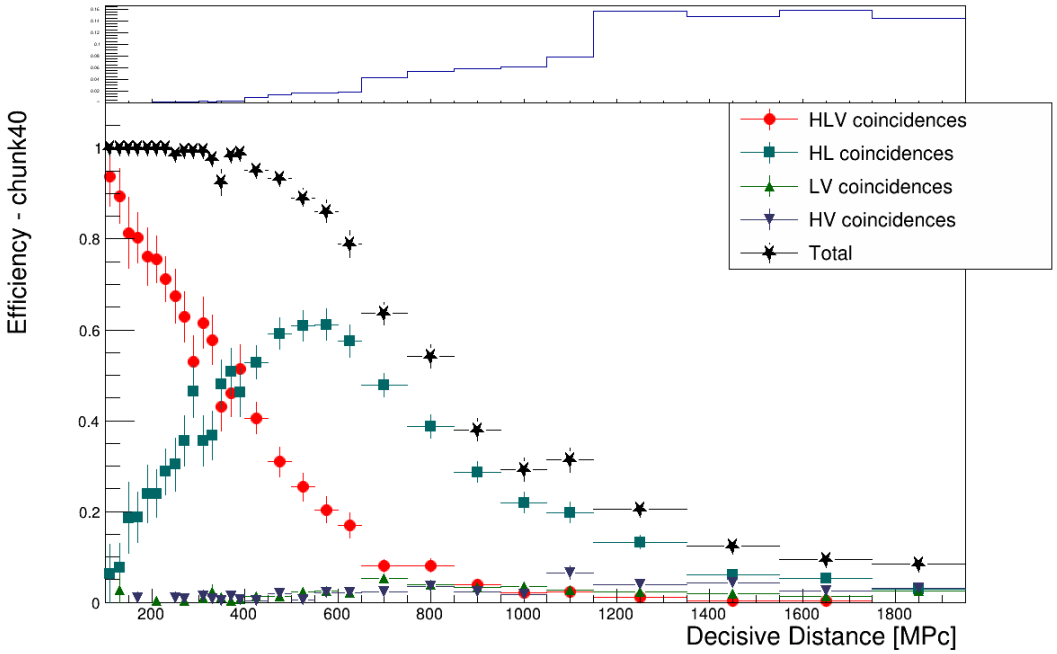

(A) Efficiency of detection as function of the decisive distance for BHNS injections.

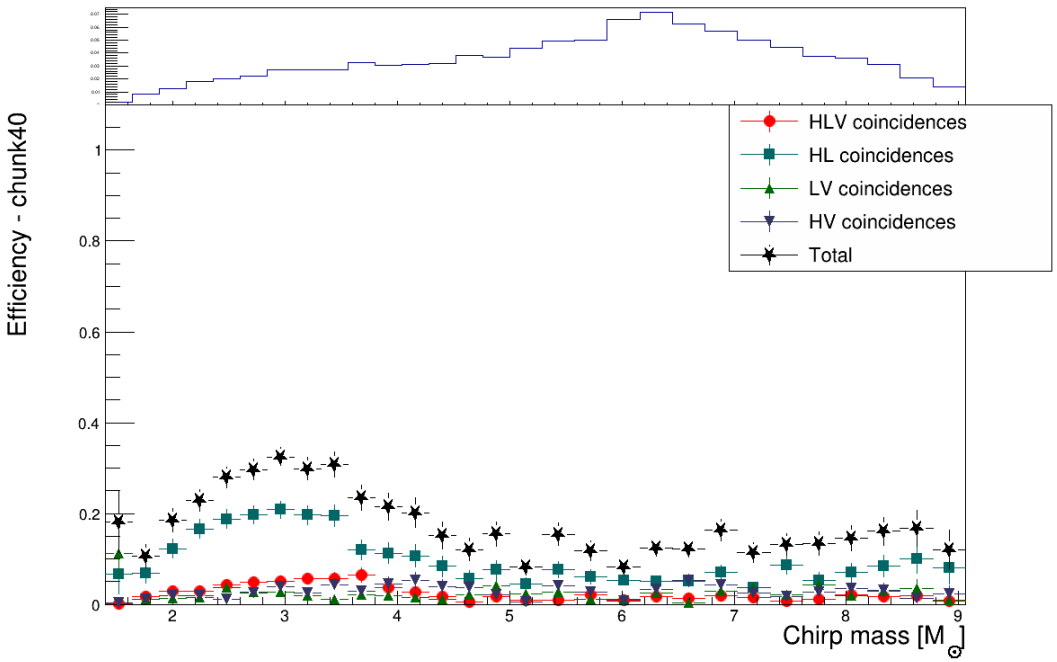

(B) Efficiency of detection as function of the chirp mass for BHNS injections.

FIGURE 4.8: Efficiency of detection for BHNS injections in a sample chunk between GPS times 1268420276 and 1269561620 for HLV (red circles), HL (dark green squares), HV (blue reversed triangles) and LV (light green triangles) for BHNS coincidences. In this plot the 4 categories of coincidences are mutually exclusive, so that the efficiencies can be summed over, resulting in the total efficiency (black stars). The insets above the plots display the distribution of injections.

In the closed box analysis, an additional figure of merit is the behaviour of the FAR in relation to the CRS, which is computed using the single detector triggers for each type of source, as shown in Fig. 4.9 for single triggers with $SNR > 8$. In practice, whenever the ranking statistic (defined in Eq. (3.18)) exceeds the threshold of 5 in a given detector, the pipeline generates a single-detector trigger corresponding to that specific detector. From these plots it is possible to identify periods of noise, corresponding to clusters of triggers, and potential real GW events, for which the re-weighted SNR closely aligns with the actual recovered SNR.

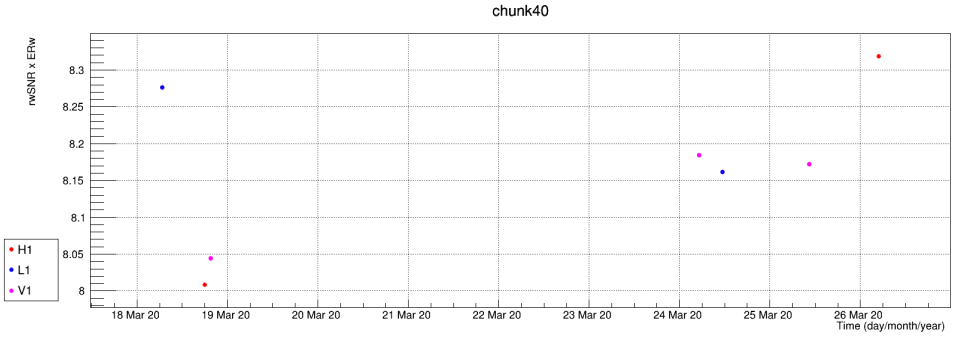

(A) Single detector BNS events.

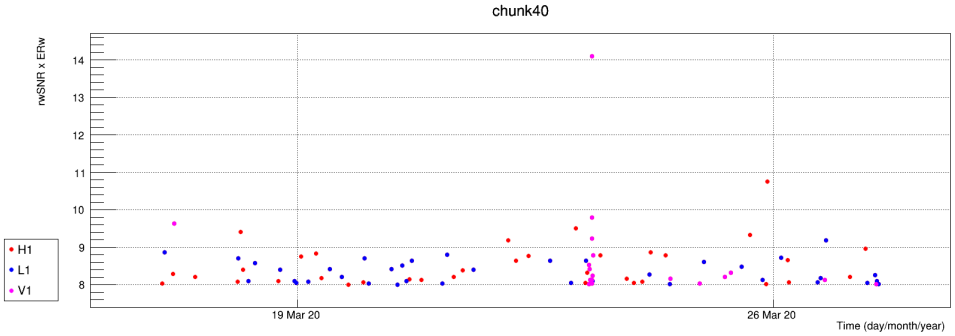

(B) Single detector BHNS events.

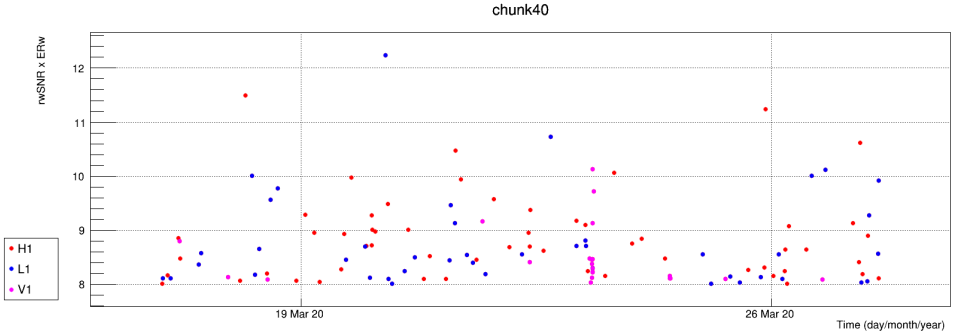

(C) Single detector BBH events.

FIGURE 4.9: Time distribution of single detector events in a sample chunk between GPS times 1268420276 and 1269561620 for the LIGO Hanford (red), LIGO Livingston (blue) and Virgo (violet) detectors for BNS (top panel), BHNS (middle panel) and BBH (bottom panel) coincidences. Clusters of triggers, resulting from noise in the detector, are visible in the Virgo detector for BBH and BHNS coincidences.

In Fig. 4.10 is shown the FAR trend in relation to the CRS for BNS, BBH and BHNS coincident triggers.

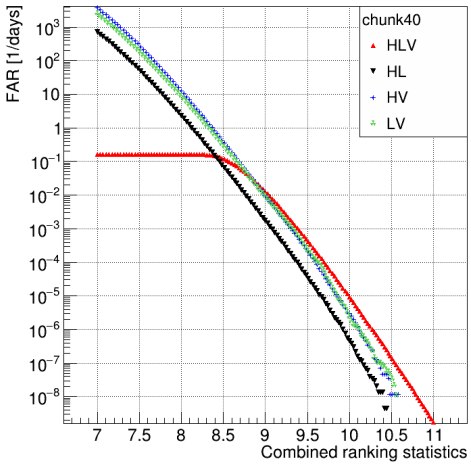

(A) FAR trend as function of the CRS for BNS injections.

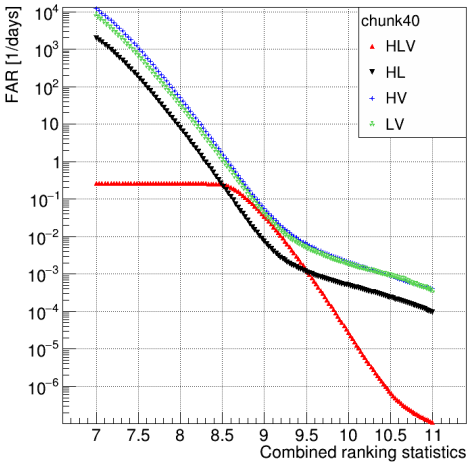

(B) FAR trend as function of the CRS for BBH injections.

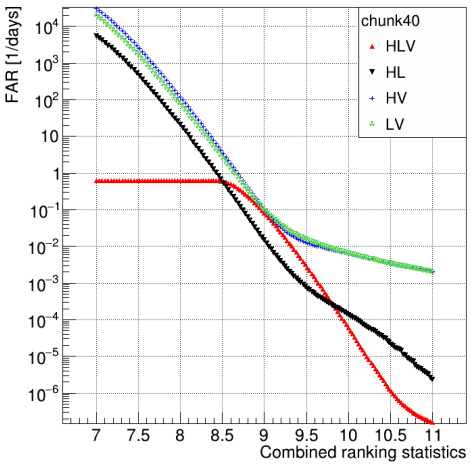

(C) FAR trend as function of the CRS for BHNS injections.

FIGURE 4.10: FAR trend as function of the CRS for BNS (top plots), BBH (bottom left plot) and BHNS (bottom right plot) in a sample chunk between GPS times 1268420276 and 1269561620 for HLV (red), HL (black), HV (blue) and LV (green) coincidences. In these plots the points are not mutually exclusive, which means that an HLV coincidence is seen also as double coincidence in HL, HV and LV.

The different patterns observed at high raking statistic in the FAR trends for the BBH, BHNS, and BNS regions are attributed to the presence of noise in the detectors during the specific showed chunk. The reason behind the more pronounced impact of noise on BBH and BHNS signals can be justified by the fact that during noisy periods more triggers of these types are generated, as displayed in Fig. 4.9 for the different types of sources. In accordance with the FAR distributions as a function of the CRS, the coincidences involving BNS do not exhibit prominent clusters of triggers. However, for BBH and BHNS coincidences, clusters of triggers are evident. This reinforces the notion that BBH and BHNS templates are more prone to be activated by noise, and that the presence of noise impacts the FAR distributions. On the

other hand, the greater impact of noise on double coincidences compared to triple coincidences can be explained by the higher probability of the former occurring relative to the latter. The observed plateau in the HLV coincidences at low ranking statistic values is an artefact related to the fact that no single triggers are recorded with an $SNR < 5$, hence the minimal combined SNR for a triple coincidence is about $\sqrt{3 \cdot 25} \approx 8.6$.

4.4 Candidate Events

Once the closed box results have been carefully analysed, the following step is to "open the box" and compare the foreground data to the background data. This comparison allows to evaluate the significance of each candidate event and determine if they are consistent with expected astrophysical GW signals or if they are due to instrumental or environmental noise. The threshold to define a candidate is arbitrary; in the first analysis of O3a [58], a trigger is considered as a candidate GW event if its FAR value is below the threshold of 2.0 yr^{-1}, while in the second analysis of O3a [59] and in O3b [60], the threshold used to identify candidate events is set to be $p_{astro} > 0.5$. Among the events that meet the selection criterion, some of them may have already been detected by the low latency analysis, while others may not have been detected, resulting in new GW discoveries. Fig. 4.11 displays the cumulative plot of number of events with IFAR exceeding a certain threshold as function of the threshold values in a sample chunk. The black curve represents the expected distribution of the background, and the red dots corresponds to the observed events. The grey bands show the Poissonian errors corresponding to the 1σ (dark grey), 2σ (grey), and 3σ (light grey) confidence intervals. These intervals indicate the uncertainty around the expected distribution, with confidence levels of 68%, 95%, and 99.7% respectively. Notably, the uncertainty is larger for events with low FAR. This is because the Poissonian error scales as $1/\sqrt{N}$, where N is the number of expected events, and since we anticipate a lower number of events at low FAR, the resulting associated error is larger. As of O3, the analyses for BBH, NSBH and BNS were implemented as separate searches with distinct template banks. In cases where multiple searches identify the same event in the data but attribute it to different sources, the plots only display the event with the lowest FAR. Furthermore, when calculating the cumulative IFAR, the assumption is made that the searches for BBH, BHNS, and BNS systems are completely uncorrelated, so that each event is counted as $1/3$ in the cumulative IFAR distribution. IFAR cumulative distributions are produced for each chunk of data, and the presence of significant candidate events is easily distinguishable as they stem out of the background distribution. However, within the example time segment displayed in Fig. 4.11, no candidates are detected by the MBTA pipeline, despite a public alert being issued within the same data period, identified as a BBH merger. Although the MBTA pipeline did identify the event also in the offline analysis, its FAR was 12.0 yr^{-1}, falling above the threshold of 2.0 yr^{-1}. Fig. 4.13a provides a clear example of the detection of a candidate event, specifically GW190503 [59], previously identified in the low-latency search and subsequently by the offline search, which was labeled as BBH event, detected by MBTA as triple coincidence in HLV with a network SNR $= 12.8$, FAR $= 0.013$ yr^{-1}, and $p_{astro} = 1.0$, shown in Fig. 4.12. On the other hand, Fig. 4.13b shows an even more effective example where the MBTA pipeline successfully identifies 5 HL coincidences, classified as BBH events: GW190519, GW190521A, GW190521B, GW190512 and GW190517.

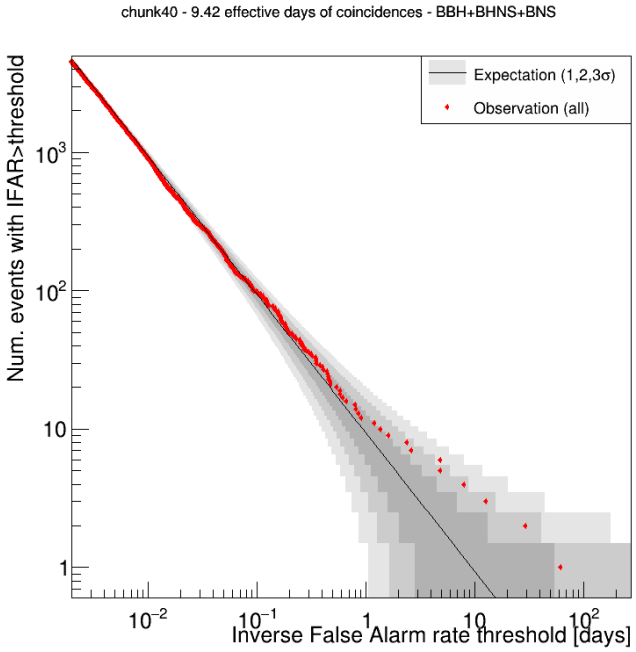

FIGURE 4.11: Cumulative IFAR distribution for doubles and triples BBH, BHNS and BNS coincidences in a sample chunk between GPS times 1268420276 and 1269561620. The black curve represents the expectation from the background, while the grey regions are the Poissonian errors corresponding to the 1σ (dark grey), 2σ (grey), and 3σ (light grey) confidence intervals. Each red dot corresponds to an observation.

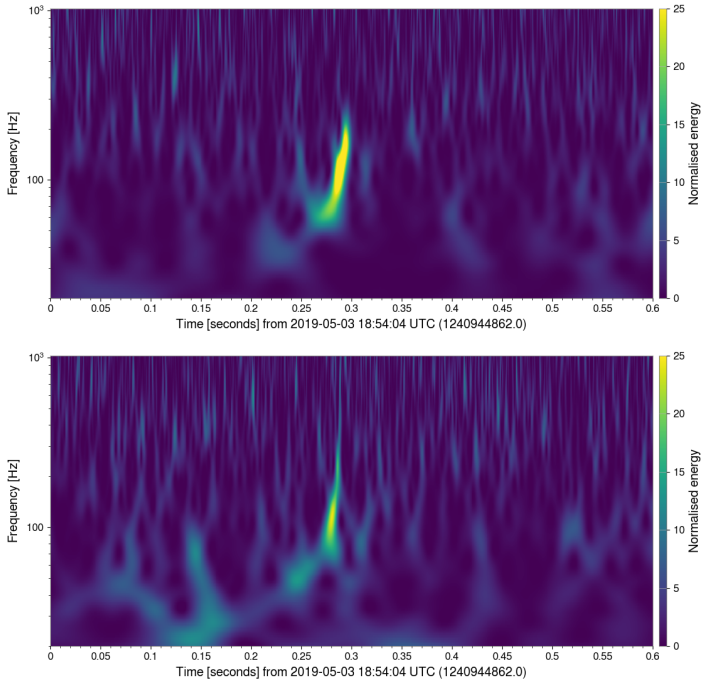

FIGURE 4.12: Time frequency representation of GW190503 observed by the LIGO Hanford (top) and LIGO Livingston (bottom) detectors. The Virgo scan is omitted as the signal is not visible. Each detector's data are whitened by their respective noise amplitude spectral density and a Q-transform is calculated. The colorbar displays the normalised energy reported by the Q-transform at each frequency.

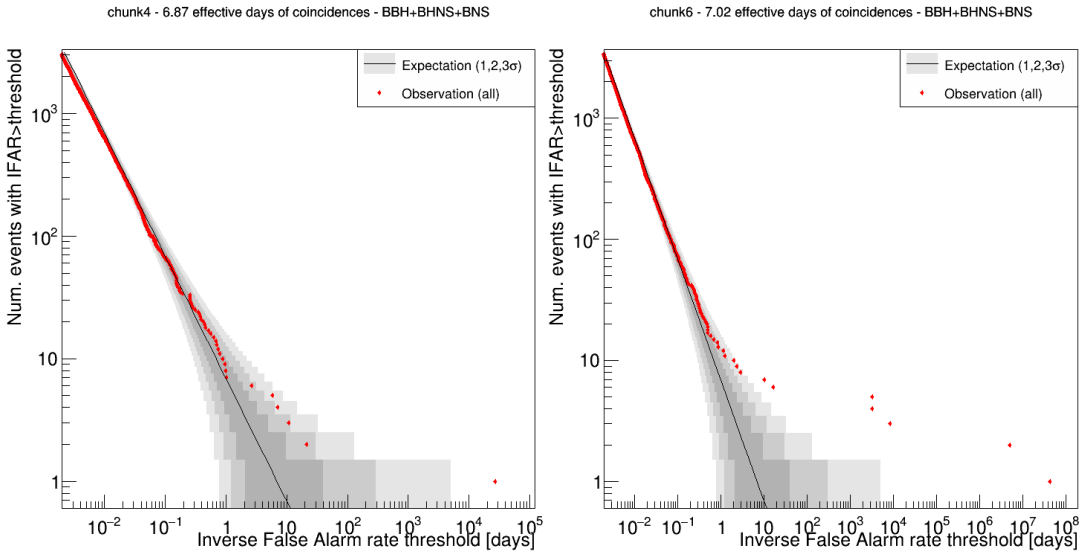

(A) Chunk between GPS times 1240333912 and 1241011124

(B) Chunk between GPS times 1241725020 and 1242485124

FIGURE 4.13: Cumulative IFAR distribution for doubles and triples BBH, BHNS and BNS coincidences in two sample chunks during O3a. The black curve represents the expectation from the background, while the grey regions are the Poissonian errors corresponding to the 1σ (dark grey), 2σ (grey), and 3σ (light grey) confidence intervals. Each red dot corresponds to an observation.

In this same chunk, MBTA did not detect the GW190514 event, despite it being identified by PyCBC [285, 348] and GstLAL [214, 267, 320] as an HL coincidence. Further investigation revealed that this missed detection was caused by noise in the LIGO Livingston detector, which led to an increased rate of triggers that down-weighted the SNR of the event, rendering it undetectable by MBTA. It is important to acknowledge that sometimes different pipelines have the capability to detect different events, with some overlapping detections. This difference arises due to variations in the implementation of the analysis performed by each pipeline, ranging from the template banks employed in the search to the estimation of the background distributions and the assessment of the probability of an event of being of astrophysical origin. Hence, this highlights the importance to employ multiple pipelines in order to cross-check, validate and corroborate findings.

4.5 Search Results

In the low-latency search, GW candidates are identified based on triggers that exceed an SNR threshold of 4 in at least one detector and a FAR threshold of 1.2 yr^{-1}, while in the offline re-analysis the FAR threshold is typically relaxed at 2.0 yr^{-1}. Out of the 27 candidates initially identified in the low-latency search during O3a in at least one of the pipelines, 11 were subsequently retracted as they were deemed not significant in the offline analysis. Additionally, the offline analysis identified 12 new candidates in the first round of analysis [58] by applying a FAR threshold of 2.0 yr^{-1}, followed by the discovery of 8 more BBH candidates in the second re-analysis [59], where the FAR threshold was replaced by a p_{astro} threshold of 0.5. This outcome is anticipated because the detection rate of BBH events is typically higher compared to BNS or NSBH events. Consequently, at a fixed FAR threshold, the p_{astro}

value for BBH events generally surpasses that of BNS or NSBH events. As a result, when switching from a FAR threshold to a p_{astro} threshold to discriminate candidates, it is expected to include more BBH events while potentially excluding some low-mass events. During O3b [60], a total of 39 candidates were initially reported in the low-latency analysis from all the pipelines combined. However, upon further investigation, 16 of these candidates were subsequently retracted as likely due to detector noise and found with a $p_{astro} < 0.5$ in the offline search, and 5 candidates were classified as marginal events, indicating that these events met either the FAR threshold or the p_{astro} threshold but not both of them. The offline analysis, on the other hand, identified 17 additional events with a $p_{astro} \geq 0.5$. Specifically, in the low-latency analysis of O3a data, the MBTA pipeline detected 33 GW events, 10 of which subsequently retracted, while in the offline analysis with a threshold of $p_{astro} > 0.5$, it identified 29 GW events. In the O3b data, MBTA detected 22 events in low latency, 8 of which retracted, and 20 events in the offline analysis, with a threshold of $p_{astro} > 0.5$. Therefore, 44 new GW events were recorded during O3a, among which 41 BBHs, 1 BNS and 2 signals compatible with BHNS signals. During O3b, 35 new GW signals were identified, of which 31 BBHs, and 4 signals compatible with BHNS binary systems, for a total of 79 confirmed new GW detections during the whole O3, and 90 globally GWs detected events between O1, O2 [31] and O3 [58–60]. Through the analysis of frequency and amplitude evolution of the detected GWs, it is possible to obtain valuable insight about the astrophysical sources that emits them, such as their masses, spins and sky-locations. The estimation of these parameters relies on Bayesian inference techniques, which involve comparing the observed GW signals with theoretical models. With this approach, the most likely values for the parameters that describe the source can be inferred. In the following, it is provided a detailed description of some of the most interesting detections during O3.

4.5.1 GW190425

GW190425 [30, 59] is a CBC event initially detected in low-latency as single-detector event in LIGO Livingston by the GstLAL pipeline with an SNR $= 12.9$, and subsequently in the first offline analysis [58] detected with a FAR $= 7.5 \cdot 10^{-4}$ yr^{-1}, and in the second offline re-analysis [59] with a FAR $= 0.034$ yr^{-1}. The Virgo detector did not contribute to the detection due to an SNR $= 2.5$, which is below the threshold of 4.0, and the LIGO Hanford detector was not in observing mode. The MBTA and PyCBC pipelines did not detect this event as they were not configured to assign FAR values to single-detector triggers during the third observing run. However, for the O4 observing period, these pipelines also consider triggers generated in only one detector in the detection process for sources with likely electromagnetic counterpart. The p_{astro} value associated to this event was 0.78 and its source properties were analysed using the PhenomPv2NRT [175] waveform model, which incorporates spin-precessing effects and tidal interactions, but to rule out any possibility of having systematic errors coming from the choice of waveform approximant the parameters estimation is normally performed with other models, in this case three further models were used: SEOBNRv4Tsurrogate [116, 225, 249, 337], IMRPhenomDNRT [172, 173, 232, 242], and TaylorF2 [241, 242]. The obtained results do not show any inconsistency. The component masses are estimated to be in the range $[1.12 - 2.52]\ M_\odot$ ($[1.46 - 1.87]\ M_\odot$ when limiting the dimensionless component spin magnitudes to values smaller than 0.05). These values indicate that the individual binary components are consistent with being NSs. However, the associated source-frame chirp mass of $1.44^{+0.02}_{-0.02}\ M_\odot$ and the total mass of $3.4^{+0.3}_{-0.1}\ M_\odot$ are significantly larger than

those observed in any other known BNS system. Considering the observed source properties and the absence of an electromagnetic counterpart, which was challenging to detect due to the poor sky-localisation of single detector triggers as well as the large estimated distance of the source, it is not possible to rule out the possibility that one or both of the binary components in the system are BHs. Therefore, the nature of the components remains uncertain based solely on GW data.

4.5.2 GW190521

GW190521 [56, 59] is a very short duration (approximately 0.1 s) GW signal detected in low-latency by PyCBC with a three-detector network SNR of 14.5 and an estimate FAR of 0.12 yr^{-1}, consistent with an unusual BBH merger of total mass $150.0^{+29.0}_{-17.0}\ M_\odot$. The event was also seen in low-latency by GstLAL, SPIIR and cWB. The MBTA offline analysis pipeline identified the signal as an HL coincidence with a network SNR $= 13.0$, FAR $= 0.042\ \mathrm{yr}^{-1}$ and $p_{astro} = 0.96$ [59]. The SNR detected in Virgo was below the threshold, at 3.48. This event stands out due to the exceptionally high masses involved in the coalescence, estimated to be $98.4^{+33.6}_{-21.7}\ M_\odot$ and $57.2^{+27.1}_{-30.1}\ M_\odot$, which produced a signal of few cycles in the detectors sensitivity range, as shown in Fig. 4.14. Under the assumption that the observed signal originated from a BBH merger, it is highly likely that at least one of the components in the binary falls within the mass range known as the Pair Instability (PI) mass gap [155, 162, 277, 287, 360, 363]. The PI mass gap refers to a range of masses in the stellar evolution where a specific type of supernova explosion, called a pair instability supernova, is expected to occur. The typical mass range associated with the PI mass gap is approximately between 60.0 $M_\odot$ and 120.0 $M_\odot$ (the exact mass boundaries are still subject to ongoing research and refinement).

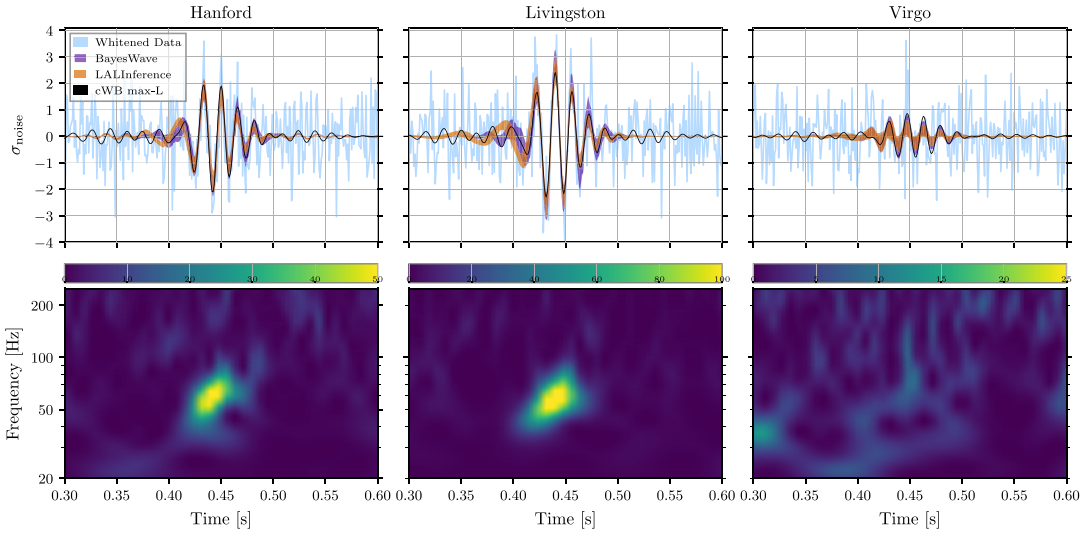

FIGURE 4.14: GW190521 observed by the LIGO Hanford (left), LIGO Livingston (middle), and Virgo (right). The top row displays the time-domain detector data after whitening by each instrument's noise amplitude spectral density (light blue lines), the estimate waveform from the CWB search (black lines), and the 90% credible intervals from the posterior probability density functions of the waveform time series, obtained via Bayesian inference (orange bands) and with a generic wavelet model (violet bands). The bottom row displays the time-frequency representation of the whitened data, where the colorbar displays the normalised energy reported by the Q-transform at each frequency [56, 138].

Within this mass range, stars are believed to be unable to undergo a conventional core collapse and instead undergo a disruptive thermonuclear explosion, thus one of the two objects involved in the merger is not likely to be of stellar origin, but rather may have undergone accretion or could be the outcome of a previous CBC merger. Nevertheless, its short duration, its wide frequency range and the uncommon massive objects involved raise the possibility that its origin cannot be solely attributed to an exceptionally massive and quasi-circular BBH coalescence. Indeed, alternative scenarios for the source of GW190521 were explored [64]. The signal is consistent with the merger of a BBH with nonzero orbital eccentricity, even if those systems are extremely rare from an astrophysical perspective, and even if the short duration of the signal makes it challenging to distinguish between amplitude modulation associated with precession [64], eccentric orbits [64, 190], or head-on collisions [190]. One potential alternative explanation for the observed signal is gravitational lensing, a phenomenon that occurs when GWs pass through massive objects like galaxies or galaxy clusters. This interaction causes the GW to bend and focus, resulting in an increased observed amplitude of the wave. Another possibility considered is that the binary components of the source may originate from PBHs, as it is unlikely for them to have formed directly from stellar collapse.

4.5.3 GW190814

The GW190814 signal [57], shown in Fig. 4.15, was initially detected in low-latency as LV coincidence by GstLAL with a network SNR $\sim$ 24.5 and by PyCBC with network SNR $\sim$ 22.5. Subsequently, it was detected by GstLAL, MBTA and PyCBC in the offline analysis [59] as a three-detector coincidence with SNR $=$ 22.2, SNR $=$ 20.4 and SNR $=$ 19.5 respectively. The estimated FAR were FAR $\leq$ 0.00001 yr^{-1} for GstLAL, FAR $\leq$ 0.0002 yr^{-1} for MBTA and FAR $\leq$ 0.17 yr^{-1} for PyCBC, while the probability of astrophysical origin was $p_{astro} = 1$ for all the pipelines. MBTA missed the low-latency detection because the SNR in Virgo data was below its single-detector detection thresholds. GW190814 is the signal with the most unequal mass ratio yet observed with GWs $0.112^{+0.008}_{-0.009}$, and its lightest component is either the lightest BH or the heaviest NS ever discovered in a compact binary system. The primary component of the binary has a BH mass of $23.3^{+1.4}_{-1.4}\ M_\odot$, while the nature of the secondary component is uncertain, falling in the lower mass gap with a mass of $2.6^{+0.1}_{-0.1}\ M_\odot$. Its mass is heavier than the most massive pulsar in the Galaxy [160], and more massive than the primary component of the outlier GW190425 (in Section 4.5.1). On the other hand its mass is compatible with the mass of two BH candidates: the merger remnant of GW170817 [29], and the light BH of $3.3^{+2.8}_{-0.7}\ M_\odot$ discovered in the J05215658 binary system [343]. It is also compatible with the millisecond pulsar PSR J1748-2021B [201], which mass is claimed to be $2.74^{+0.21}_{-0.21}\ M_\odot$. However, considering comparisons with the maximum mass of NSs inferred from studies of the remnant of GW170817 [29], our understanding of the EOS for NSs, and electromagnetic observations of NSs in binary systems, it is highly probable that the secondary component is too massive to be a NS. This theory is supported by the absence of measurable tidal effects in the signal, and the lack of electromagnetic counterparts in the sky area of 18.5 deg^2 at a distance of $241.0^{+41.0}_{-45.0}$ Mpc where the source was localised [57]. Treating this event as a novel category of CBCs, a merger rate density of $1 - 23\ \mathrm{Gpc}^{-3}\mathrm{yr}^{-1}$ has been derived for similar events.

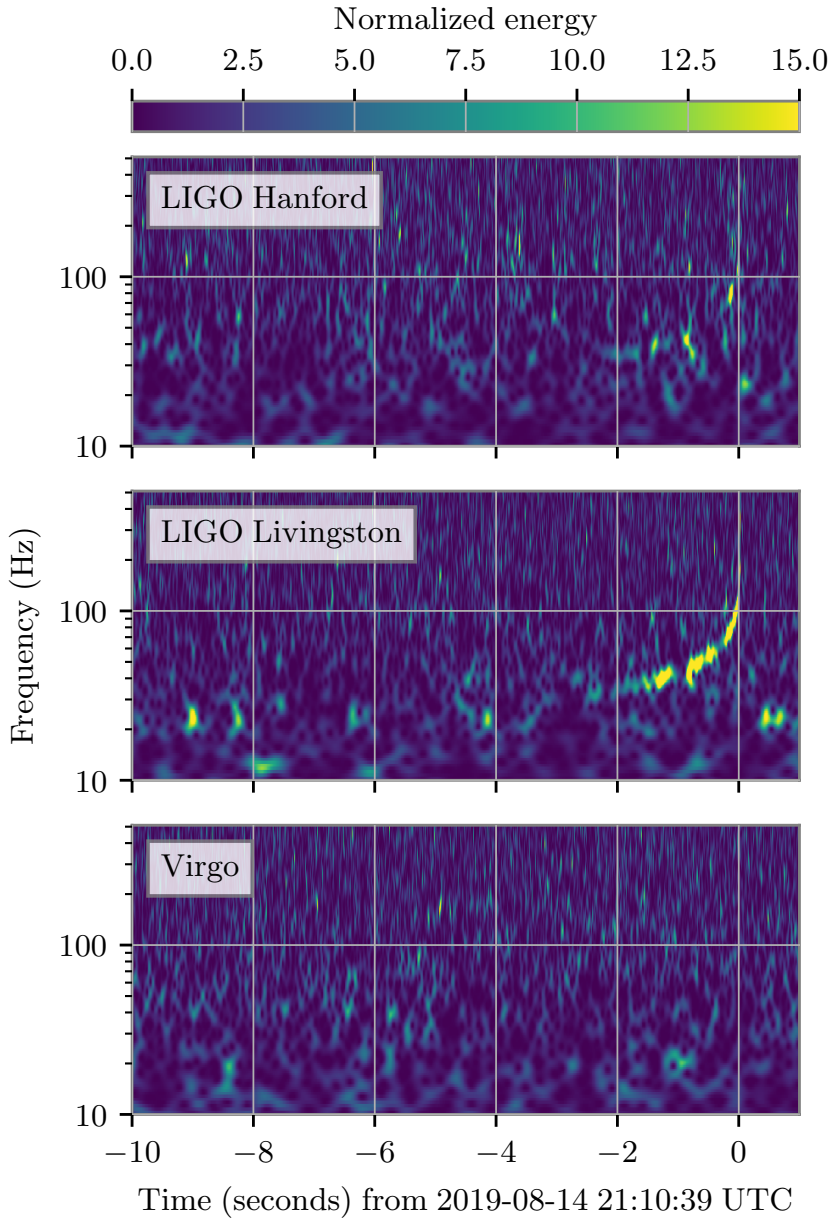

FIGURE 4.15: Time frequency representation of GW190814 observed by the LIGO Hanford (top), LIGO Livingston (middle), and Virgo (bottom) detectors.Each detector's data are whitened by their respective noise amplitude spectral density and a Q-transform is calculated. The colorbar displays the normalised energy reported by the Q-transform at each frequency.

4.5.4 NSBH Detections During O3

The third observing run has marked the first observation of GW signals from NSBH coalescences. During O3a, two events were identified as potential candidates for NSBH binaries. The first event, GW190426_152155 [58], classified as a marginal NSBH candidate due to it quietness, was detected by GstLAL in low latency, with a false alarm rate (FAR) of 1.44 yr^{-1}, and in the offline analysis by all the search pipelines, with the MBTA pipeline reporting a FAR of 31.0 yr^{-1}, PyCBC reporting a FAR of 43.0 yr^{-1}, and GstLAL reporting a FAR of 0.91 yr^{-1}. The second event, GW190814, already introduced and discussed in detail in Section 4.5.3. During O3b, four additional candidates for NSBH binaries were identified. Among them, two were initially reported in a separate paper (GW200115 and GW200105 [61]), with one of them being subsequently classified as a marginal event during the offline re-analysis. GW200115 [61], detected by all the search pipelines as a triple HLV coincidence in low latency. The MBTA offline analysis reported a FAR of $5.5 \times 10^{-3} yr^{-1}$, while the PyCBC offline analysis reported a FAR of $\leq 1.8 \times 10^{-5} yr^{-1}$, and GstLAL reported a FAR of $\leq 1.0 \times 10^{-5}$ yr^{-1}, with all pipelines estimating a $p_{astro} > 0.99$. The second event, GW200105 [61] shown in Fig. 4.16, was identified as a marginal LV coincidence, since the LIGO Hanford detector was not in observing mode at the time of the detection. Only the GstLAL pipeline detected this event, with a FAR of

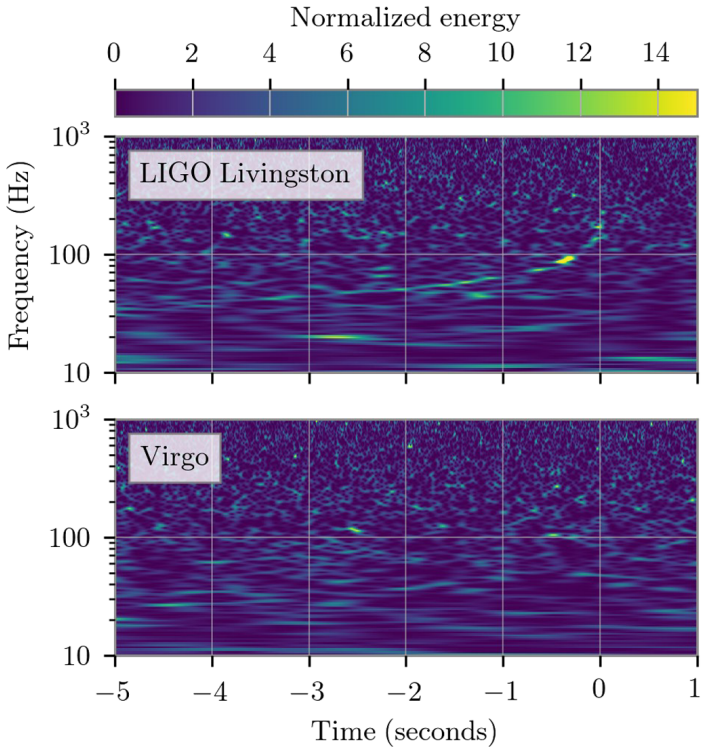

FIGURE 4.16: Time–frequency representations of the data containing GW200105 in data from the LIGO Livingston (top plot) and Virgo (bottom plot). The amplitude scale of each time–frequency tile is normalised by the respective detector's noise amplitude spectral density.

0.2 yr^{-1} but with a $p_{astro} = 0.36$. However, it was seen by the PyCBC and MBTA analyses as a Livingston trigger with an SNR of 13.1 and 13.2, respectively. This event was considered marginal in classification since it met the FAR threshold but did not meet the p_{astro} threshold. However, it stands out clearly as an outlier from

the background noise and its marginal status can be justified by the extrapolation process needed to assign a FAR and p_{astro} value to single detector triggers, considering the poor knowledge of the NSBH population used in the estimation of the p_{astro}. The third event, GW191219 [60], was found only by the PyCBC offline pipeline with a secondary mass of $m_2 = 1.17^{+0.07}_{-0.06}\ M_\odot$, and a $p_{astro} = 0.82$ when included in a bin in the BBH population, and a $p_{astro} = 0.085$ when included in a different bin. Finally, GW200210 [60], seen offline by GstLAL and PyCBC with p_{astro} of 0.42 and 0.54 respectively, and consistent with either a signal generated from an NSBH or a BBH system, as the estimated mass of the lightest component was $m_2 = 2.83^{+0.47}_{-0.42}\ M_\odot$.

NSBH GW Events in O3										
		GstLAL			MBTA			PyCBC		
		FAR [yr^{-1}]	SNR	p_{astro}	FAR [yr^{-1}]	SNR	p_{astro}	FAR [yr^{-1}]	SNR	p_{astro}
GW190426	online	0.61	10.06	-	203.28	8.89	-	30.8	9.45	-
	offline	-	-	-	-	-	-	4.1	9.6	0.75
GW190814†	online	$< 1 \cdot 10^{-25}$	24.5	-	-	-	-	-	-	-
	offline	$\leq 1 \cdot 10^{-5}$	22.2	1.0	$\leq 2 \cdot 10^{-4}$	20.4	1.0	0.17	19.5	1.0
GW191219	online	-	-	-	-	-	-	-	-	-
	offline	-	-	-	-	-	-	4.0	8.9	0.82
GW200105	online	24.21	13.89	-	-	13.3	-	-	13.2	-
	offline	-	-	-	-	-	-	-	-	-
GW200115	online	$6.6 \cdot 10^{-4}$	11.4	-	0.16	11.45	-	0.48	11.3	-
	offline	$\leq 1 \cdot 10^{-5}$	11.5	≥ 0.99	$5.5 \cdot 10^{-3}$	11.2	≥ 0.99	$1.2 \cdot 10^{-4}$	10.8	≥ 0.99
GW200210	online	-	-	-	-	-	-	-	-	-
	offline	1.2	9.5	0.42	-	-	-	7.7 17	8.9 8.9	0.54 0.53

TABLE 4.3: NSBH candidates identified during O3. The dagger † indicates the events that are unsure NSBH systems. Table made with information retrieved from [59, 60, 148]. The event GW200210 has two values of FAR, SNR and p_{astro} referred to the two different searches performed by PyCBC: PyCBC-broad (bottom value), which encompasses a wide parameter space allowing detection of many different types of CBC systems, and PyCBC-BBH (top value), focusing on BBH systems with total masses in $[10\ M_\odot, 500\ M_\odot]$, mass ratios in the range $1/3 \leq q \leq 1$, and component masses in the range $5\ M_\odot \leq m_1 \leq 350\ M_\odot$ and $m_2 \geq 5\ M_\odot$. GW200105 is a single detector event identified by the GstLAL pipeline, also MBTA and PyCBC produced consistent triggers around the event but those are not configured to assign FAR values to single-detector triggers.

4.6 Search Sensitivity

As previously described, the sensitivity of the analysis is monitored on injections during the run. To facilitate the comparison of the results across different pipelines, and their combination to constrain, e.g., the mergers populations, a common simulation campaign was performed and the sensitive volume-time $\langle VT \rangle$ was evaluated in different regions of the parameter space. The $\langle VT \rangle$ is defined in Eq. (3.26) and it reflects the ability of the analysis pipeline to detect GW sources uniformly distributed in comoving volume and observing time. To estimate the $\langle VT \rangle$, a new set of injections is superimposed to data and the pipeline's ability to recover them is investigated. Unlike the injections set employed to assess the sensitivity and performance of the search, which was specific to the MBTA pipeline, this particular set remains consistent across all the analysis pipelines. This approach allows for a reliable measurement of the $\langle VT \rangle$ and facilitates direct comparisons among different pipelines. The injections sets used during O3 are reported in Table 4.4 and

are designed to cover the parameter space of BBH, BHNS and NSBH of detected GWs. The BNS injected signals are generated using the SpinTaylorT4 [124, 125]

Injections Distributions					
	Mass distribution	Mass range ($M_\odot$)	Spin range	Spin orientations	Maximum redshift
BBH	$p(m_1) \propto m_1^{-2.35}$ $p(m_2\|m_1) \propto m_2$ POWER LAW + PEAK	$2.0 < m_1 < 100.0$ $2.0 < m_2 < 100.0$ as in [63]	$\|\chi_{1,2}\| < 0.998$	isotropic	1.9
NSBH	$p(m_1) \propto m_1^{-2.35}$ uniform	$2.5 < m_1 < 60.0$ $1.0 < m_2 < 2.5$	$\|\chi_1\| < 0.998$ $\|\chi_2\| < 0.4$	isotropic	0.25
BNS	uniform	$1.0 < m_1 < 2.5$ $1.0 < m_2 < 2.5$	$\|\chi_{1,2}\| < 0.4$	isotropic	0.15

TABLE 4.4: Parameters distributions used to generate injections for the evaluation of the sensitive volume-time during O3 [60].

waveform model, while the BBH and BHNNS sets are generated with the SEOBNRv4PHM [100, 294, 302] model. The $\langle VT \rangle$ is then computed by counting the N_{rec} injections detected above the FAR threshold of 2.0 yr^{-1}, out of the N_{tot} injected simulated signals. Additionally, a specific POWER LAW + PEAK model for BBH systems, which represents a reference population of such systems, was analysed. During O3a, the overall sensitive hypervolume $\langle VT \rangle$ values, reported in Table 4.5, were published as measured by each search pipeline individually, as well as the combined value obtained by counting all injections detected in at least one pipeline using the previously specified threshold on the FAR. During O3b, the same sets of injections

Sensitive hypervolume VT $[Gpc^3yr]$					
	GstLAL	MBTA	PyCBC-broad	PyCBC BBH	All
BBH	0.258	0.196	0.194	0.234	0.308
BBH (POWER LAW + PEAK)	1.22	0.885	0.914	1.20	1.44
BNS	0.00594	0.00631	0.00657	-	0.00781
NSBH	0.0174	0.0165	0.0181	-	0.0221

TABLE 4.5: Measures of the sensitive hypervolume of the search pipelines in data from O3a. The PyCBC pipeline is used in different configuration: PyCBC-broad, which encompasses a wide parameter space allowing detection of many different types of CBC systems, and PyCBC-BBH, focusing on BBH systems with total masses in $[10\ M_\odot, 500\ M_\odot]$, mass ratios in the range $1/3 \leq q \leq 1$, and component masses in the range $5\ M_\odot \leq m_1 \leq 350\ M_\odot$ and $m_2 \geq 5\ M_\odot$.

that were used in O3a were superimposed onto the data and, instead of considering the overall rate of signals across the entire parameter space, the computation of $\langle VT \rangle$ was focused on signals corresponding to sources with specific masses, detected with $p_{astro} > 0.5$. Among the considered mass configurations, the search sensitivity is highest for $35M_\odot + 35M_\odot$ binary systems in all analyses, as shown in Fig. 4.17. Additionally, when combining the results from all pipelines and considering injections found with $p_{astro} > 0.5$ in at least one pipeline, the overall search sensitivity is further improved. This confirms the notion that using the information from multiple pipelines not only allows for cross-checking of results but also enhances the sensitivity. However, it is relevant to point out that when combining results, under

the assumption of uncorrelated pipelines, as the sample of detected injections increases, so does the sample of false positives, leading to an increased contamination of false positives. This aspect requires studies of the purity of the selected sample to find a trade-off between sensitivity and reduction of the false positives in order to enhance the robustness of the obtained estimations. The sensitive hypervolume

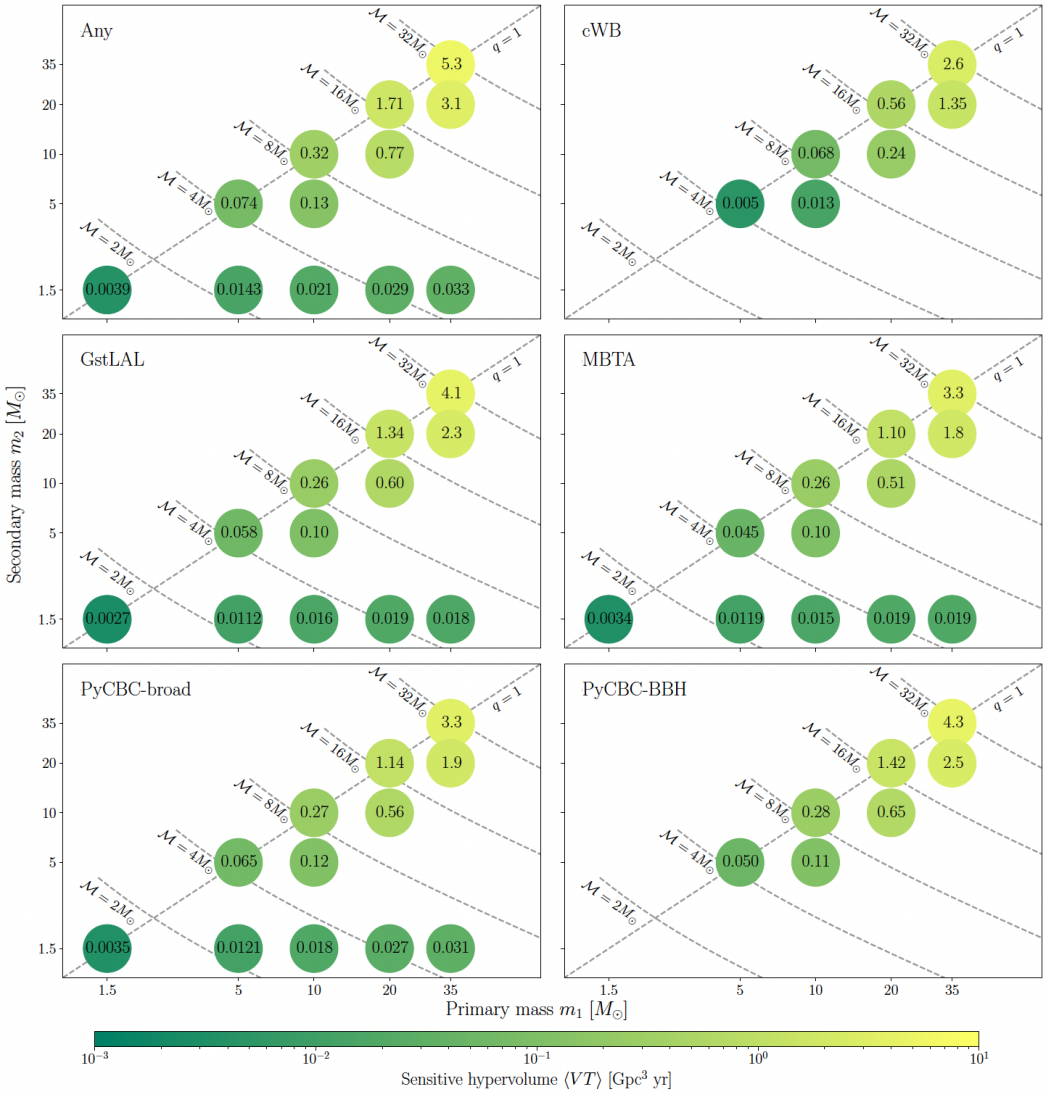

FIGURE 4.17: Sensitive hypervolume $\langle VT \rangle$ in data from O3b for the various searches. In this plot are shown also the values computed by the cWB analysis [244], which searches for transient signals without assuming a model template. The cWB results are obtained with the standard $p_{astro} > 0.5$ threshold with the requirement that $p_{astro} > 0.1$ from at least one matched-filter analysis. The PyCBC pipeline is used in different configuration: PyCBC-broad, which encompasses a wide parameter space allowing detection of many different types of CBC systems, and PyCBC-BBH, focusing on BBH systems with total masses in $[10\ M_\odot, 500\ M_\odot]$, mass ratios in the range $1/3 \leq q \leq 1$, and component masses in the range $5\ M_\odot \leq m_1 \leq 350\ M_\odot$ and $m_2 \geq 5\ M_\odot$.

measurements and the observed number of GW events are used to constrain the merger rates for such binary systems [62]. This information provides valuable insights into the populations of these astrophysical objects, with investigations into the properties and features of the signals such as the estimation of parameters like masses, spins, luminosity distance, and orientation. Furthermore, the analysis of

GW signals is used to constrain cosmological parameters [55], to explore the equation of state for dense matter in NSs [28], and to evaluate the predictions of general relativity [67].

CHAPTER5

O3 Sub-Solar Mass Search

The SSM search focuses on the detection and investigation of compact objects with masses below 1.0 $M_\odot$. In its realisation during O3, this search specifically aims to identify signals produced by spiralling binary systems in which at least one component is an object with a mass in between $0.2 - 1.0\ M_\odot$. The lower mass limit was chosen to be 0.2 $M_\odot$ to limit the computational costs of the search. The search for SSM objects in binary systems has been conducted in offline since the second Initial LIGO science run (S2) [16], as well as the initial observing run of the LIGO-Virgo collaboration [41, 42, 65, 66], and has not reported any detection of GW signals so far. Nevertheless, the null results are used to place upper limits on the merger rate of such binary systems, constraining phenomenological models that could produce SSM compact objects. Overall, the SSM search is an active area of research within GW astronomy, aiming to broaden our understanding of compact objects and potentially uncover new exotic objects and formation channels in the cosmos (see Section 1.4.2). In the SSM search during the third observing run, the author of this manuscript played a crucial role as main analyst for the MBTA pipeline, other than significantly contributing to the writing of the related papers, as well as the realisation of part of the key plots such as Figure 5.20 and Figure 5.21. Moreover, Section 5.5 presents two preliminary studies conducted by the author to address the possibility of having an electromagnetic counterpart in the scenario of an SSM BH merging to a NS, as well as the potential outcomes in the case of a SSM NS merging with a BH. Finally, Section 5.6 presents the work done by the author in preparation for the fourth observing run of the LIGO-Virgo-KAGRA collaboration, devoted to the development of the first online search for SSM mergers. In this context, the author of this thesis generated and tested the template bank that is currently being used by the MBTA pipeline, and analysed the results of the Mock Data Challenge (MDC) performed before the start of the run, other than the preliminary results of the first weeks of O4.

5.1 Template Bank

During the first observing run (O1) [42], data from the LIGO Hanford and LIGO Livingston observatories were analysed to search for GW signals emitted from equal-mass binary systems with component masses in the detector frame ranging from $[0.19, 2.0]\ M_\odot$ and negligible spins. In the second observing run (O2) [41], the template bank was upgraded to include component spins aligned with the angular momentum and with magnitudes of 0.1 or less. The bank was designed to recover equal

mass binaries with component detector frame masses in $[0.19, 2.0]\ M_\odot$ and total binary masses in $[0.4, 4.0]\ M_\odot$.

In the third observing run, MBTA was included in the offline data analysis alongside PyCBC and GstLAL. All three search pipelines used a common template bank, shown in Fig. 5.1, which was designed to recover GW signals from binary systems where at least one component is a SSM object, while the other component could be either a SSM, a NS, or a BH object. The template bank was optimised to cover a wide range of possible parameter combinations for such binary systems, ensuring comprehensive sensitivity to the different types of sources. It was generated with a geometric placement algorithm with a minimum match of 0.97, designed to recover binaries with detector frame masses of $m_1 \in [0.2, 10.0]\ M_\odot$ and $m_2 \in [0.2, 1.0]\ M_\odot$, mass ratios in the range $1.0 < m_1/m_2 < 10.0$ and dimensionless aligned spins up to 0.9 for masses greater than 0.5 $M_\odot$, and up to 0.1 otherwise. The arbitrary choice of reducing the spins magnitudes at low masses was taken in order to reduce the number of templates in the bank, and thus reduce the computational costs of the search. Moreover, a test performed with high-spin injections showed that these banks are able to successfully detect such injections without affecting the overall fitting factor. Fig. 5.1 shows that the placement of templates in the $m_1 - m_2$ plane is not uniform, resulting in apparent "holes" in the template bank. These apparent holes are not in-

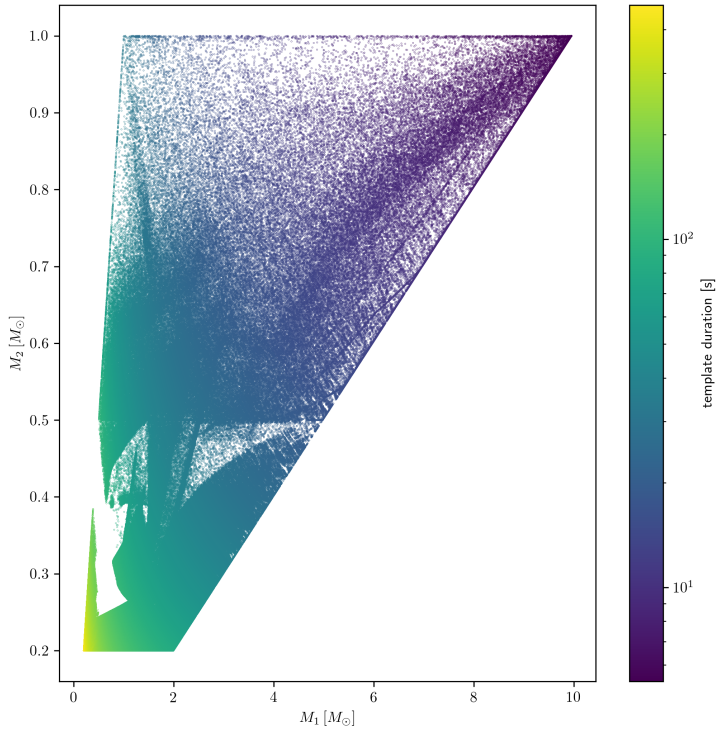

FIGURE 5.1: Template bank in the $m_1 - m_2$ plane used by GstLAL, MBTA and PyCBC in the SSM search during the third observing run. Each dot corresponds to a different template in the bank while the colorbar represents the template duration (in seconds).

dicative of missing templates but rather a result of the algorithm used to generate the bank and the limitations of the two-dimensional representation. They do not represent actual gaps in the template bank, but rather the presence within the bank of templates that have a match greater than 0.97 with the templates that appear to be absent in those regions. Furthermore, due to the multidimensional nature of the

parameter space used to construct the bank, a two-dimensional representation of it does not fully capture its complexity. To further alleviate the computational burden of matched filtering, the template waveforms were integrated between $45 - 1024$ Hz, instead of starting at 25 Hz as in the standard O3 MBTA search. The limited bandwidth leads to an estimated maximum loss of approximately 8% in the SNR across the entire parameter space, relative to the SNR that would be achieved if the data were filtered from 25 Hz, as shown in Fig. 5.2. This value is determined by computing the relative percentage of SNR loss for a set of injections as

$$\%\mathrm{SNR}_{loss} = \frac{\mathrm{SNR}_{45Hz} - \mathrm{SNR}_{25Hz}}{\mathrm{SNR}_{25Hz}} \cdot 100\,, \tag{5.1}$$

where SNR_{45Hz} and SNR_{25Hz} represent the optimal SNR obtained from matched filtering the injections against themselves, starting at 45 Hz and 25 Hz respectively. Fig. 5.2 illustrates the distribution of percentage loss in SNR in both the $m_1 - m_2$ plane and in the $m_{\mathrm{chirp}} - \chi_{\mathrm{eff}}$ plane, where the colorbar indicates the difference between the percentage loss in SNR for the considered injection and the median percentage SNR loss across all the injections. Some patterns are visible around fixed chirp mass values that have been considered not worrying given the very small differences with respect to the rest of the parameter space (note the colorbar scale).

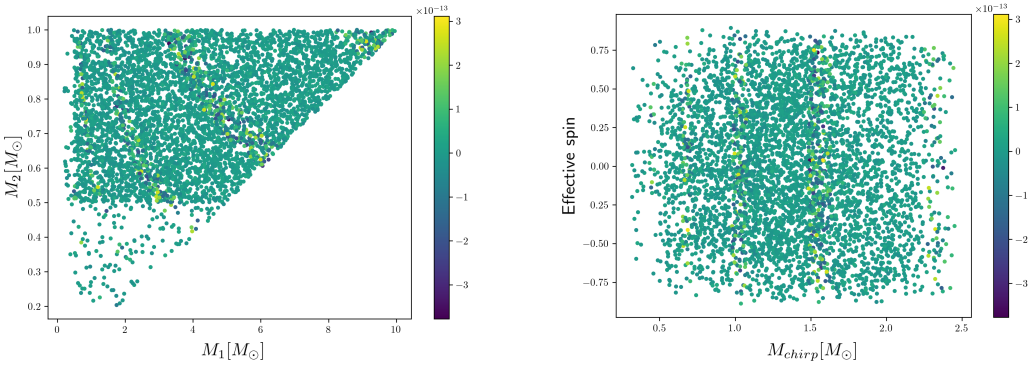

(A) Loss in SNR in the $m_1 - m_2$ plane.

(B) Loss in SNR in the $m_{chirp} - \chi_{eff}$ plane.

FIGURE 5.2: Estimated loss in SNR computed by matched filtering a set of injections starting at 45 Hz and at 25 Hz . Each dot corresponds to an injections, while the colorbar indicates how much the percentage loss in SNR of the injection differs from the median percentage loss of SNR across all injections.

5.2 Search Monitoring

To assess the performance of the SSM offline search, the same figures of merit introduced in Section 4.3 were produced. For this specific search and during the analysis of the O3a results, each pipeline was responsible for the generation of its own injections. Specifically, the MBTA pipeline generated two sets of injections, based on the parameter space described in Table 5.1, and then combined to form a single set which was subsequently analysed as a whole. The generation process followed a uniform distribution in component masses and chirp distance d_c, which is a measure of the GW source's luminosity distance d as function of the chirp mass m_{chirp}

Injections Distributions						
	Heaviest mass range ($M_\odot$)	Lightest mass range ($M_\odot$)	Total mass ($M_\odot$)	Spin range	Distance [Mpc]	Mass ratio
SSM	$0.2 < m_1 < 0.5$ $0.5 < m_1 < 10.0$	$0.2 < m_2 < 0.5$ $0.2 < m_2 < 1.0$	$0.2 < m_{tot} < 1.0$ $0.7 < m_{tot} < 11.0$	$0.0 < \lvert\chi_{1,2}\rvert < 0.1$ $0.0 < \lvert\chi_{1,2}\rvert < 0.9$	$5.0 < d < 400.0$	$1.0 < q < 10.0$

TABLE 5.1: Parameters distributions used to generate injections for the evaluation of the sensitive volume-time during O3a [65].

and redshift z of the binary system, and is defined as follows:

$$d_c = d\left(\frac{k}{m_{chirp}}\right)^{\frac{5}{6}}(1+z)^{\frac{1}{6}}, \tag{5.2}$$

where k is a constant equal to $2.8 \cdot (0.25)^{0.6}$, and z is the redshift associated to the specific injection assuming a ΛCDM model with parameters values from Planck15 [77].

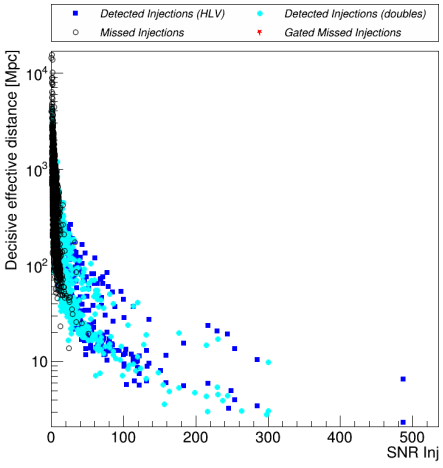

(A) SSM: scatterplot of effective distance as function of injected SNR.

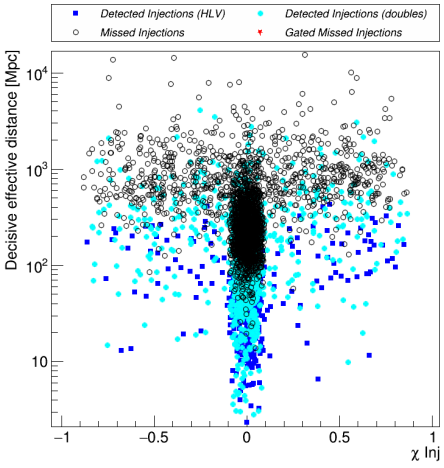

(B) SSM: scatterplot of effective distance as function of injected effective spin.

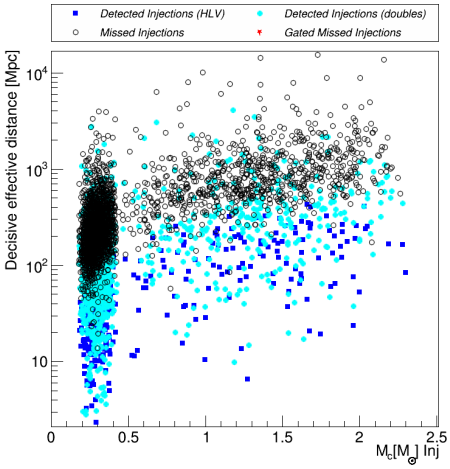

(C) SSM: scatterplot of effective distance as function of injected chirp mass.

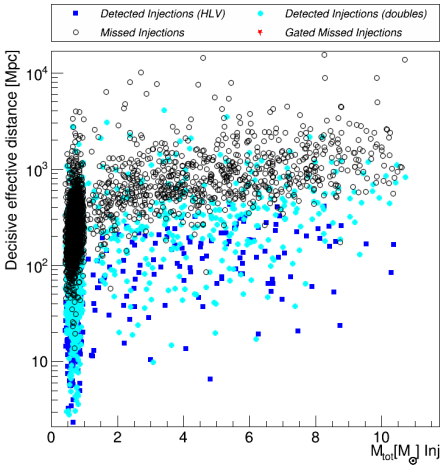

(D) SSM: scatterplot of effective distance as function of injected total mass.

FIGURE 5.3: Found and missed injections in a sample chunk between GPS times 1268420276 and 1269561620 for SSM for doubles (light blue) and triples (dark blue) detected injections, considered as such if they have an $SNR \geq 7$. The open dots show missed injections, and the red stars show missed injections that have activated the gating.

In Fig. 5.3, the injection recovery plots indicate that most of the missed injections exhibit low SNR values and high effective distances (defined in Eq. (4.1)). This trend is expected and aligns with the one observed in Fig. 4.4 for BNS systems in the standard search, which are the ones closest to the current analysis due to their low mass values. Furthermore, it is possible to notice that the gating process had no significant impact on missed injections, which is consistent with the behaviour observed in the case of BNS systems. The absence of glitch-like characteristics, even in high SNR SSM injections, is the reason why the gating process did not activate. As expected, the pipeline exhibits greater efficiency in successfully detecting injected signals at shorter distances, as illustrated in Fig. 5.4, which are anticipated to have higher SNR values. Moreover, the detection efficiency as a function of the chirp mass in Fig. 5.5 shows an approximately stable pattern across different chirp mass values as expected in the case of injections distributed flat in chirp distance.

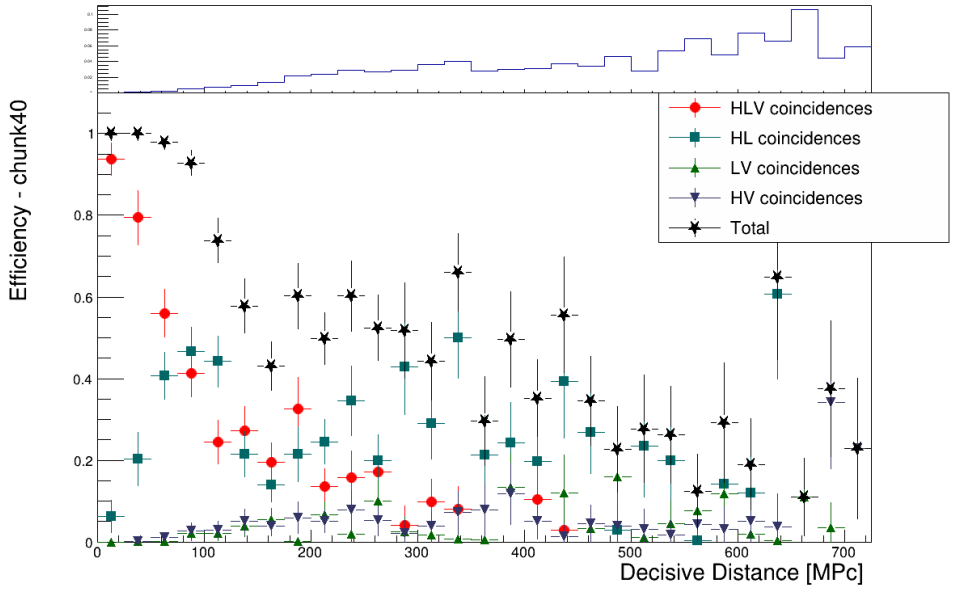

FIGURE 5.4: Efficiency of detection as function of the decisive distance in a sample chunk between GPS times 1268420276 and 1269561620 for HLV (red circles), HL (dark green squares), HV (blue reversed triangles) and LV (light green triangles) for SSM coincidences. In this plot the 4 categories of coincidences are mutually exclusive, so that the efficiencies can be summed over, resulting in the total efficiency (black stars). The inset above the plots display the distribution of injections.

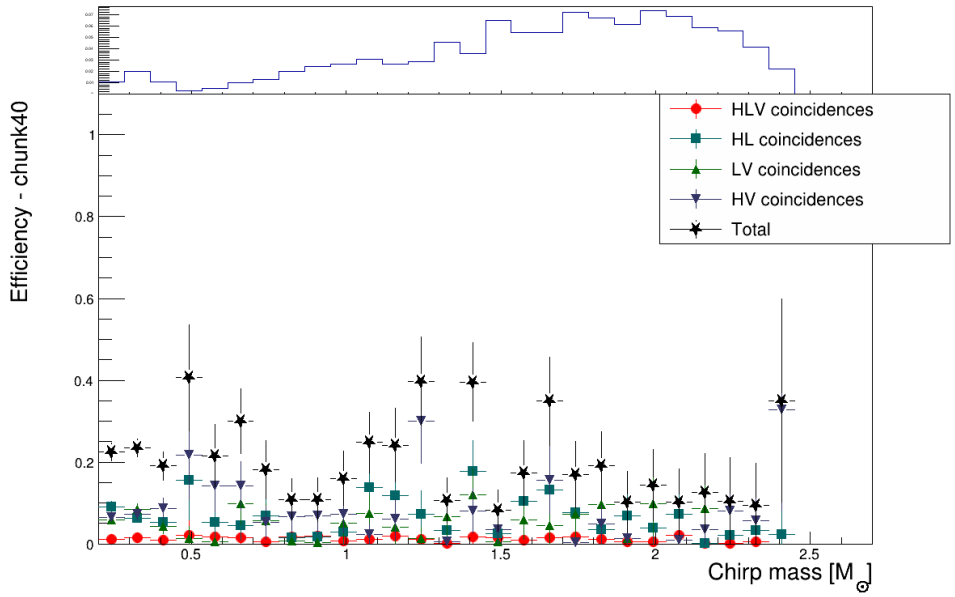

FIGURE 5.5: Efficiency of detection as function of the chirp mass in a sample chunk between GPS times 1268420276 and 1269561620 for HLV (red circles), HL (dark green squares), HV (blue reversed triangles) and LV (light green triangles) for SSM coincidences. In this plot the 4 categories of coincidences are mutually exclusive, so that the efficiencies can be summed over, resulting in the total efficiency (black stars). The inset above the plots display the distribution of injections.

Fig. 5.6 presents the cumulative trend of the IFAR over the entire duration of the third observing run. The plot provides insight into the background noise behaviour, and its consistency with the expected background distribution. Considering the lack of detected SSM GW signals during this period, there are no instances where signals deviate from the background distribution.

5.3 Sensitivity and Binary Merger Rate

No GW candidates were identified by any of the search pipeline during the entire O3. Nevertheless, in [66] and in Table 5.2, are reported the most significant triggers in the second half of the third observing run, with $FAR < 2yr^{-1}$ identified by at least one search pipeline. Upon visually examining the data surrounding the trigger times, no indications of data quality problems are observed that would definitively suggest an instrumental origin. However, the number of triggers along with their estimated FAR aligns with expectations under the assumption of the absence of any astrophysical signal in the data. This is in consideration of the 0.34-year duration of O3b and the utilisation of three CBC pipelines. The absence of detections, com-

FAR $[yr^{-1}]$	Pipeline	GPS time	m_1 $[M_\odot]$	m_2 $[M_\odot]$	χ_1	χ_2	Network SNR
0.2	GstLAL	1267725971.02	0.78	0.23	0.57	0.02	8.90
1.37	MBTA	1259157749.53	0.40	0.24	0.10	−0.05	10.25
1.56	GstLAL	1264750045.02	1.52	0.37	0.49	0.10	9.10

TABLE 5.2: Triggers with a $FAR < 2yr^{-1}$ in at least one search pipeline. The reported redshifted component masses, m_1 and m_2, and dimensionless component spins, χ_1 and χ_2, are the ones identified with the lowest FAR in the associated pipeline.

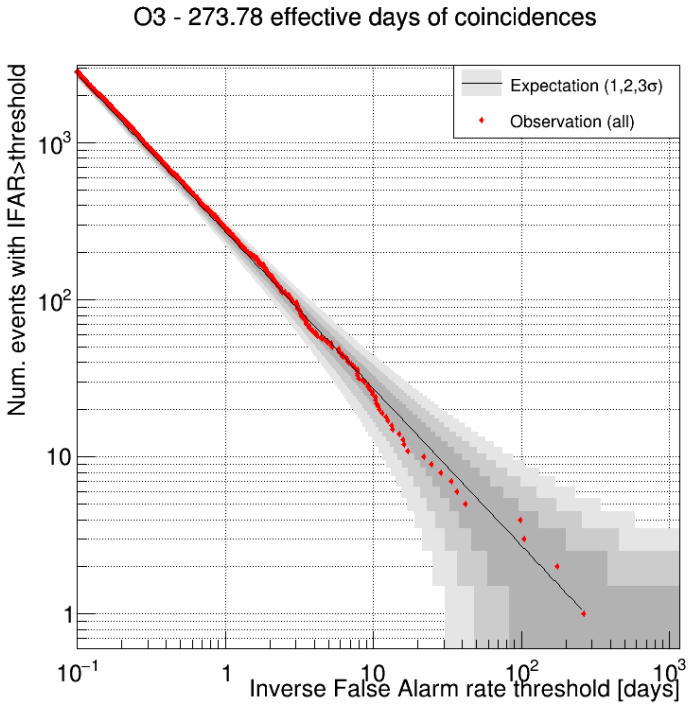

FIGURE 5.6: Cumulative IFAR distribution for doubles and triples SSM coincidences in the whole third observing run. The black curve represents the expectation from the background, while the grey regions are the Poissonian errors corresponding to the 1σ (dark grey), 2σ (grey), and 3σ (light grey) confidence intervals. Each red dot corresponds to a trigger.

patible with results from parallel searches conducted by external groups [283, 284], allows for the estimation of an upper limit on the rate at which SSM mergers occur. In the following section are outlined the two procedures used to estimate the merger rate during the first and second halves of the third observing run. It is important to remark that the two methods were applied separately on two different injections sets. For O3a, the injection set used was different for each pipeline, in particular MBTA used the one outlined in Table 5.1, generated uniformly in chirp distance. In contrast, for O3b a new injection set, common among pipelines, was generated uniformly in comoving volume. This distinction is crucial as it influences the specific procedures employed for estimating the merger rate in each period. Furthermore, in addition to being used in the O3b data analysis, the same set of common injections was superimposed on the O3a data, enabling an assessment of the merger rate throughout the entire observation period, as well as a comparison between the merger rates estimated using the two sets in O3a.

5.3.1 First Half of the Third Observing Run: O3a

During O3a, the injection set described in Table 5.1, which was initially distributed uniformly in chirp distance d_c (defined in Eq. (5.2)) and component masses m_1 and m_2, underwent a re-weighting process to ensure a uniform distribution in comoving volume, which is defined in Eq. (3.25), for each chirp mass value. The purpose of having a uniform distribution in comoving volume is to guarantee that the injections are distributed evenly across the observable Universe, without any bias towards

specific distance ranges. The weight w assigned to each injection was computed as

$$w = \frac{\partial V}{\partial d_c} = \frac{\partial}{\partial d_c}\left(\frac{4}{3}\pi d^3\right) = 4\pi d_c^2 \left(\frac{m_{chirp}}{k}\right)^{15/6} (1+z)^{-1/2}\,, \tag{5.3}$$

where d_c, m_{chirp} and z are respectively the chirp distance, chirp mass and redshift associated to the considered injection and d is the luminosity distance of the source, related to d_c through Eq. (5.2). Contrary to expectations, the resulting distribution of comoving volume, as shown in Fig. 5.7, is visibly non-uniform. To ensure the cor-

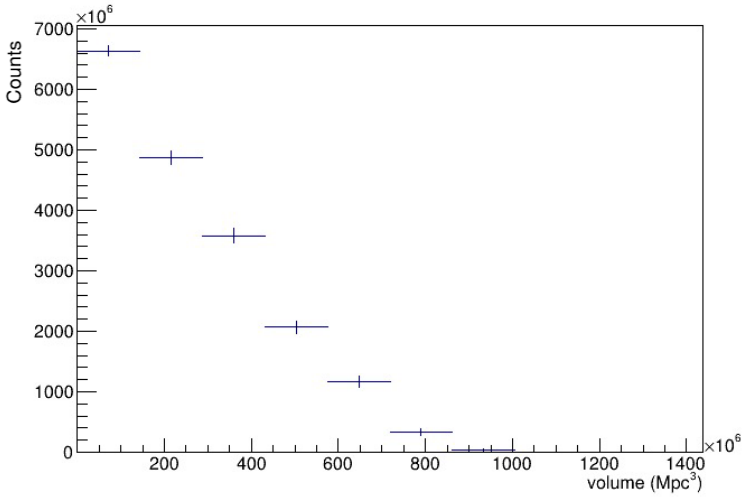

FIGURE 5.7: Distribution of comoving volume of the injection set after the re-weighting process.

rectness of the re-weighting procedure and gain a complete understanding of how the distributions changed from the initial state, a thorough crosschecking was performed. This involved generating a uniform distribution in comoving volume with a Monte Carlo toy, as shown in Fig. 5.8, and subsequently, emulating the injection generation process, selection cuts were applied to mimic the criteria used during the injection generation. As a first step, all the injections with a mass ratio greater

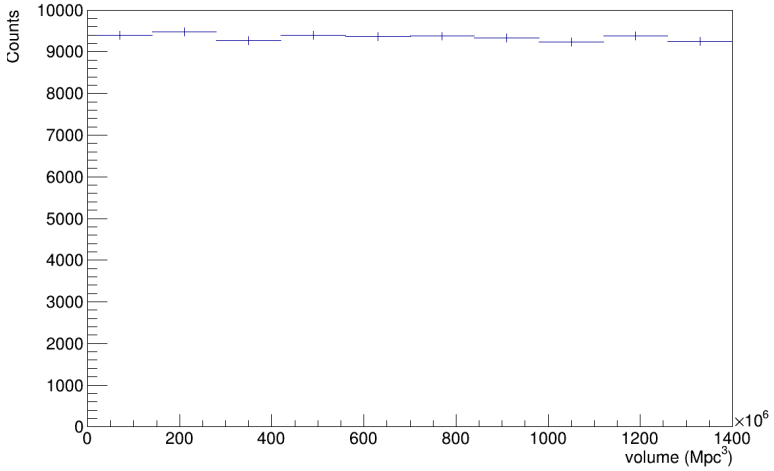

FIGURE 5.8: Distribution of comoving volume of the of the Monte Carlo toy.

than 10.0 were rejected. The comoving volume distribution remains unaffected by

this selection cut. Then, a further selection cut was applied, retaining only injections within the range of generated chirp distances between 4 Mpc and 500 Mpc. This last selection cut had a significant impact on the distributions of comoving volume, as shown in Fig. 5.9. The concentration of injections is shifted towards the lower end of the comoving volume range, indicating a higher density of injections at closer distances. The distributions obtained from the crosschecking procedure, with the

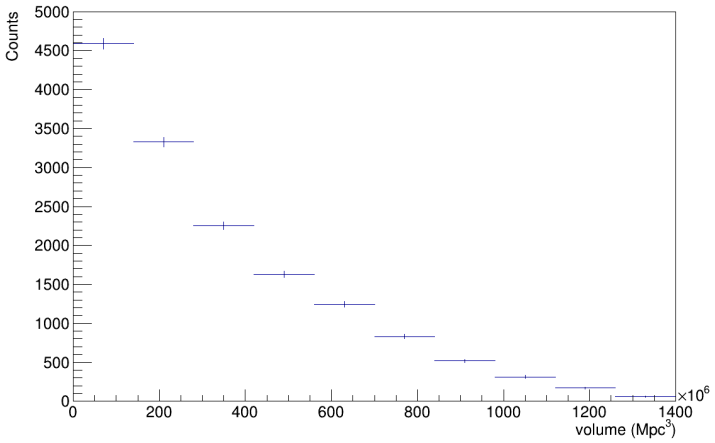

FIGURE 5.9: Distribution of comoving volume of the Monte Carlo toy after the selection cut on mass ratio and chirp distance.

selection cut on chirp distances, match with the distributions obtained from the actual set of injections used in the search, previously displayed in Fig. 5.7. This confirmed that by re-weighting the injections set it is possible to successfully reproduce the desired flat distribution in comoving volume, and that the selection cuts applied are the cause of the characteristics of the actual distribution. Furthermore, following Eq. 5.2 and given the method used in the generation, the range of minimum and maximum luminosity distances, and consequently the volume containing the injections, varied based on the chirp mass, as shown in Fig. 5.10. The minimum ac-

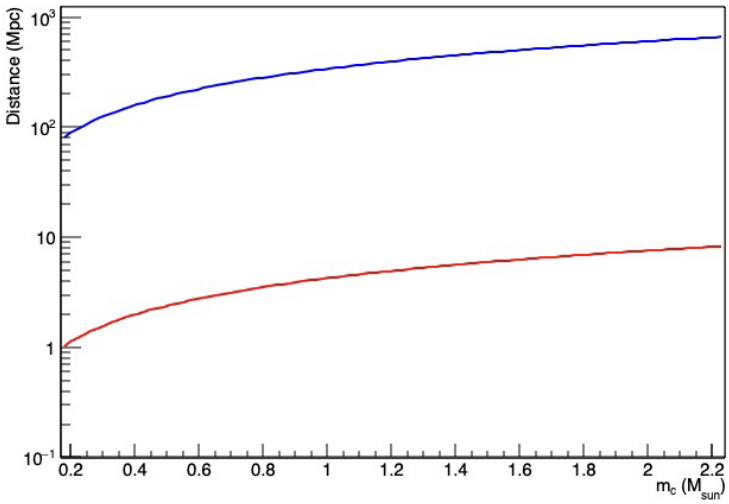

FIGURE 5.10: Distribution of minimum distances (red curve) and maximum distance (blue curve) as function of the chirp mass of the binary system.

tual generated luminosity distance in the set of injections was approximately 1 Mpc,

while the maximum luminosity distance reaches up to around 700 Mpc, corresponding to a redshift of approximately 0.15, assuming a ΛCDM model with parameters values from Planck15 [77]. Therefore, when estimating the sensitive volume $\langle V \rangle$ of the search, the maximum generated comoving volume associated with each injection, denoted as V_i^{max}, is taken into consideration, so that $\langle V \rangle$ is computed as

$$\langle V \rangle = \frac{\sum_{i=1}^{N_{det}} w_i V_i^{max}}{\sum_{i=1}^{N_{gen}} w_i} , \tag{5.4}$$

in which N_{gen} represents the total number of injections generated, while N_{det} represents the number of injections that were successfully detected, corresponding to those with mass ratio $m_1/m_2 \leq 10.0$ and FAR ≤ 1.0 yr^{-1}. The weight applied on each injection is denoted as w_i, and ϵ_i is therefore the weighted efficiency of the pipeline in recovering the injections. The sensitive volume-time is then computed as

$$\langle VT \rangle = T \langle V \rangle , \tag{5.5}$$

where T corresponds to the analysed time. The error on the sensitive volume-time accounts for the uncertainty on the efficiency and is estimated at 90% confidence interval as

$$\Delta \langle VT \rangle = 1.645 \cdot T \cdot \sqrt{\frac{\sum_{i=1}^{N_{gen}} (w_i \cdot V_i^{max})^2 \epsilon_i^{raw} (1 - \epsilon_i^{raw})}{(\sum_{i=1}^{N_{gen}} w_i)^2}} , \tag{5.6}$$

in which ϵ_i^{raw} is the unweighted efficiency for the i-th injection and the factor 1.645 takes account of the 90% confidence interval. The error formula for an efficiency in the case of a weighted sample has been derived from first principles and validated with a toy Monte Carlo.

The choice of showing the results as function of chirp mass is motivated by the fact that the search sensitivity is primarily dependent on this parameter [164]. Therefore, to estimate the behaviour of the sensitive volume-time $\langle VT \rangle$ as a function of the chirp mass, the population of injections was divided into nine equally spaced chirp mass bins within the range of $0.17 M_\odot < M < 2.39 M_\odot$. The corresponding results are shown in Fig. 5.11. Although an overall agreement between different search pipelines on the estimation of $\langle VT \rangle$ values is present, it is important to stress that small variations are caused by differences in the background estimation methods and ranking statistics among pipelines. A combination of such results would require a detailed study of pipelines correlations on background and signal. An attempt to perform this study was started during O3 but unfortunately it is not finalised yet.

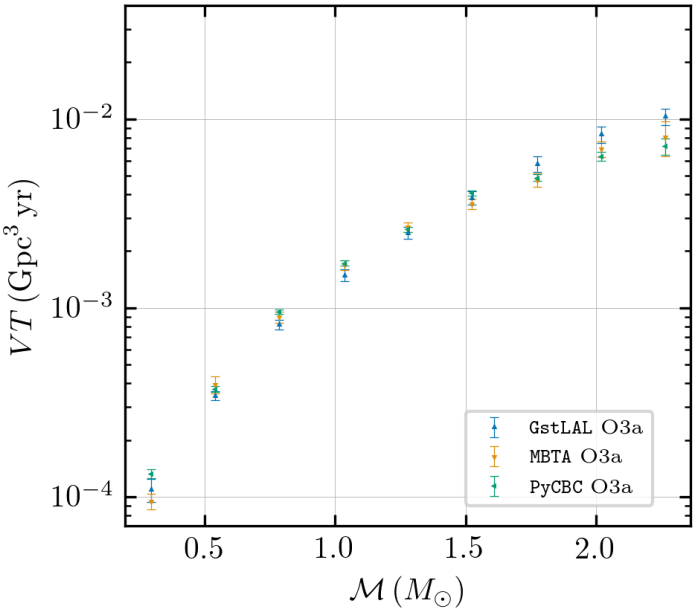

FIGURE 5.11: Sensitive volume–time as a function of the source frame chirp mass in data from O3a, obtained through the analysis of the set of injections for GstLAL (blue), MBTA(orange), and PyCBC(green). The error bars represent the statistical errors and are evaluated at 90% confidence interval, following Eq. 5.6.

By treating each chirp mass bin as a separate population, labeled by an index i, it is possible to use the surveyed volume-time for each chirp mass bin to estimate an upper limit at 90% confidence interval on the merger rate $\mathrm{R}_{90\%}$ of that population, by using the relation introduced in Eq. (3.27), as

$$\mathrm{R}_{90\%} = \frac{2.3}{\langle VT \rangle} \,. \tag{5.7}$$

Fig. 5.12 displays the merger rate estimates obtained from the three search pipelines in data from O3a. The specific values of $\langle VT \rangle$ and $\mathrm{R}_{90\%}$, obtained for the MBTA pipeline in O3a, are listed in Table 5.3. Errors for the merger rates were not estimated.

MBTA Values of $\langle VT \rangle$ and $\mathrm{R}_{90\%}$ in O3a			
m_{chirp} range $(M_\odot)$	$\langle VT \rangle$ $(\mathrm{Gpc}^3\,\mathrm{yr})$	$\Delta\langle VT \rangle$ $(\mathrm{Gpc}^3\,\mathrm{yr})$	$\mathrm{R}_{90\%}$ $(\mathrm{Gpc}^{-3}\,\mathrm{yr}^{-1})$
[0.17, 0.42]	0.000095	$9.00 \cdot 10^{-06}$	$2.42 \cdot 10^{+04}$
[0.42, 0.66]	0.000393	$4.20 \cdot 10^{-05}$	$5.85 \cdot 10^{+03}$
[0.66, 0.91]	0.000893	$6.10 \cdot 10^{-05}$	$2.58 \cdot 10^{+03}$
[0.91, 1.16]	0.001684	$1.01 \cdot 10^{-04}$	$1.37 \cdot 10^{+03}$
[1.16, 1.40]	0.002678	$1.54 \cdot 10^{-04}$	$8.59 \cdot 10^{+02}$
[1.40, 1.65]	0.003560	$2.32 \cdot 10^{-04}$	$6.46 \cdot 10^{+02}$
[1.65, 1.90]	0.004760	$3.82 \cdot 10^{-04}$	$4.83 \cdot 10^{+02}$
[1.90, 2.14]	0.006949	$6.80 \cdot 10^{-04}$	$3.31 \cdot 10^{+02}$
[2.14, 2.39]	0.008034	$1.67 \cdot 10^{-03}$	$2.86 \cdot 10^{+02}$

TABLE 5.3: Sensitive volume-time $\langle VT \rangle$ and merger rate at 90% credible interval $\mathrm{R}_{90\%}$ values for the MBTA pipeline in data from O3a in each chirp mass bin [65].

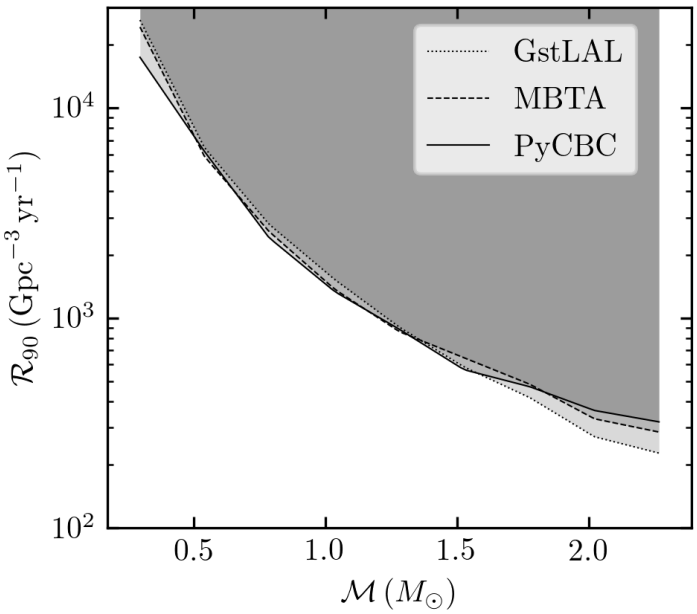

FIGURE 5.12: The constraint on the merger rate density of binaries with at least one SSM component as a function of the source frame chirp mass in data from the first half of the third observing run. The dotted, dashed, and solid lines correspond to the 90% confidence limits obtained by GstLAL, MBTA, and PyCBC, respectively [65].

5.3.2 Second Half of the Third Observing Run: O3b

For the second half of the third observing run, a new set of injections, common to all the involved pipelines, generated uniform in comoving volume, with parameters listed in Table. 5.4, was employed to estimate the sensitive volume-time. This set

Injections Distributions				
	Heaviest mass range $(M_\odot)$	Lightest mass range $(M_\odot)$	Spin range	Redshift range
SSM	$0.19 < m_1 < 11.0$	$0.19 < m_2 < 1.1$	$0.0 < \lvert\chi_{1,2}\rvert < 0.1$	$0.0 < z < 0.2$

TABLE 5.4: Parameters distributions used to generate injections for the evaluation of the sensitive volume-time during O3b [66].

of injections underwent a pruning process with the aim of reducing the file size, allowing for more efficient storage and analysis of the data. This process involved retaining only injections that were expected to have a relatively stronger signal, specifically those with an expected SNR > 4, defined assuming that the template waveform matched the signal perfectly and obtained as

$$\mathrm{SNR}_{\mathrm{expected,i}} = \frac{\sigma_i}{d_{eff,i}}\,, \tag{5.8}$$

where σ_i is the mass and spin-dependent measure of the detector sensitivity given by the SNR for a source at 1 Mpc distance, placed directly overhead the detector i and with zero inclination, and $d_{eff,i}$ is the effective distance defined in Eq. (4.1). As a result, the files used for the analysis contained a subset of the initial drawn set of injections, beneficial in terms of optimising computational resources, but with the

limitation of losing information about the total number of injections from the initial set, which was essential for the calculation of the sensitive-volume time and thus the merger rate. As a consequence, the pruned set of injections does not accurately represent the true initial distribution, and the computed efficiency based on this set is not fully representative of the actual efficiency of the pipeline. In order to accurately reproduce the actual initial distribution and to estimate the correct number of total generated injections in each chirp mass bin for computing the sensitive-volume time, a Monte Carlo toy was employed instead of relying on the code used to generate the initial set of injections. The primary motivations behind this choice were the time constraint, as the official code had a slow execution, and the statistical significance, as the Monte Carlo toy allowed for a larger sample size. The toy was generated by sampling from a distribution that matched the characteristics of the original distribution used for central generation, appropriately normalised to account for the total number of injections that were initially drawn. The validation process of this technique involved comparing the statistical properties and features of the distribution generated using the Monte Carlo toy with the distribution of a small sample generated using the original code, in which the pruning was deactivated. This comparison aimed at ensuring the consistency and similarity between the two distributions, thereby validating the use of the Monte Carlo toy as a reliable approximation of the original distribution. In practice, a small sample of injections was generated using the original code and compared to the Monte Carlo toy generation, which was normalised to the same number of samples. The generation process was carried out using parameters in the source frame, ensuring that $m_1 \geq m_2$, and that they fell within the parameter space of the template bank in the detector frame. Fig. 5.13 illustrates the comparisons between the distribution generated using the official code and the one generated using the Monte Carlo toy, showing the impact of the template bank cut on the resulting distributions.

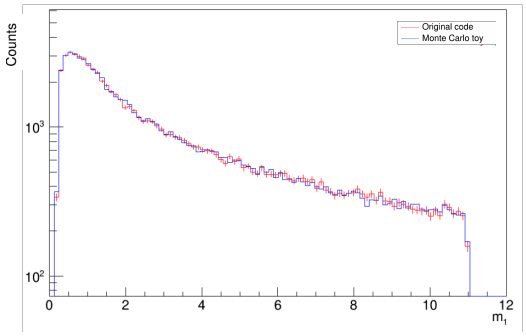

(A) Prior distribution of m_1.

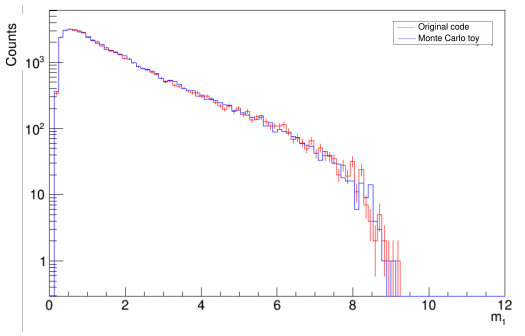

(B) Posterior distribution of m_1.

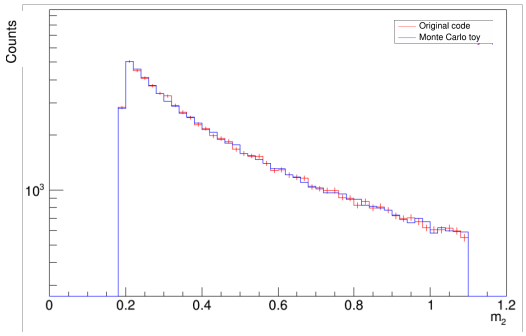

(C) Prior distribution of m_2.

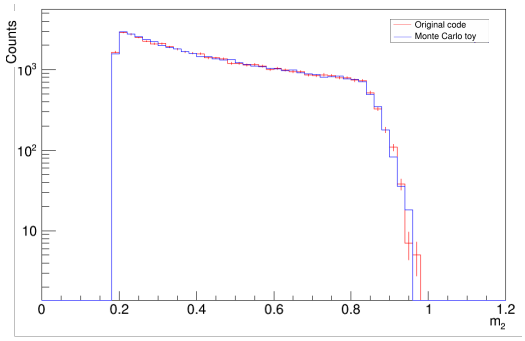

(D) Posterior distribution of m_2.

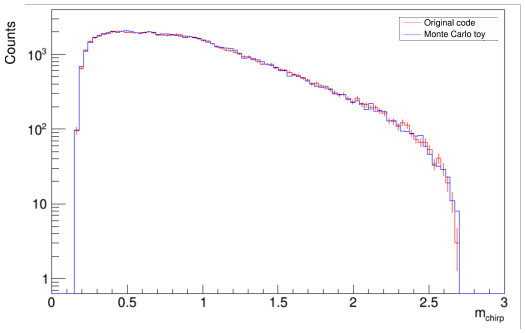

(E) Prior distribution of m_{chirp}.

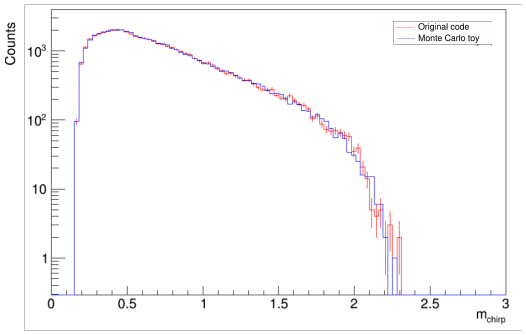

(F) Posterior distribution of m_{chirp}.

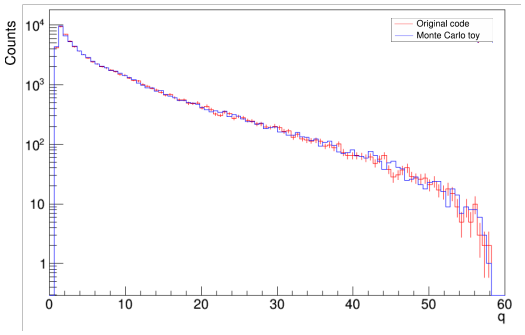

(G) Prior distribution of mass ratio q.

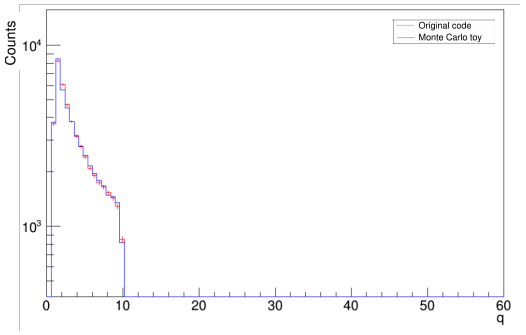

(H) Posterior distribution of mass ratio q.

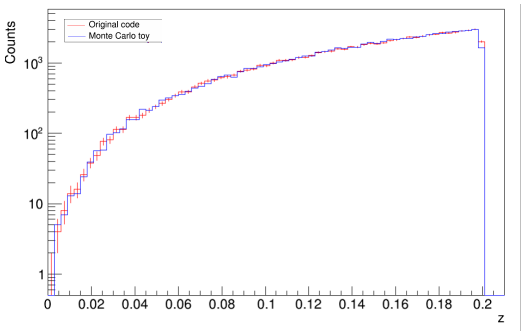

(I) Prior distribution of redshift z.

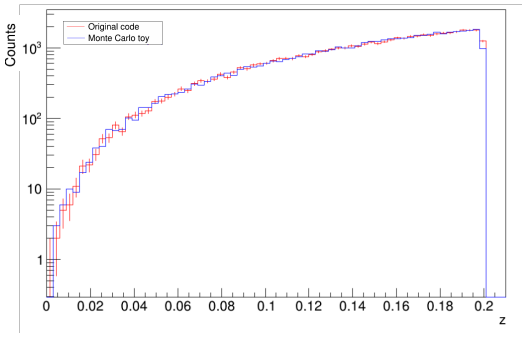

(J) Posterior distribution of redshift z.

FIGURE 5.13: Prior (left plots) and posterior (right plots) distributions of injections after the template bank cut, generated with the original code (red curves) and with the Monte carlo toy (blue curves) with the same normalization.

The plots highlight that the template bank cut has a significant influence on the distributions of m_1, m_2, and m_{chirp} due to the differences between source frame and detector frame masses, as

$$m_{source} = \frac{m_{detector}}{(1+z)} \,. \tag{5.9}$$

Additionally, the template bank cut has an effect on the distribution of mass ratio q, which was truncated at a value of 10.0, conforming with the template bank criteria; while the distribution of redshift z remains unaffected by the template bank selection cut. To evaluate the efficiency of the pruning process, the ratio between the total number of injections that underwent pruning and the total number of injections before pruning was computed as function of the chirp mass. This estimation was conducted using the original set of injections, which provided the total number of injections drawn, enabling the estimation of the overall efficiency of the pruning process, and the Monte Carlo toy set, that allowed for the estimation of the pruning

process efficiency for each chirp mass bin. The efficiency was found to be approximately 4% across the entire parameter space with both estimations, and is displayed in Fig. 5.14 as a function of the chirp mass. As expected, the pruning process demon-

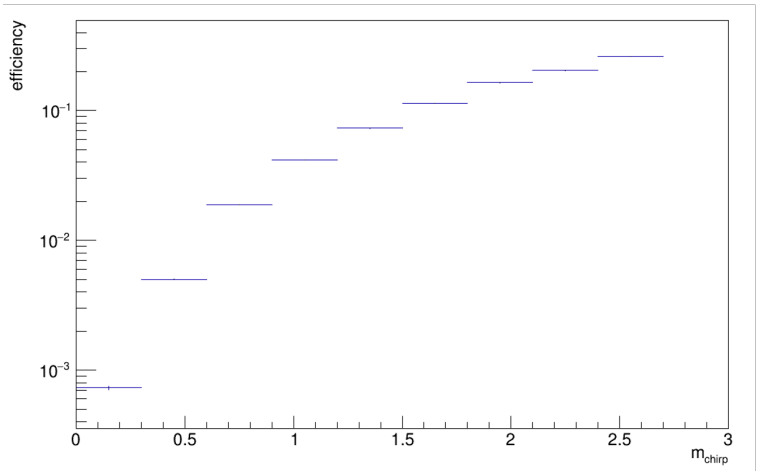

FIGURE 5.14: Efficiency of the pruning process estimated with the Monte Carlo toy, as a function of the chirp mass m_{chirp} of the binary system. Error bars are shown but barely visible due to the high statistics of the sample.

strates greater efficiency in rejecting low-mass injections compared to high-mass injections, as the former typically have lower expected SNR values than the latter.

The pruning and the template bank selection cuts have also a strong impact on the distribution of injections in comoving volume, leading to a global non-uniform distribution, as shown in Fig. 5.15, but also to a non-uniform distribution within each chirp mass bin, as shown in Fig. 5.16. Specifically, the pruning process has a greater

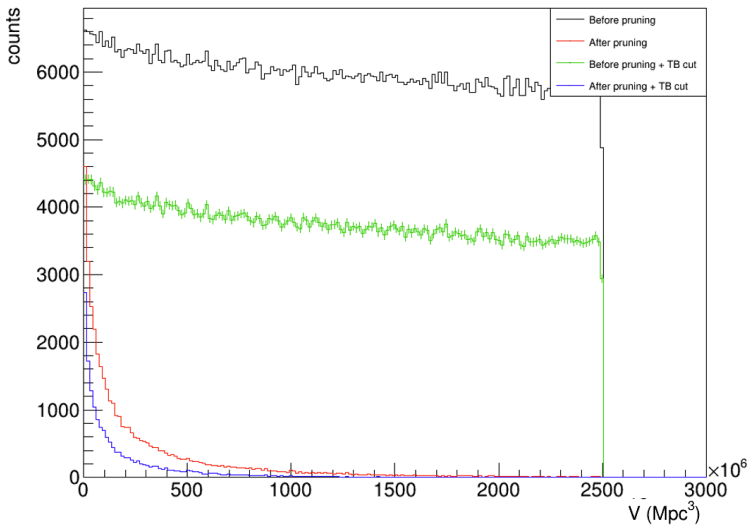

FIGURE 5.15: Impact of the pruning process and the template bank selection cut on the distribution of comoving volume of injections generated with the Monte Carlo toy. The prior distribution of comoving volume (black curves), the prior distribution after the template bank cut (green curves), the posterior distribution after the pruning process (red curves) and the posterior distribution after the template bank cut (blue curves).

impact on the low chirp mass bins, as observed in the study of its efficiency shown

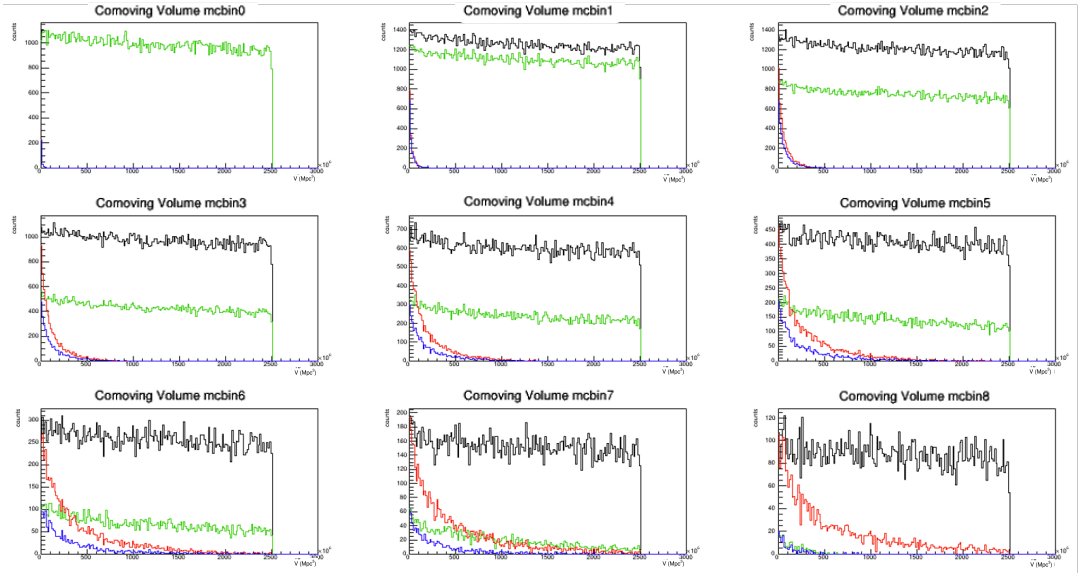

FIGURE 5.16: Impact of the pruning process and the template bank selection cut on the distribution of comoving volume of injections generated with the Monte Carlo toy, within each of the 9 chirp mass bins used to compute $\langle VT \rangle$. The same colorcode of Fig. 5.15 is used to indicate the prior distribution of comoving volume (black curves), the prior distribution after the template bank cut (green curves), the posterior distribution after the pruning process (red curves) and the posterior distribution after the template bank cut (blue curves).

in Fig. 5.14. On the other hand, the template bank cut has a more pronounced effect on the high chirp mass bins. Fig. 5.17 displays the redshift distribution within each of the 9 chirp mass bins employed to compute the $\langle VT \rangle$.

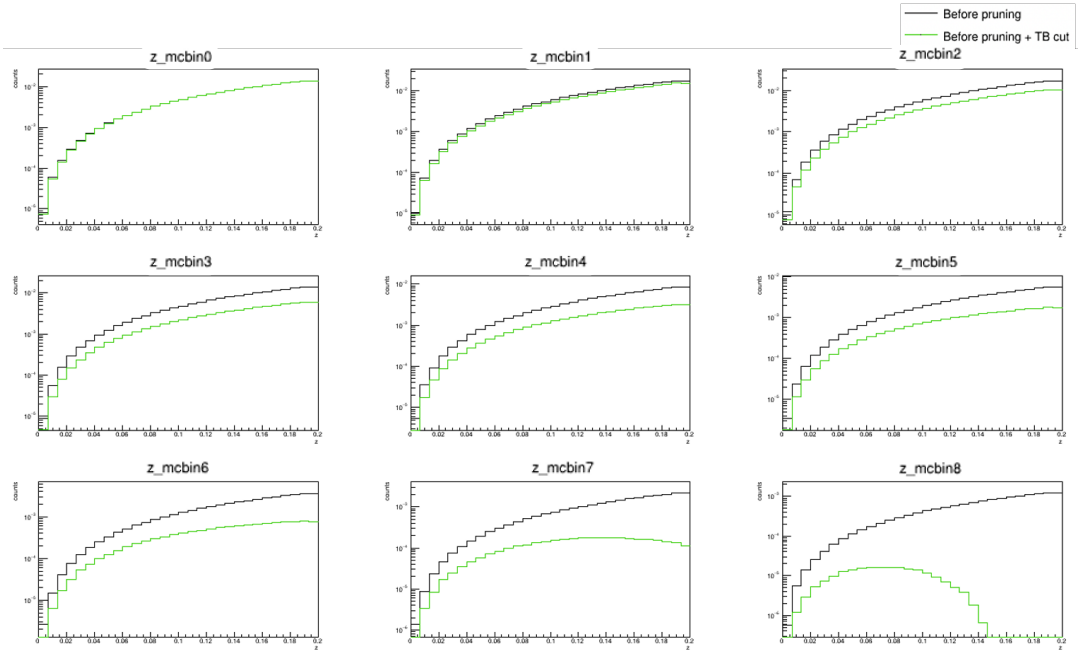

FIGURE 5.17: Impact of the pruning process and the template bank selection cut on the distribution of redshift of injections within each of the 9 chirp mass bins used to compute $\langle VT \rangle$. The black curves represent the prior distributions, while the green curves represent the posterior distributions after applying the pruning process.

It is evident that the initial assumption of generating a flat distribution in comoving volume up to a redshift of 0.2 is no longer valid due to the effects of the template bank selection cut, which have led to deviations from the initial distribution, resulting in non-uniform redshift distributions especially in the high chirp mass bins. To ensure the comparability of injection distributions between O3a and O3b, the template bank selection cut was not applied. This decision was also motivated by the fact that the pipelines have sensitivities beyond its boundaries, so that applying the cut would result in the loss of valuable information contained in regions beyond the template bank limits. By omitting the template bank cut, the explored range of chirp masses was expanded. Furthermore, in order to ensure waveform reliability, injections with a mass ratio greater than 20.0 were excluded. This choice was motivated by concerns regarding the accuracy and reliability of the injections waveform at higher mass ratios. By excluding such injections, the analysis focused on systems where the waveform model is expected to provide reliable predictions. The $\langle VT \rangle$ for each chirp mass bin is then computed as

$$\langle VT \rangle_i = \frac{N_i^{det}}{N_i^{gen}} V_{max}(z = 0.2) T \,, \tag{5.10}$$

where N_i^{det} and N_i^{gen} are the total number of detected and generated injections in the i-th chirp mass bin, $V_{max}(z = 0.2)$ is the comoving volume corresponding to the farthest injected injection, located at redshift $z = 0.2$, and T the analysed time. In this analysis, the FAR threshold for detection was determined based on the most significant candidate in O3 for each pipeline, in accordance with the loudest event statistic formalism [114]. Specifically, the chosen FAR thresholds were 0.20 yr^{-1} for GstLAL, 1.40 yr^{-1} for MBTA, and 0.14 yr^{-1} for PyCBC. The associated error is then computed at 90% confidence interval assuming a binomial distribution as following

$$\Delta\langle VT \rangle_i = 1.645 \cdot \sqrt{\frac{\epsilon_i \cdot (1 - \epsilon_i)}{N_i^{gen}}} \cdot V_{max}(z = 0.2) \cdot T \,, \tag{5.11}$$

where $\epsilon_i = N_i^{det} / N_i^{gen}$ is the efficiency in the i-th chirp mass bin. To ensure methodological consistency, the same injection set and technique were applied to the first half of the third observing run. The results of this analysis were compared to the previously obtained $\langle VT \rangle$ values in data from O3a, and Fig. 5.18 illustrates the obtained outcomes. The consistency of the obtained results in the shared chirp mass bins validates the methodology used for the analysis. While MBTA and PyCBC used the full set of injections for their results, it should be emphasized that GstLAL analysed only a subset of the injections, resulting in larger uncertainties in the estimated $\langle VT \rangle$ values for the latter, in comparison with the other pipelines. The presence of an additional bin at high chirp masses in the comparison results is attributed to the expanded parameter space, which led to the identification of signals at higher chirp masses. The larger errors associated with the $\langle VT \rangle$ values in the last chirp mass bin can be attributed to the lower statistic in that bin. This is mainly because the injections in this bin lie outside the parameter space covered by the template bank and, as a result, the number of injections available for analysis is relatively smaller, leading to increased statistical uncertainties in the $\langle VT \rangle$ estimation, as well as a lower efficiency in recovering signals.

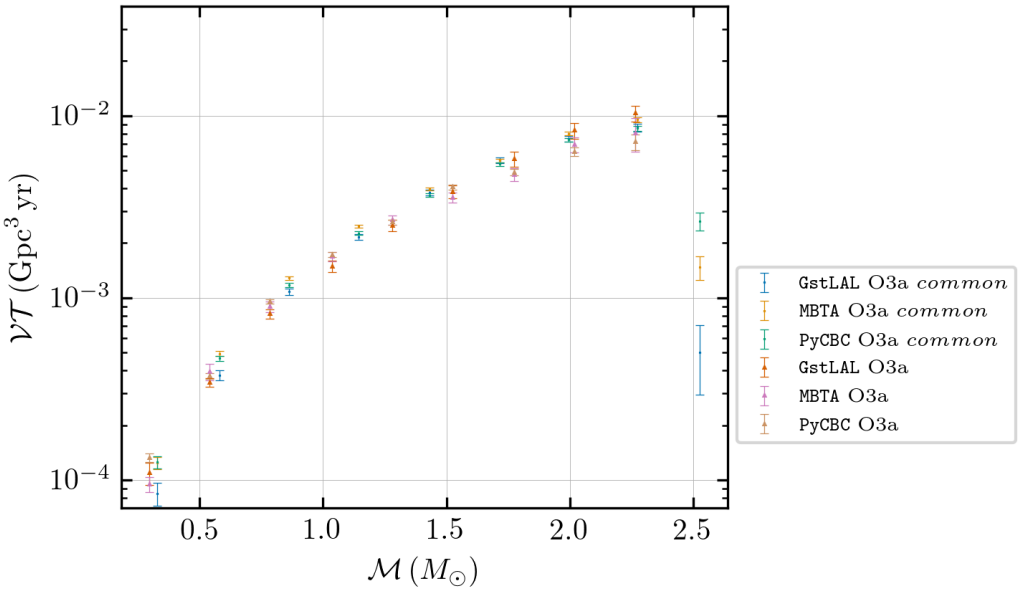

FIGURE 5.18: Comparison between values obtained with the injections set used in the O3a SSM publication [65] (red, pink and brown for GstLAL, MBTA and PyCBC respectively) and values obtained with the set of common injections in O3a (blue, gold and green for GstLAL, MBTA and PyCBC respectively). The presence of an extra bin at higher chirp masses is linked to the expanded parameter range, causing injections within this bin to fall beyond the template bank's coverage and consequently reducing signal recovery efficiency.

The consistency of the obtained results in the shared chirp mass bins allows for an overall estimation of the $\langle VT \rangle$ values by using a consistent set of injections. In Fig. 5.19 is shown the sensitive volume-time obtained in data from O3, whose values are reported in Table 5.5 along with the $\langle VT \rangle$ obtained from the analysis of O3a data with the set of common injections. Fig. 5.19 demonstrates that the uncertain-

MBTA Values of $\langle VT \rangle$ and $R_{90\%}$ in O3a, O3b and O3 with the set of common injections					
	O3a		O3		
m_{chirp} range ($M_\odot$)	$\langle VT \rangle$ (Gpc^3 yr)	$\Delta\langle VT \rangle$ (Gpc^3 yr)	$\langle VT \rangle$ (Gpc^3 yr)	$\Delta\langle VT \rangle$ (Gpc^3 yr)	$R_{90\%}$ (Gpc^{-3} yr^{-1})
[0.16, 0.44]	$1.25 \cdot 10^{-04}$	$9.50 \cdot 10^{-06}$	$2.47 \cdot 10^{-04}$	$1.40 \cdot 10^{-05}$	$9.31 \cdot 10^{+03}$
[0.44, 0.73]	$4.94 \cdot 10^{-04}$	$1.63 \cdot 10^{-05}$	$9.69 \cdot 10^{-04}$	$2.30 \cdot 10^{-05}$	$2.34 \cdot 10^{+03}$
[0.73, 1.01]	$1.28 \cdot 10^{-03}$	$3.10 \cdot 10^{-05}$	$2.52 \cdot 10^{-03}$	$4.40 \cdot 10^{-05}$	$9.12 \cdot 10^{+02}$
[1.01, 1.30]	$2.47 \cdot 10^{-03}$	$5.20 \cdot 10^{-05}$	$4.81 \cdot 10^{-03}$	$7.30 \cdot 10^{-05}$	$4.78 \cdot 10^{+02}$
[1.30, 1.58]	$3.96 \cdot 10^{-03}$	$8.40 \cdot 10^{-05}$	$7.79 \cdot 10^{-03}$	$1.17 \cdot 10^{-04}$	$2.95 \cdot 10^{+02}$
[1.58, 1.87]	$5.68 \cdot 10^{-03}$	$1.19 \cdot 10^{-04}$	$1.11 \cdot 10^{-02}$	$1.67 \cdot 10^{-04}$	$2.06 \cdot 10^{+02}$
[1.87, 2.15]	$7.98 \cdot 10^{-03}$	$1.85 \cdot 10^{-04}$	$1.58 \cdot 10^{-02}$	$2.61 \cdot 10^{-04}$	$1.45 \cdot 10^{+02}$
[2.15, 2.44]	$9.52 \cdot 10^{-03}$	$2.83 \cdot 10^{-04}$	$1.86 \cdot 10^{-02}$	$3.96 \cdot 10^{-04}$	$1.24 \cdot 10^{+02}$
[2.44, 2.72]	$1.48 \cdot 10^{-03}$	$2.18 \cdot 10^{-04}$	$2.87 \cdot 10^{-03}$	$3.05 \cdot 10^{-04}$	$8.03 \cdot 10^{+02}$

TABLE 5.5: Sensitive volume-time and merger rate at 90% credible interval values for the MBTA pipeline during O3a and O3 for each chirp mass bin.

ties in the estimated $\langle VT \rangle$ values are more pronounced for GstLAL when compared to the other pipelines. This discrepancy is again attributed to the fact that GstLAL analysed a subset of the actual injections set, leading to a smaller sample size and

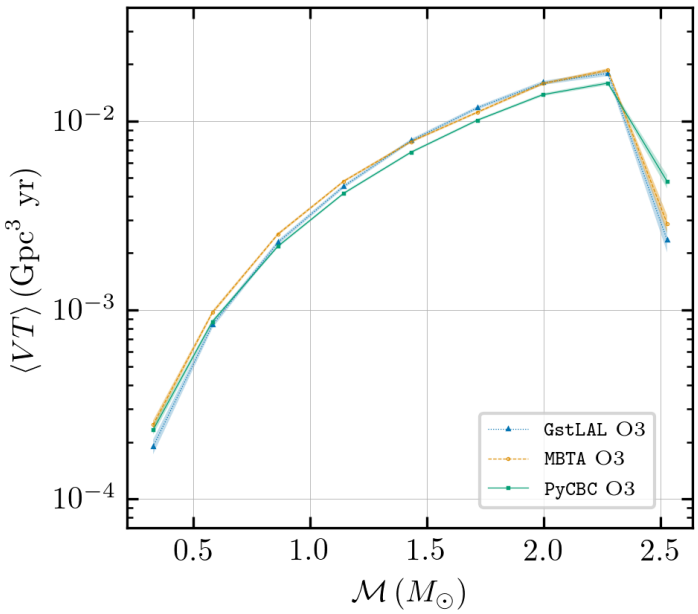

FIGURE 5.19: Sensitive volume–time as a function of the source frame chirp mass in data from O3, obtained through the analysis of the set of common injections (blue triangles with dotted lines, orange circles with dashed lines, and green squares with continuous lines correspond to GstLAL, MBTA and PyCBC respectively). The statistical errors are evaluated at 90% confidence interval, following Eq. 5.11 and represented by the shaded areas. The presence of an extra bin at higher chirp masses is linked to the expanded parameter range, causing injections within this bin to fall beyond the template bank's coverage and consequently reducing signal recovery efficiency.

consequently larger uncertainties in the $\langle VT \rangle$ estimates. By comparing the $R_{90\%}$ values obtained using the set of common injections throughout the entire O3 with the $R_{90\%}$ values obtained from previous observing runs, O1 [42] and O2 [41], it becomes evident that there has been an improvement in the precision of the merger rate measurement. This improvement is attributed to the broader parameter space that was explored, and the increased observing time during the third observing run. Overall, these factors combine to place strictest upper limits on the merger rate measurement, shown in Fig. 5.20, compared to previous observing runs. In Fig. 5.21 the upper limits on the binary merger rate in the source $m_1 - m_2$ plane are shown. The presence of an empty bin at high m_1 and low m_2 values is the result of the mass ratio cut applied during the analysis, motivated by considerations related to the validity of the waveform model used in the injections generation.

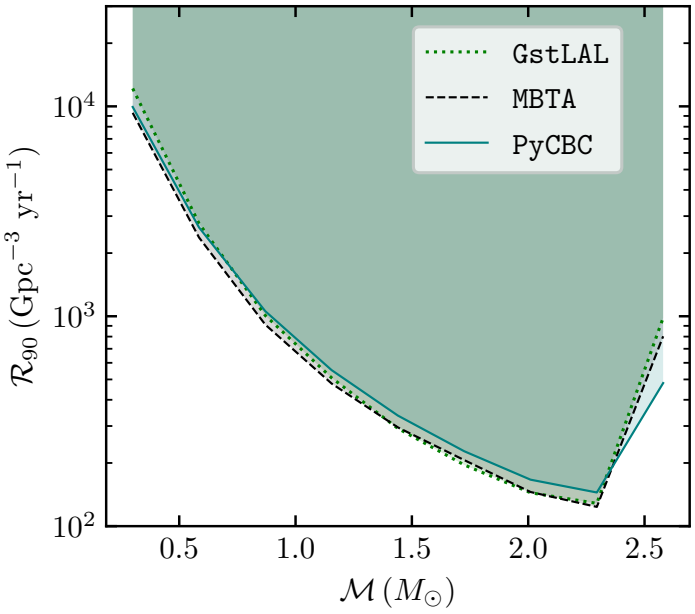

FIGURE 5.20: Merger rate limits as function of the source frame chirp mass of the binary system, in data from the full O3. The dotted light green, dashed black and solid dark green lines represent the 90% confidence limits obtained by GstLAL, MBTA and PyCBC, respectively [66].

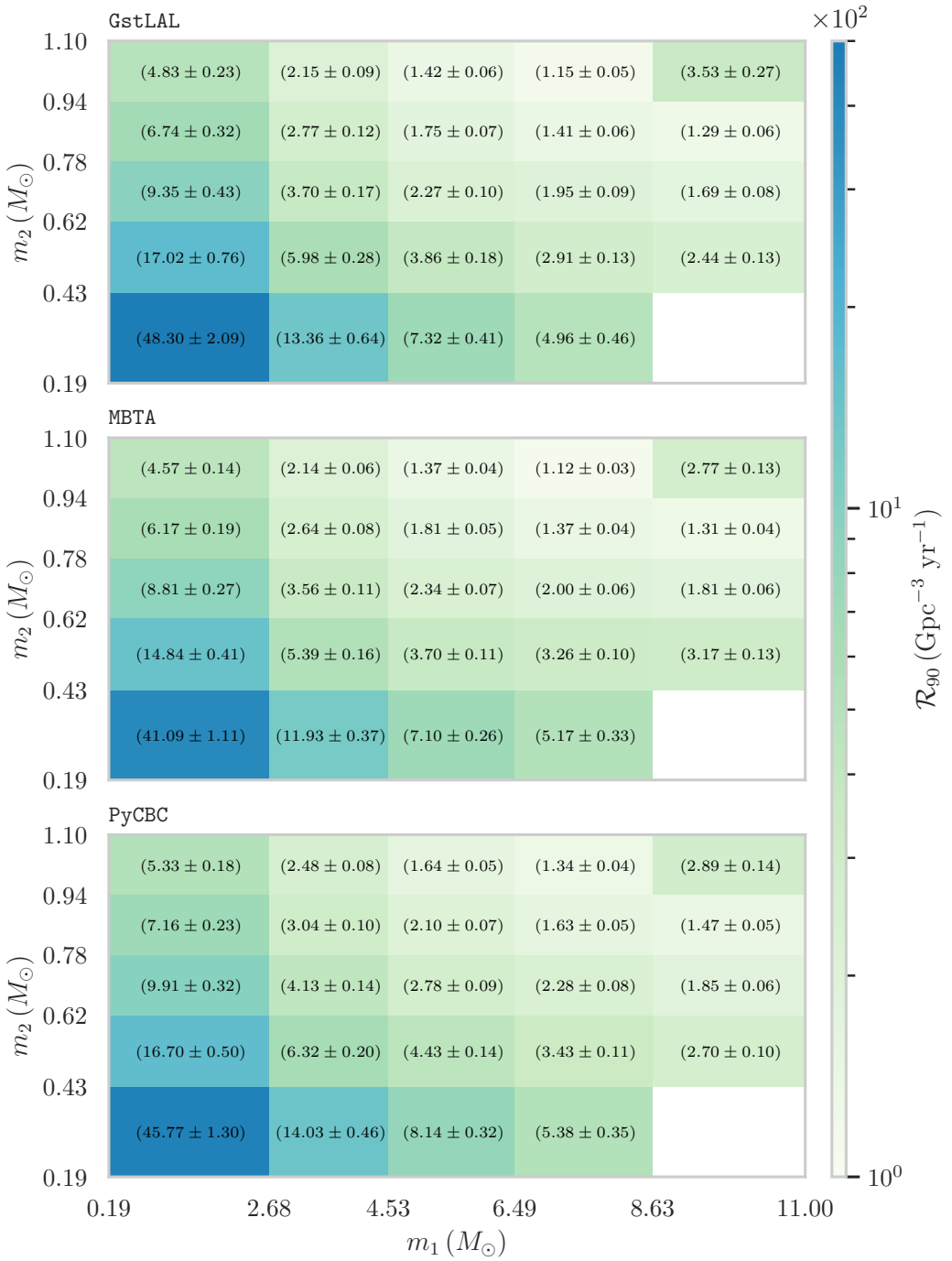

FIGURE 5.21: Merger rate limits in the source $m_1 - m_2$ plane in data from the full O3 for the GstLAL (top panel), MBTA (middle panel) and PyCBC (bottom panel) pipelines [66]. The colorbar represents the merger rate at 90% confidence interval, corresponding to the values in the bins reported with associated errors estimated with Eq. 5.11.

5.4 Constraints on Dark Matter Models

The upper limits on merger rates are used for constraining models that predict an observable population of binaries with at least one SSM component. In this study, the focus was on examining two specific models as potential sources of SSM BHs. The first model explored was a phenomenological model for primordial black holes (PBHs), discussed in Section 1.4.2.1. The second model investigated was a dissipative DM model, introduced in Section 1.4.2.2. The resulting constraints are parametrised in terms of the maximal fraction f of the DM that can be composed by compact objects allowed by each model. The following section presents the constraints derived from the analysis of the complete O3 data set, using the injections set outlined in Table 5.4.

5.4.1 Primordial Black Holes

By using the previously derived merger rate upper limits, it is possible to derive an upper limit on the fraction of DM composed of PBH, denoted as $f_{PBH} = \Omega_{PBH}/\Omega_{DM}$. In this analysis, it is assumed that the binary system consists of two objects with equal masses, even though the previous merger rate limits were obtained for both equal and unequal mass binaries, with component masses in the range $[0.2, 1.0]\ M_\odot$. It is important to emphasise that the interpretation presented here is highly dependent on the underlying model. The estimation of event rates and the probability of binary formation are influenced by factors such as the clustering of PBHs and cluster dynamics, which are active areas of research. In the analysis performed using data from O1, O2, and O3a, a single initial monochromatic distribution of PBHs in the early Universe was assumed. However, in the O3 analysis, theoretical merger rates are computed separately for early binaries, using Eq. (1.31), and for late binaries, determined using Eq. (1.32). A significant difference in the O3 analysis is the inclusion of a rate suppression factor, denoted as f_{sup}, which accounts for PBH binary disruptions caused by various factors, including Poisson fluctuations in the initial PBH separation, matter inhomogeneities, and nearby PBHs. The value of f_{sup} used in the analysis is $2.3 \times 10^{-3} f_{PBH}^{-0.65}$ [66, 233]. Fig. 5.22 shows how much the omission of such factor leads to an overestimation of the sensitivity of previous results. The plot shows the upper limits on f_{PBH} for early and late PBH binaries, illustrating the important variations in the PBH limits obtained for different binary formation scenarios. The previous searches did not completely exclude the scenario where the entire DM is composed of PBHs with the same mass. However, the results obtained from the O3 analysis strongly disfavour this scenario, particularly for early binaries with component masses up to 1.0 $M_\odot$. For these binaries, the upper limit on f_{PBH} is less than 0.6 at around 0.3 $M_\odot$, indicating a significant constraint on the fraction of DM that can be composed by PBHs. Furthermore, at masses of 1.0 $M_\odot$, the upper limit on f_{PBH} is even more stringent, with f_{PBH} being less than 0.09. These results indicate that the scenario of DM entirely composed of PBHs with the same mass is strongly disfavoured in the mass range considered for early binaries. On the other hand, for late binaries, the constraints on f_{PBH} are less stringent, as the upper limits do not significantly restrict f_{PBH} to be lower than one.

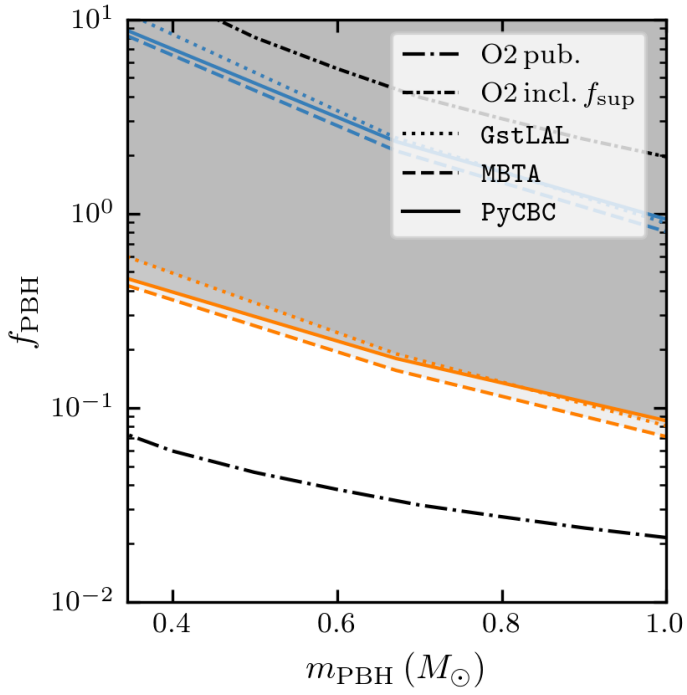

FIGURE 5.22: Constraints on DM fraction of PBHs for a monochromatic mass function and assuming the merger rates for early PBH binaries [233] (orange) and late PBH binaries [303] (blue) for GstLAL, MBTA and PyCBC (dotted, dashed and solid curves). Shown in black are results for SSM searches in O2 with and without the rate suppression factor f_{sup} [66]. The realisation of this plot has been made by computing the m_{PBH} for each chirp mass bin in Fig. 5.20 as $m_{BH} = 2^{1/5} \cdot m_{chirp}$, followed by the adjustment of the x-axis bounds accordingly.

5.4.2 Dark Black Holes

The fraction of dark matter ending in dark black holes (DBHs), denoted as $f_{DBH} = \Omega_{DBH}/\Omega_{DM}$, can be derived from the obtained merger rates using Eq. (1.34). In contrast to the case of primordial black holes (PBHs), this study considers a power-law distribution for the masses of the black holes, with an unknown lower mass cutoff. To determine the upper limits on f_{DBH}, the analysis incorporates marginalisation over the parameters of the prior mass distribution. The resulting constraints are presented as a function of the lower limit of the DBH mass distribution, denoted as M_{min}^{DBH}, in Fig. 5.23. During O3a the most stringent constraint obtained was $f_{DBH} < 0.003\%$, while in O3 the strictest limit achieved across the three pipelines is $f_{DBH} < 0.0012\% - 0.0014\%$ at a mass of 1.0 $M_\odot$. Meaningful constraints cannot be set for $M < 2 \cdot 10^{-2} M_\odot$ due to the fact that BHs with masses below this threshold would not be detectable with the current template bank and sensitivity. Moreover, the obtained results allow to infer a range for the masses of heavy dark fermions, denoted as m_X, that are probed by the search. This range is derived from the Chandrasekhar limit of the fermionic particle progenitors of DBHs [334] and is determined to be $1.1\ \mathrm{GeV/c^2} < m_X < 8.9\ \mathrm{GeV/c^2}$ [66].

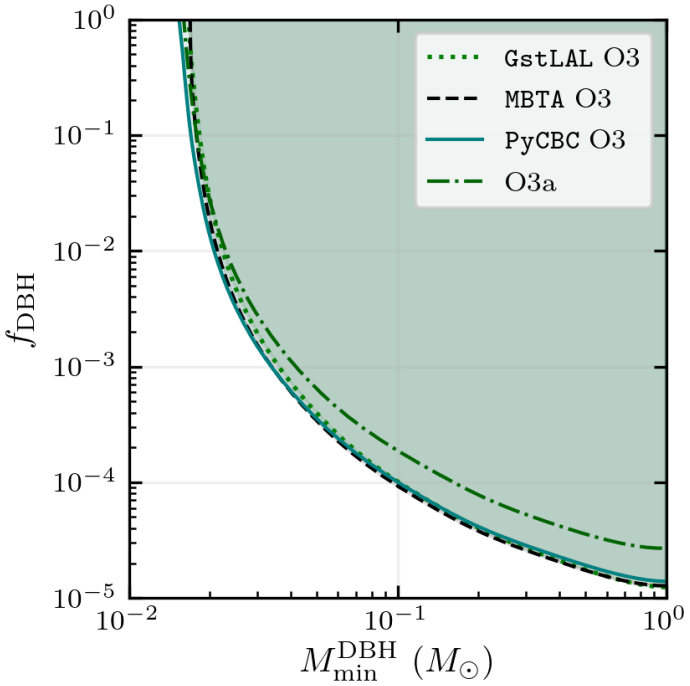

FIGURE 5.23: Constraints on DM fraction of DBHs f_{DBH} as a function of the lower limit of the DBH mass distribution M_{min}^{DBH} from O3 data for the 3 search pipelines: GstLAL (dotted), MBTA (dashed) and PyCBC (solid) [66]. Constraints from the search for SSM compact objects in O3a data are shown for comparison [65].

5.5 Phenomenological Studies

Considering that the SSM analysis has traditionally been conducted offline, with the aim of expanding its applicability to a low-latency search, we investigated the prospects of having an electromagnetic counterpart resulting from these mergers. Our findings and insights prompted the development of a low-latency search for SSM mergers, which is currently active for the MBTA pipeline in the fourth observing run (O4). The following section presents two preliminary studies conducted to address the possibility of having an electromagnetic counterpart in the scenario of a SSM BH and a NS, as well as the potential outcomes in the case of a SSM NS merging with a BH.

5.5.1 Multi-messenger with SSM Black Holes

This section focusses on binary systems composed of a SSM BH and a standard NS. A fundamental question that needs to be addressed is whether a NS could undergo tidal disruption before merging with a SSM BH, thus opening the possibility of powering an electromagnetic counterpart. To address this question it is possible to estimate the mass remaining outside the BH at late times, based on the comparison between the separation at which tidal disruption of the NS occurs d_{tidal}, with the radius of the ISCO r_{ISCO} of a BH with mass under 1.0 $M_\odot$. Intuitively, if $d_{tidal} \leq r_{ISCO}$, the NS plunges directly into the BH and no mass remains outside after the merger. On the other hand, if $d_{tidal} > r_{ISCO}$, the NS is tidally disrupted and the material that remains outside could form an accretion disk. The d_{tidal} can be estimated within the framework of Newtonian theory by balancing the gravitational acceleration caused

by the NS with the tidal acceleration due to the BH as [200]

$$\frac{m_{NS}}{r_{NS}^2} \approx \frac{3m_{BH}}{d_{tidal}^3} r_{NS} \,, \tag{5.12}$$

$$d_{tidal} \approx r_{NS} \left(\frac{3m_{BH}}{m_{NS}} \right)^{1/3} \,, \tag{5.13}$$

where $G = c = 1$, m_{NS} and m_{BH} are the masses of the two compact objects, and r_{NS} represents the radius of the NS. On the other hand, the radius of the ISCO is computed as [104]

$$Z_1 = 1 + (1 - \chi_{BH}^2)^{1/3} \left[(1 + \chi_{BH})^{1/3} + (1 - \chi_{BH})^{1/3} \right] \,, \tag{5.14}$$

$$Z_2 = \sqrt{3\chi_{BH}^2 + Z_1^2} \,, \tag{5.15}$$

$$\frac{r_{ISCO}}{m_{BH}} = 3 + Z_2 - sign(\chi_{BH}) \sqrt{(3 - Z_1)(3 + Z_1 + 2Z_2)} \,. \tag{5.16}$$

From the above equations it is possible to obtain the ratio between d_{tidal} and r_{ISCO} as

$$\frac{d_{tidal}}{r_{ISCO}} = 1.4 \cdot q^{-2/3} \cdot C^{-1} \left[3 + Z_2 - sign(\chi_{BH}) \sqrt{(3 - Z_1)(3 + Z_1 + 2Z_2)} \right] \,, \tag{5.17}$$

where the mass ratio $q = m_{BH}/m_{NS}$ and the NS compactness $C = m_{NS}/r_{NS}$. In Fig. 5.24 is shown the relationship obtained between the ratio of d_{tidal} and r_{ISCO} and the changes in mass ratio q and compactness C, for different values of the dimensionless BH spin χ_{BH}. By analysing the plot, several conclusions can be drawn. Firstly,

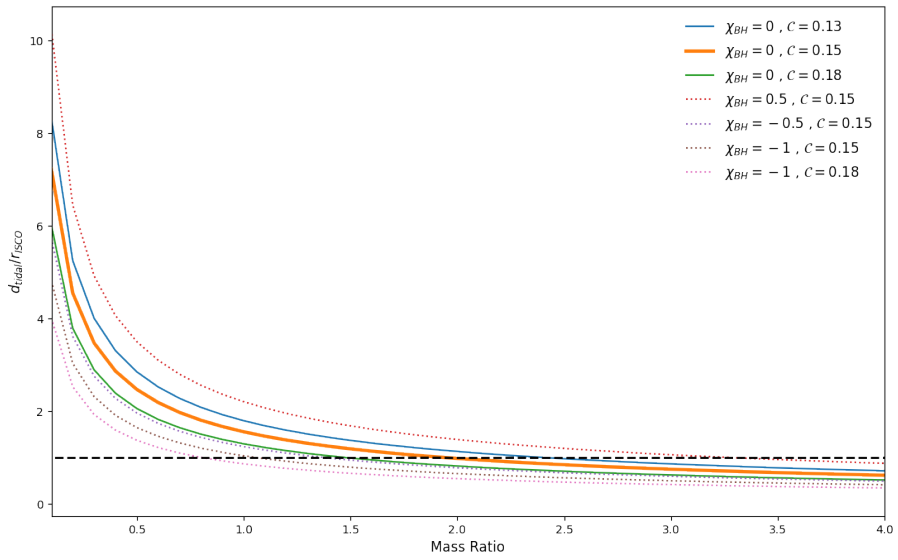

FIGURE 5.24: Trend of the d_{tidal}/r_{ISCO} as function of the mass ratio for different combinations of the dimensionless spin χ_{BH} and compactness C. The dashed black line represents $d_{tidal} = r_{ISCO}$, the solid lines represent the trend for different values of C and $\chi_{BH} = 0$, while the dotted curves represent the trend for $\chi_{BH} \neq 0$.

increasing the compactness of the NS, while keeping q constant and χ_{BH} at zero, causes d_{tidal} and r_{ISCO} to approach each other. When considering a non-zero aligned χ_{BH} with equal mass ratios and compactness, the ratio between d_{tidal} and r_{ISCO} increases. This implies that it becomes easier to disrupt the NS before it reaches the r_{ISCO}. On the contrary, when considering anti-aligned spins for equal mass ratios and compactness, the ratio decreases. This suggests that the likelihood of tidal disruption occurring before reaching r_{ISCO} diminishes. Within the region of interest where $q \leq 1$, it is observed that d_{tidal} is systematically greater than r_{ISCO} for the considered range of compactness values, validating the notion that a the merger of a NS with a SSM BH could potentially form an accretion disk, and potentially have an electromagnetic counterpart. It is important to stress that the approximation employed for this test is considered rough, particularly in the context of a small BH merging with a NS more massive that the former. Nevertheless, it provides a qualitative guidance that support the utility of having an online search and reinforces the need for numerical relativity simulations to achieve a more accurate study. Once determined the properties of the surrounding environment along with the remaining matter outside the BH, it will be possible to accurately compute each component of the electromagnetic emission.

5.5.2 SSM Neutron Stars

Traditionally the SSM search has been thought to search for SSM BH. Motivated by the recent observation of a NS with a mass compatible with being below the solar threshold [177], that sparked interest in investigating the potential outcomes of the merger between a super-solar BH and a sub-solar NS, in this section is presented an attempt to establish to what extent the results of SSM LVK searches can constrain systems containing SSM neutron stars. SSM NS can have large tidal deformabilities and large radii. The first question we addressed is if we can still consider such objects as compact. In this sense, a test has been performed by adopting a simplistic approach, computing the distance between the two compact objects for each frequency f corresponding to the cumulation of the 10%, 50%, 70%, 90% and 99% of the total SNR between 45 Hz and 1000 Hz as [51]

$$d = \sqrt[3]{\frac{G(m_{NS} + m_{BH})}{\pi^4 f^2}}\,, \tag{5.18}$$

and comparing it to the distance between the objects at which a test particle on the NS surface is in equilibrium, to the NS radius computed with the SLy4 EOS [178, 289] and to the point where the surface of the NS intersects with the radius of the BH ISCO. This test has been performed neglecting the components spins, for masses of the NS in the range $[0.1, 1.0]\ M_\odot$ and for BH masses of $[3.0, 5.0, 10.0]\ M_\odot$. Assuming the possibility of having such mergers, the plot in Fig. 5.25a illustrates that for systems with $m_{BH} = 3.0\ M_\odot$, there exist certain m_{NS} where the separation distance between the two compact objects allows for the recovery of over 90% of the SNR before reaching a critical distance that disrupts the equilibrium of matter on the NS surface. A similar trend is observed for binary systems with $m_{BH} = 5.0\ M_\odot$ (shown in Fig. 5.25b). As the m_{BH} increases, the minimum separation distance at which a test particle on the NS surface remains in equilibrium also increases, consequently reducing the maximum percentage of SNR that can be recovered compared to the scenario where the NS undergoes circular orbits up to the merger. Fig. 5.25c shows that orbital separations between the objects corresponding to the recovery of

90% of the SNR are nonphysical as always smaller than the intersection between the radius of the ISCO and the radius of the NS. Additionally, as an example, for $m_{BH} = 10.0\ M_{\odot}$, only 70% of the SNR can be recovered over the whole mass range considered in the LVK search for the hypothetical SSM NS.

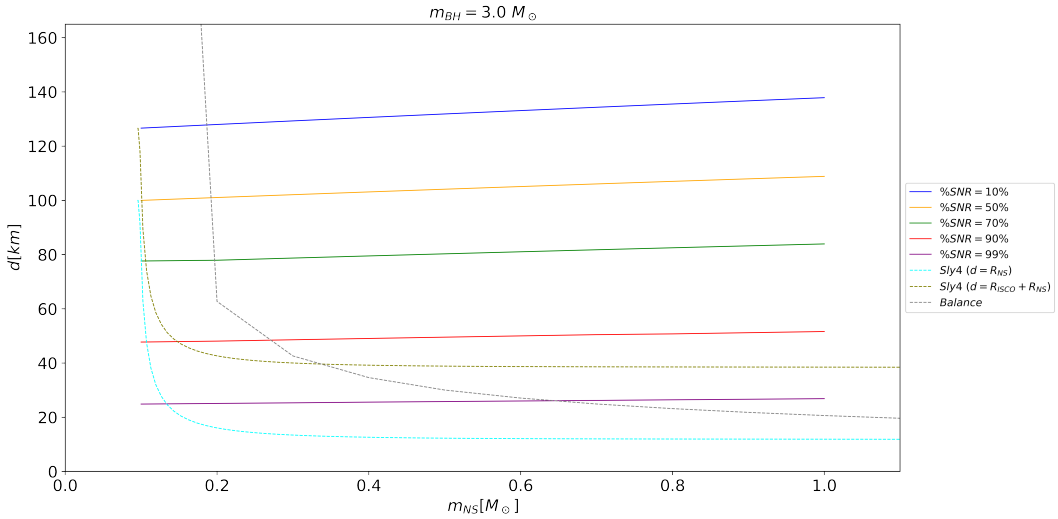

(A) Comparison with $m_{BH} = 3.0\ M_{\odot}$.

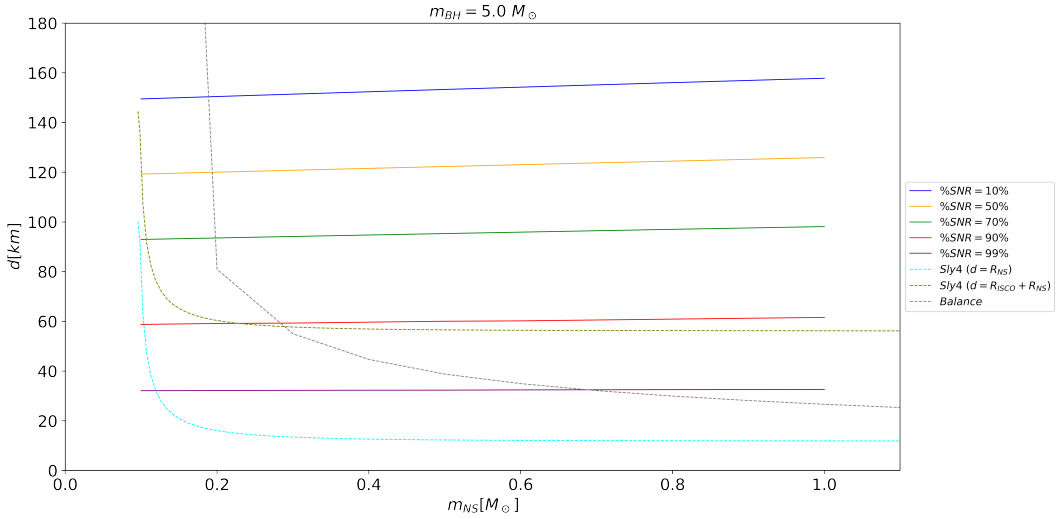

(B) Comparison with $m_{BH} = 5.0\ M_{\odot}$.

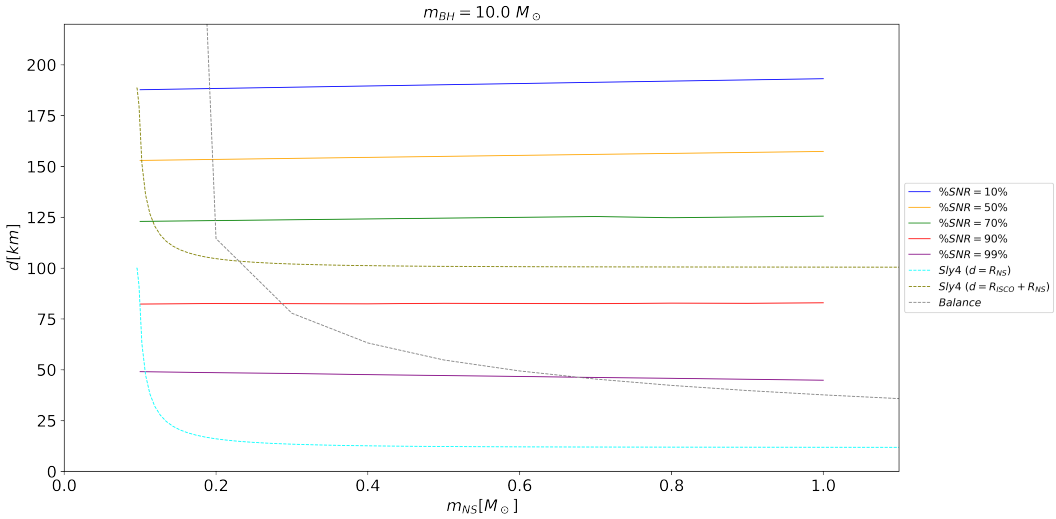

(C) Comparison with $m_{BH} = 10.0\ M_\odot$.

FIGURE 5.25: Comparison of the separation distance between a BH with m_{BH} and a NS with m_{NS} when recovering the 10% (blue solid curve), 50% (orange solid curve), 70% (green solid curve) 90% (red solid curve) and 99% (purple solid curve) the NS radius according to the SLy4 EOS (light blue dotted curve), the distance at which a test particle on the surface of the NS is in equilibrium (grey dotter curve) and the distance corresponding to the sum of the ISCO of the BH and the radius of the NS (olive dotted curve) for $m_{BH} = 3.0\ M_\odot$ (top plot), $m_{BH} = 5.0\ M_\odot$ (middle plot) and $m_{BH} = 10.0\ M_\odot$ (bottom plots).

This preliminary test shows that, assuming the existence of such binary systems, under certain conditions, the system could emit the largest part of the detectable signal during the inspiral phase before any disruption of the SSM NS occurs, depending on the mass of the companion BH.

An additional aspect investigated in this study was the loss in SNR resulting from the omission of NS tidal deformability on the waveforms for such systems. To understand the impact of neglecting the NS tidal deformability, a set of injections with masses in $[0.2, 1.0]\ M_\odot$, $m_{chirp} \in [0.18, 1.0]\ M_\odot$ and zero spins was matched-filtered using dimensionless tidal deformability values of 100 000 for both objects, as well as without considering any tidal deformability. The matched filtering is conducted using two waveform models: IMRPhenomPv2_NRTidal [174], which incorporates tidal deformability, and IMRPhenomPv2 [216], which does not consider tidal deformability. The corresponding percentage of SNR loss is computed using Eq. (5.1), taking into account the SNRs obtained with and without considering tidal deformability and its trend in the parameter space is shown in Fig. 5.26. The maximum loss in SNR, considering the PSD of O4, is approximately 0.3% and it corresponds to binary systems with high mass ratios. Assuming the IMRPhenomPv2 tidal description as reliable, the test seems to indicate that even with high values of tidal deformabilities, the effect on waveforms is quite small and definitely a second-order effect with respect to the limits imposed by the compactness of the considered astrophysical objects. This outcome is unexpected and necessitates further investigations for a better understanding and verification.

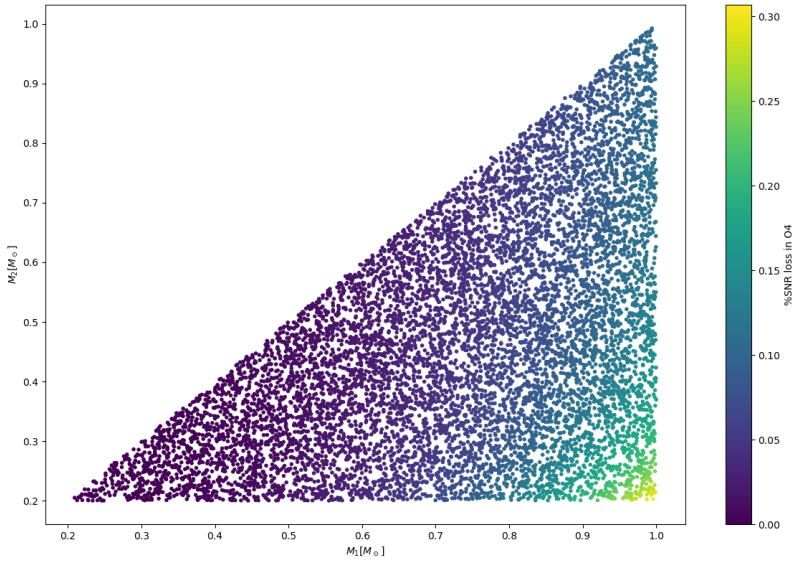

FIGURE 5.26: Estimated percentage loss in SNR in O4 computed by matched filtering a set of injections with tidal deformability and without considering any tidal deformability.

5.6 O4 SSM Online Search

The previous section provides insights into the possibility of having an electromagnetic counterpart in the merger of a SSM BH with a NS and on the possible outcomes of a merger with a SSM NS and a BH. In this section, the focus is shifted to the template bank currently used by the MBTA pipeline in the online search for SSM events in O4 and the initial tests conducted to assess its performance.

5.6.1 Online Template Bank

The MBTA virtual and real template banks for targeting SSM mergers in low-latency were constructed using the geometric placement algorithm with a minimum match of 0.97, a separation frequency of 120.0 Hz between the high and low frequency bands, and parameters listed in Table 5.6. The resulting virtual template bank, shown in Fig. 5.27 in the $m_1 - m_2$ plane, is composed of approximately 18% more templates than the bank used in the O3 SSM offline analysis, due to the more sensitive PSD.

O4 SSM low-latency templates bank			
	VT bank	RTLF bank	RTHF bank
Heaviest mass (m_1) [$M_\odot$] Lightest mass (m_2) [$M_\odot$] Mass ratio (m_1/m_2) Individual aligned spins ($\chi^z_{1,2}$)	$[0.2, 10.0]$ $[0.2, 1.0]$ $[1.0, 10.0]$ $[-0.1, 0.1]$ if $m_{1,2} \leq 0.5\,M_\odot$ $[-0.9, 0.9]$ else		
Minimal match	0.97		
Waveform approximant	TaylorF2		
PSD used for bank generation	L1 O4 high-sensitivity (BNS range $\approx$ 190 Mpc)		
Low frequency cut-off (f_0) [Hz] used for bank generation	45	45	120
High frequency cut-off (f_{max}) [Hz] used for bank generation	1000	120	1000
LF and HF bands separation frequency (f_{cut}) [Hz]	120		

TABLE 5.6: MBTA O4 SSM banks parameter space.

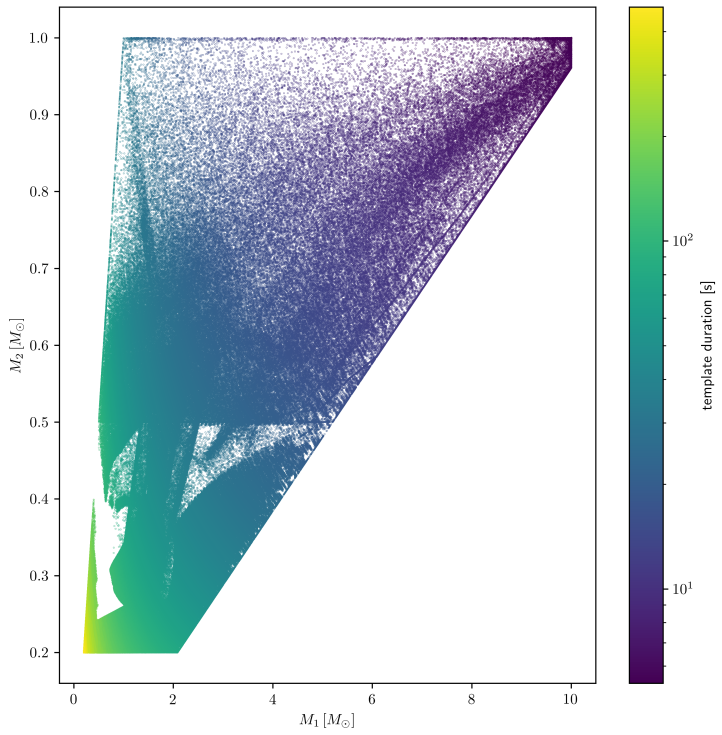

FIGURE 5.27: Template bank in the $m_1 - m_2$ plane used by MBTA in the SSM low-latency search during the fourth observing run. Each dot corresponds to a different template in the bank while the colorbar represents the template duration (in seconds)

The decision to limit the template bank within the same parameter space used in the third observing run was driven by the computing costs. To give an example, a bank generated with minimum mass of 0.1 $M_\odot$ would contain $\sim$ 12M templates, making it computationally prohibitive to perform the search efficiently, while a smaller template bank allows for a manageable number of templates while still covering a significant range of relevant masses. In order to verify the efficiency of the bank in

recovering potential GW signals before using it for the online search, it was tested against several sets of injections in different regions of the parameter space with the `pycbc_banksim` algorithm [282]. The performance of the template bank was evaluated by generating a set of 10 000 injections within the parameter space of the VT bank. These injections were generated using the TaylorF2 waveform model, and their parameters are summarised in Table 5.7. The evaluation of the templates bank

Injections parameter space	
Heaviest mass (m_1) [$M_\odot$]	$[0.2, 10.0]$
Lightest mass (m_2) [$M_\odot$]	$[0.2, 1.0]$
Mass ratio (m_1/m_2)	$[1.0, 10.0]$
Individual aligned spins ($\chi^z_{1,2}$)	$[-0.1, 0.1]$ if $m_{1,2} \leq 0.5\ M_\odot$ $[-0.9, 0.9]$ else
Waveform approximants used for analysis (freq. domain)	TaylorF2

TABLE 5.7: Injections set in the same parameter space of the template bank.

performance yielded a fitting factor of 0.987, as defined in Eq. (3.10). The minimum recovered match was 0.71047, while the maximum recovered match reached 0.99976 as shown in Fig. 5.28.

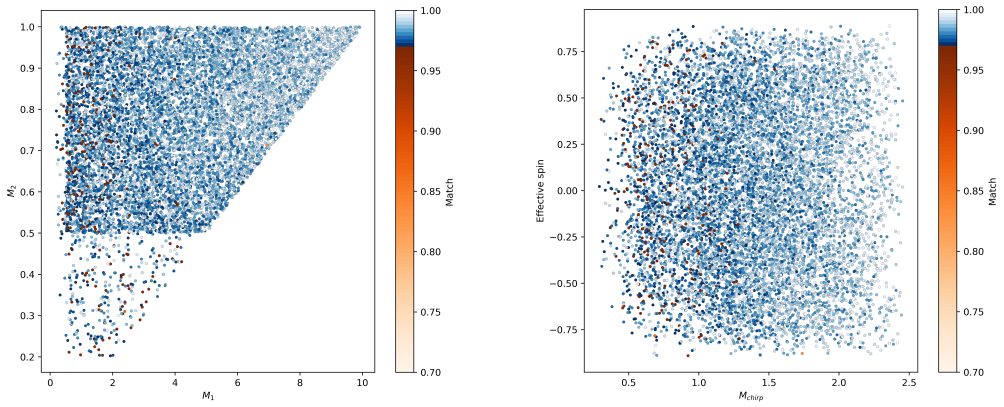

(A) Scatter plot in the $m_1 - m_2$ plane.

(B) Scatter plot in the $m_{chirp} - \chi_{eff}$ plane.

FIGURE 5.28: Scatter plots of the `pycbc_banksim` test in the $m_1 - m_2$ plane and $m_{chirp} - \chi_{eff}$ plane. The colorbar indicates the best match measured for each injection, and it is divided into two regions for match greater than 0.97 (blue) and smaller than 0.97 (red).

Fig. 5.29 displays the cumulative fraction of injections as a function of the match. The plot demonstrates that over 97% of the injections are successfully recovered with a match greater than or equal to 0.97. This observation serves as a validation of the template bank efficiency and its ability to accurately capture the majority of the injected signals. As previously stated, due to the significant increase in the number of templates associated with lower masses, the low-mass limit of the template bank was set at $0.2 M_\odot$. The second test performed had the objective of assessing the bank capability to recover low-mass injections outside its defined parameter space. The test used a set of 5 000 injection, generated within the parameter space listed in Table 5.8. This test yielded an effective fitting factor of 0.762 and its results are shown in Fig. 5.30, where the minimum recovered match is found to be 0, and the maximum

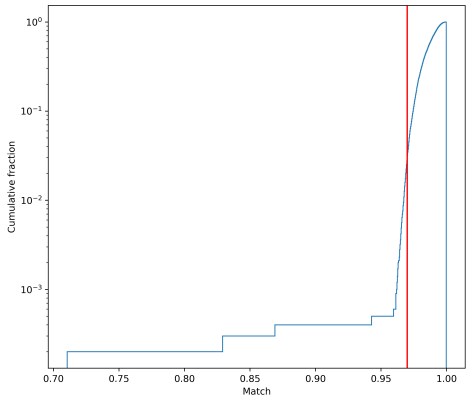

FIGURE 5.29: Cumulative density of injections that are recovered with a given match. The red line indicates the 0.97 match.

Injections parameter space	
Heaviest mass (m_1) [$M_\odot$]	$[0.15, 0.2]$ if $0.15\,M_\odot \leq m_2 \leq 1.0\,M_\odot$ $[0.15, 10.0]$ if $0.15\,M_\odot \leq m_2 \leq 0.2\,M_\odot$
Individual aligned spins ($\chi^z_{1,2}$)	$[-0.1, 0.1]$ if $m_{1,2} \leq 0.5\,M_\odot$ $[-0.9, 0.9]$ else
Waveform approximants used for analysis (freq. domain)	TaylorF2

TABLE 5.8: Injections set outside the template bank parameter space (at low masses).

recovered match reached 0.99704, indicating a broad variability in the accuracy in capturing the injected low mass signals.

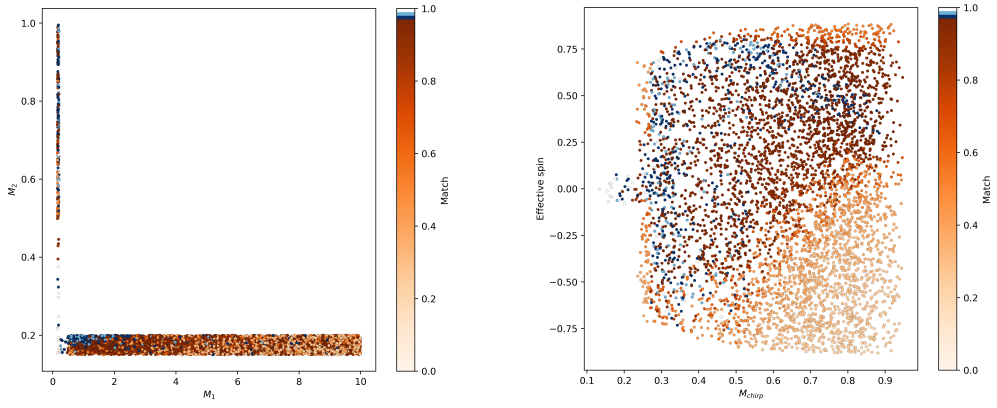

(A) Scatter plot in the $m_1 - m_2$ plane.

(B) Scatter plot in the $m_{chirp} - \chi_{eff}$ plane.

FIGURE 5.30: Scatter plots of the `pycbc_banksim` test in the $m_1 - m_2$ plane and $m_{chirp} - \chi_{eff}$ plane. The colorbar indicates the best match measured for each injection, and it is divided into two regions for match greater than 0.97 (blue) and smaller than 0.97 (red).

This test demonstrates that the template bank is partially sensitive outside its parameter space, in particular for aligned positive spins signals and low values of m_1. The 12.5% of the injections were successfully recovered with a match greater than

0.97, as shown in Fig. 5.31, demonstrating the bank ability to capture a substantial portion of low-mass injections.

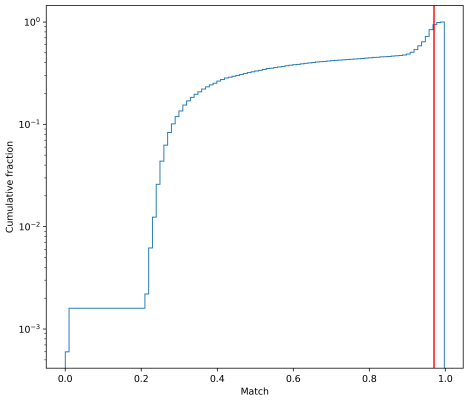

FIGURE 5.31: Cumulative density of injections that are recovered with a given match. The red line indicates the 0.97 match.

As part of the parameter space of the SSM bank is overlapping with part of the all-sky bank, the third performance test was conducted using a set of 5 000 injections, specifically generated within a parameter space that lies between the two considered banks, and with individual aligned spins up to magnitudes of 1.0 as outlined in Table 5.9.

Injections parameter space		
	Injections parameters against SSM bank	Injections parameters against BNS bank
Heaviest mass (m_1) [$M_\odot$]	$[0.5, 3.5]$	
Lightest mass (m_2) [$M_\odot$]	$[0.5, 2.0]$	
Individual aligned spins ($\chi^z_{1,2}$)	$[-1.0, 1.0]$	
Waveform approximants used for analysis (freq. domain)	TaylorF2	
Low frequency cut-off	45Hz	25Hz

TABLE 5.9: Injections set in the parameter space lying between the SSM template bank and the all-sky bank.

In this test, the SSM bank exhibits an effective fitting factor of 0.980. The minimum recovered match was measured at 0.91948, while the maximum recovered match reached 0.99915 as shown in Fig. 5.32. Notably, 93.0% of the injections were successfully recovered with a match greater than 0.97 when using the SSM templates bank (Fig. 5.34). Conversely, the all-sky BNS bank demonstrated a recovered effective fitting factor of 0.753 with a minimum recovered match at 0, while the maximum recovered match achieved a value of 0.99982 as in Fig. 5.33. In this case, 37.28% of the injections were successfully recovered with a match greater than 0.97 using the all-sky BNS bank (Fig. 5.34).

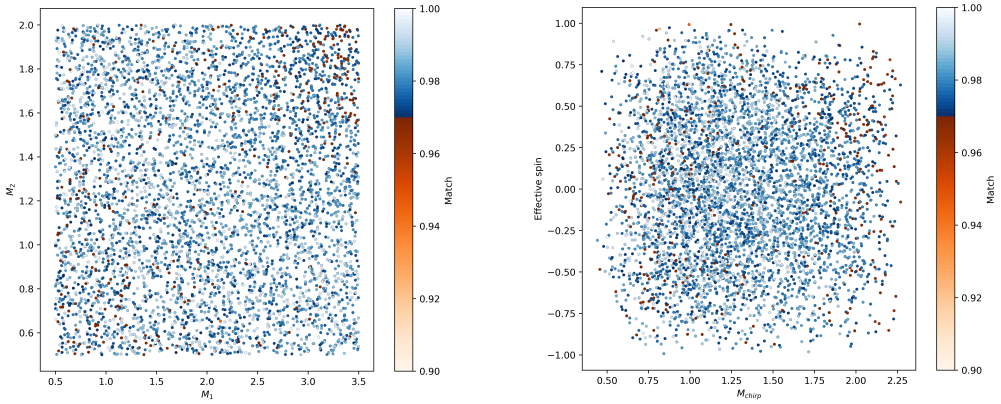

(A) Scatter plot in the $m_1 - m_2$ plane.

(B) Scatter plot in the $m_{chirp} - \chi_{eff}$ plane.

FIGURE 5.32: Scatter plots of the `pycbc_banksim` test with the SSM bank in the $m_1 - m_2$ plane and $m_{chirp} - \chi_{eff}$ plane. The colorbar indicates the best match measured for each injection, and it is divided into two regions for match greater than 0.97 (blue) and smaller than 0.97 (red).

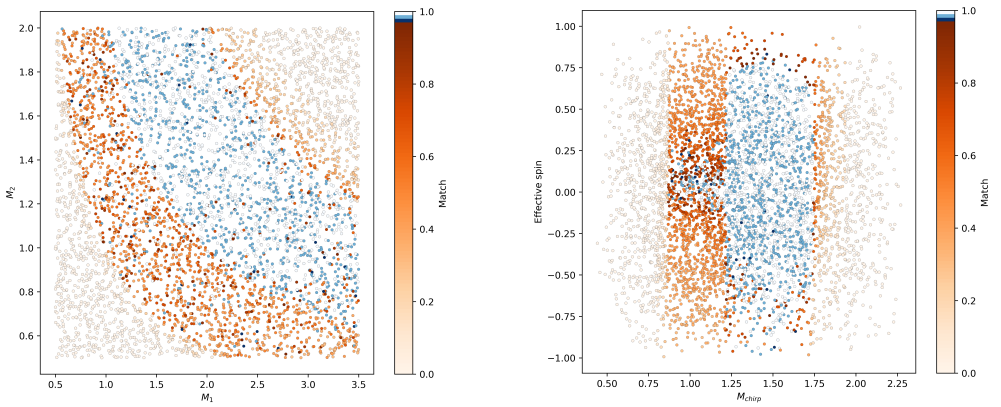

(A) Scatter plot in the $m_1 - m_2$ plane.

(B) Scatter plot in the $m_{chirp} - \chi_{eff}$ plane.

FIGURE 5.33: Scatter plots of the `pycbc_banksim` test with the all-sky BNS bank in the $m_1 - m_2$ plane and $m_{chirp} - \chi_{eff}$ plane. The colorbar indicates the best match measured for each injection, and it is divided into two regions for match greater than 0.97 (blue) and smaller than 0.97 (red).

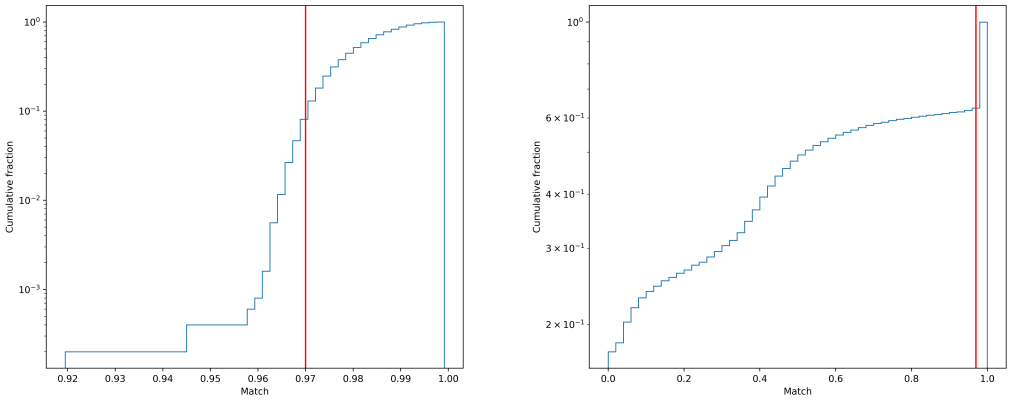

(A) Cumulative density of injections recovered with a given match with the SSM bank.

(B) Cumulative density of injections recovered with a given match with the all-sky BNS bank.

FIGURE 5.34: Cumulative density of injections that are recovered with a given match. The red line indicates the 0.97 match.

The higher overall performance of the SSM bank, including a greater proportion of successfully recovered injections and higher match values, can be attributed to its wider range of spin values in comparison to the limited spin range of the BNS portion of the all-sky bank. In the SSM bank, the templates incorporate spins up to 0.9 in absolute value, enabling the recovery of rapidly-spinning BNS systems that may not be adequately covered by the more restricted spin range of $[-0.05, 0.05]$ in the all-sky bank. This flexibility in spin coverage allows the SSM bank to effectively capture and recover signals from BNS mergers with unusual rapid spins, enhancing its performance in these scenarios.

5.6.2 Loss in Signal-to-Noise Ratio

Overall, the generated template bank has demonstrated good performance throughout the study. Nevertheless, an investigation was conducted to assess the impact of the low-frequency cutoff at $f_{low} = 45$ Hz, shown in Figure 5.35, considering the updated expected PSD in O4.

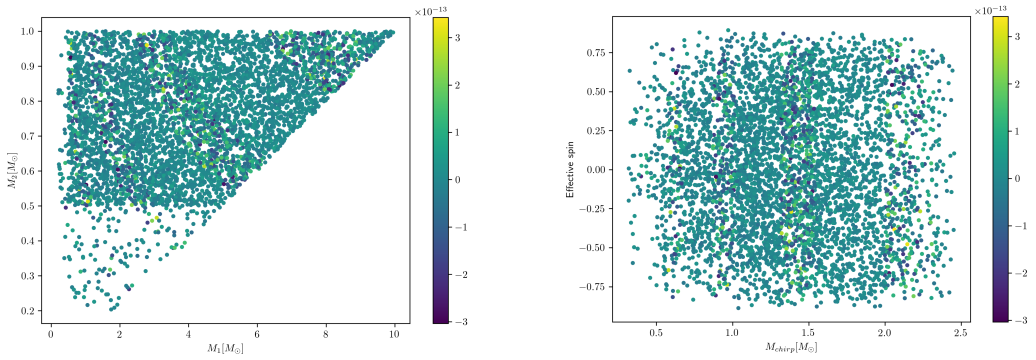

(A) Loss in SNR in the $m_1 - m_2$ plane.

(B) Loss in SNR in the $m_{chirp} - \chi_{eff}$ plane.

FIGURE 5.35: Estimated loss in SNR in O4 computed by matched filtering a set of injections starting at 45 Hz and at 25 Hz . Each dot corresponds to an injections, while the colorbar indicates how much the percentage loss in SNR of the injection differs from the median percentage loss of SNR across all injections.

As expected, the more sensitive PSD leads to an increased percentage loss in SNR to a median of 11.8 in the entire parameter space, computed with Eq. (5.1), when matched filtering data starting at 45 Hz instead of 25 Hz as in the standard BNS search.

5.6.3 Mock Data Challenge

A MDC is a data analysis exercise aimed at assessing the performance and reliability of a search pipeline before the start of an observing run. In the context of testing the online MBTA SSM search, a specific MDC was conducted using a subset of data from the third observing run, spanning a duration of 3 weeks. To evaluate the efficiency of the search pipeline, a predefined set of injections with parameters outlined in Table 5.1 was incorporated into the data. These injections were then searched for using the new template bank. In the analysis of injection recovery, as depicted in Fig. 5.36, it is observed that the majority of detected injections, characterised by a SNR $\geq$ 10, FAR $<$ 1.0 yr^{-1} and $q \leq 20$, exhibit characteristics such as low distance and low aligned or anti-aligned effective spins.

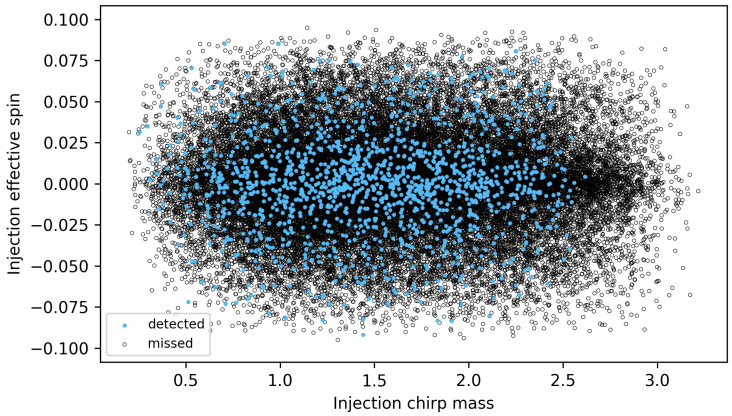

(A) Scatterplot in the plane effective spin as function of the chirp mass of the system.

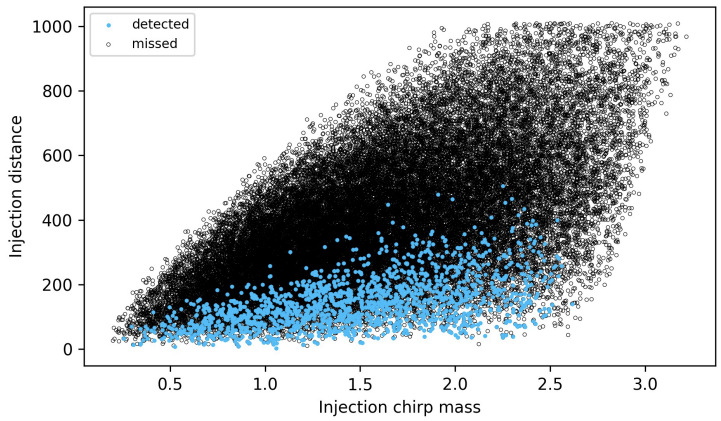

(B) Scatter plot in the plane distance as function of the chirp mass of the system.

FIGURE 5.36: Scatterplots of the MDC injection recovery in the chirp mass-effective spin plane (top plot) and in the chirp mass-distance (bottom plot). Blue dots are detected injections, corresponding to injections for which FAR $<$ 1.0 yr^{-1}, and black circles correspond to injected simulated signals.

Furthermore, the efficiency of the SSM MDC, defined as the fraction of detected injections out of the total injections generated, without the template bank cut, was compared to the efficiency of the SSM search conducted during the entire third observing run, and Fig. 5.37 shows that the efficiencies are similar and comparable. By

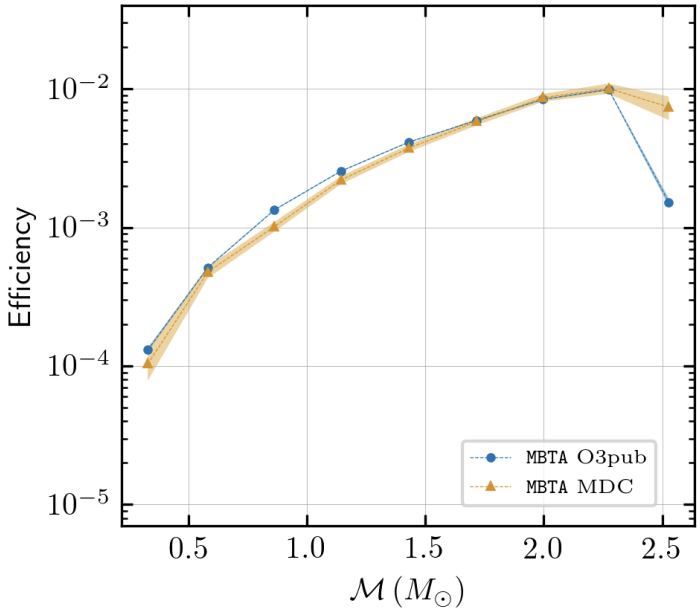

FIGURE 5.37: Comparison between the efficiency estimated in the MDC (orange) with the efficiency estimated in the SSM search during the third observing run (blue) as function of the chirp mass of the binary system.

calculating a preliminary sensitive volume-time $\langle VT \rangle$ using the data from the MDC and comparing it to the $\langle VT \rangle$ estimated using SSM data from O3, it was observed a factor of $\mathcal{O}(10)$ between the two curves, consistent with the difference in observing time between O3 (40 weeks) and the MDC (3 weeks), as shown in Fig. 5.38.

5.6.4 Online Search

Since the start of O4, the online MBTA SSM search has been approved and is operational. Online searches are associated to a real-time notification system used by the LVK collaboration to promptly share GW information with the scientific community, enabling astronomers and observatories to quickly respond and coordinate follow-up observations using various telescopes and instruments across different wavelengths. Currently, the MBTA SSM online search is generating the necessary information for alerts, although those are currently inactive due to ongoing developments in the LVK low-latency alerts infrastructure system. Nevertheless, the analysis is showing satisfactory performance, as shown in Fig. 5.39.

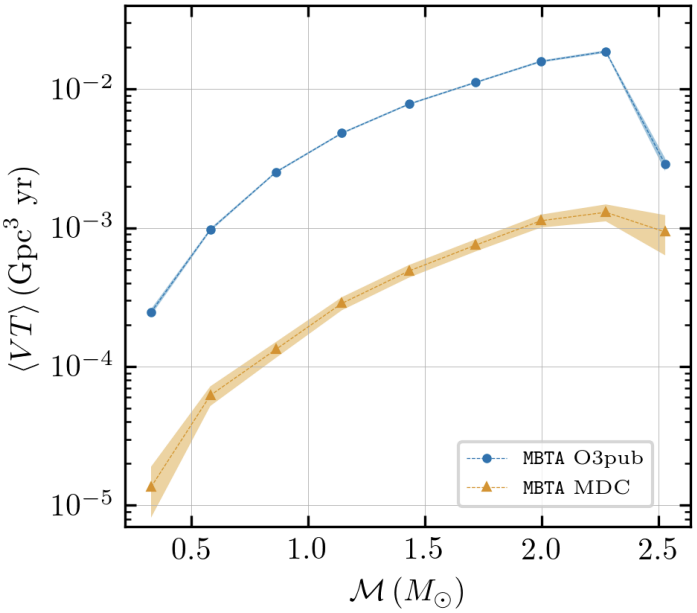

FIGURE 5.38: Comparison between the sensitive volume-time $\langle VT \rangle$ estimated in the MDC (orange) with the $\langle VT \rangle$ estimated in the SSM search during the third observing run (blue) as function of the chirp mass of the binary system.

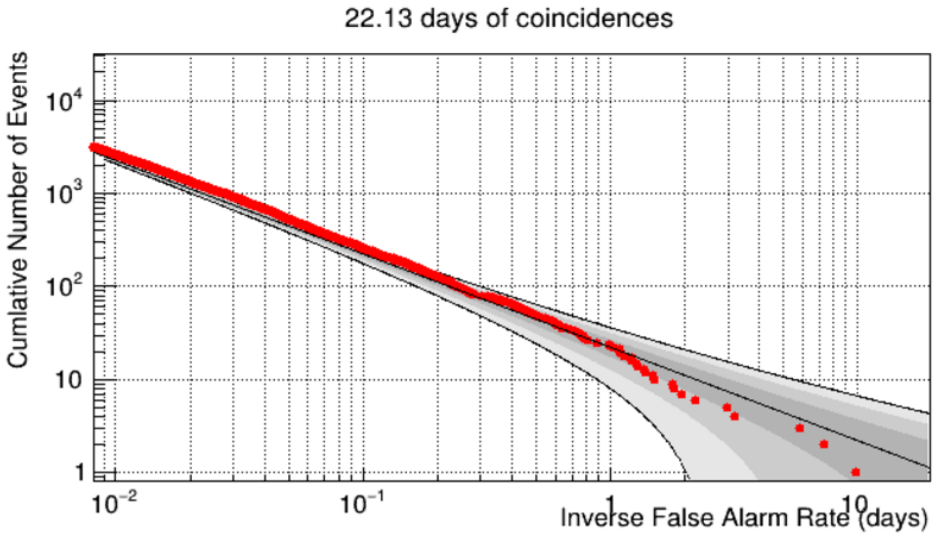

FIGURE 5.39: Cumulative IFAR distribution for doubles HL coincidences during the fourth LIGO-Virgo-KAGRA observing run (O4), between 1368982818 (UTC May 24, 2023 17h00) and 1372633218 (UTC July 05, 2023 23:00). The black curve represents the expectation from the background, while the grey regions are the Poissonian errors corresponding to the 1σ (dark grey), 2σ (grey), and 3σ (light grey) confidence intervals. Each red dot corresponds to an observation.

Conclusions

Since the initial confirmed detection in 2015, the search for gravitational waves has captivated the scientific community, unveiling a new perspective on the Universe. This field of research exhibits an extraordinary breadth of interdisciplinarity, transcending traditional boundaries and fostering collaboration among diverse scientific domains. By successfully detecting these elusive signals, it is possible to gain insights into the formation, evolution, and dynamics of their astrophysical sources. This invaluable opportunity not only allows to test the predictions of Einstein's theory of General Relativity but also enables to search for potential deviations from the standard theory, paving the way for alternative theories of gravity. Furthermore, the detection of gravitational waves can provide insights into the early moments of the Universe, and enable investigations into extreme matter, nuclear physics, dark energy, dark matter, and the formation of large-scale structures.

This manuscript focuses on the work performed by the author in collaboration with the MBTA team in the period spanning from 2020 to 2023, thus contributing to the offline data analysis of the LIGO-Virgo third observing run and the preparation undertaken for the fourth LIGO-Virgo-KAGRA observing run, started on May 2023. During the third observing run, the LIGO and Virgo interferometers achieved their highest sensitivity yet, leading to an unprecedented rate of discoveries, increasing the cumulative number of gravitational wave candidates to 90, and scoring a significant milestone: the detection of candidate neutron star-black hole mergers. In the context of the standard search for signals originating from binary black holes, binary neutron stars, and black hole-neutron star binaries the author of this manuscript played an active role in the analysis of specific data segments while during the subsolar mass search the author was the main analyst for the MBTA pipeline and played a crucial role in actively participating to the realisation of the related papers.

After an extensive examination of the fundamental principles of gravitational wave generation and detection in Chapter I and Chapter II, this thesis focused in Chapter III on the description of the MBTA pipeline, specifically designed to identify signals arising from compact binary coalescences through a matched-filtering technique. Chapter IV presented a summary of the standard CBC search performed during the third observing run, showing the template bank used by the MBTA pipeline as well as the monitoring procedure performed during the offline analysis, and the description of notable detections and significant findings. The following Chapter V reported a detailed discussion regarding the search methods and results of the subsolar mass search performed in O3. The absence of significant candidates allows to set upper limits on the merger rate of such binaries, which in turn are used to update the constraints on two chosen models for the generation of compact objects in the probed mass range. Finally, the last section of Chapter V is devoted to the study

of the phenomenology of mergers involving a sub-solar mas black hole and a neutron star and a sub-solar mass neutron star and a standard black hole. These studies laid the foundations for an online search for such binary mergers that is currently processing data in the fourth observing run.

The ongoing fourth observing run holds big promises for the field of gravitational wave research. While waiting for the Virgo detector to join the run, with the increased detector capabilities of the LIGO, and the new KAGRA detector, we are ready to discover more about the population properties, the formation, and cosmic evolution of compact objects. However, the allure of the unknown attracts us even more. As we push the boundaries of our instruments and analysis techniques, we engage in a quest to discover new frontiers and new exotic objects that lie beyond our current knowledge. These enigmatic entities, with their uncommon characteristics, have the potential to reshape our understanding of the universe and challenge existing theories. In a not too distant future, the expansion of the global detector network holds promising prospects for gravitational wave and multi-messenger discoveries. However, as the sensitivity of the detectors improve, the uncertainty in waveforms emerges as a notable source of systematics. As a consequence, it is crucial to develop enhanced waveform models that encompass a broader spectrum of source characteristics and incorporate potentially significant additional physics, such as orbital eccentricity. By doing so, it is possible to ensure a reliable interpretation of the observations in the forthcoming era of heightened sensitivity. In particular for sub-solar mass systems, the current absence of numerical relativity simulations, specialised waveform models, and N-body simulations concerning to sub-solar mass objects in clusters leaves significant room for advancement within this research field.

Bibliography

[1] LIGO Scientific Collaboration A. Stuver. *Burst Gravitational Waves*. https://www.ligo.org/science/GW-Burst.php.

[2] LIGO Scientific Collaboration A. Stuver. *Continuous Gravitational Waves*. https://www.ligo.org/science/GW-Continuous.php.

[3] LIGO Scientific Collaboration A. Stuver. *Inspiral Gravitational Waves*. https://www.ligo.org/science/GW-Inspiral.php.

[4] LIGO Scientific Collaboration A. Stuver. *Stochastic Gravitational Wave Background*. https://www.ligo.org/science/GW-Stochastic.php.

[5] J. Aasi et al. "Advanced LIGO". In: *Classical and Quantum Gravity* 32.7 (Mar. 2015), p. 074001. DOI: 10.1088/0264-9381/32/7/074001. URL: https://dx.doi.org/10.1088/0264-9381/32/7/074001.

[6] J. Aasi et al. "Characterization of the LIGO detectors during their sixth science run". In: *Class. Quant. Grav.* 32.11 (2015), p. 115012. DOI: 10.1088/0264-9381/32/11/115012. arXiv: 1410.7764 [gr-qc].

[7] J. Aasi et al. "First all-sky search for continuous gravitational waves from unknown sources in binary systems". In: *Phys. Rev. D* 90.6 (2014), p. 062010. DOI: 10.1103/PhysRevD.90.062010. arXiv: 1405.7904 [gr-qc].

[8] J. Aasi et al. "Search for gravitational radiation from intermediate mass black hole binaries in data from the second LIGO-Virgo joint science run". In: *Phys. Rev. D* 89.12 (2014), p. 122003. DOI: 10.1103/PhysRevD.89.122003. arXiv: 1404.2199 [gr-qc].

[9] J. Abadie et al. "All-sky search for gravitational-wave bursts in the second joint LIGO-Virgo run". In: *Phys. Rev. D* 85 (2012), p. 122007. DOI: 10.1103/PhysRevD.85.122007. arXiv: 1202.2788 [gr-qc].

[10] J. Abadie et al. "First Low-Latency LIGO+Virgo Search for Binary Inspirals and their Electromagnetic Counterparts". In: *Astron. Astrophys.* 541 (2012), A155. DOI: 10.1051/0004-6361/201218860. arXiv: 1112.6005 [astro-ph.CO].

[11] J. Abadie et al. "Search for Gravitational Waves from Compact Binary Coalescence in LIGO and Virgo Data from S5 and VSR1". In: *Phys. Rev. D* 82 (2010), p. 102001. DOI: 10.1103/PhysRevD.82.102001. arXiv: 1005.4655 [gr-qc].

[12] J. Abadie et al. "Search for Gravitational Waves from Low Mass Compact Binary Coalescence in LIGO's Sixth Science Run and Virgo's Science Runs 2 and 3". In: *Phys. Rev. D* 85 (2012), p. 082002. DOI: 10.1103/PhysRevD.85.082002. arXiv: 1111.7314 [gr-qc].

[13] J. Abadie et al. "Sensitivity Achieved by the LIGO and Virgo Gravitational Wave Detectors during LIGO's Sixth and Virgo's Second and Third Science Runs". In: (Mar. 2012). arXiv: 1203.2674 [gr-qc].

[14] B P Abbott et al. "Effects of data quality vetoes on a search for compact binary coalescences in Advanced LIGO's first observing run". In: *Class. Quant. Grav.* 35.6 (2018), p. 065010. DOI: 10.1088/1361-6382/aaaafa. arXiv: 1710.02185 [gr-qc].

[15] B. Abbott et al. "All-sky LIGO Search for Periodic Gravitational Waves in the Early S5 Data". In: *Phys. Rev. Lett.* 102 (2009), p. 111102. DOI: 10.1103/PhysRevLett.102.111102. arXiv: 0810.0283 [gr-qc].

[16] B. Abbott et al. "Search for gravitational waves from primordial black hole binary coalescences in the galactic halo". In: *Phys. Rev. D* 72 (2005), p. 082002. DOI: 10.1103/PhysRevD.72.082002. arXiv: gr-qc/0505042.

[17] B. P. Abbott et al. "All-Sky Search for Short Gravitational-Wave Bursts in the Second Advanced LIGO and Advanced Virgo Run". In: *Phys. Rev. D* 100.2 (2019), p. 024017. DOI: 10.1103/PhysRevD.100.024017. arXiv: 1905.03457 [gr-qc].

[18] B. P. Abbott et al. "Astrophysical Implications of the Binary Black-Hole Merger GW150914". In: *Astrophys. J. Lett.* 818.2 (2016), p. L22. DOI: 10.3847/2041-8205/818/2/L22. arXiv: 1602.03846 [astro-ph.HE].

[19] B. P. Abbott et al. "Binary Black Hole Mergers in the first Advanced LIGO Observing Run". In: *Phys. Rev. X* 6.4 (2016). [Erratum: Phys. Rev. X 8, 039903 (2018)], p. 041015. DOI: 10.1103/PhysRevX.6.041015. arXiv: 1606.04856 [gr-qc].

[20] B. P. Abbott et al. "Calibration of the Advanced LIGO detectors for the discovery of the binary black-hole merger GW150914". In: *Phys. Rev. D* 95.6 (2017), p. 062003. DOI: 10.1103/PhysRevD.95.062003. arXiv: 1602.03845 [gr-qc].

[21] B. P. Abbott et al. "Characterization of transient noise in Advanced LIGO relevant to gravitational wave signal GW150914". In: *Class. Quant. Grav.* 33.13 (2016), p. 134001. DOI: 10.1088/0264-9381/33/13/134001. arXiv: 1602.03844 [gr-qc].

[22] B. P. Abbott et al. "Directly comparing GW150914 with numerical solutions of Einstein's equations for binary black hole coalescence". In: *Phys. Rev. D* 94.6 (2016), p. 064035. DOI: 10.1103/PhysRevD.94.064035. arXiv: 1606.01262 [gr-qc].

[23] B. P. Abbott et al. "Estimating the Contribution of Dynamical Ejecta in the Kilonova Associated with GW170817". In: *Astrophys. J. Lett.* 850.2 (2017), p. L39. DOI: 10.3847/2041-8213/aa9478. arXiv: 1710.05836 [astro-ph.HE].

[24] B. P. Abbott et al. "Gravitational Waves and Gamma-rays from a Binary Neutron Star Merger: GW170817 and GRB 170817A". In: *Astrophys. J. Lett.* 848.2 (2017), p. L13. DOI: 10.3847/2041-8213/aa920c. arXiv: 1710.05834 [astro-ph.HE].

[25] B. P. Abbott et al. "GW150914: Implications for the stochastic gravitational wave background from binary black holes". In: *Phys. Rev. Lett.* 116.13 (2016), p. 131102. DOI: 10.1103/PhysRevLett.116.131102. arXiv: 1602.03847 [gr-qc].

[26] B. P. Abbott et al. "GW150914: The Advanced LIGO Detectors in the Era of First Discoveries". In: *Phys. Rev. Lett.* 116.13 (2016), p. 131103. DOI: 10.1103/PhysRevLett.116.131103. arXiv: 1602.03838 [gr-qc].

[27] B. P. Abbott et al. "GW151226: Observation of Gravitational Waves from a 22-Solar-Mass Binary Black Hole Coalescence". In: *Phys. Rev. Lett.* 116.24 (2016), p. 241103. DOI: 10.1103/PhysRevLett.116.241103. arXiv: 1606.04855 [gr-qc].

[28] B. P. Abbott et al. "GW170817: Measurements of neutron star radii and equation of state". In: *Phys. Rev. Lett.* 121.16 (2018), p. 161101. DOI: 10.1103/PhysRevLett.121.161101. arXiv: 1805.11581 [gr-qc].

[29] B. P. Abbott et al. "GW170817: Observation of Gravitational Waves from a Binary Neutron Star Inspiral". In: *Phys. Rev. Lett.* 119.16 (2017), p. 161101. DOI: 10.1103/PhysRevLett.119.161101. arXiv: 1710.05832 [gr-qc].

[30] B. P. Abbott et al. "GW190425: Observation of a Compact Binary Coalescence with Total Mass $\sim 3.4 M_{\odot}$". In: *Astrophys. J. Lett.* 892.1 (2020), p. L3. DOI: 10.3847/2041-8213/ab75f5. arXiv: 2001.01761 [astro-ph.HE].

[31] B. P. Abbott et al. "GWTC-1: A Gravitational-Wave Transient Catalog of Compact Binary Mergers Observed by LIGO and Virgo during the First and Second Observing Runs". In: *Phys. Rev. X* 9.3 (2019), p. 031040. DOI: 10.1103/PhysRevX.9.031040. arXiv: 1811.12907 [astro-ph.HE].

[32] B. P. Abbott et al. "Localization and broadband follow-up of the gravitational-wave transient GW150914". In: *Astrophys. J. Lett.* 826.1 (2016), p. L13. DOI: 10.3847/2041-8205/826/1/L13. arXiv: 1602.08492 [astro-ph.HE].

[33] B. P. Abbott et al. "Multi-messenger Observations of a Binary Neutron Star Merger". In: *Astrophys. J. Lett.* 848.2 (2017), p. L12. DOI: 10.3847/2041-8213/aa91c9. arXiv: 1710.05833 [astro-ph.HE].

[34] B. P. Abbott et al. "Observation of Gravitational Waves from a Binary Black Hole Merger". In: *Phys. Rev. Lett.* 116.6 (2016), p. 061102. DOI: 10.1103/PhysRevLett.116.061102. arXiv: 1602.03837 [gr-qc].

[35] B. P. Abbott et al. "Observing gravitational-wave transient GW150914 with minimal assumptions". In: *Phys. Rev. D* 93.12 (2016). [Addendum: Phys.Rev.D 94, 069903 (2016)], p. 122004. DOI: 10.1103/PhysRevD.93.122004. arXiv: 1602.03843 [gr-qc].

[36] B. P. Abbott et al. "Properties of the Binary Black Hole Merger GW150914". In: *Phys. Rev. Lett.* 116.24 (2016), p. 241102. DOI: 10.1103/PhysRevLett.116.241102. arXiv: 1602.03840 [gr-qc].

[37] B. P. Abbott et al. "Search for Gravitational Waves from Low Mass Binary Coalescences in the First Year of LIGO's S5 Data". In: *Phys. Rev. D* 79 (2009), p. 122001. DOI: 10.1103/PhysRevD.79.122001. arXiv: 0901.0302 [gr-qc].

[38] B. P. Abbott et al. "Search for gravitational-wave bursts associated with gamma-ray bursts using data from LIGO Science Run 5 and Virgo Science Run 1". In: *Astrophys. J.* 715 (2010), pp. 1438–1452. DOI: 10.1088/0004-637X/715/2/1438. arXiv: 0908.3824 [astro-ph.HE].

[39] B. P. Abbott et al. "Search for gravitational-wave bursts in the first year of the fifth LIGO science run". In: *Phys. Rev. D* 80 (2009), p. 102001. DOI: 10.1103/PhysRevD.80.102001. arXiv: 0905.0020 [gr-qc].

[40] B. P. Abbott et al. "Search for intermediate mass black hole binaries in the first and second observing runs of the Advanced LIGO and Virgo network". In: *Phys. Rev. D* 100.6 (2019), p. 064064. DOI: 10.1103/PhysRevD.100.064064. arXiv: 1906.08000 [gr-qc].

[41] B. P. Abbott et al. "Search for Subsolar Mass Ultracompact Binaries in Advanced LIGO's Second Observing Run". In: *Phys. Rev. Lett.* 123.16 (2019), p. 161102. DOI: 10.1103/PhysRevLett.123.161102. arXiv: 1904.08976 [astro-ph.CO].

[42] B. P. Abbott et al. "Search for Subsolar-Mass Ultracompact Binaries in Advanced LIGO's First Observing Run". In: *Phys. Rev. Lett.* 121.23 (2018), p. 231103. DOI: 10.1103/PhysRevLett.121.231103. arXiv: 1808.04771 [astro-ph.CO].

[43] B. P. Abbott et al. "Searches for gravitational waves from known pulsars with S5 LIGO data". In: *Astrophys. J.* 713 (2010), pp. 671–685. DOI: 10.1088/0004-637X/713/1/671. arXiv: 0909.3583 [astro-ph.HE].

[44] B. P. Abbott et al. "Tests of general relativity with GW150914". In: *Phys. Rev. Lett.* 116.22 (2016). [Erratum: Phys. Rev. Lett. 121, 129902 (2018)], p. 221101. DOI: 10.1103/PhysRevLett.116.221101. arXiv: 1602.03841 [gr-qc].

[45] B. P. Abbott et al. "The Rate of Binary Black Hole Mergers Inferred from Advanced LIGO Observations Surrounding GW150914". In: *Astrophys. J. Lett.* 833.1 (2016), p. L1. DOI: 10.3847/2041-8205/833/1/L1. arXiv: 1602.03842 [astro-ph.HE].

[46] Benjamin P Abbott et al. "Exploring the Sensitivity of Next Generation Gravitational Wave Detectors". In: *Class. Quant. Grav.* 34.4 (2017), p. 044001. DOI: 10.1088/1361-6382/aa51f4. arXiv: 1607.08697 [astro-ph.IM].

[47] Benjamin P. Abbott et al. "All-sky search for short gravitational-wave bursts in the first Advanced LIGO run". In: *Phys. Rev. D* 95.4 (2017), p. 042003. DOI: 10.1103/PhysRevD.95.042003. arXiv: 1611.02972 [gr-qc].

[48] Benjamin P. Abbott et al. "Effects of waveform model systematics on the interpretation of GW150914". In: *Class. Quant. Grav.* 34.10 (2017), p. 104002. DOI: 10.1088/1361-6382/aa6854. arXiv: 1611.07531 [gr-qc].

[49] Benjamin P. Abbott et al. "Search for intermediate mass black hole binaries in the first observing run of Advanced LIGO". In: *Phys. Rev. D* 96.2 (2017), p. 022001. DOI: 10.1103/PhysRevD.96.022001. arXiv: 1704.04628 [gr-qc].

[50] Benjamin P. Abbott et al. "Sensitivity of the Advanced LIGO detectors at the beginning of gravitational wave astronomy". In: *Phys. Rev. D* 93.11 (2016). [Addendum: Phys.Rev.D 97, 059901 (2018)], p. 112004. DOI: 10.1103/PhysRevD.93.112004. arXiv: 1604.00439 [astro-ph.IM].

[51] Benjamin P. Abbott et al. "The basic physics of the binary black hole merger GW150914". In: *Annalen Phys.* 529.1-2 (2017), p. 1600209. DOI: 10.1002/andp.201600209. arXiv: 1608.01940 [gr-qc].

[52] R. Abbott et al. "All-sky search for continuous gravitational waves from isolated neutron stars in the early O3 LIGO data". In: *Phys. Rev. D* 104.8 (2021), p. 082004. DOI: 10.1103/PhysRevD.104.082004. arXiv: 2107.00600 [gr-qc].

[53] R. Abbott et al. "All-sky search for continuous gravitational waves from isolated neutron stars using Advanced LIGO and Advanced Virgo O3 data". In: *Phys. Rev. D* 106.10 (2022), p. 102008. DOI: 10.1103/PhysRevD.106.102008. arXiv: 2201.00697 [gr-qc].

[54] R. Abbott et al. "All-sky search for long-duration gravitational-wave bursts in the third Advanced LIGO and Advanced Virgo run". In: *Phys. Rev. D* 104.10 (2021), p. 102001. DOI: 10.1103/PhysRevD.104.102001. arXiv: 2107.13796 [gr-qc].

[55] R. Abbott et al. "Constraints on the Cosmic Expansion History from GWTC–3". In: *Astrophys. J.* 949.2 (2023), p. 76. DOI: 10.3847/1538-4357/ac74bb. arXiv: 2111.03604 [astro-ph.CO].

[56] R. Abbott et al. "GW190521: A Binary Black Hole Merger with a Total Mass of $150M_{\odot}$". In: *Phys. Rev. Lett.* 125.10 (2020), p. 101102. DOI: 10.1103/PhysRevLett.125.101102. arXiv: 2009.01075 [gr-qc].

[57] R. Abbott et al. "GW190814: Gravitational Waves from the Coalescence of a 23 Solar Mass Black Hole with a 2.6 Solar Mass Compact Object". In: *Astrophys. J. Lett.* 896.2 (2020), p. L44. DOI: 10.3847/2041-8213/ab960f. arXiv: 2006.12611 [astro-ph.HE].

[58] R. Abbott et al. "GWTC-2: Compact Binary Coalescences Observed by LIGO and Virgo During the First Half of the Third Observing Run". In: *Phys. Rev. X* 11 (2021), p. 021053. DOI: 10.1103/PhysRevX.11.021053. arXiv: 2010.14527 [gr-qc].

[59] R. Abbott et al. "GWTC-2.1: Deep Extended Catalog of Compact Binary Coalescences Observed by LIGO and Virgo During the First Half of the Third Observing Run". In: (Aug. 2021). arXiv: 2108.01045 [gr-qc].

[60] R. Abbott et al. "GWTC-3: Compact Binary Coalescences Observed by LIGO and Virgo During the Second Part of the Third Observing Run". In: (Nov. 2021). arXiv: 2111.03606 [gr-qc].

[61] R. Abbott et al. "Observation of Gravitational Waves from Two Neutron Star–Black Hole Coalescences". In: *Astrophys. J. Lett.* 915.1 (2021), p. L5. DOI: 10.3847/2041-8213/ac082e. arXiv: 2106.15163 [astro-ph.HE].

[62] R. Abbott et al. "Population of Merging Compact Binaries Inferred Using Gravitational Waves through GWTC-3". In: *Phys. Rev. X* 13.1 (2023), p. 011048. DOI: 10.1103/PhysRevX.13.011048. arXiv: 2111.03634 [astro-ph.HE].

[63] R. Abbott et al. "Population Properties of Compact Objects from the Second LIGO-Virgo Gravitational-Wave Transient Catalog". In: *Astrophys. J. Lett.* 913.1 (2021), p. L7. DOI: 10.3847/2041-8213/abe949. arXiv: 2010.14533 [astro-ph.HE].

[64] R. Abbott et al. "Properties and Astrophysical Implications of the 150 $M_{\odot}$ Binary Black Hole Merger GW190521". In: *Astrophys. J. Lett.* 900.1 (2020), p. L13. DOI: 10.3847/2041-8213/aba493. arXiv: 2009.01190 [astro-ph.HE].

[65] R. Abbott et al. "Search for Subsolar-Mass Binaries in the First Half of Advanced LIGO's and Advanced Virgo's Third Observing Run". In: *Phys. Rev. Lett.* 129.6 (2022), p. 061104. DOI: 10.1103/PhysRevLett.129.061104. arXiv: 2109.12197 [astro-ph.CO].

[66] R. Abbott et al. "Search for subsolar-mass black hole binaries in the second part of Advanced LIGO's and Advanced Virgo's third observing run". In: *Monthly Notices of the Royal Astronomical Society* (Feb. 2023). stad588. ISSN: 0035-8711. DOI: 10.1093/mnras/stad588. eprint: https://academic.oup.com/mnras/advance-article-pdf/doi/10.1093/mnras/stad588/49357833/stad588.pdf. URL: https://doi.org/10.1093/mnras/stad588.

[67] R. Abbott et al. "Tests of General Relativity with GWTC-3". In: (Dec. 2021). arXiv: 2112.06861 [gr-qc].

[68] R. Abbott et al. "Upper limits on the isotropic gravitational-wave background from Advanced LIGO and Advanced Virgo's third observing run". In: *Phys. Rev. D* 104.2 (2021), p. 022004. DOI: 10.1103/PhysRevD.104.022004. arXiv: 2101.12130 [gr-qc].

[69] Rich Abbott et al. "Search for intermediate-mass black hole binaries in the third observing run of Advanced LIGO and Advanced Virgo". In: *Astron. Astrophys.* 659 (2022), A84. DOI: 10.1051/0004-6361/202141452. arXiv: 2105.15120 [astro-ph.HE].

[70] Thomas D. Abbott et al. "Improved analysis of GW150914 using a fully spin-precessing waveform Model". In: *Phys. Rev. X* 6.4 (2016), p. 041014. DOI: 10.1103/PhysRevX.6.041014. arXiv: 1606.01210 [gr-qc].

[71] F Acernese et al. "Advanced Virgo: a second-generation interferometric gravitational wave detector". In: *Classical and Quantum Gravity* 32.2 (Dec. 2014), p. 024001. DOI: 10.1088/0264-9381/32/2/024001. URL: https://dx.doi.org/10.1088/0264-9381/32/2/024001.

[72] F. Acernese et al. "Virgo Detector Characterization and Data Quality during the O3 run". In: (May 2022). arXiv: 2205.01555 [gr-qc].

[73] F. Acernese et al. "Virgo Detector Characterization and Data Quality: results from the O3 run". In: (Oct. 2022). arXiv: 2210.15633 [gr-qc].

[74] Lotty Ackerman et al. "Dark matter and dark radiation". In: *Phys. Rev. D* 79 (2 Jan. 2009), p. 023519. DOI: 10.1103/PhysRevD.79.023519. URL: https://link.aps.org/doi/10.1103/PhysRevD.79.023519.

[75] T. Adams. "Low–latency search for compact binary coalescences using MBTA". In: (July 2015). arXiv: 1507.01787.

[76] T. Adams et al. "Low-latency analysis pipeline for compact binary coalescences in the advanced gravitational wave detector era". In: *Class. Quant. Grav.* 33.17 (2016), p. 175012. DOI: 10.1088/0264-9381/33/17/175012. arXiv: 1512.02864 [gr-qc].

[77] P. A. R. Ade et al. "Planck 2015 results. XIII. Cosmological parameters". In: *Astron. Astrophys.* 594 (2016), A13. DOI: 10.1051/0004-6361/201525830. arXiv: 1502.01589 [astro-ph.CO].

[78] S. Adrian-Martinez et al. "High-energy Neutrino follow-up search of Gravitational Wave Event GW150914 with ANTARES and IceCube". In: *Phys. Rev. D* 93.12 (2016), p. 122010. DOI: 10.1103/PhysRevD.93.122010. arXiv: 1602.05411 [astro-ph.HE].

[79] N. Afshordi, P. McDonald, and D. N. Spergel. "Primordial Black Holes as Dark Matter: The Power Spectrum and Evaporation of Early Structures". In: *The Astrophysical Journal* 594.2 (Aug. 2003), pp. L71–L74. DOI: 10.1086/378763. URL: https://doi.org/10.1086%2F378763.

[80] N. Aghanim et al. "Planck 2018 results. I. Overview and the cosmological legacy of Planck". In: *Astron. Astrophys.* 641 (2020), A1. DOI: 10.1051/0004-6361/201833880. arXiv: 1807.06205 [astro-ph.CO].

[81] L. Aiello et al. "Thermal compensation system in advanced and third generation gravitational wave interferometric detectors". In: *J. Phys. Conf. Ser.* 1226.1 (2019), p. 012019. DOI: 10.1088/1742-6596/1226/1/012019.

[82] A. Albert et al. "Search for High-energy Neutrinos from Binary Neutron Star Merger GW170817 with ANTARES, IceCube, and the Pierre Auger Observatory". In: *Astrophys. J. Lett.* 850.2 (2017), p. L35. DOI: 10.3847/2041-8213/aa9aed. arXiv: 1710.05839 [astro-ph.HE].

[83] K. D. Alexander et al. "The Electromagnetic Counterpart of the Binary Neutron Star Merger LIGO/VIRGO GW170817. VI. Radio Constraints on a Relativistic Jet and Predictions for Late-Time Emission from the Kilonova Ejecta". In: *Astrophys. J. Lett.* 848.2 (2017), p. L21. DOI: 10.3847/2041-8213/aa905d. arXiv: 1710.05457 [astro-ph.HE].

[84] Yacine Ali-Haımoud, Ely D. Kovetz, and Marc Kamionkowski. "Merger rate of primordial black-hole binaries". In: *Phys. Rev. D* 96.12 (2017), p. 123523. DOI: 10.1103/PhysRevD.96.123523. arXiv: 1709.06576 [astro-ph.CO].

[85] Bruce Allen et al. "FINDCHIRP: An Algorithm for detection of gravitational waves from inspiraling compact binaries". In: *Phys. Rev. D* 85 (2012), p. 122006. DOI: 10.1103/PhysRevD.85.122006. arXiv: gr-qc/0509116.

[86] R. A. Allsman et al. "MACHO project limits on black hole dark matter in the 1-30 solar mass range". In: *Astrophys. J. Lett.* 550 (2001), p. L169. DOI: 10.1086/319636. arXiv: astro-ph/0011506.

[87] N. Andersson et al. "Gravitational waves from neutron stars: promises and challenges". In: *General Relativity and Gravitation* 43.2 (Aug. 2010), pp. 409–436. DOI: 10.1007/s10714-010-1059-4. URL: https://doi.org/10.1007%2Fs10714-010-1059-4.

[88] Nicolas Andres et al. "Assessing the compact-binary merger candidates reported by the MBTA pipeline in the LIGO–Virgo O3 run: probability of astrophysical origin, classification, and associated uncertainties". In: *Class. Quant. Grav.* 39.5 (2022), p. 055002. DOI: 10.1088/1361-6382/ac482a. arXiv: 2110.10997 [gr-qc].

[89] T. A. Apostolatos. "Search templates for gravitational waves from precessing, inspiraling binaries". In: *Phys. Rev. D* 52 (1995), pp. 605–620. DOI: 10.1103/PhysRevD.52.605.

[90] A. Arbey and F. Mahmoudi. "Dark matter and the early Universe: A review". In: *Progress in Particle and Nuclear Physics* 119 (July 2021), p. 103865. DOI: 10.1016/j.ppnp.2021.103865. URL: https://doi.org/10.1016%2Fj.ppnp.2021.103865.

[91] Alexandre Arbey. "Dark fluid: A complex scalar field to unify dark energy and dark matter". In: *Physical Review D* 74.4 (Aug. 2006). DOI: 10.1103/physrevd.74.043516. URL: https://doi.org/10.1103%2Fphysrevd.74.043516.

[92] Nicolas Arnaud. "LIGO and Virgo detector characterization and data quality: Contributions to the O3 run and preparation for O4". In: *Nucl. Instrum. Meth. A* 1048 (2023), p. 167945. DOI: 10.1016/j.nima.2022.167945.

[93] International Pulsar Timing Array. *A Global, Galactic-Scale Gravitational Wave DetectorPermalink*. https://ipta4gw.org.

[94] Yoichi Aso et al. "Interferometer design of the KAGRA gravitational wave detector". In: *Phys. Rev. D* 88.4 (2013), p. 043007. DOI: 10.1103/PhysRevD.88.043007. arXiv: 1306.6747 [gr-qc].

[95] S. M. Aston et al. "Update on quadruple suspension design for Advanced LIGO". In: *Class. Quant. Grav.* 29.23 (2012), p. 235004. DOI: 10.1088/0264-9381/29/23/235004.

[96] F. Aubin et al. "The MBTA pipeline for detecting compact binary coalescences in the third LIGO–Virgo observing run". In: *Class. Quant. Grav.* 38.9 (2021), p. 095004. DOI: 10.1088/1361-6382/abe913. arXiv: 2012.11512 [gr-qc].

[97] Florian Aubin. "Recherche à faible latence d'ondes gravitationnelles émises lors de coalescences de binaires compactes durant la troisième période d'observation de Advanced Virgo et Advanced LIGO". 2020CHAMA024. PhD thesis. 2020. URL: http://www.theses.fr/2020CHAMA024/document.

[98] S. Babak et al. "A Template bank to search for gravitational waves from inspiralling compact binaries. I. Physical models". In: *Class. Quant. Grav.* 23 (2006), pp. 5477–5504. DOI: 10.1088/0264-9381/23/18/002. arXiv: gr-qc/0604037.

[99] Stanislav Babak. "Building a stochastic template bank for detecting massive black hole binaries". In: *Class. Quant. Grav.* 25 (2008), p. 195011. DOI: 10.1088/0264-9381/25/19/195011. arXiv: 0801.4070 [gr-qc].

[100] Stanislav Babak, Andrea Taracchini, and Alessandra Buonanno. "Validating the effective-one-body model of spinning, precessing binary black holes against numerical relativity". In: *Phys. Rev. D* 95.2 (2017), p. 024010. DOI: 10.1103/PhysRevD.95.024010. arXiv: 1607.05661 [gr-qc].

[101] Neta A Bahcall and Andrea Kulier. "Tracing mass and light in the Universe: where is the dark matter?" In: *Monthly Notices of the Royal Astronomical Society* 439.3 (2014), pp. 2505–2514.

[102] Neta A Bahcall, Lori M Lubin, and Victoria Dorman. "Where is the dark matter?" In: *The Astrophysical Journal* 447.2 (1995), p. L81.

[103] Neta A. Bahcall, Xiaohui Fan, and Renyue Cen. "Constraining omega with cluster evolution". In: *Astrophys. J. Lett.* 485 (1997), p. L53. DOI: 10.1086/310814. arXiv: astro-ph/9706018.

[104] James M. Bardeen, William H. Press, and Saul A Teukolsky. "Rotating black holes: Locally nonrotating frames, energy extraction, and scalar synchrotron radiation". In: *Astrophys. J.* 178 (1972), p. 347. DOI: 10.1086/151796.

[105] C. G. Bassa et al. "LOFAR discovery of the fastest-spinning millisecond pulsar in the Galactic field". In: *Astrophys. J. Lett.* 846.2 (2017), p. L20. DOI: 10.3847/2041-8213/aa8400. arXiv: 1709.01453 [astro-ph.HE].

[106] Thomas W. Baumgarte and Stuart L. Shapiro. "Binary black hole mergers". In: *Phys. Today* 64N10 (2011), pp. 32–37. DOI: 10.1063/PT.3.1294.

[107] A. Bauswein, T. W. Baumgarte, and H. -T. Janka. "Prompt merger collapse and the maximum mass of neutron stars". In: *Phys. Rev. Lett.* 111.13 (2013), p. 131101. DOI: 10.1103/PhysRevLett.111.131101. arXiv: 1307.5191 [astro-ph.SR].

[108] M. G. Beker et al. "Newtonian noise and ambient ground motion for gravitational wave detectors". In: *J. Phys. Conf. Ser.* 363 (2012). Ed. by Mark Hannam et al., p. 012004. DOI: 10.1088/1742-6596/363/1/012004.

[109] Omar Benhar. "Neutron star matter equation of state and gravitational wave emission". In: *Mod. Phys. Lett. A* 20 (2005), pp. 2335–2350. DOI: 10.1142/S0217732305018335. arXiv: astro-ph/0507497.

[110] Charles L Bennett et al. "Nine-year Wilkinson Microwave Anisotropy Probe (WMAP) observations: final maps and results". In: *The Astrophysical Journal Supplement Series* 208.2 (2013), p. 20.

[111] Sebastiano Bernuzzi and Alessandro Nagar. "Gravitational waves from pulsations of neutron stars described by realistic Equations of State". In: *Phys. Rev. D* 78 (2008), p. 024024. DOI: 10.1103/PhysRevD.78.024024. arXiv: 0803.3804 [gr-qc].

[112] Neven Bilić, Gary B Tupper, and Raoul D Viollier. "Unification of dark matter and dark energy: the inhomogeneous Chaplygin gas". In: *Physics Letters B* 535.1-4 (May 2002), pp. 17–21. DOI: 10.1016/s0370-2693(02)01716-1. URL: https://doi.org/10.1016%2Fs0370-2693%2802%2901716-1.

[113] Nigel T. Bishop and Luciano Rezzolla. "Extraction of Gravitational Waves in Numerical Relativity". In: *Living Rev. Rel.* 19 (2016), p. 2. DOI: 10.1007/s41114-016-0001-9. arXiv: 1606.02532 [gr-qc].

[114] Rahul Biswas et al. "The Loudest event statistic: General formulation, properties and applications". In: *Class. Quant. Grav.* 26 (2009). [Erratum: Class. Quant. Grav. 30, 079502 (2013)], p. 175009. DOI: 10.1088/0264-9381/26/17/175009. arXiv: 0710.0465 [gr-qc].

[115] P. K. Blanchard et al. "The Electromagnetic Counterpart of the Binary Neutron Star Merger LIGO/VIRGO GW170817. VII. Properties of the Host Galaxy and Constraints on the Merger Timescale". In: *Astrophys. J. Lett.* 848.2 (2017), p. L22. DOI: 10.3847/2041-8213/aa9055. arXiv: 1710.05458 [astro-ph.HE].

[116] Alejandro Bohé et al. "Improved effective-one-body model of spinning, nonprecessing binary black holes for the era of gravitational-wave astrophysics with advanced detectors". In: *Phys. Rev. D* 95.4 (2017), p. 044028. DOI: 10.1103/PhysRevD.95.044028. arXiv: 1611.03703 [gr-qc].

[117] Judd D. Bowman et al. "An absorption profile centred at 78 megahertz in the sky-averaged spectrum". In: *Nature* 555.7694 (2018), pp. 67–70. DOI: 10.1038/nature25792. arXiv: 1810.05912 [astro-ph.CO].

[118] Latham A. Boyle, Robert R. Caldwell, and Marc Kamionkowski. "Spintessence! New models for dark matter and dark energy". In: *Phys. Lett. B* 545 (2002), pp. 17–22. DOI: 10.1016/S0370-2693(02)02590-X. arXiv: astro-ph/0105318.

[119] Richard F. Bradley et al. "A Ground Plane Artifact that Induces an Absorption Profile in Averaged Spectra from Global 21 cm Measurements, with Possible Application to EDGES". In: *The Astrophysical Journal* 874.2 (Apr. 2019), p. 153. DOI: 10.3847/1538-4357/ab0d8b. URL: https://doi.org/10.3847%2F1538-4357%2Fab0d8b.

[120] Marica Branchesi et al. "Science with the Einstein Telescope: a comparison of different designs". In: *JCAP* 07 (2023), p. 068. DOI: 10.1088/1475-7516/2023/07/068. arXiv: 2303.15923 [gr-qc].

[121] Timothy D. Brandt. "Constraints on MACHO Dark Matter from Compact Stellar Systems in Ultra-Faint Dwarf Galaxies". In: *Astrophys. J. Lett.* 824.2 (2016), p. L31. DOI: 10.3847/2041-8205/824/2/L31. arXiv: 1605.03665 [astro-ph.GA].

[122] Volker Bromm and Richard B. Larson. "The First Stars". In: *Annual Review of Astronomy and Astrophysics* 42.1 (2004), pp. 79–118. DOI: 10.1146/annurev.astro.42.053102.134034. eprint: https://doi.org/10.1146/annurev.astro.42.053102.134034. URL: https://doi.org/10.1146/annurev.astro.42.053102.134034.

[123] Volker Bromm and Richard B. Larson. "The First Stars". In: *Annual Review of Astronomy and Astrophysics* 42.1 (Sept. 2004), pp. 79–118. DOI: 10.1146/annurev.astro.42.053102.134034. URL: https://doi.org/10.1146%5C%2Fannurev.astro.42.053102.134034.

[124] Alessandra Buonanno, Yan-bei Chen, and Michele Vallisneri. "Detecting gravitational waves from precessing binaries of spinning compact objects: Adiabatic limit". In: *Phys. Rev. D* 67 (2003). [Erratum: Phys. Rev. D 74, 029904 (2006)], p. 104025. DOI: 10.1103/PhysRevD.67.104025. arXiv: gr-qc/0211087.

[125] Alessandra Buonanno et al. "Comparison of post-Newtonian templates for compact binary inspiral signals in gravitational-wave detectors". In: *Phys. Rev. D* 80 (2009), p. 084043. DOI: 10.1103/PhysRevD.80.084043. arXiv: 0907.0700 [gr-qc].

[126] Craig Cahillane and Georgia Mansell. "Review of the Advanced LIGO Gravitational Wave Observatories Leading to Observing Run Four". In: *Galaxies* 10.1 (2022), p. 36. DOI: 10.3390/galaxies10010036. arXiv: 2202.00847 [gr-qc].

[127] Juan Calderón Bustillo et al. "Sensitivity of gravitational wave searches to the full signal of intermediate-mass black hole binaries during the first observing run of Advanced LIGO". In: *Phys. Rev. D* 97.2 (2018), p. 024016. DOI: 10.1103/PhysRevD.97.024016. arXiv: 1711.02009 [gr-qc].

[128] Eric D. Carlson, Marie E. Machacek, and Lawrence J. Hall. "Self-interacting dark matter". In: *Astrophys. J.* 398 (1992), pp. 43–52. DOI: 10.1086/171833.

[129] B. J. Carr. "Primordial Black Holes - Recent Developments". In: (2005). arXiv: astro-ph/0504034 [astro-ph].

[130] B. J. Carr et al. "New cosmological constraints on primordial black holes". In: *Phys. Rev. D* 81 (2010), p. 104019. DOI: 10.1103/PhysRevD.81.104019. arXiv: 0912.5297 [astro-ph.CO].

[131] Bernard Carr, Florian Kuhnel, and Marit Sandstad. "Primordial Black Holes as Dark Matter". In: *Phys. Rev. D* 94.8 (2016), p. 083504. DOI: 10.1103/PhysRevD.94.083504. arXiv: 1607.06077 [astro-ph.CO].

[132] Bernard Carr et al. "Constraints on primordial black holes". In: *Rept. Prog. Phys.* 84.11 (2021), p. 116902. DOI: 10.1088/1361-6633/ac1e31. arXiv: 2002.12778 [astro-ph.CO].

[133] Bernard J. Carr. "The Primordial black hole mass spectrum". In: *Astrophys. J.* 201 (1975), pp. 1–19. DOI: 10.1086/153853.

[134] Gravitational Wave Open Science Center. *GWTC-1: A Gravitational-Wave Transient Catalog of Compact Binary Mergers Observed by LIGO and Virgo during the First and Second Observing Runs*. https://www.gw-openscience.org/eventapi/html/GWTC-1-confident/.

[135] Katie Chamberlain and Nicolas Yunes. "Theoretical Physics Implications of Gravitational Wave Observation with Future Detectors". In: *Phys. Rev. D* 96.8 (2017), p. 084039. DOI: 10.1103/PhysRevD.96.084039. arXiv: 1704.08268 [gr-qc].

[136] Subrahmanyan Chandrasekhar. "The maximum mass of ideal white dwarfs". In: *Astrophys. J.* 74 (1931), pp. 81–82. DOI: 10.1086/143324.

[137] George F. Chapline. "Cosmological effects of primordial black holes". In: *Nature* 253.5489 (1975), pp. 251–252. DOI: 10.1038/253251a0.

[138] S. Chatterji et al. "Multiresolution techniques for the detection of gravitational-wave bursts". In: *Class. Quant. Grav.* 21 (2004), S1809–S1818. DOI: 10.1088/0264-9381/21/20/024. arXiv: gr-qc/0412119.

[139] Zu-Cheng Chen and Qing-Guo Huang. "Distinguishing Primordial Black Holes from Astrophysical Black Holes by Einstein Telescope and Cosmic Explorer". In: *JCAP* 08 (2020), p. 039. DOI: 10.1088/1475-7516/2020/08/039. arXiv: 1904.02396 [astro-ph.CO].

[140] Jeremie Choquette, James M. Cline, and Jonathan M. Cornell. "Early formation of supermassive black holes via dark matter self-interactions". In: *JCAP* 07 (2019), p. 036. DOI: 10.1088/1475-7516/2019/07/036. arXiv: 1812.05088 [astro-ph.CO].

[141] R. Chornock et al. "The Electromagnetic Counterpart of the Binary Neutron Star Merger LIGO/VIRGO GW170817. IV. Detection of Near infrared Signatures of r-process Nucleosynthesis with Gemini-South". In: *Astrophys. J. Lett.* 848.2 (2017), p. L19. DOI: 10.3847/2041-8213/aa905c. arXiv: 1710.05454 [astro-ph.HE].

[142] Nelson Christensen. "LIGO S6 detector characterization studies". In: *Class. Quant. Grav.* 27 (2010). Ed. by Fulvio Ricci, p. 194010. DOI: 10.1088/0264-9381/27/19/194010.

[143] Nelson Christensen. "Stochastic Gravitational Wave Backgrounds". In: *Rept. Prog. Phys.* 82.1 (2019), p. 016903. DOI: 10.1088/1361-6633/aae6b5. arXiv: 1811.08797 [gr-qc].

[144] Sebastien Clesse and Juan Garcia Bellido. "GW190425, GW190521 and GW190814. Three candidate mergers of primordial black holes from the QCD epoch". In: *Phys. Dark Univ.* 38 (2022), p. 101111. DOI: 10.1016/j.dark.2022.101111. arXiv: 2007.06481 [astro-ph.CO].

[145] Sébastien Clesse and Juan Garcıa-Bellido. "The clustering of massive Primordial Black Holes as Dark Matter: Measuring their mass distribution with advanced LIGO". In: *Physics of the Dark Universe* 15 (Mar. 2017), pp. 142–147. DOI: 10.1016/j.dark.2016.10.002. URL: https://doi.org/10.1016%5C%2Fj.dark.2016.10.002.

[146] CNRS.org. *Two CNRS 2017 Gold Medals awarded to physicists Alain Brillet and Thibault Damour*. https://www.cnrs.fr/en/two-cnrs-2017-gold-medals-awarded-physicists-alain-brillet-and-thibault-damour.

[147] T. Cokelaer, S. Babak, and B. S. Sathyaprakash. "Efficiency of template banks for binary black-hole detection". In: *Class. Quant. Grav.* 21 (2004), S1635–S1644. DOI: 10.1088/0264-9381/21/20/006.

[148] LIGO Scientific Collaboration. *Gravitational Wave Candidate Event Database*. https://gracedb.ligo.org.

[149] VIRGO Collaboration. *VIRGO Optical Layout*. https://www.virgo-gw.eu/science/detector/optical-layout/.

[150] Virgo Collaboration. *Sketch Of A Virgo Mirror Suspension Used To Reduce The Seismic Noise*. http://public.virgo-gw.eu/gmedia/virgosuperattenuator_vacuumtower_sketch-jpg/.

[151] Virgo Collaboration. *Virgo History*. https://www.virgo-gw.eu/about/virgo-history/.

[152] Adam Coogan, Logan Morrison, and Stefano Profumo. "Direct Detection of Hawking Radiation from Asteroid-Mass Primordial Black Holes". In: *Phys. Rev. Lett.* 126.17 (2021), p. 171101. DOI: 10.1103/PhysRevLett.126.171101. arXiv: 2010.04797 [astro-ph.CO].

[153] Thomas Corbitt and Nergis Mavalvala. "Quantum noise in gravitational wave interferometers: an overview and recent developments". In: *SPIE Proceedings*. Ed. by Derek Abbott, Jeffrey H. Shapiro, and Yoshihisa Yamamoto. SPIE, May 2003. DOI: 10.1117/12.507487. URL: https://doi.org/10.1117%2F12.507487.

[154] *Cosmic Explorer*. URL: https://cosmicexplorer.org.

[155] Guglielmo Costa et al. "Formation of black holes in the pair-instability mass gap: Evolution of a post-collision star". In: *Mon. Not. Roy. Astron. Soc.* 516.1 (2022), pp. 1072–1080. DOI: 10.1093/mnras/stac2222. arXiv: 2204.03492 [astro-ph.SR].

[156] Michael Coughlin. "Noise line identification in LIGO S6 and Virgo VSR2". In: *J. Phys. Conf. Ser.* 243 (2010). Ed. by Fulvio Ricci, p. 012010. DOI: 10.1088/1742-6596/243/1/012010. arXiv: 1109.0330 [gr-qc].

[157] P. S. Cowperthwaite et al. "The Electromagnetic Counterpart of the Binary Neutron Star Merger LIGO/Virgo GW170817. II. UV, Optical, and Near-infrared Light Curves and Comparison to Kilonova Models". In: *Astrophys. J. Lett.* 848.2 (2017), p. L17. DOI: 10.3847/2041-8213/aa8fc7. arXiv: 1710.05840 [astro-ph.HE].

[158] Jolied D.E. Creighton and Warren G. Anderson. *Gravitational-wave physics and astronomy an introduction to theory, experiment and data analysis*. Wiley-VCH, 2011.

[159] Teviet Creighton. "Tumbleweeds and airborne gravitational noise sources for LIGO". In: *Class. Quant. Grav.* 25 (2008), p. 125011. DOI: 10.1088/0264-9381/25/12/125011. arXiv: gr-qc/0007050.

[160] H. T. Cromartie et al. "Relativistic Shapiro delay measurements of an extremely massive millisecond pulsar". In: *Nature Astron.* 4.1 (2019), pp. 72–76. DOI: 10.1038/s41550-019-0880-2. arXiv: 1904.06759 [astro-ph.HE].

[161] Djuna Croon et al. "Subaru-HSC through a different lens: Microlensing by extended dark matter structures". In: *Physical Review D* 102.8 (Oct. 2020). DOI: 10.1103/physrevd.102.083021. URL: https://doi.org/10.1103/PhysRevD.102.083021.

[162] Zhe Cui and Xiang-Dong Li. "On the Formation of GW190521-like Binary Black Hole Merger Systems". In: (June 2023). DOI: 10.1093/mnras/stad1800. arXiv: 2306.08441 [astro-ph.HE].

[163] Elena Cuoco et al. "Strategy for signal classification to improve data quality for Advanced Detectors gravitational-wave searches". In: *Nuovo Cim. C* 40.3 (2017). Ed. by M. Razzano, G. Spandre, and B. Patricelli, p. 124. DOI: 10.1393/ncc/i2017-17124-4.

[164] Curt Cutler and Éanna E. Flanagan. "Gravitational waves from merging compact binaries: How accurately can one extract the binary's parameters from the inspiral waveform?" In: *Physical Review D* 49.6 (Mar. 1994), pp. 2658–2697. DOI: 10.1103/physrevd.49.2658. URL: https://doi.org/10.1103%5C%2Fphysrevd.49.2658.

[165] Guido D'Amico et al. "Massive Black Holes from Dissipative Dark Matter". In: *Mon. Not. Roy. Astron. Soc.* 473.1 (2018), pp. 328–335. DOI: 10.1093/mnras/stx2419. arXiv: 1707.03419 [astro-ph.CO].

[166] Basudeb Dasgupta, Ranjan Laha, and Anupam Ray. "Neutrino and positron constraints on spinning primordial black hole dark matter". In: *Phys. Rev. Lett.* 125.10 (2020), p. 101101. DOI: 10.1103/PhysRevLett.125.101101. arXiv: 1912.01014 [hep-ph].

[167] Derek Davis et al. "LIGO detector characterization in the second and third observing runs". In: *Class. Quant. Grav.* 38.13 (2021), p. 135014. DOI: 10.1088/1361-6382/abfd85. arXiv: 2101.11673 [astro-ph.IM].

[168] Derek Davis and Marissa Walker. "Detector Characterization and Mitigation of Noise in Ground-Based Gravitational-Wave Interferometers". In: *Galaxies* 10.1 (2022), p. 12. DOI: 10.3390/galaxies10010012.

[169] William DeRocco and Peter W. Graham. "Constraining Primordial Black Hole Abundance with the Galactic 511 keV Line". In: *Phys. Rev. Lett.* 123.25 (2019), p. 251102. DOI: 10.1103/PhysRevLett.123.251102. arXiv: 1906.07740 [astro-ph.CO].

[170] Steven L. Detweiler. "Pulsar timing measurements and the search for gravitational waves". In: *Astrophys. J.* 234 (1979), pp. 1100–1104. DOI: 10.1086/157593.

[171] Johannes Dickmann et al. "Thermal noise of beam splitters in laser gravitational wave detectors". In: *Phys. Rev. D* 98.8 (2018), p. 082002. DOI: 10.1103/PhysRevD.98.082002. arXiv: 1809.10994 [astro-ph.IM].

[172] Tim Dietrich et al. "Matter imprints in waveform models for neutron star binaries: Tidal and self-spin effects". In: *Phys. Rev. D* 99.2 (2019), p. 024029. DOI: 10.1103/PhysRevD.99.024029. arXiv: 1804.02235 [gr-qc].

[173] Tim Dietrich, Sebastiano Bernuzzi, and Wolfgang Tichy. "Closed-form tidal approximants for binary neutron star gravitational waveforms constructed from high-resolution numerical relativity simulations". In: *Physical Review D* 96.12 (Dec. 2017). DOI: 10.1103/physrevd.96.121501. URL: https://doi.org/10.1103%5C%2Fphysrevd.96.121501.

[174] Tim Dietrich, Sebastiano Bernuzzi, and Wolfgang Tichy. "Closed-form tidal approximants for binary neutron star gravitational waveforms constructed from high-resolution numerical relativity simulations". In: *Phys. Rev. D* 96.12 (2017), p. 121501. DOI: 10.1103/PhysRevD.96.121501. arXiv: 1706.02969 [gr-qc].

[175] Tim Dietrich et al. "Matter imprints in waveform models for neutron star binaries: Tidal and self-spin effects". In: *Phys. Rev. D* 99 (2 Jan. 2019), p. 024029. DOI: 10.1103/PhysRevD.99.024029. URL: https://link.aps.org/doi/10.1103/PhysRevD.99.024029.

[176] Artemiy Dmitriev, Haixing Miao, and Denis Martynov. "Enhancing the sensitivity of interferometers with stable phase-insensitive quantum filters". In: *Phys. Rev. D* 106.2 (2022), p. 022007. DOI: 10.1103/PhysRevD.106.022007. arXiv: 2110.15354 [quant-ph].

[177] V. Doroshenko et al. "A strangely light neutron star within a supernova remnant". In: *Nature Astronomy* (Dec. 2022). DOI: https://doi.org/10.1038/s41550-022-01800-1.

[178] F. Douchin and P. Haensel. "A unified equation of state of dense matter and neutron star structure". In: *Astronomy &amp Astrophysics* 380.1 (Dec. 2001), pp. 151–167. DOI: 10.1051/0004-6361:20011402. URL: https://doi.org/10.1051%2F0004-6361%3A20011402.

[179] Sheila Dwyer et al. "Gravitational wave detector with cosmological reach". In: *Phys. Rev. D* 91.8 (2015), p. 082001. DOI: 10.1103/PhysRevD.91.082001. arXiv: 1410.0612 [astro-ph.IM].

[180] David Eichler et al. "Nucleosynthesis, neutrino bursts and γ-rays from coalescing neutron stars". In: 340.6229 (July 1989), pp. 126–128. DOI: 10.1038/340126a0.

[181] Jaan Einasto, Ants Kaasik, and Enn Saar. "Dynamic evidence on massive coronas of galaxies". In: *Nature* 250.5464 (1974), pp. 309–310.

[182] Albert Einstein. "The Foundation of the General Theory of Relativity". In: *Annalen Phys.* 49.7 (1916). Ed. by Jong-Ping Hsu and D. Fine, pp. 769–822. DOI: 10.1002/andp.19163540702.

[183] *Einstein Telescope*. URL: https://www.et-gw.eu/index.php.

[184] Reed Essick, Salvatore Vitale, and Matthew Evans. "Frequency-dependent responses in third generation gravitational-wave detectors". In: *Phys. Rev. D* 96.8 (2017), p. 084004. DOI: 10.1103/PhysRevD.96.084004. arXiv: 1708.06843 [gr-qc].

[185] Alex Amato et al. "High-Reflection Coatings for Gravitational-Wave Detectors:iState of The Art and Future Developments/i". In: *Journal of Physics: Conference Series* 957 (Feb. 2018), p. 012006. DOI: 10.1088/1742-6596/957/1/012006. URL: https://doi.org/10.1088%2F1742-6596%2F957%2F1%2F012006.

[186] B P Abbott et al. "A guide to LIGO–Virgo detector noise and extraction of transient gravitational-wave signals". In: *Classical and Quantum Gravity* 37.5 (Feb. 2020), p. 055002. DOI: 10.1088/1361-6382/ab685e. URL: https://doi.org/10.1088%2F1361-6382%2Fab685e.

[187] D. Davis et al. *Data Quality Vetoes Applied to the Analysis of LIGO Data from the Third Observing Run*. https://dcc.ligo.org/LIGO-T2100045/public.

[188] F Matichard et al. "Seismic isolation of Advanced LIGO: Review of strategy, instrumentation and performance". In: *Classical and Quantum Gravity* 32.18 (Aug. 2015), p. 185003. DOI: 10.1088/0264-9381/32/18/185003. URL: https://doi.org/10.1088%2F0264-9381%2F32%2F18%2F185003.

[189] J Aasi et al. "The characterization of Virgo data and its impact on gravitational-wave searches". In: *Classical and Quantum Gravity* 29.15 (June 2012), p. 155002.

[190] Juan Calderon Bustillo et al. *Confusing head-on and precessing intermediate-mass binary black hole collisions*. https://dcc.ligo.org/LIGO-P1900363/public.

[191] Matthew Evans et al. *Design Stage RD for Cosmic Explorer: a Review of Critical Technologies*. https://dcc.cosmicexplorer.org/public/0163/P2100005/002/ce-design-rnd.pdf.

[192] T. Akutsu et al. *Overview of KAGRA: Calibration, detector characterization, physical environmental monitors, and the geophysics interferometer*. 2021. arXiv: 2009.09305 [gr-qc].

[193] JiJi Fan et al. "Dark-Disk Universe". In: *Phys. Rev. Lett.* 110 (21 May 2013), p. 211302. DOI: 10.1103/PhysRevLett.110.211302. URL: https://link.aps.org/doi/10.1103/PhysRevLett.110.211302.

[194] JiJi Fan et al. "Double-Disk Dark Matter". In: *Physics of the Dark Universe* 2.3 (Sept. 2013), pp. 139–156. DOI: 10.1016/j.dark.2013.07.001. URL: https://doi.org/10.1016%5C%2Fj.dark.2013.07.001.

[195] Jonathan L. Feng et al. "Hidden charged dark matter". In: *Journal of Cosmology and Astroparticle Physics* 2009.07 (July 2009), p. 004. DOI: 10.1088/1475-7516/2009/07/004. URL: https://dx.doi.org/10.1088/1475-7516/2009/07/004.

[196] V. Ferrari, L. Gualtieri, and P. Pani. *General Relativity and its Applications: Black Holes, Compact Stars and Gravitational Waves (1st ed.)* CRC Press., 2020.

[197] W. M. Folkner. "The LISA mission design". In: *AIP Conf. Proc.* 456.1 (1998). Ed. by W. M. Folkner, pp. 11–16. DOI: 10.1063/1.57401.

[198] W. Fong et al. "The Electromagnetic Counterpart of the Binary Neutron Star Merger LIGO/VIRGO GW170817. VIII. A Comparison to Cosmological Short-duration Gamma-ray Bursts". In: *Astrophys. J. Lett.* 848.2 (2017), p. L23. DOI: 10.3847/2041-8213/aa9018. arXiv: 1710.05438 [astro-ph.HE].

[199] R. L. Forward. "Wide Band Laser Interferometer Gravitational Radiation Experiment". In: *Phys. Rev. D* 17 (1978), pp. 379–390. DOI: 10.1103/PhysRevD.17.379.

[200] Francois Foucart. "Black-hole–neutron-star mergers: Disk mass predictions". In: *Physical Review D* 86.12 (Dec. 2012). DOI: 10.1103/physrevd.86.124007. URL: https://doi.org/10.1103%2Fphysrevd.86.124007.

[201] Paulo Cesar Carvalho Freire et al. "Eight New Millisecond Pulsars in NGC 6440 and NGC 6441". In: *Astrophys. J.* 675 (2008), p. 670. DOI: 10.1086/526338. arXiv: 0711.0925 [astro-ph].

[202] Raymond E. Frey. "LIGO: Status and recent results". In: *AIP Conf. Proc.* 928.1 (2007). Ed. by S. Mani Tripathi and Richard E. Breedon, pp. 11–22. DOI: 10.1063/1.2775891.

[203] M. E. Gertsenshtein and V. I. Pustovoit. "On the Detection of Low Frequency Gravitational Waves". In: *Sov. Phys. JETP* 16 (1962), p. 433.

[204] J. Glanzer et al. "Data quality up to the third observing run of advanced LIGO: Gravity Spy glitch classifications". In: *Class. Quant. Grav.* 40.6 (2023), p. 065004. DOI: 10.1088/1361-6382/acb633. arXiv: 2208.12849 [gr-qc].

[205] A. Goldstein et al. "An Ordinary Short Gamma-Ray Burst with Extraordinary Implications: Fermi-GBM Detection of GRB 170817A". In: *The Astrophysical Journal* 848.2 (Oct. 2017), p. L14. DOI: 10.3847/2041-8213/aa8f41.

[206] Andrew D. Gow et al. "Primordial black hole merger rates: distributions for multiple LIGO observables". In: *Journal of Cosmology and Astroparticle Physics* 2020.01 (Jan. 2020), pp. 031–031. DOI: 10.1088/1475-7516/2020/01/031. URL: https://doi.org/10.1088%5C%2F1475-7516%5C%2F2020%5C%2F01%5C%2F031.

[207] Anne M. Green and Bradley J. Kavanagh. "Primordial Black Holes as a dark matter candidate". In: *J. Phys. G* 48.4 (2021), p. 043001. DOI: 10.1088/1361-6471/abc534. arXiv: 2007.10722 [astro-ph.CO].

[208] Kim Griest, Agnieszka M. Cieplak, and Matthew J. Lehner. "Experimental Limits on Primordial Black Hole Dark Matter from the First 2 yr of Kepler Data". In: *Astrophys. J.* 786.2 (2014), p. 158. DOI: 10.1088/0004-637X/786/2/158. arXiv: 1307.5798 [astro-ph.CO].

[209] Zong-Kuan Guo and Yuan-Zhong Zhang. "Cosmology with a variable Chaplygin gas". In: *Phys. Lett. B* 645 (2007), pp. 326–329. DOI: 10.1016/j.physletb.2006.12.063. arXiv: astro-ph/0506091.

[210] Francisco Siddhartha Guzman and Tonatiuh Matos. "Answer to the comment about the letter entitled 'Scalar fields as dark matter in spiral galaxies'". In: (June 2000). arXiv: gr-qc/0006056.

[211] Francisco Siddhartha Guzman, Tonatiuh Matos, and H. B. Villegas. "Scalar fields as dark matter in spiral galaxies: Comparison with experiment". In: *Astron. Nachr.* 320 (1999), pp. 97–104.

[212] GWOSC. *GWOSC: O3a Summary*. https://gwosc.org/detector_status/O3a/.

[213] GWOSC. *GWOSC: O3b Summary*. https://gwosc.org/detector_status/O3b/.

[214] Chad Hanna et al. "Fast evaluation of multidetector consistency for real-time gravitational wave searches". In: *Phys. Rev. D* 101.2 (2020), p. 022003. DOI: 10.1103/PhysRevD.101.022003. arXiv: 1901.02227 [gr-qc].

[215] Mark Hannam et al. "Length requirements for numerical-relativity waveforms". In: *Phys. Rev. D* 82 (2010), p. 124052. DOI: 10.1103/PhysRevD.82.124052. arXiv: 1008.2961 [gr-qc].

[216] Mark Hannam et al. "Simple Model of Complete Precessing Black-Hole-Binary Gravitational Waveforms". In: *Physical Review Letters* 113.15 (Oct. 2014). DOI: 10.1103/physrevlett.113.151101. URL: https://doi.org/10.1103%2Fphysrevlett.113.151101.

[217] Gregory M. Harry et al. "Thermal noise in interferometric gravitational wave detectors due to dielectric optical coatings". In: *Class. Quant. Grav.* 19 (2002), pp. 897–918. DOI: 10.1088/0264-9381/19/5/305. arXiv: gr-qc/0109073.

[218] Ian Harry et al. "Searching for Gravitational Waves from Compact Binaries with Precessing Spins". In: *Phys. Rev. D* 94.2 (2016), p. 024012. DOI: 10.1103/PhysRevD.94.024012. arXiv: 1603.02444 [gr-qc].

[219] Ian W. Harry et al. "Investigating the effect of precession on searches for neutron-star-black-hole binaries with Advanced LIGO". In: *Phys. Rev. D* 89.2 (2014), p. 024010. DOI: 10.1103/PhysRevD.89.024010. arXiv: 1307.3562 [gr-qc].

[220] S. W. Hawking. "Black hole explosions". In: *Nature* 248 (1974), pp. 30–31. DOI: 10.1038/248030a0.

[221] S. W. Hawking. "Black holes in general relativity". In: *Commun. Math. Phys.* 25 (1972), pp. 152–166. DOI: 10.1007/BF01877517.

[222] S. W. Hawking and W. Israel. *Three Hundred Years of Gravitation*. 1989.

[223] Stephen Hawking. "Gravitationally collapsed objects of very low mass". In: *Mon. Not. Roy. Astron. Soc.* 152 (1971), p. 75.

[224] Richard Hills et al. "Concerns about modelling of the EDGES data". In: *Nature* 564.7736 (2018), E32–E34. DOI: 10.1038/s41586-018-0796-5. arXiv: 1805.01421 [astro-ph.CO].

[225] Tanja Hinderer et al. "Effects of neutron-star dynamic tides on gravitational waveforms within the effective-one-body approach". In: *Phys. Rev. Lett.* 116.18 (2016), p. 181101. DOI: 10.1103/PhysRevLett.116.181101. arXiv: 1602.00599 [gr-qc].

[226] Shaun Hooper et al. "Summed parallel infinite impulse response filters for low-latency detection of chirping gravitational waves". In: *Phys. Rev. D* 86 (2 July 2012), p. 024012. DOI: 10.1103/PhysRevD.86.024012. URL: https://link.aps.org/doi/10.1103/PhysRevD.86.024012.

[227] Kenta Hotokezaka et al. "Binary Neutron Star Mergers: Dependence on the Nuclear Equation of State". In: *Phys. Rev. D* 83 (2011), p. 124008. DOI: 10.1103/PhysRevD.83.124008. arXiv: 1105.4370 [astro-ph.HE].

[228] Kenta Hotokezaka et al. "Mass ejection from the merger of binary neutron stars". In: *Phys. Rev. D* 87 (2013), p. 024001. DOI: 10.1103/PhysRevD.87.024001. arXiv: 1212.0905 [astro-ph.HE].

[229] Wayne Hu, Rennan Barkana, and Andrei Gruzinov. "Cold and fuzzy dark matter". In: *Phys. Rev. Lett.* 85 (2000), pp. 1158–1161. DOI: 10.1103/PhysRevLett.85.1158. arXiv: astro-ph/0003365.

[230] Lam Hui et al. "Ultralight scalars as cosmological dark matter". In: *Phys. Rev. D* 95.4 (2017), p. 043541. DOI: 10.1103/PhysRevD.95.043541. arXiv: 1610.08297 [astro-ph.CO].

[231] R. A. Hulse and J. H. Taylor. "Discovery of a pulsar in a binary system". In: *Astrophys. J. Lett.* 195 (1975), pp. L51–L53. DOI: 10.1086/181708.

[232] Sascha Husa et al. "Frequency-domain gravitational waves from nonprecessing black-hole binaries. I. New numerical waveforms and anatomy of the signal". In: *Phys. Rev. D* 93.4 (2016), p. 044006. DOI: 10.1103/PhysRevD.93.044006. arXiv: 1508.07250 [gr-qc].

[233] Gert Hütsi et al. "Two populations of LIGO-Virgo black holes". In: *JCAP* 03 (2021), p. 068. DOI: 10.1088/1475-7516/2021/03/068. arXiv: 2012.02786 [astro-ph.CO].

[234] Derek Inman and Yacine Ali-Haımoud. "Early structure formation in primordial black hole cosmologies". In: *Phys. Rev. D* 100.8 (2019), p. 083528. DOI: 10.1103/PhysRevD.100.083528. arXiv: 1907.08129 [astro-ph.CO].

[235] Vid Iršič et al. "First constraints on fuzzy dark matter from Lyman-α forest data and hydrodynamical simulations". In: *Phys. Rev. Lett.* 119.3 (2017), p. 031302. DOI: 10.1103/PhysRevLett.119.031302. arXiv: 1703.04683 [astro-ph.CO].

[236] Piotr Jaranowski and Andrzej Krolak. "Gravitational-Wave Data Analysis. Formalism and Sample Applications: The Gaussian Case". In: *Living Rev. Rel.* 8 (2005), p. 3. DOI: 10.12942/lrr-2012-4. arXiv: 0711.1115 [gr-qc].

[237] Fredrick A. Jenet and Joseph D. Romano. "Understanding the gravitational-wave Hellings and Downs curve for pulsar timing arrays in terms of sound and electromagnetic waves". In: *Am. J. Phys.* 83 (2015), p. 635. DOI: 10.1119/1.4916358. arXiv: 1412.1142 [gr-qc].

[238] David E. Kaplan et al. "Atomic dark matter". In: *Journal of Cosmology and Astroparticle Physics* 2010.05 (May 2010), p. 021. DOI: 10.1088/1475-7516/2010/05/021. URL: https://dx.doi.org/10.1088/1475-7516/2010/05/021.

[239] David E. Kaplan et al. "Dark Atoms: Asymmetry and Direct Detection". In: *JCAP* 10 (2011), p. 011. DOI: 10.1088/1475-7516/2011/10/011. arXiv: 1105.2073 [hep-ph].

[240] Bradley J. Kavanagh, Daniele Gaggero, and Gianfranco Bertone. "Merger rate of a subdominant population of primordial black holes". In: *Phys. Rev. D* 98.2 (2018), p. 023536. DOI: 10.1103/PhysRevD.98.023536. arXiv: 1805.09034 [astro-ph.CO].

[241] Kyohei Kawaguchi et al. "Frequency-domain gravitational waveform models for inspiraling binary neutron stars". In: *Phys. Rev. D* 97.4 (2018), p. 044044. DOI: 10.1103/PhysRevD.97.044044. arXiv: 1802.06518 [gr-qc].

[242] Sebastian Khan et al. "Frequency-domain gravitational waves from nonprecessing black-hole binaries. II. A phenomenological model for the advanced detector era". In: *Phys. Rev. D* 93.4 (2016), p. 044007. DOI: 10.1103/PhysRevD.93.044007. arXiv: 1508.07253 [gr-qc].

[243] Stephen F. King and Alexander Merle. "Warm Dark Matter from keVins". In: *JCAP* 08 (2012), p. 016. DOI: 10.1088/1475-7516/2012/08/016. arXiv: 1205.0551 [hep-ph].

[244] S. Klimenko et al. "Method for detection and reconstruction of gravitational wave transients with networks of advanced detectors". In: *Phys. Rev. D* 93.4 (2016), p. 042004. DOI: 10.1103/PhysRevD.93.042004. arXiv: 1511.05999 [gr-qc].

[245] Bence Kocsis et al. "Hidden Universality in the Merger Rate Distribution in the Primordial Black Hole Scenario". In: *The Astrophysical Journal* 854.1 (Feb. 2018), p. 41. DOI: 10.3847/1538-4357/aaa7f4. URL: https://doi.org/10.3847%5C%2F1538-4357%5C%2Faaa7f4.

[246] Polychronis S. Koliogiannis, Alkiviadis Kanakis-Pegios, and Charalampos C. Moustakidis. "Neutron Stars and Gravitational Waves: The Key Role of Nuclear Equation of State". In: *Foundations* 1.2 (2021), pp. 217–255. DOI: 10.3390/foundations1020017. arXiv: 2110.13557 [nucl-th].

[247] Koutarou Kyutoku, Masaru Shibata, and Keisuke Taniguchi. "Gravitational waves from nonspinning black hole-neutron star binaries: dependence on equations of state". In: *Phys. Rev. D* 82 (2010). [Erratum: Phys.Rev.D 84, 049902 (2011)], p. 044049. DOI: 10.1103/PhysRevD.82.044049. arXiv: 1008.1460 [astro-ph.HE].

[248] Benjamin D. Lackey et al. "Extracting equation of state parameters from black hole-neutron star mergers. I. Nonspinning black holes". In: *Phys. Rev. D* 85 (2012), p. 044061. DOI: 10.1103/PhysRevD.85.044061. arXiv: 1109.3402 [astro-ph.HE].

[249] Benjamin D. Lackey et al. "Surrogate model for an aligned-spin effective one body waveform model of binary neutron star inspirals using Gaussian process regression". In: *Phys. Rev. D* 100.2 (2019), p. 024002. DOI: 10.1103/PhysRevD.100.024002. arXiv: 1812.08643 [gr-qc].

[250] Ranjan Laha. "Primordial Black Holes as a Dark Matter Candidate Are Severely Constrained by the Galactic Center 511 keV γ -Ray Line". In: *Phys. Rev. Lett.* 123.25 (2019), p. 251101. DOI: 10.1103/PhysRevLett.123.251101. arXiv: 1906.09994 [astro-ph.HE].

[251] Ranjan Laha, Julian B. Muñoz, and Tracy R. Slatyer. "INTEGRAL constraints on primordial black holes and particle dark matter". In: *Phys. Rev. D* 101.12 (2020), p. 123514. DOI: 10.1103/PhysRevD.101.123514. arXiv: 2004.00627 [astro-ph.CO].

[252] *Laser Interferometer Space Antenna*. URL: https://lisa.nasa.gov.

[253] Paul D. Lasky. "Gravitational Waves from Neutron Stars: A Review". In: *Publications of the Astronomical Society of Australia* 32 (2015). DOI: 10.1017/pasa.2015.35. URL: https://doi.org/10.1017%2Fpasa.2015.35.

[254] J. M. Lattimer and M. Prakash. "The physics of neutron stars". In: *Science* 304 (2004), pp. 536–542. DOI: 10.1126/science.1090720. arXiv: astro-ph/0405262.

[255] J. M. Lattimer and D. N. Schramm. "Black-hole-neutron-star collisions". In: *Astrophys. J. Lett.* 192 (1974), p. L145. DOI: 10.1086/181612.

[256] *LIGO India*. URL: https://www.ligo-india.in.

[257] LIGO Scientific Collaboration. *LIGO Algorithm Library - LALSuite*. free software (GPL). 2018. DOI: 10.7935/GT1W-FZ16.

[258] Andrea N. Lommen. "Pulsar timing arrays: the promise of gravitational wave detection". In: *Rept. Prog. Phys.* 78.12 (2015), p. 124901. DOI: 10.1088/0034-4885/78/12/124901.

[259] Alexander Lukanenkov. "Gravitational Telescope". In: *Journal of High Energy Physics, Gravitation and Cosmology* 02 (Jan. 2016), pp. 209–225. DOI: 10.4236/jhepgc.2016.22019.

[260] Michele Maggiore. *Gravitational Waves Volume 1: Theory and Experiments*. London: Oxford University Press, 2008.

[261] Jiao-Jiao Mao et al. "Residual gas damping noise in constrained volume in space-borne gravitational wave detection". In: *Class. Quant. Grav.* 40.7 (2023), p. 075015. DOI: 10.1088/1361-6382/acc167.

[262] R. Margutti et al. "The Electromagnetic Counterpart of the Binary Neutron Star Merger LIGO/Virgo GW170817. V. Rising X-Ray Emission from an Off-axis Jet". In: *The Astrophysical Journal Letters* 848.2 (Oct. 2017), p. L20. DOI: 10.3847/2041-8213/aa9057. URL: https://dx.doi.org/10.3847/2041-8213/aa9057.

[263] Tonatiuh Matos and Francisco Siddhartha Guzman. "Scalar fields as dark matter in spiral galaxies". In: *Class. Quant. Grav.* 17 (2000), pp. L9–L16. DOI: 10.1088/0264-9381/17/1/102. arXiv: gr-qc/9810028.

[264] Jessica McIver. "Data Quality Studies of Enhanced Interferometric Gravitational Wave Detectors". In: *Class. Quant. Grav.* 29 (2012). Ed. by Mark Hannam et al., p. 124010. DOI: 10.1088/0264-9381/29/12/124010. arXiv: 1204.2497 [gr-qc].

[265] D. J. A. McKechan. "On the use of higher order waveforms in the search for gravitational waves emitted by compact binary coalescences". In: *arXiv* (2011).

[266] Olga Mena et al. "Constraining the primordial black hole abundance with 21-cm cosmology". In: *Phys. Rev. D* 100.4 (2019), p. 043540. DOI: 10.1103/PhysRevD.100.043540. arXiv: 1906.07735 [astro-ph.CO].

[267] Cody Messick et al. "Analysis Framework for the Prompt Discovery of Compact Binary Mergers in Gravitational-wave Data". In: *Phys. Rev. D* 95.4 (2017), p. 042001. DOI: 10.1103/PhysRevD.95.042001. arXiv: 1604.04324 [astro-ph.IM].

[268] P. Meszaros. "Primeval black holes and galaxy formation". In: *Astron. Astrophys.* 38 (1975), pp. 5–13.

[269] S. D. Mohanty. "Hierarchical search strategy for the detection of gravitational waves from coalescing binaries: Extension to postNewtonian wave forms". In: *Phys. Rev. D* 57 (1998), pp. 630–658. DOI: 10.1103/PhysRevD.57.630. arXiv: gr-qc/9703081.

[270] S. D. Mohanty and S. V. Dhurandhar. "A hierarchical search strategy for the detection of gravitational waves from coalescing binaries". In: *Phys. Rev. D* 54 (1996), pp. 7108–7128. DOI: 10.1103/PhysRevD.54.7108.

[271] Miguel A. Monroy-Rodriguez and Christine Allen. "THE END OF THE MACHO ERA, REVISITED: NEW LIMITS ON MACHO MASSES FROM HALO WIDE BINARIES". In: *The Astrophysical Journal* 790.2 (July 2014), p. 159. DOI: 10.1088/0004-637x/790/2/159. URL: https://doi.org/10.1088/0004-637X/790/2/159.

[272] G. E. Moss, L. R. Miller, and R. L. Forward. "Photon-noise-limited laser transducer for gravitational antenna". In: *Appl. Opt.* 10 (1971), pp. 2495–2498. DOI: 10.1364/AO.10.002495.

[273] Przemek Mróz et al. "No large population of unbound or wide-orbit Jupiter-mass planets". In: *Nature* 548.7666 (July 2017), pp. 183–186. DOI: 10.1038/nature23276. URL: https://doi.org/10.1038%2Fnature23276.

[274] S. Mukherjee, R. Obaid, and B. Matkarimov. "Classification of glitch waveforms in gravitational wave detector characterization". In: *J. Phys. Conf. Ser.* 243 (2010). Ed. by Fulvio Ricci, p. 012006. DOI: 10.1088/1742-6596/243/1/012006.

[275] Riccardo Murgia et al. "Lyman-α Forest Constraints on Primordial Black Holes as Dark Matter". In: *Phys. Rev. Lett.* 123.7 (2019), p. 071102. DOI: 10.1103/PhysRevLett.123.071102. arXiv: 1903.10509 [astro-ph.CO].

[276] Takashi Nakamura et al. "Gravitational waves from coalescing black hole MACHO binaries". In: *Astrophys. J. Lett.* 487 (1997), pp. L139–L142. DOI: 10.1086/310886. arXiv: astro-ph/9708060.

[277] Raghav Narasimha et al. "Escaping the Pair-Instability Mass Gap with the Help of Dark Matter". In: *Phys. Sci. Forum* 7.1 (2023), p. 24. DOI: 10.3390/ECU2023-14059.

[278] M. Nicholl et al. "The Electromagnetic Counterpart of the Binary Neutron Star Merger LIGO/VIRGO GW170817. III. Optical and UV Spectra of a Blue Kilonova From Fast Polar Ejecta". In: *Astrophys. J. Lett.* 848.2 (2017), p. L18. DOI: 10.3847/2041-8213/aa9029. arXiv: 1710.05456 [astro-ph.HE].

[279] T. M. Niebauer et al. "Nonstationary shot noise and its effect on the sensitivity of interferometers". In: *Phys. Rev. A* 43.9 (1991), p. 5022. DOI: 10.1103/PhysRevA.43.5022.

[280] Hiroko Niikura et al. "Microlensing constraints on primordial black holes with Subaru/HSC Andromeda observations". In: *Nature Astron.* 3.6 (2019), pp. 524–534. DOI: 10.1038/s41550-019-0723-1. arXiv: 1701.02151 [astro-ph.CO].

[281] Hiroko Niikura et al. "Constraints on Earth-mass primordial black holes from OGLE 5-year microlensing events". In: *Phys. Rev. D* 99.8 (2019), p. 083503. DOI: 10.1103/PhysRevD.99.083503. arXiv: 1901.07120 [astro-ph.CO].

[282] Alex Nitz et al. *gwastro/pycbc: v2.1.2 release of PyCBC*. Version v2.1.2. May 2023. DOI: 10.5281/zenodo.7885796. URL: https://doi.org/10.5281/zenodo.7885796.

[283] Alexander H. Nitz and Yi-Fan Wang. "Broad search for gravitational waves from subsolar-mass binaries through LIGO and Virgo's third observing run". In: *Phys. Rev. D* 106.2 (2022), p. 023024. DOI: 10.1103/PhysRevD.106.023024. arXiv: 2202.11024 [astro-ph.HE].

[284] Alexander H. Nitz and Yi-Fan Wang. "Search for Gravitational Waves from the Coalescence of Subsolar-Mass Binaries in the First Half of Advanced LIGO and Virgo's Third Observing Run". In: *Phys. Rev. Lett.* 127.15 (2021), p. 151101. DOI: 10.1103/PhysRevLett.127.151101. arXiv: 2106.08979 [astro-ph.HE].

[285] Alexander H. Nitz et al. "Detecting Binary Compact-object Mergers with Gravitational Waves: Understanding and Improving the Sensitivity of the PyCBC Search". In: *The Astrophysical Journal* 849.2 (Nov. 2017), p. 118. DOI: 10.3847/1538-4357/aa8f50. URL: https://doi.org/10.3847%5C%2F1538-4357%5C%2Faa8f50.

[286] NobelPrize.org. *Press release: Gravitational waves finally captured*. https://www.nobelprize.org/prizes/physics/2017/press-release/.

[287] Brendan O'Brien et al. "Detection of LIGO-Virgo binary black holes in the pair-instability mass gap". In: *Phys. Rev. D* 104.8 (2021), p. 082003. DOI: 10.1103/PhysRevD.104.082003. arXiv: 2106.00605 [gr-qc].

[288] Roland Oechslin, H. -T. Janka, and A. Marek. "Relativistic neutron star merger simulations with non-zero temperature equations of state. 1. Variation of binary parameters and equation of state". In: *Astron. Astrophys.* 467 (2007), p. 395. DOI: 10.1051/0004-6361:20066682. arXiv: astro-ph/0611047.

[289] M. Oertel et al. "Equations of state for supernovae and compact stars". In: *Rev. Mod. Phys.* 89.1 (2017), p. 015007. DOI: 10.1103/RevModPhys.89.015007. arXiv: 1610.03361 [astro-ph.HE].

[290] Masamune Oguri et al. "Understanding caustic crossings in giant arcs: Characteristic scales, event rates, and constraints on compact dark matter". In: *Physical Review D* 97.2 (Jan. 2018). DOI: 10.1103/physrevd.97.023518. URL: https://doi.org/10.1103/PhysRevD.97.023518.

[291] J. R. Oppenheimer and H. Snyder. "On Continued gravitational contraction". In: *Phys. Rev.* 56 (1939), pp. 455–459. DOI: 10.1103/PhysRev.56.455.

[292] J. R. Oppenheimer and G. M. Volkoff. "On Massive Neutron Cores". In: *Phys. Rev.* 55 (4 Feb. 1939), pp. 374–381. DOI: 10.1103/PhysRev.55.374. URL: https://link.aps.org/doi/10.1103/PhysRev.55.374.

[293] J. R. Oppenheimer and G. M. Volkoff. "On massive neutron cores". In: *Phys. Rev.* 55 (1939), pp. 374–381. DOI: 10.1103/PhysRev.55.374.

[294] Serguei Ossokine et al. "Multipolar effective-one-body waveforms for precessing binary black holes: Construction and validation". In: *Physical Review D* 102.4 (Aug. 2020). DOI: 10.1103/physrevd.102.044055. URL: https://doi.org/10.1103%5C%2Fphysrevd.102.044055.

[295] J. P. Ostriker, P. J. E. Peebles, and A. Yahil. "The size and mass of galaxies, and the mass of the universe". In: *Astrophys. J. Lett.* 193 (1974), pp. L1–L4. DOI: 10.1086/181617.

[296] Jeremiah Paul Ostriker and Philip JE Peebles. "A numerical study of the stability of flattened galaxies: or, can cold galaxies survive?" In: *The Astrophysical Journal* 186 (1973), pp. 467–480.

[297] Benjamin J. Owen. "Search templates for gravitational waves from inspiraling binaries: Choice of template spacing". In: *Phys. Rev. D* 53 (12 June 1996), pp. 6749–6761. DOI: 10.1103/PhysRevD.53.6749. URL: https://link.aps.org/doi/10.1103/PhysRevD.53.6749.

[298] Benjamin J. Owen and B. S. Sathyaprakash. "Matched filtering of gravitational waves from inspiraling compact binaries: Computational cost and template placement". In: *Phys. Rev. D* 60 (2 June 1999), p. 022002. DOI: 10.1103/PhysRevD.60.022002. URL: https://link.aps.org/doi/10.1103/PhysRevD.60.022002.

[299] Bohdan Paczynski. "Gravitational microlensing by the galactic halo". In: *Astrophys. J.* 304 (1986), pp. 1–5. DOI: 10.1086/164140.

[300] Michael A. Page et al. "Quantum noise enhancement for gravitational wave detectors: Status of squeezed vacuum research at TAMA and KAGRA". In: *PoS* ICRC2023 (2023), p. 1565. DOI: 10.22323/1.444.1565.

[301] Yi Pan et al. "A Physical template family for gravitational waves from precessing binaries of spinning compact objects: Application to single spin binaries". In: *Phys. Rev. D* 69 (2004). [Erratum: Phys.Rev.D 74, 029905 (2006)], p. 104017. DOI: 10.1103/PhysRevD.69.104017. arXiv: gr-qc/0310034.

[302] Yi Pan et al. "Inspiral-merger-ringdown waveforms of spinning, precessing black-hole binaries in the effective-one-body formalism". In: *Phys. Rev. D* 89.8 (2014), p. 084006. DOI: 10.1103/PhysRevD.89.084006. arXiv: 1307.6232 [gr-qc].

[303] Khun Sang Phukon et al. "The hunt for sub-solar primordial black holes in low mass ratio binaries is open". In: (May 2021). arXiv: 2105.11449 [astro-ph.CO].

[304] Vivian Poulin et al. "CMB bounds on disk-accreting massive primordial black holes". In: *Phys. Rev. D* 96.8 (2017), p. 083524. DOI: 10.1103/PhysRevD.96.083524. arXiv: 1707.04206 [astro-ph.CO].

[305] Adam Pound and Barry Wardell. "Black hole perturbation theory and gravitational self-force". In: (Jan. 2021). DOI: 10.1007/978-981-15-4702-7_38-1. arXiv: 2101.04592 [gr-qc].

[306] Jade Powell et al. "Classification methods for noise transients in advanced gravitational-wave detectors II: performance tests on Advanced LIGO data". In: *Class. Quant. Grav.* 34.3 (2017), p. 034002. DOI: 10.1088/1361-6382/34/3/034002. arXiv: 1609.06262 [astro-ph.IM].

[307] David Radice et al. "Binary Neutron Star Mergers: Mass Ejection, Electromagnetic Counterparts and Nucleosynthesis". In: *Astrophys. J.* 869.2 (2018), p. 130. DOI: 10.3847/1538-4357/aaf054. arXiv: 1809.11161 [astro-ph.HE].

[308] David Radice et al. "Dynamical Mass Ejection from Binary Neutron Star Mergers". In: *Mon. Not. Roy. Astron. Soc.* 460.3 (2016), pp. 3255–3271. DOI: 10.1093/mnras/stw1227. arXiv: 1601.02426 [astro-ph.HE].

[309] Martti Raidal, Ville Vaskonen, and Hardi Veermäe. "Gravitational Waves from Primordial Black Hole Mergers". In: *JCAP* 09 (2017), p. 037. DOI: 10.1088/1475-7516/2017/09/037. arXiv: 1707.01480 [astro-ph.CO].

[310] Martti Raidal et al. "Formation and Evolution of Primordial Black Hole Binaries in the Early Universe". In: *JCAP* 02 (2019), p. 018. DOI: 10.1088/1475-7516/2019/02/018. arXiv: 1812.01930 [astro-ph.CO].

[311] David Reitze et al. "Cosmic Explorer: The U.S. Contribution to Gravitational-Wave Astronomy beyond LIGO". In: (2019). arXiv: 1907.04833 [astro-ph.IM].

[312] Arianna I. Renzini et al. "Stochastic Gravitational-Wave Backgrounds: Current Detection Efforts and Future Prospects". In: *Galaxies* (2022). URL: https://api.semanticscholar.org/CorpusID:246442002.

[313] MS Roberts and AH Rots. "Comparison of rotation curves of different galaxy types". In: *Astronomy and Astrophysics, Vol. 26, p. 483-485 (1973)* 26 (1973), pp. 483–485.

[314] Florent Robinet. "Data quality in gravitational wave bursts and inspiral searches in the second Virgo Science Run". In: *Class. Quant. Grav.* 27 (2010). Ed. by Fulvio Ricci, p. 194012. DOI: 10.1088/0264-9381/27/19/194012.

[315] S. Rosswog et al. "Mass ejection in neutron star mergers". In: *Astron. Astrophys.* 341 (1999), pp. 499–526. arXiv: astro-ph/9811367.

[316] Javier Roulet et al. "Template bank for compact binary coalescence searches in gravitational wave data: A general geometric placement algorithm". In: *Phys. Rev. D* 99 (12 June 2019), p. 123022. DOI: 10.1103/PhysRevD.99.123022. URL: https://link.aps.org/doi/10.1103/PhysRevD.99.123022.

[317] V. C. Rubin, N. Thonnard, and W. K. Ford Jr. "Rotational properties of 21 SC galaxies with a large range of luminosities and radii, from NGC 4605 /R = 4kpc/ to UGC 2885 /R = 122 kpc/". In: *Astrophys. J.* 238 (1980), p. 471. DOI: 10.1086/158003.

[318] Vera C. Rubin and W. Kent Ford Jr. "Rotation of the Andromeda Nebula from a Spectroscopic Survey of Emission Regions". In: *Astrophys. J.* 159 (1970), pp. 379–403. DOI: 10.1086/150317.

[319] Achim Weiss Rudolf Kippenhahn Alfred Weigert. *Stellar Structure and Evolution*. Heidelberg: Springer-Verlag Berlin, 2012.

[320] Surabhi Sachdev et al. "The GstLAL Search Analysis Methods for Compact Binary Mergers in Advanced LIGO's Second and Advanced Virgo's First Observing Runs". In: (2019). arXiv: 1901.08580 [gr-qc].

[321] Jam Sadiq et al. "Hybrid waveforms for generic precessing binaries for gravitational-wave data analysis". In: *Phys. Rev. D* 102.2 (2020), p. 024012. DOI: 10.1103/PhysRevD.102.024012. arXiv: 2001.07109 [gr-qc].

[322] Peter R. Saulson et al. "INTERFEROMETRIC GRAVITATIONAL WAVE DETECTION AT MIT". In: *Conf. Proc. C* 861214 (1986). Ed. by M. P. Ulmer, pp. 15–17.

[323] Didier Saumon, Simon Blouin, and Pier-Emmanuel Tremblay. "Current challenges in the physics of white dwarf stars". In: *Phys. Rept.* 988 (2022), pp. 1–63. DOI: 10.1016/j.physrep.2022.09.001. arXiv: 2209.02846 [astro-ph.SR].

[324] V. Savchenko et al. "INTEGRAL Detection of the First Prompt Gamma-Ray Signal Coincident with the Gravitational-wave Event GW170817". In: *The Astrophysical Journal Letters* 848.2 (Oct. 2017), p. L15. DOI: 10.3847/2041-8213/aa8f94. URL: https://dx.doi.org/10.3847/2041-8213/aa8f94.

[325] Pasquale D. Serpico et al. "Cosmic microwave background bounds on primordial black holes including dark matter halo accretion". In: *Phys. Rev. Res.* 2.2 (2020), p. 023204. DOI: 10.1103/PhysRevResearch.2.023204. arXiv: 2002.10771 [astro-ph.CO].

[326] Sarah Shandera, Donghui Jeong, and Henry S. Grasshorn Gebhardt. "Gravitational Waves from Binary Mergers of Subsolar Mass Dark Black Holes". In: *Phys. Rev. Lett.* 120.24 (2018), p. 241102. DOI: 10.1103/PhysRevLett.120.241102. arXiv: 1802.08206 [astro-ph.CO].

[327] Sarah Shandera, Donghui Jeong, and Henry S. Grasshorn Gebhardt. "Gravitational Waves from Binary Mergers of Subsolar Mass Dark Black Holes". In: *Physical Review Letters* 120.24 (June 2018). DOI: 10.1103/physrevlett.120.241102. URL: https://doi.org/10.1103%5C%2Fphysrevlett.120.241102.

[328] S. L. Shapiro and S. A. Teukolsky. *Black holes, white dwarfs, and neutron stars: The physics of compact objects*. 1983. ISBN: 978-0-471-87316-7.

[329] Erin S. Sheldon et al. "CROSS-CORRELATION WEAK LENSING OF SDSS GALAXY CLUSTERS. III. MASS-TO-LIGHT RATIOS". In: *The Astrophysical Journal* 703.2 (Sept. 2009), pp. 2232–2248. DOI: 10.1088/0004-637x/703/2/2232. URL: https://doi.org/10.1088%2F0004-637x%2F703%2F2%2F2232.

[330] D. Shoemaker et al. "Noise Behavior of the Garching 30-meter Prototype Gravitational Wave Detector". In: *Phys. Rev. D* 38 (1988), pp. 423–432. DOI: 10.1103/PhysRevD.38.423.

[331] Magdalena Sieniawska and Michal Bejger. "Continuous Gravitational Waves from Neutron Stars: Current Status and Prospects". In: *Universe* 5.11 (Oct. 2019), p. 217. DOI: 10.3390/universe5110217. URL: https://doi.org/10.3390%2Funiverse5110217.

[332] Peter H Sims and Jonathan C Pober. "Testing for calibration systematics in the EDGES low-band data using Bayesian model selection". In: *Monthly Notices of the Royal Astronomical Society* 492.1 (Dec. 2019), pp. 22–38. DOI: 10.1093/mnras/stz3388. URL: https://doi.org/10.1093%2Fmnras%2Fstz3388.

[333] Divya Singh et al. "Gravitational-wave limit on the Chandrasekhar mass of dark matter". In: *Phys. Rev. D* 104 (4 Aug. 2021), p. 044015. DOI: 10.1103/PhysRevD.104.044015. URL: https://link.aps.org/doi/10.1103/PhysRevD.104.044015.

[334] Divya Singh et al. "Gravitational-wave limit on the Chandrasekhar mass of dark matter". In: *Physical Review D* 104.4 (Aug. 2021). DOI: 10.1103/physrevd.104.044015. URL: https://doi.org/10.1103%5C%2Fphysrevd.104.044015.

[335] M. Soares-Santos et al. "The Electromagnetic Counterpart of the Binary Neutron Star Merger LIGO/Virgo GW170817. I. Discovery of the Optical Counterpart Using the Dark Energy Camera". In: *Astrophys. J. Lett.* 848.2 (2017), p. L16. DOI: 10.3847/2041-8213/aa9059. arXiv: 1710.05459 [astro-ph.HE].

[336] David N. Spergel and Paul J. Steinhardt. "Observational evidence for selfinteracting cold dark matter". In: *Phys. Rev. Lett.* 84 (2000), pp. 3760–3763. DOI: 10.1103/PhysRevLett.84.3760. arXiv: astro-ph/9909386.

[337] Jan Steinhoff et al. "Dynamical Tides in General Relativity: Effective Action and Effective-One-Body Hamiltonian". In: *Phys. Rev. D* 94.10 (2016), p. 104028. DOI: 10.1103/PhysRevD.94.104028. arXiv: 1608.01907 [gr-qc].

[338] B. Steltner et al. "Deep Einstein@Home All-sky Search for Continuous Gravitational Waves in LIGO O3 Public Data". In: *Astrophys. J.* 952.1 (2023), p. 55. DOI: 10.3847/1538-4357/acdad4. arXiv: 2303.04109 [gr-qc].

[339] Daniel Sudarsky. "Comment about the letter entitled 'Scalar fields as dark matter in spiral galaxies'". In: *Class. Quant. Grav.* 18 (2001), p. 2851. DOI: 10.1088/0264-9381/18/14/401. arXiv: gr-qc/0006051.

[340] Yudai Suwa et al. "On the minimum mass of neutron stars". In: *Mon. Not. Roy. Astron. Soc.* 481.3 (2018), pp. 3305–3312. DOI: 10.1093/mnras/sty2460. arXiv: 1808.02328 [astro-ph.HE].

[341] E. Symbalisty and D. N. Schramm. "Neutron Star Collisions and the r-Process". In: 22 (Jan. 1982), p. 143.

[342] Rodrigo Tenorio, David Keitel, and Alicia M. Sintes. "Search Methods for Continuous Gravitational-Wave Signals from Unknown Sources in the Advanced-Detector Era". In: *Universe* 7.12 (2021), p. 474. DOI: 10.3390/universe7120474. arXiv: 2111.12575 [gr-qc].

[343] Todd A. Thompson et al. "A noninteracting low-mass black hole–giant star binary system". In: *Science* 366.6465 (2019), pp. 637–640. DOI: 10.1126/science.aau4005. eprint: https://www.science.org/doi/pdf/10.1126/science.aau4005. URL: https://www.science.org/doi/abs/10.1126/science.aau4005.

[344] Kip Thorne and Rai Weiss. *A Brief History of LIGO*. https://www.caltech.edu/about/news/brief-history-ligo.

[345] P. Tisserand et al. "Limits on the Macho Content of the Galactic Halo from the EROS-2 Survey of the Magellanic Clouds". In: *Astron. Astrophys.* 469 (2007), pp. 387–404. DOI: 10.1051/0004-6361:20066017. arXiv: astro-ph/0607207.

[346] Richard C. Tolman. "Static Solutions of Einstein's Field Equations for Spheres of Fluid". In: *Phys. Rev.* 55 (4 Feb. 1939), pp. 364–373. DOI: 10.1103/PhysRev.55.364. URL: https://link.aps.org/doi/10.1103/PhysRev.55.364.

[347] Virginia Trimble. "Existence and Nature of Dark Matter in the Universe". In: *Ann. Rev. Astron. Astrophys.* 25 (1987), pp. 425–472. DOI: 10.1146/annurev.aa.25.090187.002233.

[348] Samantha A. Usman et al. "The PyCBC search for gravitational waves from compact binary coalescence". In: *Class. Quant. Grav.* 33.21 (2016), p. 215004. DOI: 10.1088/0264-9381/33/21/215004. arXiv: 1508.02357 [gr-qc].

[349] Stefano Valenti et al. "The discovery of the electromagnetic counterpart of GW170817: kilonova AT 2017gfo/DLT17ck". In: *Astrophys. J. Lett.* 848.2 (2017), p. L24. DOI: 10.3847/2041-8213/aa8edf. arXiv: 1710.05854 [astro-ph.HE].

[350] Ville Vaskonen and Hardi Veermäe. "Lower bound on the primordial black hole merger rate". In: *Phys. Rev. D* 101.4 (2020), p. 043015. DOI: 10.1103/PhysRevD.101.043015. arXiv: 1908.09752 [astro-ph.CO].

[351] Matteo Viel et al. "Constraining warm dark matter candidates including sterile neutrinos and light gravitinos with WMAP and the Lyman-alpha forest". In: *Phys. Rev. D* 71 (2005), p. 063534. DOI: 10.1103/PhysRevD.71.063534. arXiv: astro-ph/0501562.

[352] Pablo Villanueva-Domingo and Kiyotomo Ichiki. "21 cm Forest Constraints on Primordial Black Holes". In: (Apr. 2021). DOI: 10.1093/pasj/psab119. arXiv: 2104.10695 [astro-ph.CO].

[353] Pablo Villanueva-Domingo, Olga Mena, and Sergio Palomares-Ruiz. "A Brief Review on Primordial Black Holes as Dark Matter". In: *Frontiers in Astronomy and Space Sciences* 8 (May 2021). DOI: 10.3389/fspas.2021.681084. URL: https://doi.org/10.3389/fspas.2021.681084.

[354] S. J. Waldmann. "Status of LIGO at the start of the fifth science run". In: *Class. Quant. Grav.* 23 (2006). Ed. by M. Diaz and S. Mohanty, S653–S660. DOI: 10.1088/0264-9381/23/19/S03.

[355] Shinya Wanajo et al. "Production of all the *r*-process nuclides in the dynamical ejecta of neutron star mergers". In: *Astrophys. J. Lett.* 789 (2014), p. L39. DOI: 10.1088/2041-8205/789/2/L39. arXiv: 1402.7317 [astro-ph.SR].

[356] J. Weber. "Evidence for Discovery of Gravitational Radiation". In: *Phys. Rev. Lett.* 22 (1969), pp. 1320–1324.

[357] John T. Whelan. *The geometry of gravitational wave detection*. https://dcc.ligo.org/public/0106/T1300666/003/Whelan_geometry.pdf.

[358] Chris Whittle et al. "Unification of Thermal and Quantum Noises in Gravitational-Wave Detectors". In: *Phys. Rev. Lett.* 130.24 (2023), p. 241401. DOI: 10.1103/PhysRevLett.130.241401. arXiv: 2301.00338 [astro-ph.IM].

[359] Clifford M. Will. "Gravitational waves from inspiraling compact binaries: A PostNewtonian approach". In: *8th Nishinomiya-Yukawa Memorial Symposium: Relativistic Cosmology*. Mar. 1994, pp. 83–98. arXiv: gr-qc/9403033.

[360] S. E. Woosley and Alexander Heger. "The Pair-Instability Mass Gap for Black Holes". In: *Astrophys. J. Lett.* 912.2 (2021), p. L31. DOI: 10.3847/2041-8213/abf2c4. arXiv: 2103.07933 [astro-ph.SR].

[361] Hirotaka Yuzurihara. "Detector characterization of KAGRA for the fourth observing run". In: *PoS* ICRC2023 (2023), p. 1564. DOI: 10.22323/1.444.1564.

[362] Ya. B. Zel'dovich and I. D. Novikov. "The Hypothesis of Cores Retarded during Expansion and the Hot Cosmological Model". In: *Soviet Astron. AJ (Engl. Transl.)*, 10 (1967), p. 602.

[363] Joshua Ziegler and Katherine Freese. "A Gap No More: Mechanism for Non-Nuclear Energy to Fill in the Black Hole Mass Gap". In: (Dec. 2022). arXiv: 2212.13903 [astro-ph.HE].

[364] F. Zwicky. "Die Rotverschiebung von extragalaktischen Nebeln". In: *Helv. Phys. Acta* 6 (1933), pp. 110–127. DOI: 10.1007/s10714-008-0707-4.